THE UNIVERSITY *of* EDINBURGH

Triphenylamine-based Hole Transport Materials for Perovskite Solar Cells

Rosinda Fuentes Pineda

Thesis submitted for the Degree of PhD

The University of Edinburgh

March 2018

To my family

Declaration

I hereby declare that this thesis has been composed entirely by me and that the work is a presentation of my own research project except where clearly stated either in acknowledgement, reference or text. It has not been submitted in whole or part for any other degree, diploma or other qualification.

Rosinda Fuentes Pineda.

Acknowledgements

This dissertation would not have been possible without the support and help of many people. First and foremost, I would like to thank my supervisor Professor Neil Robertson for his guidance and encouragement, for all the stimulating discussions and for giving me a lot of freedom in my projects and his advice whenever I needed. I am particularly grateful to CONACyT for trusting me and financing my studies throughout these years.

I also would like to express my deepest gratitude to many people at The University of Edinburgh that have helped me during my PhD. To the Edinburgh Crystallography Service, especially Dr. Gary S. Nichol for resolving the crystal structures and performing the powder diffraction and differential scanning calorimetry measurements. I also extend my gratitude to Dr. Ben Lake and Professor Michael Shaver for the preparation of the polymeric molecules. Likewise, I thank Dr. Oleg Nerushev and Professor Eleanor Campbell for allowing me to use the evaporator where the first perovskites solar cells were fabricated and specially to Oleg for his help and patience in teaching me how to use the equipment.

I have been lucky enough to collaborate with some fantastic groups from many places. I gratefully acknowledge Dr. Irene Sanchez Molina and Dr. Saif A. Haque for the time-correlated single photon counting measurements and also, for welcoming me at Imperial College London to measure the transient absorption spectroscopy. Similarly, to Professor Dima Perepichka and Dr. Rajesh Malakalapalli for welcoming me at Mcgill University and the successful collaboration. My gratitude is also extended to Dr. Joel Troughton and Dr. Trystan Watson for the fabrication and testing of the solar cells reported in this work.

I would like to recognize all members from the Robertson group, both past and present, for their friendship, and useful discussions with special mention to Aruna Ivaturi,

Helen Benjamin, Yaroslav Zems, German Soto and Yue Hu. Thanks to Yue for being my first friend in Edinburgh and all the fun. To German for his support and friendship. To our postdocs at the Robertson group: Dr. Aruna Ivaturi, Dr. Michal Maciejczyk and Dr. Helen Benjamin for their advice in device fabrication and synthesis. Thanks to Yaroslav Zems for the large-scale synthesis of 1,3-difluoro-2-nitrobenzene, all his help in the synthesis of the star-shaped molecules, the time playing videogames and all the lovely moments we spent together.

I also would like to thank to all my previous supervisors Dr. Fernando Cortés Guzmán, Benjamín Ruíz Loyola, José Manuel Méndez Stivalet, Yvonne Grillasca Rangel, Gustavo García de la Mora and José Guadalupe López Cortés for all their support during my PhD application. Thanks to my friends in México specially to Ricardo, Fernanda and Flor for dreaming together and for not making it all about the academic stuff.

Last but not least, I am profoundly grateful to my mother, my father, my brother, my sisters and my niece for their unconditional love and support through all these years and for being my magical relationship and my day-to-day motivation to smile. I dedicate my work to all of you. I would like to give a special mention to the person I admire the most: my mother for being the best example of working hard, dedication and kindness for me and my siblings. None of this would have been possible without you.

Abstract

The rapid development in perovskite solar cells (PSC) has generated a tremendous interest in the photovoltaic community. The power conversion efficiency (PCE) of these devices has increased from 3.8% in 2009 to a recent certified efficiency of over 20% which is mainly the product of the remarkable properties of the perovskite absorber material. One of the most important advances occurred with the replacement of the liquid electrolyte with a solid state hole conductor which enhanced PCE values and improved the device stability. Spiro-OMeTAD (2,2′,7,7′-tetrakis(N,N′-di-p-methoxyphenylamine)-9,9′-spirobifluorene) is the most common hole transport material in perovskite solar cells. Nevertheless, the poor conductivity, low charge transport and expensive synthetic procedure and purification have limited its commercialisation. Triphenylamines (TPA) like Spiro-OMeTAD are commonly employed due to the easy oxidation of the nitrogen centre and good charge transport. Other triarylamines have similar properties to Spiro-OMeTAD but are easier to synthesise. The aim of this doctoral thesis is to investigate different types of hole transport materials in perovskite solar cells. Three different series of triphenylamine-based HTM were designed, synthesised, characterised and studied their function in perovskite solar cells.

A series of five diacetylide-triphenylamine (DATPA) derivatives (Chapter 3) with different alkyl chain length in the para position was successfully synthesised through a five step synthesis procedure. A range of characterisation techniques was carried out on the molecules including; optical, electrochemical, thermal and computational methods. The results show that the new HTMs have desirable optical and electrochemical properties, with absorption in the UV, a reversible redox property and a suitable highest occupied molecular orbital (HOMO) energy level for hole transport. Perovskite solar cell device performances were studied and discussed in detail. This project studied the effect of varying the alkyl chain length on structurally similar triarylamine-based hole transport materials on their thermal, optical, electrochemical and charge transport properties as well as their molecular packing and solar cell

parameters, thus providing insightful information on the design of hole transport materials in the future. The methoxy derivative showed the best semiconductive properties with the highest charge mobility, better interfacial charge transfer properties and highest PCE value (5.63%).

The use of p-type semiconducting polymers are advantageous over small molecules because of their simple deposition, low cost and reproducibility. Styrenic triarylamines (Chapter 4) were prepared by the Hartwig-Buchwald coupling followed by their radical polymerization. All monomers and polymers were fully characterised through electrochemical, spectroscopic and computational techniques showing suitable HOMO energy levels and desirable optoelectrochemical properties. The properties and performance of these monomers and polymers as HTMs in perovskite solar cells were compared in terms of their structure. Despite the lower efficiencies, the polymers showed superior reproducibility on each of the device parameters in comparison with the monomers and spiro-OMeTAD.

Finally, star-shaped structures combine the advantages of both small molecules, like well-defined structures and physical properties, and polymers such as good thermal stability. Two star-shaped triarylamine-based molecules (Chapter 5) were synthesised, fully characterised and their function as hole-transport materials in perovskite solar cells studied. These materials afford a PCE of 13.63% and high reproducibility and device stability. In total this work provided three series of triarylamine-based hole transport materials for perovskite solar cells application and enabled a comparison of the pros and cons of different design structures: small-molecule, polymeric and star-shaped.

List of Figures

Contents

Abbreviations

AM	Air mass
B3LYP	Becke's three parameter exchange functional with the Lee-Yang-Parr
CB	Conduction band
CE	Counter electrode
CV	cyclic voltammetry
DCM	Dichloromethane
DFT	Density Functional Theory
DMF	Dimethylformamide
DMSO	Dimethylsulfoxide
DPV	Differential Pulse Voltammetry
DSSC	Dye-Sensitized Solar Cells
ε	Molar extinction coecient
E_c	Conduction band
E_g	Band gap
ESI-MS	Electrospray ionisation mass spectrometry
E_v	Valence band
FF	Fill Factor
FTO	Fluorine Doped Tin Oxide
HOMO	Highest Occupied Molecular Orbital
HTM	Hole Transport Material
ISC	Intersystem Crossing
J_{mpp}	Current at maximum power
J_{SC}	Short-circuit current density
J-V	Photocurrent density-Voltage
Li-TFSI	Lithium bistrifluoromethylsulfonyl imide

LUMO	Lowest Unoccupied Molecular Orbital
NMR	Nuclear Magnetic Resonance
μ	Mobility
OLED	Organic light emitting diode
OPV	Organic photovoltaics
PCE	power conversion efficiency
PES	Potential Energy Surface
P_{max}	Power maxima
PSC	Perovskite solar cells
PV	Photovoltaic
RE	Reference electrode
spiro-OMeTAD	2,2',7,7'-Tetrakis(N,N-dimethoxyphenylamine)-9,9'-spirobifluorene
ssDSSC	Solid state dye-sensitised solar cell
SWV	Square-wave voltametry
TAA	Triarylamine
TAS	Transient absorption spectroscopy
TBP	4-Tert-butylpyridine
T_g	Glass transition temperature
T_m	Melting point
TPA	Triphenylamine
UV/vis	Ultraviolet/visible spectroscopy
VB	Valence band
V_{mpp}	Voltage at maximum power
V_{oc}	Open-circuit voltage
WE	Working electrode

1 Introduction

1.1 The Energy Crisis

Energy has always been the main motor for the development of human society. Energy is never created but only converted from one form to another one more flexible and convenient for human use. Chemical energy in coal can be transformed successively into thermal and mechanical energy and finally into electricity. It was basically coal that powered the Industrial Revolution and transformed the living conditions of the world population. Nowadays, humanity faces an enormous energy problem. The growing world population and the increase of living standards are raising the energy demand day by day. The International Energy Outlook 2016 has estimated that the global energy requirements will increase 48% by 2040 in reference to 2012[1]. In order to maintain our modern lifestyle a significant change in the current energy system is needed.

Currently, more than 80% of the primary energy supply used by humans heavily depends on fossil fuels like oil, coal and natural gas (Figure 1.1)[2]. Fossil fuels are organic compounds formed millions of years ago through the lengthy anaerobic decomposition of dead organisms submerged under the sediments, containing energy from photosynthesis[3]. The dilemma is that humans consume these fossil fuels more rapidly than photosynthesis produces them. Therefore, they are considered a non-sustainable energy source. As the energy demand increases, the easy-to-access fossil fuel reserves deplete. Many industries are taking higher risks moving into deposits that are harder to extract and employing unconventional methods such as offshore drilling deep into the ocean. These methods are not only dangerous but also have a high energy cost and potential environmental damage like the Deepwater Horizon oil spill in the Gulf of Mexico in 2010.[4–6]

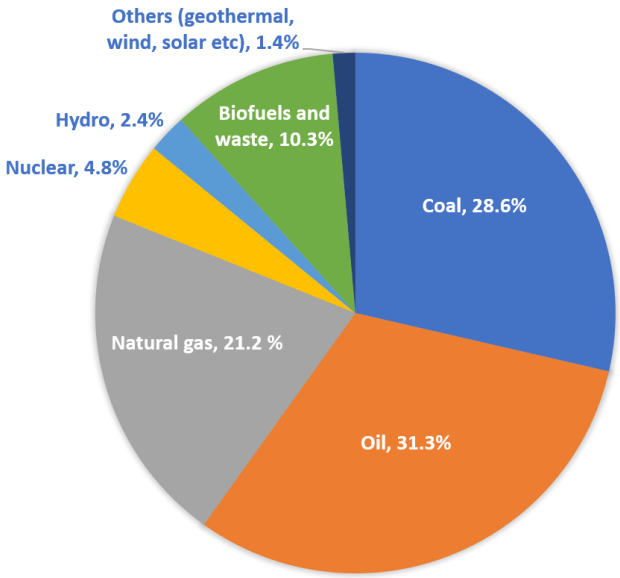

Figure 1.1 Total world energy consumption in 2016.[2]

Furthermore, fossil fuels are unevenly distributed over the earth which, in addition to other political and economic aspects has led to a noticeable disproportion of the quality of life around the world, where more than 1 billion of the global population still do not have access to electricity[6]. Additionally, the combustion of fossil fuels produces harmful pollutants such as sulfur-containing compounds and the so-called greenhouse gases. Greenhouse gases are gases in the atmosphere such as water vapour, carbon dioxide, nitrous oxide and ozone that absorb and emit radiation in the infra-red range of the electromagnetic spectrum, delaying heat from escaping and causing the greenhouse effect[7]. Over the last decades, human activities, in particular from burning fossil fuels, have increased the concentration of atmospheric carbon dioxide (CO_2) by more than a third since the beginning of the Industrial Revolution, modifying the natural greenhouse process, increasing global temperature and causing global warming[8]. Higher temperatures lead to higher concentrations of water vapour, which increase the water cycle. Even a small increase in the global temperature can originate an enormous impact on the environment. The effects of global climate change are already observable: glaciers are shrinking, weather patterns are changing, oceans are

becoming more acidic, and sea levels are rising year by year. Although the exact consequences of altering the environment are uncertain, it is evident that the effects of human activities in the environment are noticeable on a scale never seen before and the indications for an immediate climate change are undeniable.[9]

Global awareness of climate change and the energy problem have increased in the last couple of years and have become central topics of discussion amongst people from different backgrounds and professional interest (science, art, politics and more). They are all recognizing the need to shift to a de-carbonized energy system and develop affordable, reliable and sustainable energy technologies that can meet the global energy demand and also secure the development and future of the world population. On the 15th December 2016, at the 21st Conference of the Parties of the United Nations Framework Convention on Climate Change (UNFCCC), representatives of 194 countries, including China, India and the EU in unanimity, signed the Paris Agreement to take actions and reduce the effect of global warming. This accord targets to moderate carbon emission and has a long-term goal for net zero emission and effectively phase out fossil fuels[10]. Alternative energy resources to fossil fuels that have been considered to tackle the energy problem include nuclear power and renewable energy resources. A nuclear power plant uses a reaction called nuclear fission. In this process, the nucleus of a radioactive element such as uranium split into lighter nuclei releasing a large amount of heat that can be converted into electricity. Several unsolved issues have limited the expansion of nuclear power such as cost, availability of uranium, disposal of nuclear waste and safety, in particular after the accident caused by a 9.0 magnitude earthquake involving four reactors at the Fukushima Daiichi power plant in Japan on March 2011[4,11]. The safest method is to use renewable energy resources. In contrast to fossil fuels, renewable sources can be found over vast geographical areas around the earth, and as their environmental impact is minor, they could help to mitigate several health and pollution issues associated with burning fossil fuels. Furthermore, the use of renewable energies will also provide energy security because there is no need to depend on one single resource[6]. The mainstream of renewables includes solar, wind, hydropower, geothermal and biomass

and it is likely that in the future electricity will be obtained by a combination of them. Among all, solar energy is one of the best ways to fulfill the world's growing thirst for energy. In just one hour of light the sun can produce more energy onto Earth than the world energy requirements for an entire year. The maximum theoretical power of the sun (<120,000 TW) is around 10000 times the energy demand.[12–14] The challenge now is to develop technologies to capture and utilize this resource.

1.2 Solar Energy

The energy of the sun reaches the earth as radiation across the electromagnetic spectrum from infra-red to ultraviolet. The energy of this radiation can be transformed into chemical energy, heat or electricity by using different technologies. In a solar fuel[15], light is converted into chemical energy by the photochemical production of hydrogen. A solar fuel enables stored solar energy in the form of chemical bonds that can be later utilised when sunlight is not available. Concentrated solar power technologies (CSP) use mirrors or lenses to concentrate sunlight into heat which then can be converted into electricity[16]. One of the most conspicuous approaches to utilise solar energy is the direct conversion of solar energy into electricity using photovoltaic devices (PVs). Currently, PV is the most widely deployed solar technology in the world due to its flexibility and cost of installation. As CSP only works with direct irradiation and large plants, the areas for installations are restricted. On the other hand, PV technologies can operate even with diffuse light and therefore can be installed in almost any location covering residential and industrial sectors.[12]

1.3 Photovoltaic Solar Cells

A photovoltaic solar cell is a device that converts sunlight directly into electricity. When semiconductor materials are exposed to electromagnetic radiation such as visible light, they absorb some of the photons of light and release a significant number of electrons. These electrons can be captured to generate electricity[17,18]. The field of photovoltaics started almost 180 years ago with the discovery of the photovoltaic effect. In 1839, Edmund Becquerel first observed this phenomenon when a voltage

and a current were produced by illuminating a silver chloride electrode immersed in an electrolytic solution[19,20]. During the following years, scientists were focused to understand the photoconductivity of different metals like selenium. Then, in 1883 Charles Fritts developed the first working solid-state photovoltaic device with 1% power conversion efficiency (η), using selenium coated with a thin layer of gold (Au). Four years later, Heinrich Hertz discovered the photoelectric effect when two different metals where exposed to visible and UV light[21]. The photovoltaic effect is associated with the photoelectric effect. The difference is that in the photoelectric effect the electrons are emitted to a vacuum while in the photovoltaic effect the electrons move into a new material. In 1901, Max Planck published the relationship between frequency and energy with his famous equation 1.1.

$$E = h\nu \qquad \textbf{Equation 1.1}$$

Where h represents the Planck's constant and ν is the frequency of the light[22]. The principle of how light could create electricity remained poorly understood until the interpretation of the photoelectric effect was proposed by Albert Einstein. In 1905, Albert Einstein explained the photoelectric effect by assuming that the light is formed by packs of energy or energy quanta, called photons. The energy of such photons depends on the frequency of the light and some of them have enough energy to eject electrons from some materials. These free electron can move and create a current[23]. For the elucidation of the photoelectric effect and the nature of the light, Albert Einstein was awarded the Nobel Prize in Physics in 1921.[24]

Photovoltaic technologies are based on three important principles: 1) Light absorption and generation of charge carriers, 2) Charge separation and 3) Collection of the free carriers. In PV devices, light is absorbed above a certain minimum onset energy called the "band gap" E_g that depends on the properties of the light-absorbing material used. According to the energy band theory, in an inorganic semiconductor the energy levels are no longer discrete like in free atoms, but form continuum bands of permitted energy values[25]. The valence band (E_v) is the nearly filled band containing electrons with the highest energies, and the conduction band (E_c) is the lowest nearly empty energy band.

In an ideal semiconductor, there are no allowed energy states between those two bands and the energy difference between them is called the bandgap, $E_g=E_c-E_v$.

When photons are absorbed by semiconductor materials, the energy is used to promote electrons from the valence band to the conduction band. Only photons with energies above the band gap can be absorbed. The excitation of an electron to higher energy levels leaves behind a void with a positive charge called a hole in the valence band and frees an electron to move in the conduction band. In a solar cell, the photo-generated electrons and holes move to opposite sides of the cell where they are collected by an electrode to generate electricity. The efficiency of charge separation and collection modulates the photo-current whereas the energy difference between the electron and holes at the final stage before reaching the contacts determines the voltage of the solar cell.[17,18,26]

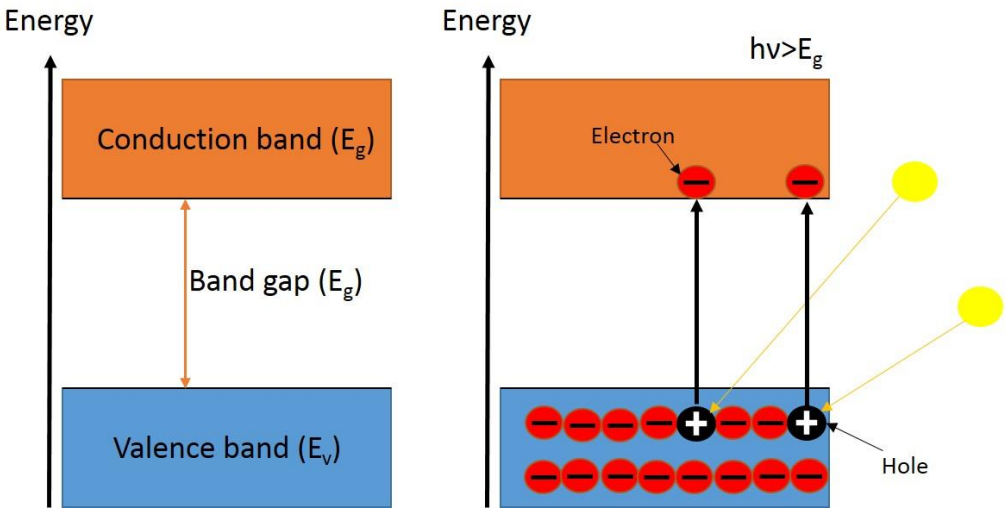

Figure 1.2*: Left:* Semiconductor band structure, *Right:* Illustration of the absorption of photons in a semiconductor.

Photovoltaic solar cells are typically named according to the light-absorbing material that can be either inorganic semiconductors, organic materials or a combination of both. Solar cell technologies can be classified into first, second and third generation cells. First generation solar cells are centred on crystalline silicon wafers. The second

generation cells are called thin-film solar cells and include amorphous silicon, CdTe and CIGS cells. Third generation solar cells are often described as emerging photovoltaics and cover all new technologies such as organic photovoltaics, multi-junction solar cells, perovskite solar cells and more. Later in this section, we will give a brief explanation of the most important PV technologies to date.[17,18]

1.3.1 Silicon Solar Cells

Crystalline silicon PV is at the moment the leading PV technology with more than 80% of the PV market share[27]. In 1954, at Bell Laboratories in New Jersey, Gerald Pearson and Calvin Fuller developed the first practical silicon photovoltaic device with an efficiency of about 6%[28]. Considering the high cost of production, the first silicon solar cells were mainly used for space application to power satellites. Later, the development of better processing technologies helped to significantly reduce the cost of fabrication of silicon solar cell making possible their application in the public sector. In this PV technology, the silicon is n-doped with phosphorus and p-doped with boron. When these two semiconductors form a junction, the free carriers diffuse in opposite directions across the junction creating an electric field at the interface between these materials, known as the depletion zone (Figure 1.3). At present, silicon-based laboratory cells have reached record power conversion efficiency (PCE) of over 25% for single-crystal, over 20% for multi-crystalline cells and around 14% for amorphous silicon cells, and the majority of commercial single crystalline silicon solar cells reach efficiencies of 13-19%.[29,30]

The maximum theoretical power conversion efficiency for a single p-n junction device with a band gap of 1.34 eV is around 33.7% noted as the Shockley-Queisser (SQ) limit[31]. This limit was first calculated by William Shockley and Hans Queisser in 1961 by examining the total amount of electricity produced per photon of light in a single junction solar cell and assuming no light concentration. Silicon is an indirect band gap material with a band gap (1.12 eV) that is slightly narrow for an optimum solar cell. Therefore, a relatively thick absorption layer from high purity grade silicon and controlled doping levels are used to absorb enough sunlight. The thickness of the

absorber layer increases the cost of the solar modules and makes them rigid and fragile which limit their application in the portable market. Although silicon is one of the most abundant elements on the earth, the fabrication of silicon solar cells is considerably energy intensive and expensive primarily due to the purification and crystallisation of silicon.[27,32] In fact, some studies estimated that the energy payback for the current multi-crystalline silicon PV modules is four years.[33] Therefore, research is focused to reduce the energy cost without sacrificing efficiency.

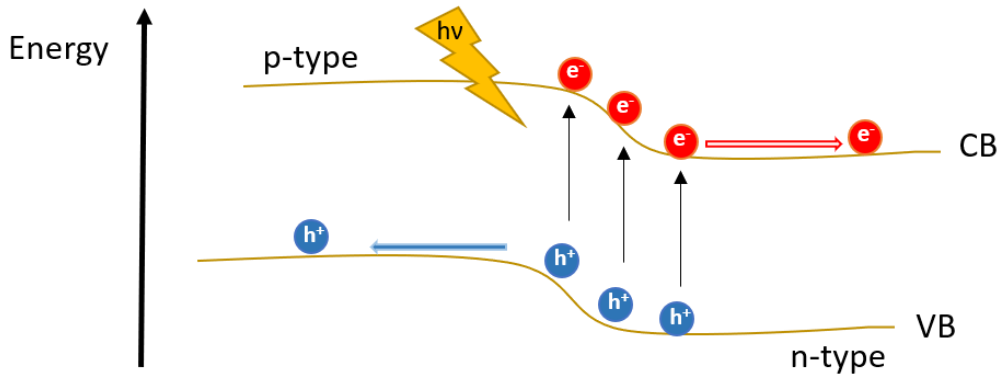

Figure 1.3: Formation of the depletion layer in silicon solar cells (top) and charge separation across the p-n junction.

1.3.2 Thin-Films Solar Cells

Solar energy seeks to prove to be a reliable, cost-effective and sustainable source to compete with other conventional sources. To that end, photovoltaic reseachers aim to reduce the energy cost and diminish the waste produced by the first generation photovoltaics. Thin-film technologies, also known as the second generation PV, bring valuable advantages that allow an extended market penetration of solar electricity. In comparison to silicon wafer technologies, thin film solar cells reduce the material usage and shorten the energy payback time. Thin-film technologies use a direct band gap semiconductor that allow reduction of the thickness of the absorber layer without reducing device efficiency. Furthermore, because of the properties of the semiconductor material, thin-film solar cells perform better than silicon solar cells,

under low light conditions. To this family belong thin-films solar cells based on amorphous silicon, CdTe and Cu(In,Ga)(S, $Se)_2$ (CIGS). From these, amorphous silicon (α-Si), CIGS and CdTe solar cells are the most popular in the PV market. In fact, for decades α-Si solar cells have been used to power consumer electronics such as calculators. Initially, thin-film solar cells were expected to be less expensive than c-Si-based solar modules. Nevertheless, due to the price decline in the production of silicon wafers through economies of scale, low cost is no longer the main advantage of these technologies.[34–36]

Up to now, amorphous silicon solar cells have reached 14% power conversion efficiency. Both CdTe and CIGS have higher absorption coefficient than silicon hence performance of 22.1% for CdTe and 22.6% for CIGS have been achieved.[30,37] However, despite offering numerous advantages over the previous generation, it has been difficult to produce highly-efficient large-scale thin film modules. Furthermore, the low natural abundance of indium, tellurium and selenium and the toxicity levels of cadmium have limited their application. Most recently copper zinc tin sulphide $Cu_2ZnSn(S,Se)_4$[38] commonly named CZTS has been proposed as a less-toxic and more abundant alternative with the highest efficiency of 12.6% achieved in 2014.[39]

1.3.3 Tandem Solar Cells

One of the strategies to exceed the Shockley-Queisser limit is with tandem cells or multi-junction cells which comprise a stack of multiple solar cells on top of each other using semiconductor materials with different band gaps. The use of various semiconductor materials, each covering different region of the solar spectrum, improves the absorption of light and reduces energy losses which leads to better energy conversion efficiencies. $GaInP_2$ (1.85 eV) is usually the preferred material for the top cell converting the short-wavelength region of the solar spectrum. The next solar cell is made of GaAs (1.42 eV) which captures near-infrared (IR) light. Finally at the bottom of the structure, a solar cell based on germanium (0.67 eV) absorbs some of the lower photons of the IR region. It is also common to incorporate light concentrator systems with the multi-junction cells to further increase the efficiency of the solar

cell[40,41]. Multi-junction solar cells with light concentrators have reached efficiencies of 46%[30,42]. However, the high efficiencies come along with an increase of the complexity of the structure and the manufacturing price which limit their application. Currently, this technology is employed in aerospace where high efficiencies are more important than cost.

1.3.4 Dye Sensitised Solar Cells

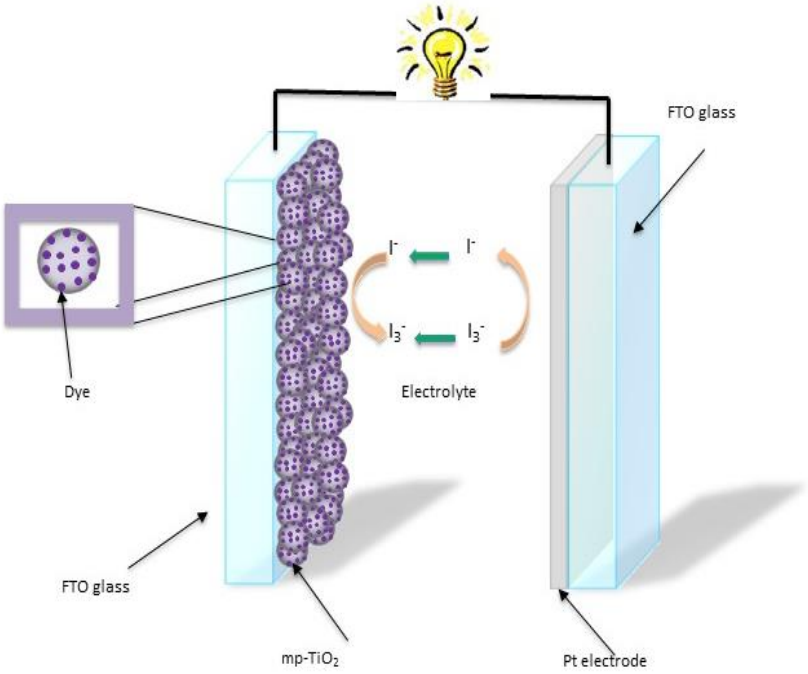

Figure 1.4 Schematic structure of liquid dye-sensitised solar cells.

Dye-sensitised solar cells (DSSCs) were popularised by Brian O'Regan and Michael Grätzel in the early 1990s.[43,44] A dye sensitised solar cell has in essence a "sandwich" arrangement formed by six key components: 1) a glass with a transparent conductive oxide layer (TCO), 2) a compact TiO_2 layer, 3) a nanocrystalline semiconducting oxide, 4) a dye, 5) a redox electrolyte and 5) a TCO coated glass with platinum as a counter electrode. A schematic of the device structure is shown in Figure 1.4. The working principle of dye sensitised solar cells mimics naturally occurring photosynthesis. Visible light is absorbed by dye molecules that are anchored to a wide-

band gap mesoporous semiconductor oxide (typically TiO_2) of around 10 µm thick to increase the surface area for maximum light absorption. The most common dyes are ruthenium-based complexes which are attached onto the TiO_2 nanoparticles's surface through carboxylate groups.[45,46] When light is absorbed the dye is excited from the ground state to its electronically excited states. The molecule in the excited state can decay back to the ground state or continue injecting electrons into the conduction band of the titanium dioxide. The injected electrons diffuse through the mesoporous TiO_2 (mp-TiO_2) to reach the contact electrode and pass through the external circuit until they reach the counter electrode. The oxidised dye molecules are reduced rapidly to the ground state by a redox electrolyte, usually an iodide-triiodide redox couple in an organic solvent.

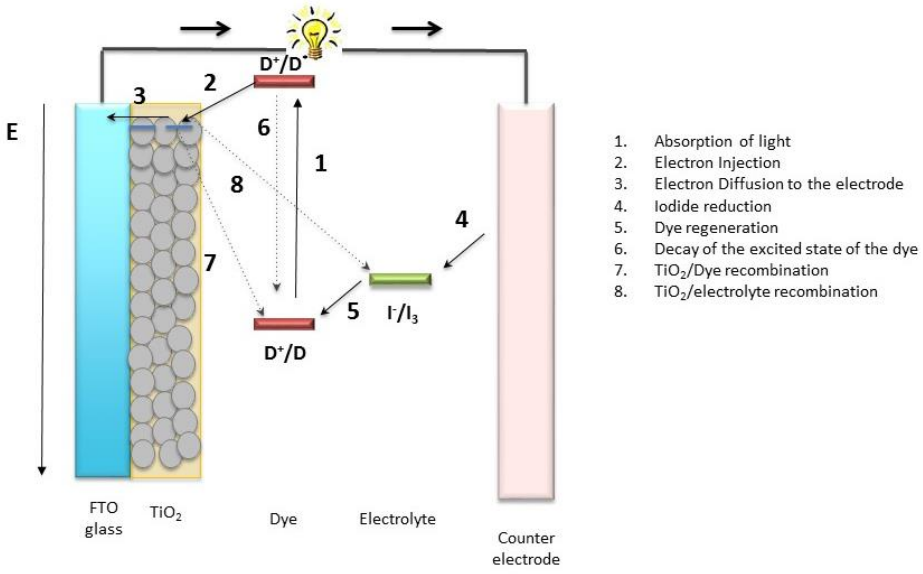

Figure 1.5: Summary of the working principle of dye-sensitised solar cells.

A summary of the working operation and loss mechanisms of a DSSC is illustrated in Figure 1.5. Ideally, light absorption, electron injection, dye regeneration and charge transport should be kinetically favoured over loss pathways of excited-state decay to ground state and electron recombination processes.[47] The conducting substrate acts as a current collector, a support structure and a sealing layer to the cell. Currently, fluoride doped oxide (FTO) is the most common substrate in dye-sensitised solar cells and can be deposited on a wide variety of substrates including polymer-based plastics, glass

and thin metal foils. The compact TiO_2 film underneath the mesoporous layer acts as a blocking layer to recombination of electrons in the FTO substrate and the electrolyte.[48,49]

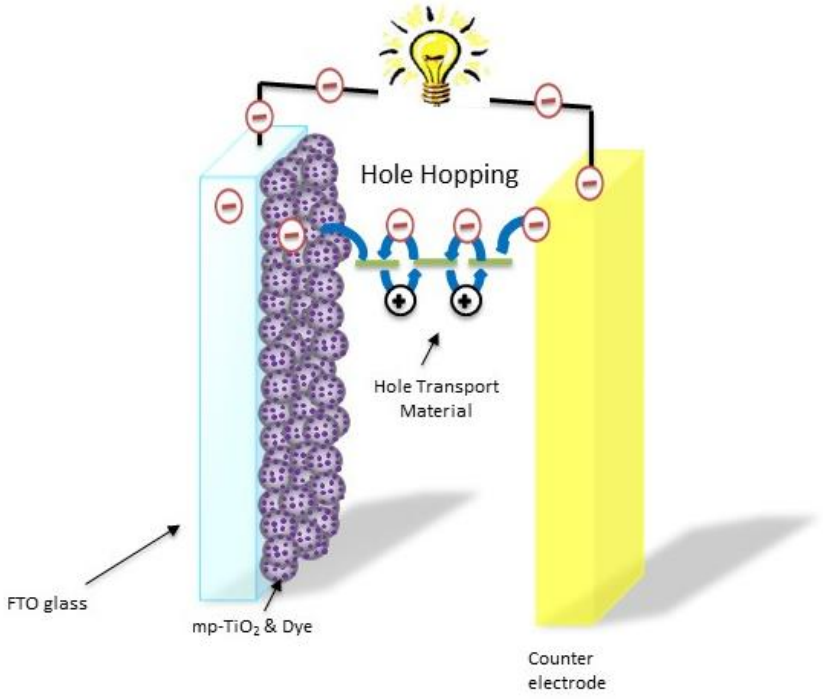

Figure 1.6: Schematic structure of solid state dye-sensitised solar cells.

To date, 14% efficiencies have been achieved for DSSCs at lab scale using a carboxy-anchor organic dye coded as LEG4 and co-photosensitized with an alkoxy silyl-anchor dye with an optimized cobalt(III/II) redox electrolyte solution.[50] Although these efficiencies lag behind other technologies, DSSCs offer a number of advantages including low cost, ease of fabrication, non-toxic materials and good response under low light intensities. Moreover, one of the characteristics that distinguish DSSCs from other technologies is the range of colours that can be used in the devices, which makes them attractive in architecture and building design. Nevertheless, stability concerns due to solvent leakage, corrosion and volatility of the liquid electrolyte have limited the large-scale commercialization of DSSCs. These concerns led to the development of all-solid-state dye-sensitised solar cells (ssDSSCs).[51,52] Figure 1.6 illustrates the device architecture of solid-state DSSCs. The working mechanism is similar to the

previous liquid-based solar cells. However, here the liquid electrolyte is replaced by a solid hole conductor known as the hole transport material (HTM) for dye regeneration and hole transfer. The limitation in ssDSSC comes from the insufficient filling of the mp-TiO_2 with the solid-state HTM. To solve this, researchers proposed to reduce the thickness of the mp-TiO_2 to an optimum of 2 μm that facilitates pore filling of the HTM for efficient hole transfer and minimum recombination. However, the thickness restrictions in ssDSSCs limits light absorption. Since the absorption coefficient is proportional to the thickness of the mesoporous TiO_2, the available dyes that can be used in ssDSSCs must exhibit a very high absorption coefficient to efficiently harvest light. Thus, research has been focused in the design and synthesis of new light absorber materials for ssDSSCs including recently a group of organic-inorganic halide perovskite materials.[48,53]

1.4 Methylammonium lead halide perovskite solar cells

In the strictest sense of the word, perovskite - bearing the name of Russian mineralogist L. A. Perovski - is simply the calcium titanium oxide mineral ($CaTiO_3$), discovered by Gustav Rose in 1839.[54] Perovskite also refers to the group of compounds sharing the same crystal structure of calcium titanate, known as the perovskite structure with the general chemical formula of AMX_3, where A and M are two cations of different sizes (A larger than M), and X is an anion. Ideally, the perovskite structure has a cubic geometry. Nevertheless, in nature they are usually pseudo-cubic or distorted cubic. In an ideal perovskite structure, M and X form an octahedral arrangement MX_6 that consists of the cation M in the centre of the octahedron surrounded by six anions X. This arrangement extends to form a three-dimensional network. Each cation A is in a 12-fold cuboctahedral coordination site shared with twelve X anions and balances the charge of the whole system.[55] The crystal structure of perovskite is depicted in Figure 1.7.

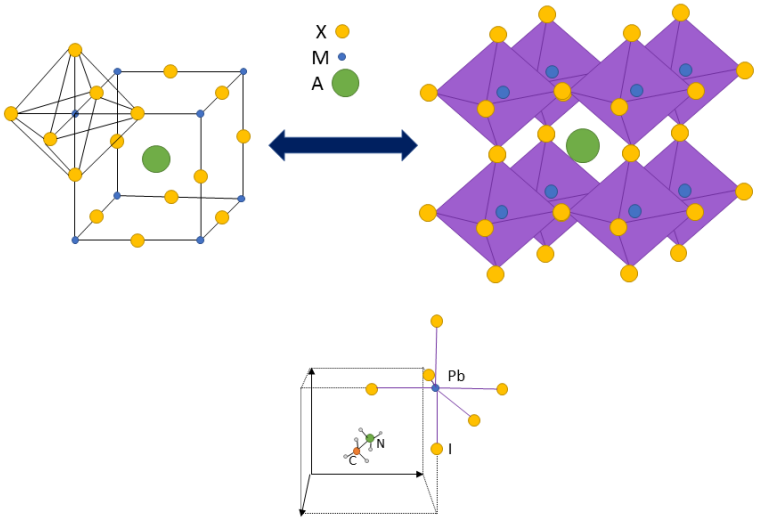

Figure 1.7: *Top-left:* Unit cell of basic crystal structure of perovskite with the chemical formula ABX_3. *Top-right*: Extended perovskite structure. *Bottom*: Unit cell of organic-inorganic halide perovskite.

In the organic-inorganic halide perovskite materials, the larger A cation is typically methylammonium ion. The anion X^- is a halogen. In general iodide is the most common one, but both bromide and chloride are also used in a mixed halide perovskite and the cation M^{2+} is generally Pb^{2+}(Figure 1.7 bottom)[56]. This class of materials has been studied for decades. In 1978, Weber first reported the physical properties of organic-inorganic lead halide perovskite $CH_3NH_3PbI_3$[57] and in the following years research was focused on the properties of perovskite materials for organic light-emitting diode (OLED) and thin film transistor (TFT) applications[58,59]. It was not until 2009 that Miyasaka and co-workers first reported organo-lead halide perovskite as light absorbers in dye sensitised solar cells in which the molecular dye was replaced by $CH_3NH_3PbBr_3$ and $CH_3NH_3PbI_3$ reaching efficiencies of 2.2% and 3.8% respectively. An electrolyte solution containing lithium halide was used as the redox couple[60]. These devices however showed very low stability and degraded very quickly. Later in 2011, using similar structures, Park reported an efficiency of 6.5% when using perovskite nanoparticles of approximately 2.5 nm in diameter[61]. Due to the ionic nature of the perovskite materials, they dissolve easily in polar solvents generally used for the

liquid electrolyte in DSSC. Concerns about the stability of the perovskite devices motivated the use of a solid-state hole-conductor instead of liquid electrolytes. In 2012 Kanatzidis and co-workers reported a metal halide perovskite $CsSnI_3$ as p-type hole transport material in a ssDSSC configuration using a ruthenium complex called N719 as the light absorber[62]. These devices reached efficiencies of 10.2%, a big improvement in performance for ssDSSCs whose previous best-reported device reached just over 7% efficiency[63]. Later in 2012, Park, Grätzel and colleagues used $CH_3NH_3PbI_3$ as the light absorber in the original ssDSSCs architecture and replaced the liquid electrolyte with spiro-MeOTAD (2,2',7,7'-tetrakis(N,N-di-p-methoxyphenylamine)-9,9'-spirobifluorene), an organic hole conductor originally developed for OLED applications[64]. In comparison to the previous reports by Miyasaka and Park, these devices not only showed better stability but also exhibited efficiencies of 9.7%.[65]

Another big breakthrough came also in 2012 when Henry Snaith and collaborators replaced the n-type mesoporous TiO_2 with an insulating scaffold Al_2O_3, on top of which $CH_3NH_3PbI_{3-x}Cl_x$ was used as the light absorber and spiro-MeOTAD as the HTM[66]. Surprisingly, these devices showed efficiencies of over 10% and higher open circuit voltage (V_{oc}) in comparison to the mp-TiO_2-based devices. Since Al_2O_3 is an insulator the injection of electrons from the perovskite is blocked due to the higher conduction band which explain the increase in the V_{oc} values. These results led to the hypothesis that the scaffold was also not needed, which was later proved correct when over 10% efficiencies were achieved with planar structure perovskite solar cells with no mesoporous scaffold[67]. Almost simultaneously, Etgar and collaborators proposed a HTM-free heterojunction device structure in which $CH_3NH_3PbI_3$ was used as a p-type semiconductor and a 500 nm mesoscopic layer was deposited as an n-type semiconductor. These devices showed 5.5% power conversion efficiency (PCE)[68]. All these previous findings demonstrated the great potential of the perovskite material as more than just a sensitizer as they were able to transport both electrons and holes. Later in 2013, Docampo fabricated an inverted solar cell architecture with up to 10% efficiency. The perovskite $CH_3NH_3PbI_{3-x}Cl_x$ was deposited on top of the hole transport material, followed by the electron collector in a planar film.[69] This work showed the

potential and versatility of the perovskite absorber to be applied in photovoltaic technologies. These discoveries showed that perovskite-based solar cells can no longer be seen as dye-sensitised solar cells but as a new type of photovoltaic system.

The extensive research in the perovskite field and consequently improvement in device fabrication and deposition techniques in the following years, led to a quick increase in device efficiencies. Initially, the perovskite material was deposited in a single step process, but in 2013 a sequential deposition method was introduced for perovskite fabrication which gave a PCE of 15%[70]. In this work, a mesoporous-TiO_2 perovskite structure was fabricated in which a high concentrated solution of lead iodide (PbI_2) was first introduced into the TiO_2 nanopores by spin-coating to obtain a high loading into the mesoporous film followed by a brief dip into a dilute CH_3NH_3I solution. The perovskite crystallized quickly within the pores resulting in an increase in the device performance[70]. After that, the vapour deposition method for the fabrication of planar perovskite solar cells showed 15.4% PCE[67]. Following that a sequence of striking improvements of the PCE values were reported. To date perovskite solar cells have reached efficiencies over 20%[30] surpassing values of the commercialised polycrystalline silicon solar cells. This rapid development is mainly the product of the remarkable properties of the perovskite absorber materials, such as high panchromatic absorption, large carrier diffusion length, low non-radiative recombination and easy processability, leading to great potential for low-cost and large-scale technologies.[55,71]

1.5 Structure and Mechanisms of Perovskite solar cells

Perovskite solar cells can be divided into four groups based on their architecture and components: a)mesoporous active structure such as mp-TiO_2 or similar oxides, b)mesoporous-superstructure (Al_2O_3 and others) c)planar structure and d)inverted configuration. Figure 1.8 gives a broad overview of the various configurations of PSCs. Among the different PSC architectures, the mesoscopic device configuration of FTO/c-TiO_2/mp-TiO_2/Perovskite/HTM/Au is the most widely used due to the ease of fabrication and high efficiencies obtained. FTO is the fluorine-doped tin oxide layer deposited on glass, c-TiO_2 is a compact layer of titanium dioxide (around 50 nm), mp-

TiO_2 is the mesoporous layer (450 nm), HTM is an organic hole transport material and the metal contact used is gold.

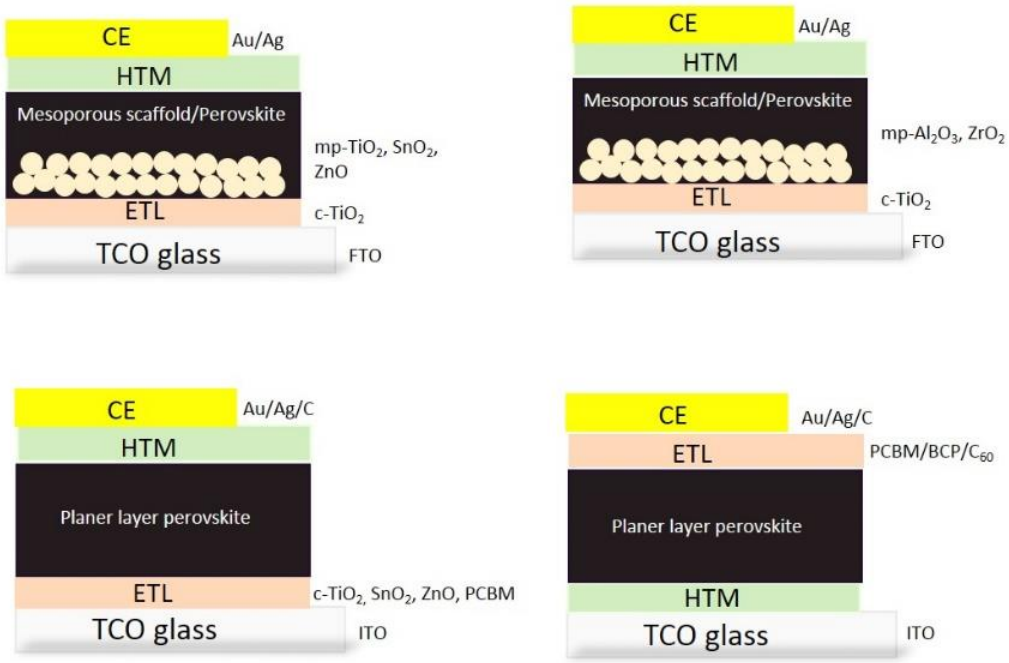

Figure 1.8: Diagram of the device assembly of each group in PSCs. *Top-left:* mesoporous active structure. *Top-right:* Mesoporous-superstructure. *Bottom-left:* Planar configuration. *Bottom-right:* Inverted structure.

The working mechanism of PSCs has some key differences to dye-sensitised solar cells (see Figure 1.9). Light is absorbed in the perovskite layer and generates free electrons and holes. In dye molecules, electrons and holes are tightly bound together as excitons. To dissociate excitons into free electron and hole pairs, these excitons need to overcome its binding energy. The small binding energy of halide perovskite leads to an efficient generation of free carriers upon light absorption in comparison to dye molecules. The free electrons formed at the perovskite/HTM interface need to diffuse through the absorber layer before being extracted at the mp-TiO_2/perovskite interface. Charge separation occurs by the injection of the electrons into the conduction band of the electron transport material or the hole transfer into the HOMO orbital of the HTM. It is crucial that these steps are kinetically faster that the recombination process at the interfaces TiO_2/perovskite/HTM. The injected electrons then travel through the

mesoporous particles to reach the electrode and pass through the external circuit until they reach the counter electrode[72]. Interfacial properties largely determine the device performance. The use of mesoporous TiO_2 leads to faster charge collection due to the large interface between the TiO_2/perovskite which leads to better efficiencies in comparison to the mesosuperstructure and planar configuration. In order to improve both device performance and stability, there has been extensive research to optimise each component of the perovskite structure. Here we will review some of these developments.

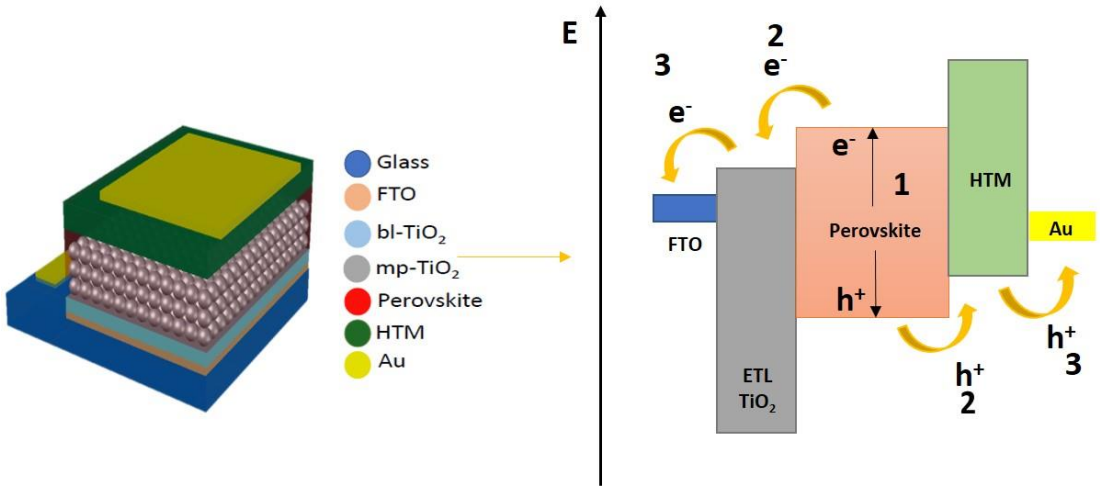

Figure 1.9 *Left:* Schematic view of the perovskite solar cell configuration of FTO/c-TiO_2/mp-TiO_2/Perovskite/HTM/Au. *Right:* Energy band diagram and main process of the solar cell: 1. Absorption of light and generation of free carriers, 2. Charge collection and 3. Charge extraction.

1.5.1 Electron Transport Material (ETL)

- Compact Layer

For the typical mesoscopic perovskite cell configuration a thin and dense layer is deposited between the transparent conducting oxide (TCO) layer and the mesoporous scaffold. The compact layer facilitates the electron transport through the FTO layer and acts as a blocking layer to avoid direct contact between the conducting substrate and the HTM layer which minimises charge recombination. The most widely used blocking layer is TiO_2 which is generally deposited by spin-coating methods or spray

pyrolysis[73,74] and often requires high temperature sintering to obtain a dense structure. Because the blocking layer can significantly affect the device performance, there has been numerous studies to optimize it. Interface engineering such as $TiCl_4$ and $UV(O_3)$ treatment has been employed to further improve stability and power conversion efficiency of perovskite solar cells[75,76]. The $TiCl_4$ treatment increases the quality of the compact TiO_2 film which minimises charge recombination. On the other side, the $UV(O_3)$ treatment removes organic contaminants from the surface and enhances wettability of the TiO_2 surface which reduces the defects at the interface and improves contact with the perovskite layer. Doping strategies have also been employed to improve the properties of the compact layer. For instance the use of F-doped TiO_2[77] and Mg-doped TiO_2[78] as blocking layers in perovskite solar cells led to an increase of the PCE from 13% to 14.12% for F-doped TiO_2 and from 9.16% to 12.28% for Mg-doped TiO_2. The superior properties of the doped TiO_2 including higher conductivity and improved electron transfer process originated the better device performances.

Low temperature sintering is important to construct flexible substrates and reduce cost of device fabrication. Therefore, there have been several strategies to reduce the high temperature process required for TiO_2. One approach is the use of low temperature techniques for TiO_2 deposition[79–83] such as spin coating followed by low temperature annealing[79], ultrasonic spray coating[81] and dip coating[83]. For example, Wojciechowski, et al. 2014 successfully developed a low-temperature (<150 ℃) route to process the TiO_2 compact layer reaching a PCE of 15.9%[79]. Another approach is replacing TiO_2 with other materials. Zinc oxide (ZnO)[84,85], tin oxide (SnO_2)[86], caesium carbonate (Cs_2CO_3)[87], graphene[88], fullerene[89] are some of the alternative materials proposed as blocking layers that have demonstrated considerable device performance.

- Mesoporous Scaffold Layer

Among other metal oxides, TiO_2 nanomaterials have received greater attention due to chemical stability, non-toxicity and low cost. The main function of the mp-TiO_2 is transporting the photo-generated electrons from the perovskite layer. The mesoporous layer is usually deposited by screen-printing or spin-coating on top of the compact

layer followed by a high temperature sintering treatment. The quality of the mesoporous TiO_2 film affects the crystallisation of the perovskite material. For high device performance, an efficient infiltration of the perovskite precursor into the pores of the mesoporous layer is crucial[90]. Research has been focused on studying the impact of the mesoporous scaffold on device performance. In 2013, Kim[91] and collaborators reported the influence of the TiO_2 film thickness on the device parameters. A 9.7% PCE was achieved by using $CH_3NH_3PbI_3$ as the light absorber which was deposited on a mesoporous TiO_2 film (0.6 μm). Increasing the thickness of the TiO_2 did not significantly affect the current density (J_{sc}) mainly due to the large optical absorption. However, upon increasing the thickness of TiO_2, FF (fill factor) and V_{oc} (open circuit voltage) values decreased matching the drop in PCE to 5.9% (1.58 μm) which is mainly attributed to an increase of the electron transport resistance in the film. As a result, studies have found that the optimized thickness for mesoporous TiO_2 is in the range of 400-600 nm.[92]

The size and shape of the TiO_2 nanoparticle (NP) also impacts the device performance of perovskite solar cells. On one hand, smaller TiO_2 nanoparticles are required for larger surface area at the interface perovskite/TiO_2 which led to efficient electron injection from the perovskite to the TiO_2. On the other hand, larger nanoparticle size facilitates the infiltration of the perovskite which is crucial for blocking the direct contact between the HTM and TiO_2 and reducing charge recombination. Furthermore, a larger TiO_2 NP size is beneficial to minimise grain boundaries in the TiO_2 layer for efficient electron transport[93,94]. Han and collaborators studied the effect of the TiO_2 NP size on a hole-conductor-free mesoscopic perovskite device structure. It was found that the size of the TiO_2 nanoparticles influenced the infiltration of the perovskite sensitizer into the pores and the charge transfer kinetics between the perovskite and the TiO_2. The highest PCE of 13.41% was obtained with a diameter of 25 nm TiO_2 NP[93]. In a different study, Sung and colleagues prepared spherical TiO_2 nanoparticles of different diameters (from 30 to 65 nm) and used them in mesoporous perovskite solar cells. The results demonstrated that the 50 nm TiO_2 nanoparticles exhibited the best morphology (pore size, shape and pore size distribution) for mesoscopic solar

cells providing better device performance (17.19%) and a highly reproducible PCE attributed to an efficient infiltration of the perovskite sensitizer into the mesoporous TiO_2.[94]

Titanium dioxide is a wide-band gap semiconductor with three crystallographic forms in nature: anatase (tetragonal), rutile (tetragonal) and brookite (orthorhombic). The band-gaps of the crystalline forms are 3.2 eV for anatase and 3.0 eV for rutile. Rutile is thermodynamically the most stable form of TiO_2. However, anatase is the most common structure used for solar cells applications due to its higher conduction band edge showing lower charge recombination[95,96]. The crystal structure of TiO_2 can also influence device performance of PSCs. Incomplete infiltration of the perovskite absorber into the pores of the mesoporous layer and inefficient electron mobility are the main complications of the 3D mesoporous layer. Therefore, different forms such as one-dimensional (1D), three-dimensional (3D) and hierarchical structures have been examined in perovskite solar cells. One-dimensional nanostructures provide a direct route for electron transport and better perovskite infiltration which is beneficial for device performance. Some 1D nanostructures studied in perovskite solar cells include nanowires[97], nanorods[91,98], nanofibers[99] and nanotubes[100]. Hierarchical structures[101,102] and other 3D nanostructures[103,104] have also been examined to increase the low surface area presented in the 1D nanostructures[105]. Furthermore, interface engineering and elemental doping have been important to improve the electronic properties of the mp-TiO_2 and enhance the stability and device performance of perovskite solar cells[106–109]. Other oxide semiconductors that have been employed in the fabrication of perovskite devices include SnO_2[110,111], ZrO_2[112], SiO_2[113,114] and ZnO[115]. SnO_2 has a higher band gap (3.8 eV than TiO_2 (3.2 eV) which improves device stability under UV light (a common problem with TiO_2). Additionally, the larger electron mobility and deeper conduction band of SnO_2 facilitate electron transport. Furthermore, SnO_2 is compatible with flexible substrates due to the lower temperature sintering required in comparison with TiO_2. Devices of 17.21% have been achieved using SnO_2 as an electron transport layer with $CH_3NH_3PbI_3$ as the light absorber[111]. ZnO has a similar band gap to TiO_2. The higher conductivity and lower temperature processing required for ZnO in

comparison to TiO_2 makes it an ideal candidate for flexible solar cells[115]. A PCE of 15.7% on PSC was obtained based on ZnO nanoparticles as the ETL with a planar layer of $CH_3NH_3PbI_{3-x}Cl_x$ ($MAPbI_{3-x}Cl_x$ or MAPIC) as the absorber layer[85]. For mesosuperstructure architectures, SiO_2[113,114] and ZrO_2 [112] are some of the nanostructured oxides examined. A PCE of up to 12.4% for SiO_2 and 10.8% for ZrO_2 have been reported.

1.5.2 Light absorber perovskites

Methyl ammonium lead iodide ($CH_3NH_3PbI_3$, $MAPbI_3$ or simply MAPI) has been the most studied hybrid perovskite for solar cell applications and it is commonly referred to as the "standard perovskite" material. Ideally a good light absorber should have a panchromatic absorption covering all visible light as well as the near infrared region of the solar spectrum with high absorption coefficient. $MAPbI_3$ is a direct band gap semiconductor with an absorption coefficient of 1.5×10^4 cm^{-1} measured at 550 nm which makes it an efficient light absorber material. Nevertheless, $MAPbI_3$ presents relatively weak absorption over 800 nm due to its band gap of 1.55 eV[71]. Band gap engineering is one of the strategies to modulate the optoelectronic properties of the perovskite absorber. For instance, by decreasing the atomic size of the halide from iodide to bromide or chloride, the band gap increases from 1.55 eV for $CH_3NH_3PbI_3$ to 2.39 eV for $CH_3NH_3PbBr_3$ (or MAPbBr) and 3.17 eV for $CH_3NH_3PbCl_3$ (or MAPbCl). This is due to an increase of the covalent interaction between the halide anion and lead. Because of the lower band gap, it is expected that both MAPbBr and MAPbCl show lower performance in perovskite solar cells[116]. In the case of perovskite structure with mixed halides, $CH_3NH_3PbI_{3-x}Cl_x$ has been used in several studies showing a similar band gap to $MAPbI_3$ but longer carrier diffusion length[66,69]. Additionally, by increasing the composition of Br in $MAPb(I_{1-x}Br_x)_2$ ($0 \leq x \leq 1$) the absorption band shifts to shorter wavelengths which causes a decrease of the photocurrent density.[116,117]

The organic cation MA in $MAPbI_3$ has also been exchanged with other cations like formamidinium $HC(NH_2)_2^{2+}$. This modification caused a slight decrease of the energy

band gap to 1.5 eV and the absorption wavelength extended by about 40 nm[118,119]. Moreover, the mixed-organic cation perovskite $MA_{0.6}FA_{0.4}PbI_3$ exhibited an even smaller band gap (1.48 eV) producing a higher PCE and less hysteresis than $MAPbI_3$[120]. Another approach to tune the band gap is by replacing the metal cation. The bandgap decreases from 1.55 eV to 1.17 eV when Pb^{+2} in $MAPbI_3$ is mixed with Sn^{+2}. Perovskite solar cells with $MASn_{0.5}Pb_{0.5}I_3$ as the light absorber showed 4.18% PCE. This material can absorb light up to 1060 nm which might be beneficial for tandem solar cells[121]. The use of mixed cations and halides in perovskite not only enhanced the optoelectronic properties, but also has helped to improve the stability of the perovskite material. Although currently the best efficiency devices are achieved with mixed ion perovskites, $MAPbI_3$ is still widely used due its ease of synthesis and high efficiencies.[122]

One of the major concerns is the toxicity of lead in perovskite solar cells. Thus, to solve this problem, extensive research has been done to find other non-toxic metal cations[123,124]. Attention has been focused mainly on tin perovskites showing up to 6% efficiencies for $MASnI_3$[125,126]. Nonetheless, the poor stability of the perovskite material is the major problem due to the easy oxidation of Sn^{2+} to Sn^{4+}. Additionally, some studies have pointed out that tin might be as harmful to humans and the environment as lead[127]. Therefore more recently, Bi-based compounds have been studied due to the excellent stability and non-toxicity[128,129]. Nevertheless, lead-free perovskites give significantly lower efficiencies. Another route to not only avoid leakage of lead but also improve stability is better encapsulation and recycling of the perovskite solar cells.[130,131]

1.5.3 Counter Electrode

The counter electrode is the place where the holes from the oxidised perovskite are transported and where they recombine with the electrons which travel around the circuit. Usually, for perovskite solar cells, a thin layer of precious metal such as gold or silver is deposited on top of the hole transport material as the back contact. Both silver and gold have good conductivity and their work function matches with the

perovskite absorber and the hole transport layer. In order to replace the expensive gold, various alternatives have been investigated in perovskite solar cells[132,133]. Subodh G. Mhaisalkar and colleagues fabricated perovskite solar cells using laminated films of carbon nanotubes (CNT) as a hole collector with 6.87% efficiency. The efficiency was later improved to 9.90% by the addition of the hole transport material[134]. Compared to Ag and Au, carbon counter electrodes are much cheaper and easier to deposit especially for large-scale modules.

1.6 Hole-Transport Materials

The HTM plays an important role in the mechanism of perovskite solar cells and is a key component in almost all device architectures. The HTM extracts the photo-generated holes from the perovskite and transports them to the back contact electrode improving the hole transfer efficiency. The HTM also serves as an energetic barrier between anode and perovskite layer minimising charge recombination at the TiO_2/perovskite/HTM interface which leads to better device performance[135–137]. Similarly, the HTM influences the open circuit voltage[138,139] and reduces the degradation at the Au/perovskite interface[140,141]. For efficient solar cells, the HTM should meet a list of desirable properties: 1) compatible HOMO energy level layout with the valence band of the perovskite for efficient charge extraction, 2) good solubility in organic solvents, 3) sufficient hole mobility and conductivity, 4) good thermal and photochemical stability 5) minimal absorption in the visible and near infra-red region of the solar spectrum.

1.6.1 Inorganic Hole Transport Materials

Inorganic materials are a good choice for the HTM because of their intrinsic stability, low cost and high conductivity. Kamat and collaborators reported copper iodide (CuI) as the first inorganic HTM in mesoscopic PSC showing a modest 6.0% PCE. The poor performance was attributed to the high recombination measured by impedance spectroscopy. However, due to the higher conductivity in comparison to spiro-OMeTAD better fill factors were obtained with CuI devices[142]. Later, CuI was

introduced in a planar inverted perovskite structure showing an impressive PCE of 16.8%. The unsealed CuI devices showed higher air stability than the reference cells[143]. Later, the Ito group reported CuSCN as HTM using a mesoscopic inverted structure with only 4.85% of PCE[144] which was later improved to 12.4%[145] by using a low-temperature solution-process deposition method.

Moreover, Cu_2O and CuO were deposited as HTMs in PSCs by spin-coating and gave power conversion efficiencies of 13.35% and 12.16% respectively[146]. Previously, nickel oxide was used in DSSCs and now it is one of the most relevant inorganic HTMs in PSCs showing efficient (16.1%) and stable solar cells[147]. In order to further improve the stability of the perovskite solar cells, Grätzel, Han and colleagues reported the addition of Li and Mg in the NiO layer to create $Li_{0.05}Mg_{0.15}Ni_{0.8}O$ and achieved a 15.0% PCE in a 1.017 cm^2 device.[148]

The distinct properties of quantum dots have also attracted interest for application as HTMs in PSCs obtaining a maximum PCE of 8.4% using a $CuInS_2$/ZnS core-shell structure in mesoscopic perovskite solar cells. The good solubility of $CuInS_2$ in polar solvents makes it compatible with solution processing techniques[149]. Although inorganic materials offer relatively high efficiencies, these are still lower than organic HTMs and bring problems about stability in humid air. Furthermore, there are concerns about methods of deposition for inorganic HTMs such as solution processing where the solvent can also dissolve the perovskite.[150]

1.6.2 Organic Hole Transport Materials

Organic molecules have been extensively studied due to their unique advantages such as high solubility in organic solvents, suitable hole mobility, thermal and photochemical stability and tunability of the electronic properties via molecular engineering. Organic HTMs can be divided in two major categories: small organic molecules and polymers. Numerous alternative organic HTMs with different motifs has been studied for photovoltaic applications. Carbazoles,[151,152] triazatruxenes,[153] azulenes[154] and triphenylamines[155] are some of the structures that have been

investigated as HTMs in perovskite solar cells among others[156,157]. Figure 1.10 displays some HTMs with different structural cores studied previously. Among all the molecular motifs used for HTMs, triarylamines are one of the best candidates for high efficient solar cells as a result of their good charge transport and thermal stability. Triarylamine derivatives are well-known photo-conducting materials and have been used extensively in the xerographic industry. Triphenylamines are good electron donors as a result of the easy oxidation of the nitrogen centre and their capacity to transport positive charges via radical cations. The triphenylamine (TPA) unit can be used to build a wide variety of both low molecular weight compounds and polymers.[158,159]

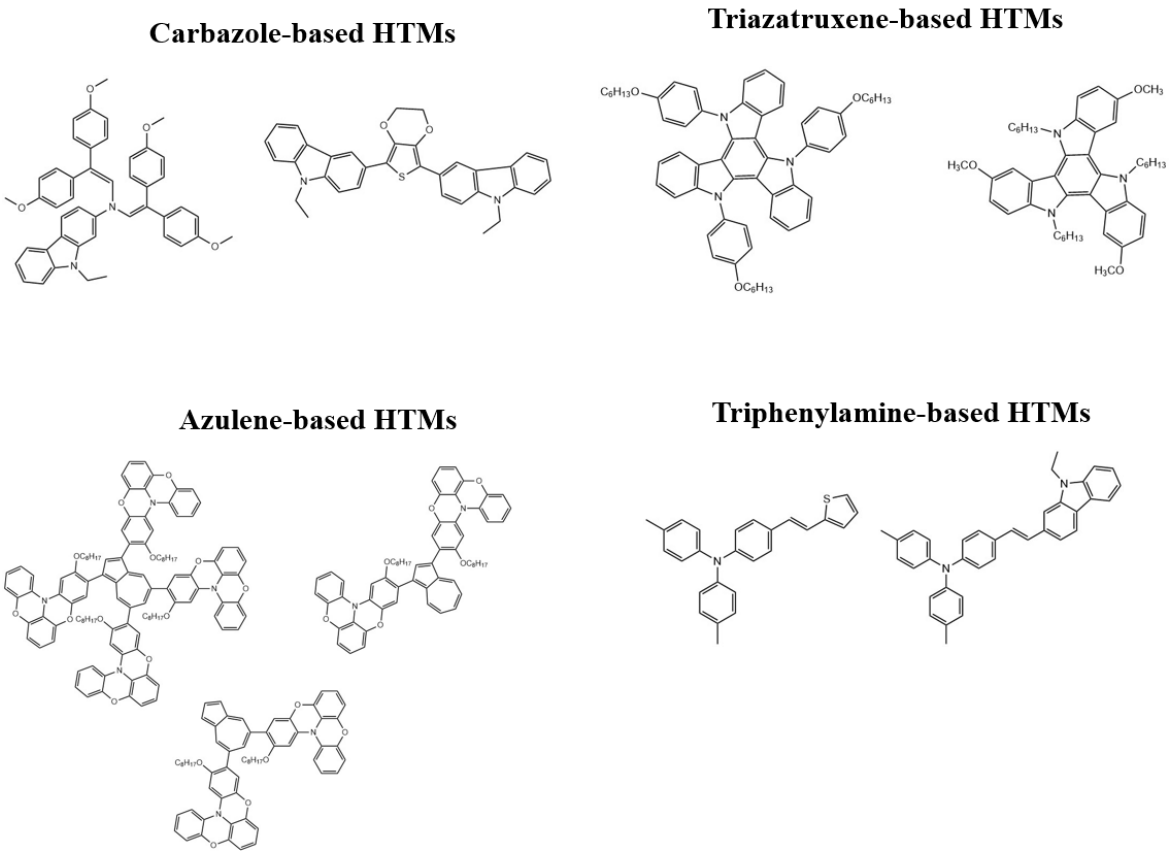

Figure 1.10 Representatives molecular structures of hole transporting materials used before.

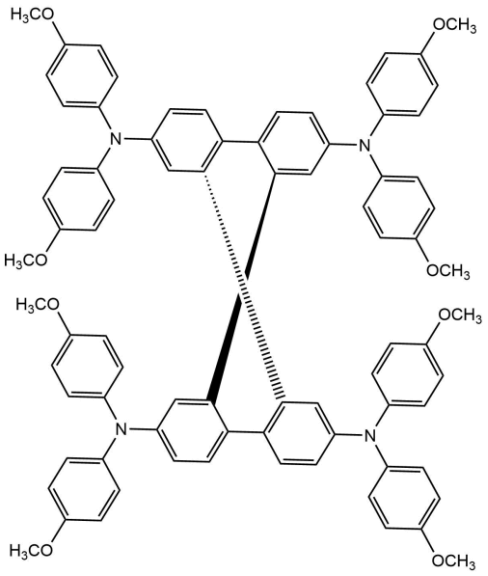

Figure 1.11 Molecular structure of Spiro-OMeTAD.

Small organic molecules are usually more efficient that polymer-based HTMs and have attracted most attention due to their simplicity, ease of purification, batch-to-batch consistency and easy modification. Spiro-OMeTAD (Figure 1.11) is the most studied HTM and is often used as a reference to compare other HTMs in photovoltaic devices. In 1998, it was first introduced as a HTM in a ssDSSC delivering a PCE of just 0.7%[52]. To date, spiro-OMeTAD is widely employed in perovskite solar cells when high efficiency is required. Nevertheless, spiro-OMeTAD in its pristine form has poor conductivity causing high series resistance (R_s) in the devices due to poor charge transport. This leads to the need to use p-type dopants such as tert-butylpyridine (TBP) and lithium bis(trifluoromethylsulfonyl)imide (Li-TFSI) to enhance the conductivity and improve device performance[160]. The use of additives increases the cost of fabrication and induces device instability.

One strategy to tune the properties of spiro-OMeTAD is to change the position of the methoxy groups (-OCH_3). Depending on the substitution, the methoxy group can exhibit a electron-withdrawing effect in the meta position and an electron-donating effect in the para position. Meanwhile, the ortho position influences the oxidation potential by steric effects. Seok and collaborators altered the optoelectronic properties

of Spiro-OMeTAD by changing the position of the methoxy groups. The ortho-substituted derivative exhibited better device performance than the para- and meta-substituted analogues with an overall PCE of 16.7%[161]. Despite offering high efficiencies, Spiro-OMeTAD is expensive due to its lengthy synthetic procedure and problematic purification which have limited its commercialisation. Therefore, researchers have focused on replacing Spiro-OMeTAD with cheaper alternatives that can provide similar efficiencies and better stability in perovskite solar cells. Recently, Maciejczyk and colleagues reported a low cost synthesis of four novel triarylamine-based HTMs using the spiro[fluorene-9,90 -xanthene] (SFX) core coded as SFX-TAD, SFX-TCz, SFX-TPTZ and SFX-MeOTAD (Figure 1.12). The solubility of SFX- TCz, SFX-TPTZ and SFXTAD was too low to test them in solar cells. Nevertheless, SFX-MeOTAD demonstrated a high efficiency of 12.4% in which 13.0% was obtained with Spiro-OMeTAD.[162]

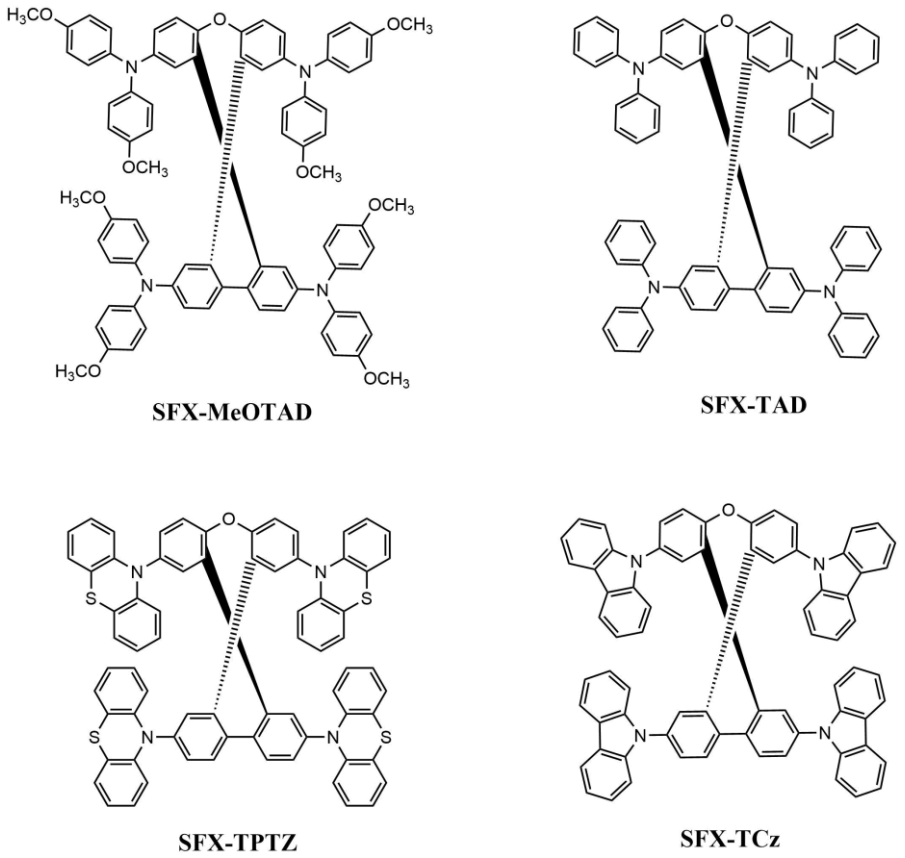

Figure 1.12 Molecular structures of spiro-based hole transport materials.

Other molecules have similar properties to spiro-OMeTAD but they are smaller and easier to synthesize and purify. There has been extensive research on the synthesis of new small organic molecules for HTMs. For instance, Songtao and co-workers reported two triphenylamine-based HTMs with butadiene derivatives noted as HTM_1 and HTM_2 (Figure 1.13) in perovskite solar cells. These HTMs are easier to synthesize, exhibited higher hole mobility and very close PCE (11.34% for HTM_1 and 11.64% for HTM_2) to that achieved with spiro-OMeTAD making them promising alternatives[163]. In another example, Hairong also reported a low cost synthesis of new HTMs by using the available EDOT (3,4-ethylenedioxythiophene) unit as the core structure. PCEs were comparable with solar cells using spiro-OMeTAD.[164]

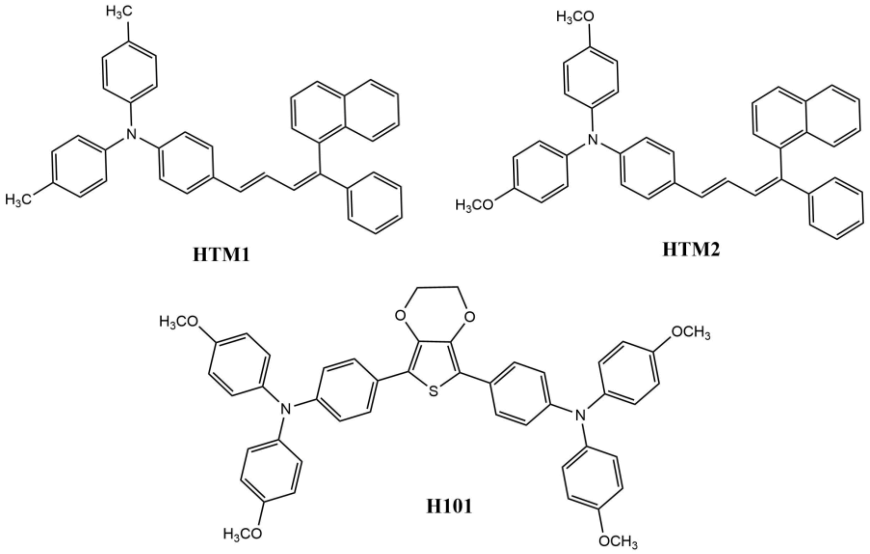

Figure 1.13 Molecular structure of simple hole transport materials.

One of the mains concerns in the fabrication of perovskite solar cells is the stability of the HTM. The morphology of the HTM film, which depends on the molecular structure, can significantly affect the stability of devices. An amorphous glassy state is the most beneficial for PSCs due to the easy formation and absence of grain boundaries. The stability of the morphology of any HTM is given by the glass transition temperature (T_g). A relative high T_g is required because devices usually work at higher temperatures than room temperatures and it is crucial that the deposited HTM film sustains the amorphous glassy state throughout those temperature changes [156].

One of the problems with small organic molecules with low molecular weight is that they crystallise easily with some crystals forming below the melting point which leads to the formation of grain boundaries. Polymers present some improved properties compared to their low molecular weight equivalents such as excellent film formation which allows an easy and low-cost manufacture of large scale technologies. One of the most notable improvements is that polymers have higher T_g and do not crystallise easily bringing an important potential advantage for the stability of the devices. Furthermore, the hydrophobic properties of polymers act as a protecting layer for the perovskite film to the ambient which enhances the solar cell stability. Previous studies of polymers as promising HTMs in PSCs include (Figure 1.14): poly(3-hexylthiophene)(P3HT)[165], poly[2,6-(4,4-bis-(2-ethylhexyl)-4H-cyclopenta[2,1-b;3,4-b']dithiophene)-alt-4,7-(2,1,3-benzothiadiazole)] (PCPDTBT)[166], poly[N-9'-heptadecanyl-2,7-carbazole-alt-5,5-(4',7'-di-2-thienyl-2',1',3'-benzothiadiazole)] (PCDTBT)[167], poly[bis(4-phenyl)(2,4,6-trimethylphenyl)amine] (PTAA)[168] and others.[156,157]

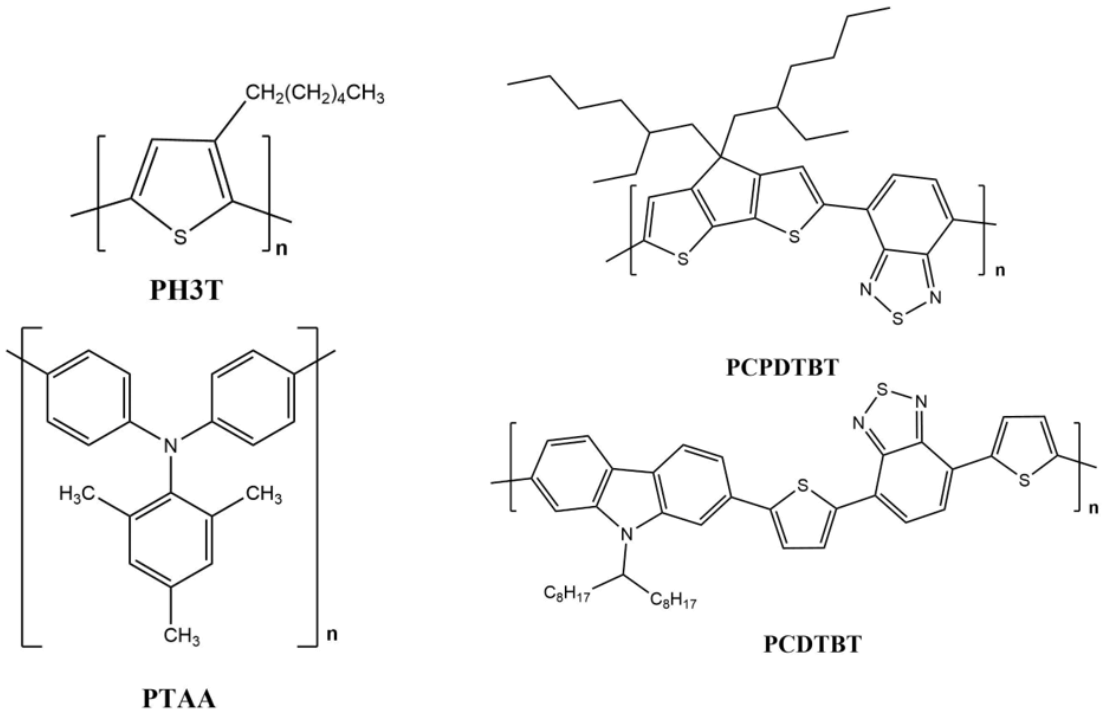

Figure 1.14 Molecular structures of most representatives polymers used as HTM.

1.7 Research Proposal

As discussed previously, spiro-OMeTAD is the most common HTM in perovskite solar cells largely due to its extensive research as an HTM in OLEDs and solid state dye-sensitised solar cells. Nevertheless Spiro-OMeTAD is expensive because of its lengthy synthetic procedure, low yielding synthesis and problematic purification. These issues have hampered the commercialization of efficient, low cost perovskite solar cells. Therefore, it has become important to design and develop more economical alternative HTMs. Triphenylamine (TPA) like Spiro-OMeTAD are widely used due to the easy oxidation of the nitrogen centre and good charge transport. Other triarylamines have similar properties to Spiro-OMeTAD but are easier to synthesise. The purpose of this work is to analyse different HTMs in perovskite solar cells. Therefore, three series of triphenylamine-based HTM were designed, synthesised and characterised for application in perovskite solar cells.

Triarylamines with lower molecular weight than spiro-OMeTAD, are easier to prepare and present similar properties making it relatively easy to create a series of HTMs with parallel structures via molecular engineering. A new series of diacetylide-triphenylamine (DATPA) derivatives with five different alkyl chains in the para position MeO, EtO, nPrO, iPrO and BuO was synthesised, fully characterised and their function as hole-transport materials in perovskite solar cells (PSC) studied. Their thermal, optical and electrochemical properties were investigated along with their molecular packing and charge transport properties to analyse the influence of different alkyl chains in the solar cells parameters. The alkyl chain length of semiconductive molecules plays an important role for achieving high performance perovskite solar cells.

Another option for HTMs is the utilization of p-type conducting polymers. These polymers are advantageous over small molecules due to their low cost, good device stability, simple device fabrication and easy preparation of designable structures. Styrenic triarylamines (Chapter 4) were prepared by the Hartwig-Buchwald coupling followed by their radical polymerization. All monomers and polymers were fully

characterised through electrochemical, spectroscopic and computational techniques showing suitable HOMO energy levels and desirable optoelectrochemical properties. The properties and performance of these monomers and polymers as HTMs in perovskite solar cells were compared in terms of their structure. Despite the lower efficiencies, the polymers showed superior reproducibility on each of the device parameters in comparison with the monomers and spiro-OMeTAD.

Finally, star-shaped structures (Chapter 5) combine the advantages of both small molecules, like well-defined structures and physical properties, and polymers such as good thermal stabilities. Two star-shaped triarylamine-based molecules were synthesised, fully characterised and studied for their function in perovskite solar cells. In total this work provides three series of triarylamine-based hole transport materials for perovskite solar cells application and enables a comparison of the pros and cons of different design structures: small-molecule, polymeric and star-shaped.

2 Experimental Methods

2.1 Characterisation methods

To confirm the structural identity of each novel hole transport material synthesised, a variety of techniques was required, principally NMR spectroscopy, mass spectrometry and elemental analysis. ^{1}H and ^{13}C NMR spectra were recorded on a Bruker Advance 500 spectrometer (500 MHz). The deuterated solvents are indicated in the synthesis description. Chemical shifts, δ, are given in ppm, using the solvent residual as an internal standard. MS were recorded on Micro-Tof using electrospray ionisation (ESI-MS) and Electron Ionization (EI-MS) techniques. Elemental analyses were carried out by Stephen Boyer at London Metropolitan University.

2.2 Electronic Absorption Spectroscopy

Hole transport materials with poor absorption in the visible to near infrared region (400 to 800 nm) bring additional benefits and flexibility in their application in inverted and tandem configurations where any absorption in the visible range of light is undesirable to avoid competition with the absorber material. Electronic Absorption Spectroscopy is a powerful technique to study the optical properties and gain understanding about the electronic energy states of molecules.

When molecules absorb radiation, the energy from the incoming photons are used to excite electrons from the ground state to higher electronic states. Only photons with the exact frequency can cause transitions from one electronic state to another one. Depending on the frequency of the radiation, different processes within the molecules can be studied. The total potential energy of a molecule is the sum of all the electronic, vibrational and rotational energies (Equation 2.1)[169].

$$E_{Total} = E_{Electronic} + E_{Vibrational} + E_{Rotational} \qquad \textbf{Equation 2.1}$$

Within the electronic states (n=1,2,3…) are vibrational energy levels (v=1,2,3...) and within these are rotational levels (j=1,2,3...). A given excitation/transition process should give rise to a sharp absorption line. Nevertheless, for molecules, excitations to different vibrational and rotational levels overlap, such that upon absorption of light many transitions with different energies occur and a broad band of wavelengths is obtained. Additionally, in solution this effect is even greater due to intermolecular interactions[169].

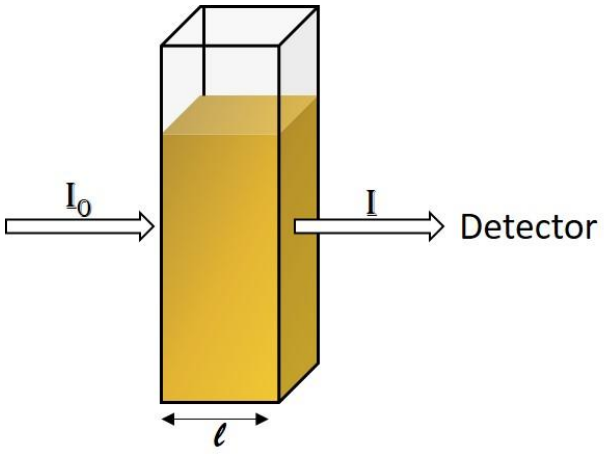

Figure 2.1 Schematic representation of the typical set-up of an absorption experiment. A polychromatic light passing through a sample where some of the light is absorbed and causes excitation of electrons. I_0 is the incident light, I is the light transmitted light through the samples, l is the length of the cell.

A UV-visible spectrometer is used to measure the absorbance of UV or visible light by a sample at a single wavelength or over a scan range in the spectrum. The UV region ranges from 190 to 400 nm and the visible region from 400 to 750 nm. In this technique usually the sample is fully dissolved in an appropriate solvent and the solution is held in an optically transparent cuvette. The reference cell contains the solvent used to dissolve the sample and it is commonly referred to as the blank. A beam light is passed through the sample (Figure 2.1) . The intensity of light passing through the sample (I) is compared to the intensity of the incident light (I_0) measured with the reference cell. It is assumed that the portion of the light not transmitted by the samples has all been absorbed by the sample. The transmittance is given by the following equation:

$$T = \frac{I}{I_o}$$ **Equation 2.2**

The absorbance (A) of the sample is related through the following equation:

$$A = -\log_{10} T$$ **Equation 2.3**

A UV-visible absorption spectrum expresses the absorbance as a function of wavelength. The higher the absorbance, the more of that particular wavelength is absorbed. The wavelength most strongly absorbed is usually referred to as the "lambda maximum" (λ_{max}). The intensity of light that can be absorbed is specific for each material and varies with its chemical structure. The absorption of light by a sample is directly proportional to the concentration of absorbing molecules (for dilute solutions) and the thickness of the cuvette holding the sample in the light path. This relationship is given by the Beer-Lambert Law (Equation 2.4)[169,170].

$$A = \varepsilon c \ell$$ **Equation 2.4**

Where c is the concentration of the sample, ℓ is the path length and ε is the molar absorption coefficient. The molar absorption coefficient determines how strongly a substance reduces the intensity of light when passing through the sample which is constant for a particular sample.

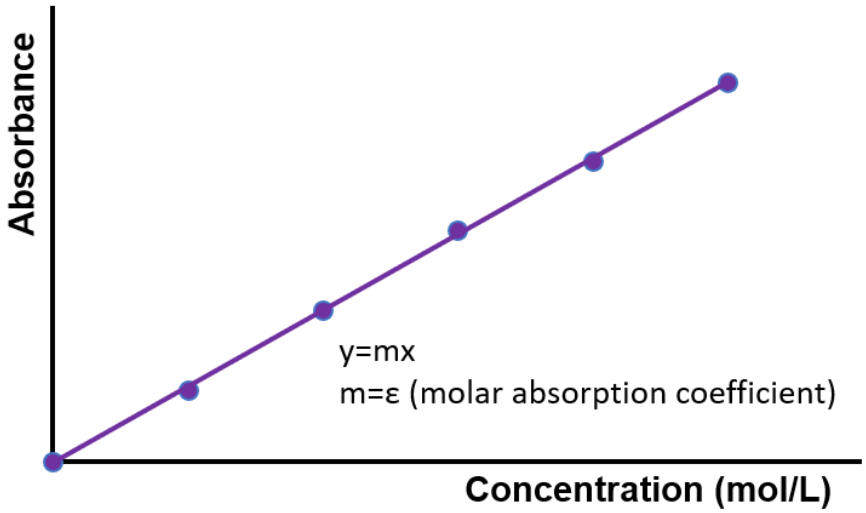

Figure 2.2 Example of the Beer-Lambert plot.

The molar absorption coefficient for a material can be calculated by measuring the absorbance of a series of sample solutions of known concentration and drawing a graph of absorbance versus concentration (Figure 2.2). The Beer-Lambert plot should be linear and the gradient of the resulting line gives the molar absorption coefficient. Deviation away from the linear dependence of the absorbance on concentration of the Beer-Lambert Law may be due to aggregation effects at high concentrations or the presence of undissolved species. This issue can be solved by using lower concentrations and a better choice of solvent.

Some transitions are more likely to happen than others. Allowed transitions typically have high probability of occurring and forbidden transitions are less probable. Theoretically, the allowed transitions should follow three main selection rules[171]:

1) **Spin Selection Rule (ΔS=0):** The overall spin state must not change during an electronic transition. Theoretically, a transition of an electron in a singlet state (S=0) to a triplet state (S=1) is forbidden.

2) **The Laporte selection rule:** In a molecule with centre of symmetry, transitions between the same parity (inversion symmetry) are forbidden. For instance, d orbitals have inversion symmetry, therefore d-d transitions (g→g) are forbidden, but transitions from d and p orbitals are allowed (g→u) because p orbitals are antisymmetric to inversion.

3) **Δl=±1:** Thus transitions involving Δl=±1 are allowed. For instance electrons can jump from 2p orbitals to 3s orbitals but the electron cannot jump between the three 2p orbitals because in that case Δl=0. Therefore, s→s, p→p, d→d and f→f transitions are forbidden.

2.3 Photoluminescence

Once a molecule is excited to higher energy levels (S_1, S_2….S_n) by absorption of light, it can return back to the ground state by non-radiative decay (heat) or radiative decay (photoluminescence). A fluorimeter spectrometer is used to measure the

photoluminescence of a molecule by determining the energy of an emitted photon. The instrument comprises four basic items: a source of light, a monochromator, a sample holder and a detector (Figure 2.3). The two representative spectra obtained from a fluorimeter are the emission and excitation spectra. The emission spectrum is produced by exciting the sample at a fixed wavelength and monitoring the photons emitted across a range of wavelengths. The excitation scan is obtained by exciting the sample across a range of wavelengths and monitoring only the emitted radiation at a fixed emission wavelength. Generally, the excitation spectrum should be similar to the absorption spectrum of the molecule measured by UV/Vis spectroscopy. Upon excitation to higher vibrational levels of an excited state, the molecules loses the excess vibrational energy and relaxes back to the lowest vibrational level of the excited state. Therefore, the emission spectrum is usually a mirror image of the excitation spectrum at a wavelength longer than the exciting spectrum.[172,173]

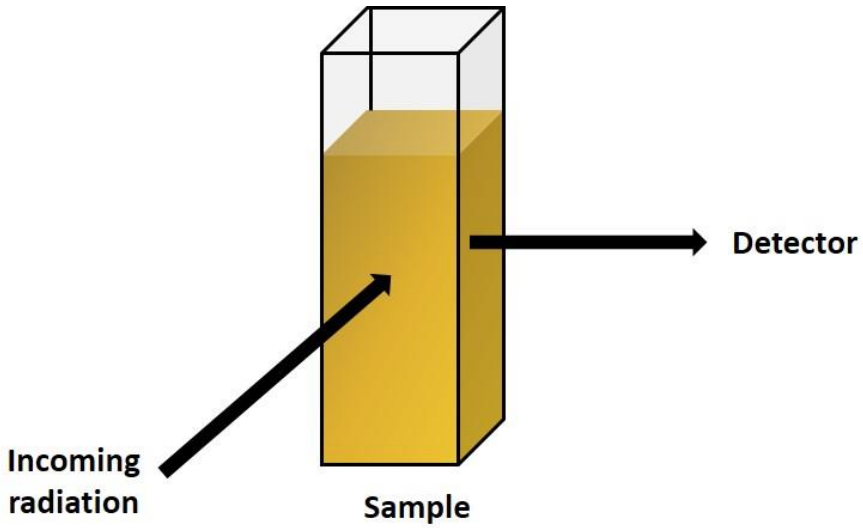

Figure 2.3 Schematic representation of a typical emission spectroscopy experiment.

When a molecule is excited to higher electronic states, not all the energy absorbed is re-emitted as radiative decay. Some of the energy is released via non-radiative decay. Non-radiative decay usually take place in two ways. The first one comprises intramolecular redistribution of the energy between electronic and vibrational states called internal conversion and vibrational relaxation respectively. In vibrational

relaxation, the molecule relaxes back to the lowest vibrational level before emission without any change in the electronic state. However, if there is a change in electronic state, the process is called internal conversion. The second way for non-radiative decay to take place is called 'inter-system crossing'. Inter-system crossing involves a change in the spin multiplicity from an excited singlet state to an excited triplet state which has a lower energy than the singlet. Then the electron can relax back by radiative decay by phosphorescence. In phosphorescence, the process involves a transition from a triplet excited state to a singlet ground state. The other non-radiative process is called external quenching and is where the excited molecule loses energy by interaction with another molecule in the surroundings and relaxes back to the ground state without emission. The interaction could be with the solvent, an impurity or oxygen. The possible process occurring in a photoluminescent molecule following absorption of a photon is illustrated in the Jablonski diagram (Figure 2.4).[174]

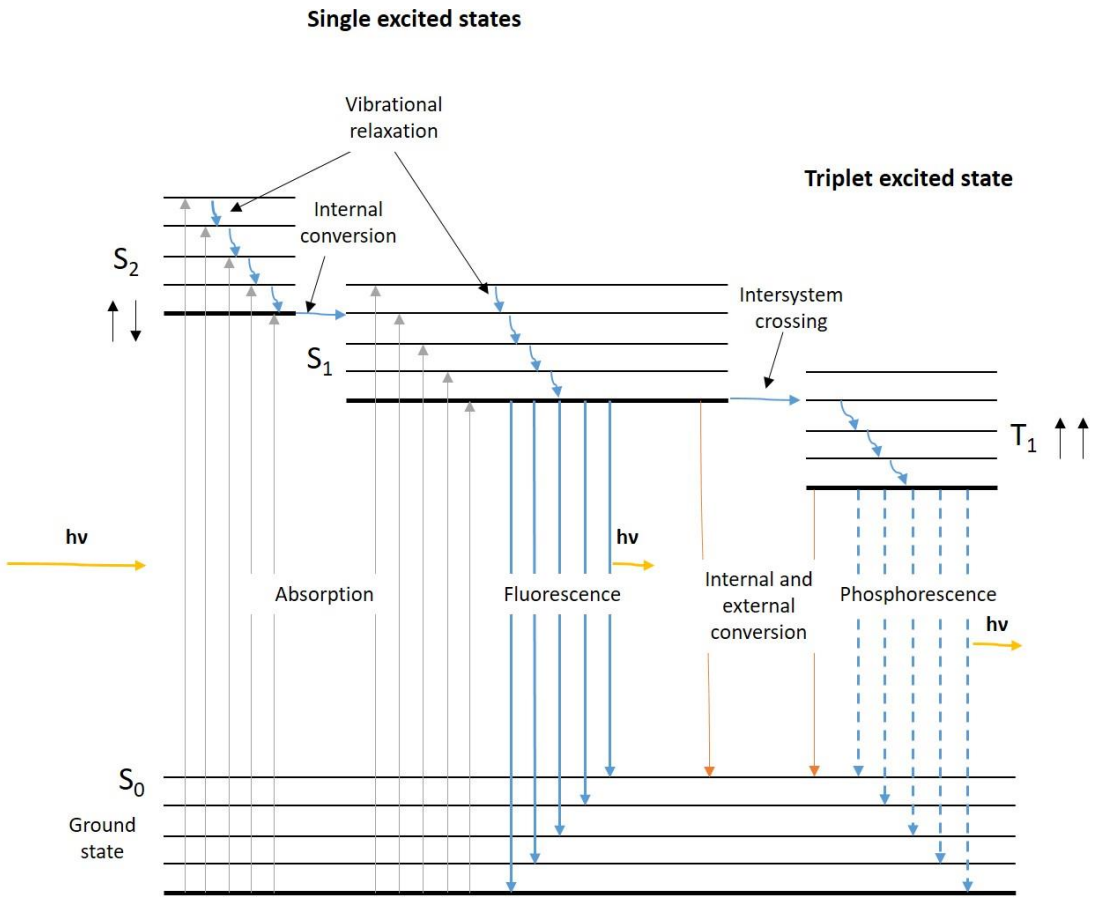

Figure 2.4 Jablonski diagram[174].

2.4 Electrochemistry

Electrochemistry is very important in material characterisation because it helps to estimate the position of the HOMO and LUMO energy levels of materials. This information is relevant for assessing the success or failure of a particular material in its desired application. For perovskite solar cells, a proper energy alignment with the HOMO energy level of the HTM and the valence band of the perovskite is crucial for effective hole transfer and efficient solar cells. Furthermore, electrochemistry techniques are also used to evaluate the reversibility and stability of the redox process. The oxidation involves an electron extraction from the HOMO level and is commonly correlated to the ionization potential, whereas the reduction is linked with electron affinity and gives information on the LUMO level.

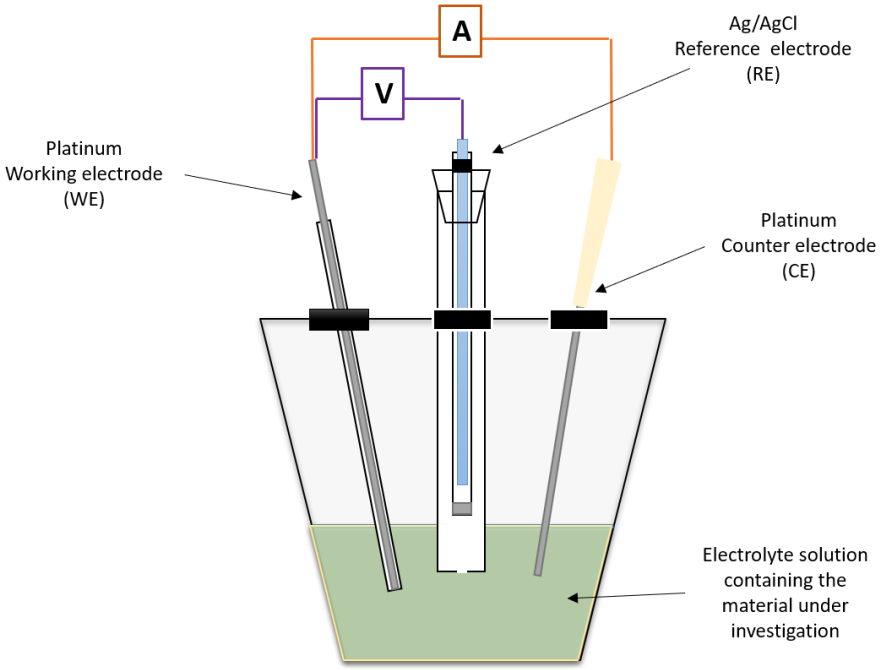

Figure 2.5 The three-electrode system.

The three-electrode system which comprises a working (WE), a counter (CE) and a reference electrode (RE), is the most common experimental setup used in electrochemistry (Figure 2.5). The reference electrode consists of a half-cell with a stable and well-defined potential. The reference electrode used in this work is the

silver/silver chloride electrode (Ag/AgCl) that is composed of a silver wire coated with a layer of silver chloride (AgCl) immersed in a saturated solution with LiCl. The half reaction is:

$$AgCl_{(s)} + e^{-} \leftrightarrow Ag_{(s)} + Cl^{-} \qquad \textbf{Equation 2.5}$$

The working electrode is where the redox reaction of interest takes place. Common working electrodes are made of inert materials such as gold, silver, platinum or glassy carbon. In this work, a platinum wire with a small surface area was used. A counter electrode is used to close the circuit in the system and it is also commonly made of an inert material such as platinum, gold, graphite or glassy carbon. The surface area of the counter electrode is generally larger than the working electrode to ensure that the process at the CE will not be a limiting factor in the kinetics of the redox process of interest occurring at the WE. In this work a platinum (Pt) rod was used as the counter electrode. The working and counter electrode must be constructed with inert materials to avoid interference with the redox process under investigation. The potential is applied across the WE and the CE and the overall voltage is measured between the RE using Equation 2.6.

$$\Delta E = V = E_{WE} - E_{RE} \qquad \textbf{Equation 2.6}$$

The current flows between the counter electrode and the working electrode. The three electrodes are immersed in the electrolyte solution which consists of the active species (usually at low concentrations) dissolved in a solvent (such as acetonitrile or dichloromethane) with a high concentration of an ionised salt. The redox process occurring at the WE typically involves three steps:

1. Mass transport: The reactants move from the solution to the electrode.
2. Electron transfer: The reaction at the interface
3. Mass transport: The product moves away from the electrode surface to the bulk solution.

Commonly the electron transfer depends upon the potential applied. There are three types of mass transfer regimes which are convection, migration and diffusion. Electrochemical experiments are usually set up to neglect one or two of the mass

transfer regimes. Convection can be removed by avoiding stirring, gas bubbling or any vibration in the cell. The migration component can be neglected by the addition of an inert electrolyte at a higher concentration than the active species. The electrolyte also increases the conductivity to avoid resistance through the solution.[175]

2.4.1 Cyclic Voltammetry

Cyclic voltammetry (CV) is one of the most common techniques in electrochemistry. This technique is performed by sweeping the potential of the working electrode at a fixed rate in cyclical segments from an initial potential to a maximum and then back to the initial potential as illustrated in Figure 2.6. A cyclic voltammogram is obtained by plotting the resulting current as a function of the potential during the scan process. The shape of the graph can be explained by understanding the different processes happening at the proximities of the working electrode.

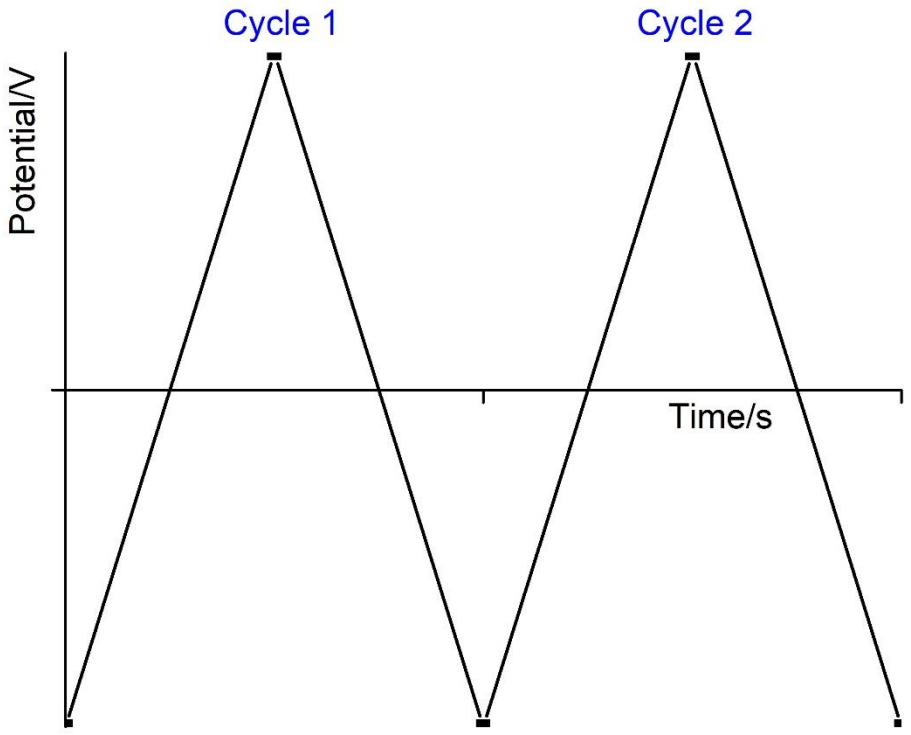

Figure 2.6 Cyclic voltammetry waveform

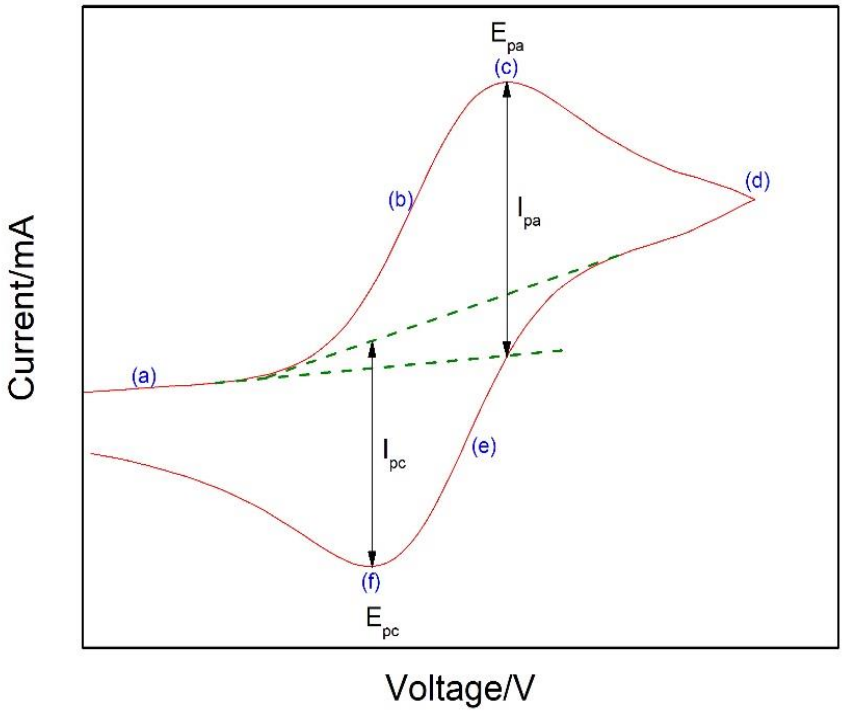

Figure 2.7 Cyclic voltammogram for a reversible one-electron process.

In Figure 2.7, the oxidation process occurs from point (a) to (d). Initially, the current is very small as the potential applied is insufficient to oxidise the active species (point a). As the scan continues, the potential becomes sufficient to induce oxidation and leads to an exponential increase of the current (point b). The current increases until it reaches a peak where all the species at the surface of the working electrode have been oxidised (point c). This resulting current is called the anodic peak current (i_{pa}) and the corresponding peak potential is called the anodic peak potential (E_{pa}). As the concentration of the non-oxidised species depletes and the oxidised species accumulates between the working electrode and the bulk, a diffusion layer is formed which increases the distance that the non-oxidised species have to travel to reach the electrode and restricts further oxidation processes. During this step, the current begins to decline as mass transport become the limiting factor and fewer non-oxidised species approach the working electrode (point d). Once the direction of the scan is reversed, initially the oxidation process continues until the potential becomes sufficient to reduced the oxidised species and a negative current increases exponentially until a

peak is reach (point e). This peak is characterised by the cathodic peak current (i_{pc}) and the cathodic peak potential (E_{pc}). The steps of the reduction process resemble that of oxidation but with opposite sign (point f).[176,177]

The experiment is repeated at different scan rates to check that the process is chemically and electrochemically reversible. If the compound studied and their respectively oxidised/reduced species are stable throughout the experiment and the rate of electron transfer is sufficiently fast on an electrochemical timescale, then the process can be thought of being chemically and electrochemically reversible. These are confirmed using certain well-defined criteria:

i. The position of the current peaks, E_{pa} and E_{pc} should be approximately:

$$E_{pa} - E_{pc} = \frac{59}{n} mV \qquad \textbf{Equation 2.7}$$

Where n is the number of electrons transferred

ii. The ratio of the current peaks should be one.

$$\left|\frac{I_{pa}}{I_{pc}}\right| = 1 \qquad \textbf{Equation 2.8}$$

iii. The position of E_{pa} and E_{pc} should not change with the scan rate.

iv. The current maxima are proportional to the square root of the scan rate

$$I_p \propto \sqrt{scan\ rate} \qquad \textbf{Equation 2.9}$$

This means that the plot of the peak current (I_{pa} or I_{pc}) versus $\sqrt{scan\ rate}$ should give a straight line.

If the position of E_{pa} and E_{pc} vary with the scan rate it means that the rate of electron transfer is slower than the experiment scan and the reaction is electrochemically irreversible. If there is no reverse peak in the process, then the reaction is chemically irreversible. This means that the electrochemically species formed has reacted to form a new compound such that the reverse scan cannot return the species to its original state.[175]

2.4.2 Differential Pulse Voltammetry

Instead of a linear sweep experiment, in differential pulse voltammetry (DPV) a series of potential steps is used to measure the current. The waveform of the process (Figure 2.8) consists of a series of small pulses with constant amplitude which have been placed on a staircase waveform. The potential of the working electrode is stepped between two values. The current is measured twice during a single step, before (i_1) and after (i_2) the pulse period (the time required for one potential cycle). The voltammogram is obtained by plotting the current difference (i_2-i_1) against the average potential producing a Gaussian peak (Figure 2.9). For DPV symmetric peaks indicate reversible reactions whereas irreversible reactions show asymmetrical peaks.

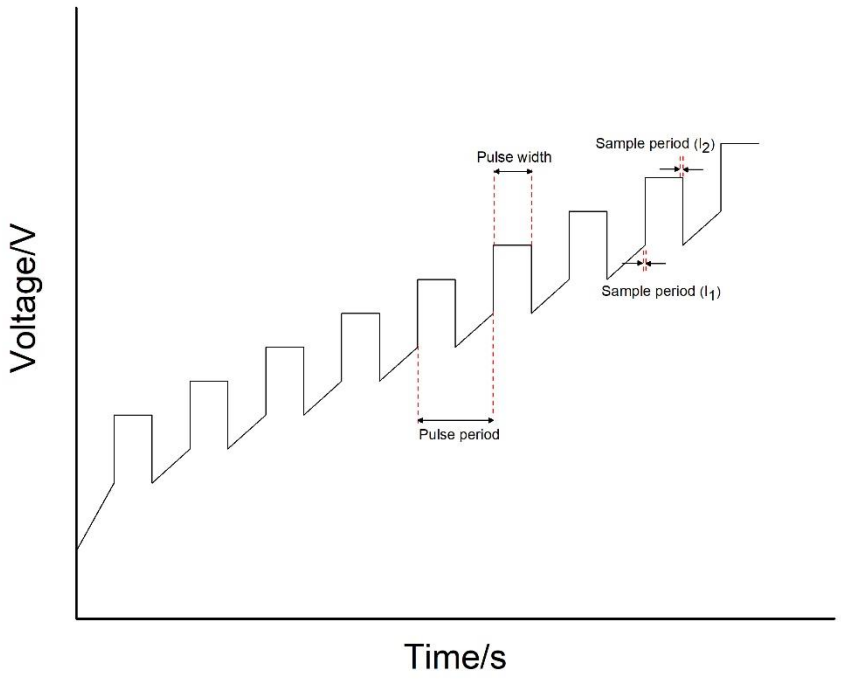

Figure 2.8 The waveform for differential pulse voltammetry

The peak potential is equal to $E_{1/2}$ in cyclic voltammetry and the peak current depends on the concentration of the species under investigation. This technique has better resolution than cyclic voltammetry and is very useful to elucidate the exact potential

of overlapping peaks found in CV experiments. Nevertheless, the technique requires more time than cyclic voltammetry as the scan rate is usually measured at 0.02 Vs^{-1} which could lead to complications when the material studied produces unstable species during the electrochemical process.

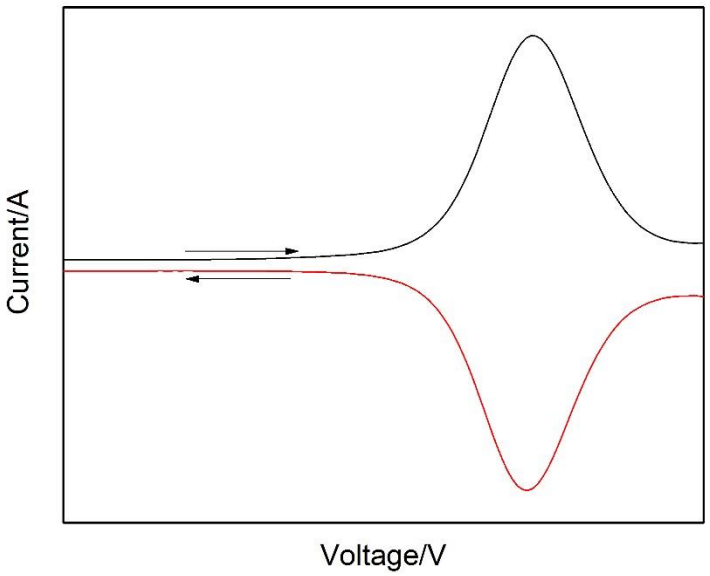

Figure 2.9 Differential pulse voltammogram of one reversible process.

2.4.3 Square Wave Voltammetry

The square wave voltammetry (SWV) technique combines a staircase potential waveform with a series of potential pulses (Figure 2.10). The current is measured twice, one at the end of the forward pulse and the other one at the end of the reverse potential pulse. This process is repeated at each step of the staircase ramp throughout the experiment. This technique is not only more sensitive but also faster than differential pulse voltammetry. The shape of the curve is similar to DPV as shown in Figure 2.9.[178,179]

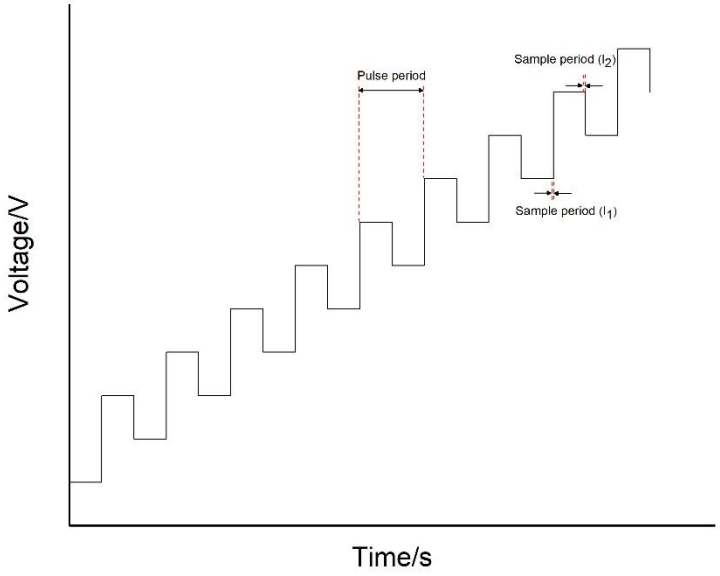

Figure 2.10 The waveform for square wave voltammetry.

2.5 X-Ray Diffraction

The crystal structure (the arrangement of atoms in a given crystal) plays an important role in determining the properties of a material. X-rays have a wavelength comparable with the spacing of the atoms in a molecule which causes the X-rays to diffract in all directions. X-ray diffraction is a non-destructive analytical technique which provides information about the entire crystal structure.

When X-rays are directed onto a crystalline solid which has a regular distribution of atoms, a characteristic diffraction pattern is observed in the photographic film (Figure 2.11). The Bragg's Law gives an explanation of this process. Consider two beams with identical wavelength approaching a crystalline solid and scattering off two different atoms within the crystal as illustrated in Figure 2.12. One beams strikes point A and the other travels an extra distance BC and strikes point D on the lattice plane below. The additional distance travelled by the lower beam is equal to BD + CD. Using basic trigonometry, it is found that this distance is equal to $2d \sin\theta$ where θ is the angle between the incident beam and reflecting plane and d is the interplanar distance. If the

path length difference (BD + CD) is equal to an integer multiple of the wavelength of the radiation, then the reflected waves are in phase (constructive interference) and diffracted X-rays will be observed. However, if this path length difference is not an integer number of wavelengths then the reflected X-rays will be out of phase and they will partially cancel one another (destructive interference). This is known as the Bragg condition and is given by the following equation.[180]

$$n\lambda = 2d \sin\theta \qquad \textbf{Equation 2.10}$$

Where n is an integer and λ is the wavelength of the X-rays. This model can be extended to 3D to solve the complete structure.[181]

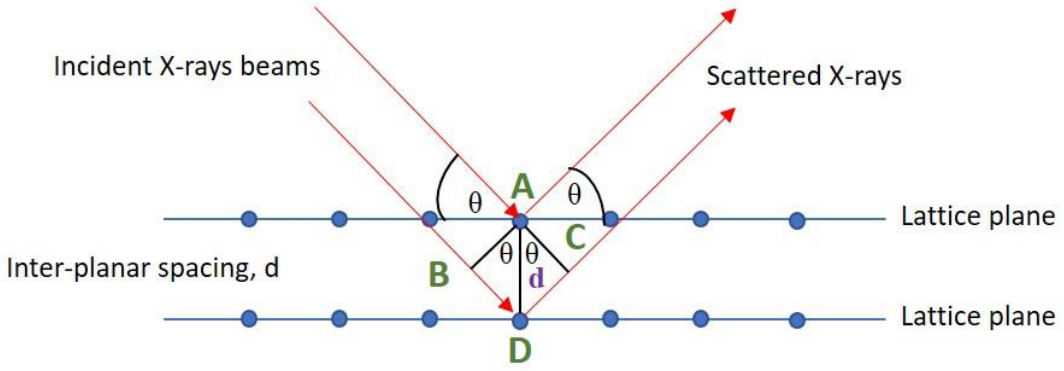

Figure 2.11 Scattering of X-rays by points A & D on parallel lattice planes.

In a typical XRD experiment for single crystals, the sample is rotated in the beam (so the angle θ changes). The diffracted X-rays are recorded using a detector onto a photographic film producing a series of bright spots and dark regions corresponding to conditions of constructive and destructive interference (Figure 2.12). The position, intensity and pattern symmetry of the spots provide information in the crystal structure. From the diffraction pattern obtained, a unit cell is first found. The X-ray intensity can be plotted against the angle θ (usually reported as 2θ) and then by using the Bragg equation, the angle 2θ for each diffraction peak can be converted to d-spacing. A crystal is treated as a collection of atoms and each peak is attributed to the scattering from a specific set of parallel planes. One can then work out the crystal structure and associate each of the diffraction peaks with a different atomic plane in terms of the

Miller Index for that plane (hkl), where h, k and l are coordinates defining the crystal plane. The entire structure can be solved using one of two methods. The first one is the Patterson method that finds the heavy atoms first and then works out the structure on a trial and error basis. The second one is the direct methods and it is the one used by the crystallographer Dr. Gary S Nichol to solve the crystal structures in this work.

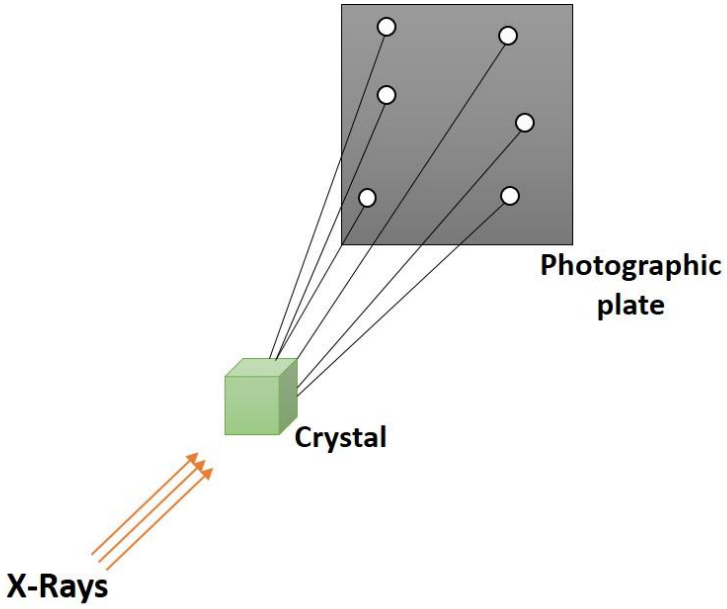

Figure 2.12 Schematic representation of the simplified experimental set-up for studying X-rays diffraction by single crystals.

All structures reported in this thesis were determined by Dr. Gary S Nichol**.** A suitable crystal was selected and mounted on a MITIGEN holder in Paratone oil on a Rigaku Oxford Diffraction SuperNova diffractometer. The crystal was kept at T = 120.0 K during data collection. Using **Olex2**, the structure was solved with the **ShelXS** structure solution program, using the Direct Methods solution method. The model was refined with a version of **ShelXL**.

Powder diffraction is a fast analytical technique in which the diffraction pattern is obtained from a powder or polycrystalline sample rather than a single crystal. This technique is easier than single crystal diffraction because of the minimal sample preparation required (no single crystal needs to be grown). A powder or polycrystalline

material is composed of an enormous number of randomly oriented tiny crystals. Each crystallite will diffract in a different direction which depends on its particular orientation. As there are many orientations of the crystal, multiple spots are produced forming a ring of different 2θ values. The result is a plot of the intensity of the signal versus 2θ. The shape of the diffraction peaks is related to the crystallinity of the sample. More crystalline materials in a sample give rise to a sharp intense peak whereas less crystalline materials result in broad and less defined peaks. Powder diffraction is usually used to determine the phase purity of a polycrystalline sample by comparing with the diffraction pattern obtained in single crystal X-ray diffraction.[182]

In this work, powder diffraction was performed on a Bruker Discover D8 with CuKa1/2 source and a scintillation detector. The powder diffraction patterns reported in this thesis were determined by Dr. Gary S Nichol**.**

2.6 Charge Mobility

Carrier mobility is an important parameter in determining device performance in photovoltaics as it characterises how fast an electron or hole can move in the material.The application of an external voltage in a semiconductor produces an electric field across the material that causes charge carries to move with an average velocity called the drift velocity. The mobility μ is then defined as the ratio between the drift velocity v_d and the applied electric field E as noted in Equation 2.11.

$$\mu = \frac{v_d}{E} \qquad \textbf{Equation 2.11}$$

In the absence of an electric field charge transport is simply described by diffusion of charges. The charge mobility of a material depends on many factors including molecular properties, impurities, temperature and molecular packing.[183]

In organic materials the transport is intermolecular and is also referred to as hopping transport. In other words, charge transfer occurs from HOMO to HOMO or LUMO to LUMO between individual molecules and not via delocalised bands like in a metal or inorganic materials. A polaron hopping model has been suggested for the charge

transport mechanism[184]. When an electron is taken or added into an organic material, this changes the spatial distribution of electrons. This adjustment leads to a polarization locally centred on the charge carrier. The combination of the charge with the geometric distortion of the molecule is referred to as a polaron. If the interaction of the polaron with the surrounding molecules is strong enough, the charge may become trapped and move via thermally induced hopping with charges jumping between interacting molecules. This means that charge mobility increases with temperature.[184]

The efficiency of charge transport is associated with the position of the interacting molecules and therefore to crystal packing. Therefore the analysis of the molecular packing is important to understand charge transport in a semiconductor. The packing of a molecule can be modified by using molecular engineering by changing side groups without modifying the position of the frontier orbitals.

The charge mobility is also influenced by the presence of charge traps in the semiconducting material which can arise from grain boundaries in thin films or impurities, hence decreasing the mobility.

Charge mobility can be measured by several techniques including time-of-flight (TOF), Field-Effect Transistor configuration and diode configuration. In this work charge mobilities were obtained using the Field-Effect Transistor configuration due to its simplicity.[185]

2.6.1 Organic Field Effect Transistors

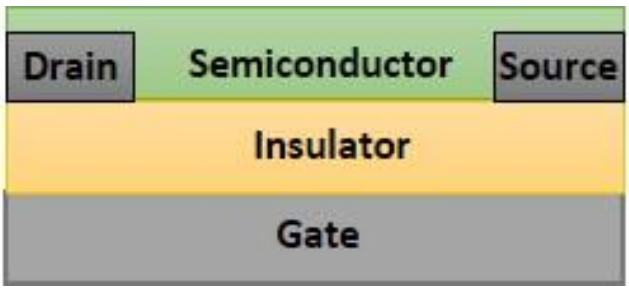

Figure 2.13 Schematic of a bottom-gate & bottom-contact field effect transistor.

The FET (field-effect transistor) is a three-terminal transistor that uses an electric field produced by one electrode to control the current flow between the two others. A typical design of a FET comprises a semiconductor layer which is separated from a gate electrode by the insulating layer. Two electrodes, the source and the drain of width W (channel width) separated by a distance L (channel length) are in contact with the semiconducting layer (Figure 2.13). There are four existing device configurations: 1)top-gate/top-contact, 2)bottom-gate/top-contact, 3)top-gate/bottom-contact and 4)bottom-gate/bottom contact. In this work, pre-fabricated devices with the configuration bottom-gate/bottom-contact were used and a layer of the semiconductor material was deposited on top. The voltage applied between the source and gate electrodes, produces an electric field which causes the energy levels (HOMO and LUMO) to either shift down and accumulate electrons or shift up and accumulate holes. The minimum potential necessary to induce mobile charges between the drain and source is called the threshold voltage (V_T).

In a typical experiment, the source/drain current (I_{SD}) is monitored in response to the voltage between the drain and the source (V_{SD}) and the potential applied at the gate electrode (V_G). For a given voltage V_{SD}, the current I_{SD} strongly depends on the potential V_G applied to the gate.

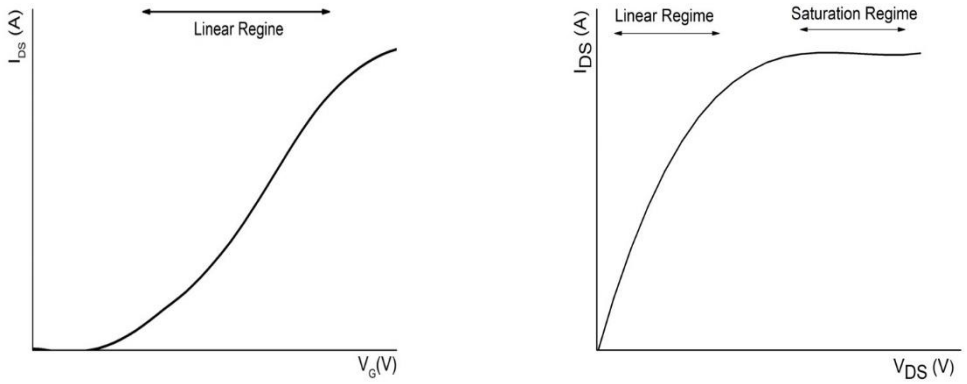

Figure 2.14 Transfer (left) and output (right) curves of an FET device.

Typically, two types of experiments can be performed to characterise FETs. In the first one, the voltage V_G is kept constant, and the potential V_{SD} is swept. This is commonly referred to as the output curve (Figure 2.14, right). The second way is keeping V_{SD} constant and sweeping V_G. This is usually referred as the transfer curve (Figure 2.14 left).[186]

Output Characteristic

Linear Regime $$I_{\mathrm{DS}} = \left(\frac{W}{L}\right)\mu_{\mathrm{lin}}C_{\mathrm{i}}(V_{\mathrm{G}} - V_{\mathrm{T}})V_{\mathrm{DS}}$$ **Equation 2.12**

Saturation Regime $$I_{\mathrm{DS}} = \left(\frac{W}{2L}\right)\mu_{\mathrm{sat}}C_{\mathrm{i}}(V_{\mathrm{G}} - V_{\mathrm{T}})^2$$ **Equation 2.13**

Transfer Characteristic

Linear Regime $$\mu_{\mathrm{lin}} = \left(\frac{\partial I_{\mathrm{DS}}}{\partial V_{\mathrm{G}}}\right)\cdot\left(\frac{L}{WC_{\mathrm{i}}V_{\mathrm{DS}}}\right)$$ **Equation 2.14**

Saturation Regime $$\mu_{\mathrm{sat}} = \left(\frac{\sqrt{\partial I_{\mathrm{DS}}}}{\partial V_{\mathrm{G}}}\right)^2\cdot\left(\frac{2L}{WC_{\mathrm{i}}}\right)$$ **Equation 2.15**

Where **W** is the width channel, **L** is the length channel, $\mathbf{C_i}$ is the capacitance of the insulator, $\mathbf{I_{DS}}$ is the drain-source current, $\mathbf{V_{DS}}$ is the drain-source voltage, $\mathbf{V_G}$ is the gate voltage and $\mathbf{V_T}$ is the threshold voltage.

When a small source-drain voltage in applied ($V_{SD} \ll V_G$) a linear regime is formed in which the current I_{SD} is directly proportional to V_{SD} (Equations 2.12 and 2.14). As V_{SD} increase and approaches the value of the gate voltage ($V_G - V_T$) a depletion region is formed giving a space-charge-limited saturation (I_{sat}) flow across the channel (Equation 2.13 and 2.15). At this point any further increases in source-drain voltage will not significantly increase the current I_{SD} in the device. Mobilities can be extracted from both the output or transfer characteristic curves in the linear or saturation regime using the corresponding equations presented above. The mobility in the linear regime is referred as μ_{lin} and the mobility in the saturation regime as μ_{sat}.[186]

2.7 Differential Scanning Calorimetry

The stability of the morphology of amorphous, glassy HTM is given by the glass transition temperature (T_g). Solar cells work usually at higher temperatures than room temperature (~80 ℃) and can undergo temperatures changes depending on the time, location and season. Therefore, it is important that the deposited HTM film maintains its morphology throughout those temperature changes.

Differential scanning calorimetry (DSC) is a thermal analysis technique in which the heat capacity of a material is measured as a function of temperature and time. The heat capacity of a system is defined as the amount of energy needed to increase the temperature of the system. In a DSC experiment, there are two pans. In one of them, a sample of known mass is placed and the other one is empty. Both pans are heated at the same time using the same rate (usually 10 ℃ $/min$). The empty pan serves as a reference. The pan with the sample will require more heat to increase the temperature and therefore it is possible to compare this with the empty one by measuring this extra heat needed. This measurement provides quantitative and qualitative information about physical and chemical changes including melting point, boiling points, glass transition temperature, crystallization temperature, purity and others. This technique allows us to study the thermal transitions of a sample.[187,188]

One of the most important properties that we can measure for a glassy or amorphous material is the glass transition temperature which is the temperature where an amorphous material (e.g. a polymer) changes from a hard and rigid state to a more flexible or "rubbery" state. When a hard and rigid material is heated, at some point there is enough energy in the material that it can be mobile (more flexible). This point appears as a step change in the instrument baseline.[189]

2.8 Solar Cells

2.8.1 Fabrication

The solar cells were fabricated at Swansea University by Dr. Joel Troughton. A fluorine doped tin oxide (FTO) coated glass (7 Ω/sq) was cut into 1.4 x 1.4 cm^2, and etched with zinc powder and HCl 2M to remove the FTO in the desired electrode patterning. The substrates were cleaned in a solution of detergent and deionised water before sequential sonication in deionised water, acetone and isopropanol and a 10 minute oxygen plasma treatment to remove the last traces of organics. A compact TiO_2 layer was deposited on the glass substrate through spray pyrolysis of a 0.2M solution of titanium diisopropoxide bis(acetylacetonate) in isopropanol at 450 ℃. Upon cooling, a mesoporous layer of TiO_2 nanoparticles was spin-coated from a 2:7 wt suspension of Dyesol 30NR-D paste in ethanol (4500 rpm for 30 seconds), followed by sintering at 550 ℃ for 30 minutes. A $CH_3NH_3PbI_3$ perovskite precursor solution was prepared by dissolving 576 mg PbI_2, and 199 mg CH_3NH_3I in a 4:1 vol solution of DMF:DMSO. The perovskite precursor solution (100 µL) was deposited onto the TiO_2 films and spin-coated at 4000 rpm for 30 seconds, with 200 µL of ethyl acetate dripped onto the spinning substrate 10 seconds prior to the end of the spin-coating process. Perovskite films were annealed at 100 ℃ for 10 minutes. The hole transport materials were dissolved in chlorobenzene with the corresponding additives and spin coated on top of the perovskite layer after which a 80 nm thick gold electrode was evaporated at 10^{-4} Torr.

2.8.2 Testing the efficiency

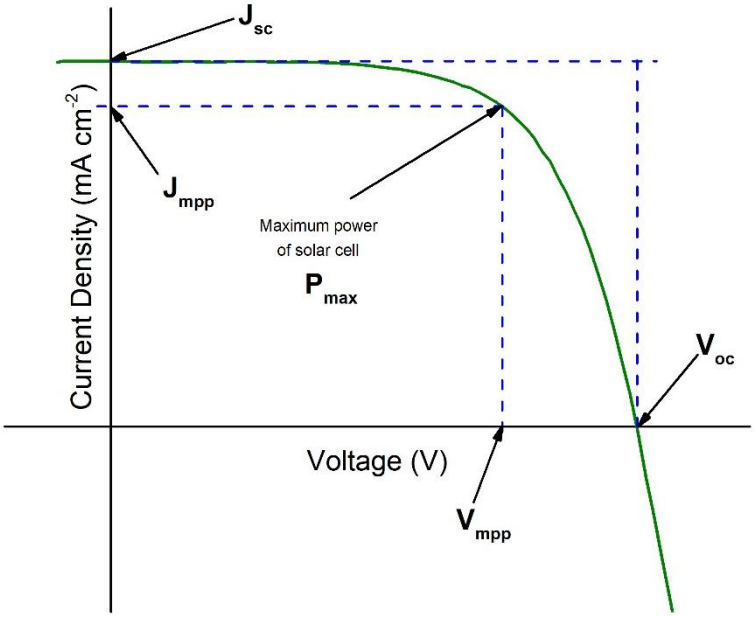

Figure 2.15 Example of current-voltage characteristics of a solar cell under illumination

The efficiency (η) of a solar cell is given by the ratio of the power generated by the cell (P_{out}) to the optical power entering the cell (P_{in}) as described in Equation 2.16. The power input (P_{in}) is determined by the light intensity of the lamp employed for testing. The solar cells are tested by scanning an applied voltage across the cell and measuring the current generated. To consider the surface area of the cell, current density (J/A cm^{-2}) is calculated and then plotted against voltage to produce a J-V curve (Figure 2.15). The efficiency of the solar cells depends on the incident light used and the temperature of the solar cell. Therefore, for reliable comparison between solar cells, the measurements are performed under standard test conditions (STC) using an AM1.5 spectrum with an incident light intensity of 100 mW cm^{-2}.

$$\eta = \frac{P_{out}}{P_{in}} \times 100\% \qquad \textbf{Equation 2.16}$$

The four main parameters used to characterise the performance of solar cells are the open-circuit voltage (V_{oc}), the short-circuit current density (J_{sc}), fill factor (FF) and

the power maximum ($P_{\max}$). These parameters can be obtained from the J-curves and are used to determine the power conversion efficiency (η).

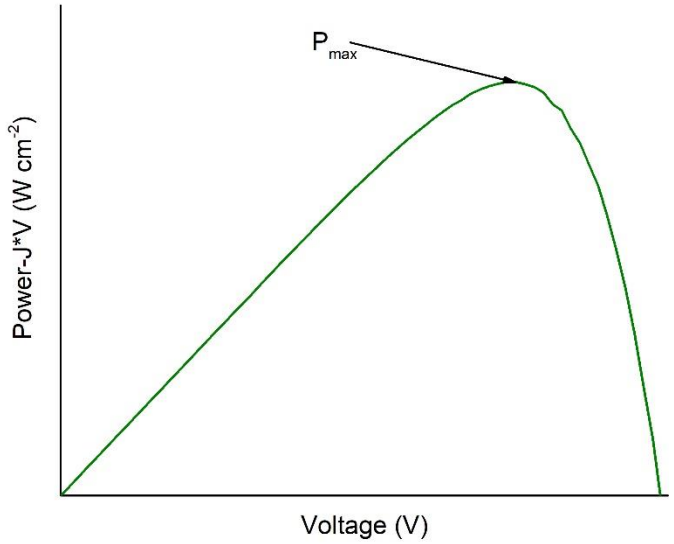

Figure 2.16 Example of power-voltage characteristics of a solar cell under illumination.

The open-circuit voltage V_{oc} is the maximum voltage that a solar cell can deliver at which the current is zero. The short-circuit current density J_{sc} is the current that flows through the circuit when the voltage across the solar cell is zero (solar cell is short-circuited). The fill factor FF is the ratio between the maximum power ($P_{\max} = I_{mpp} \times V_{mpp}$) generated by a solar cell to the product of V_{oc} and J_{sc} (Equation 2.17).

$$\mathrm{FF} = \frac{\mathrm{P_{max}}}{\mathrm{J_{sc} \times V_{oc}}} = \frac{\mathrm{I_{mpp} \times V_{mpp}}}{\mathrm{J_{sc} \times V_{oc}}} \qquad \textbf{Equation 2.17}$$

Where mpp denoted the maximum power point of the solar cell, the point on the J-V curve at which the solar cell has the maximum power output (Figure 2.16).[190]

2.9 Transient Absorption Spectroscopy

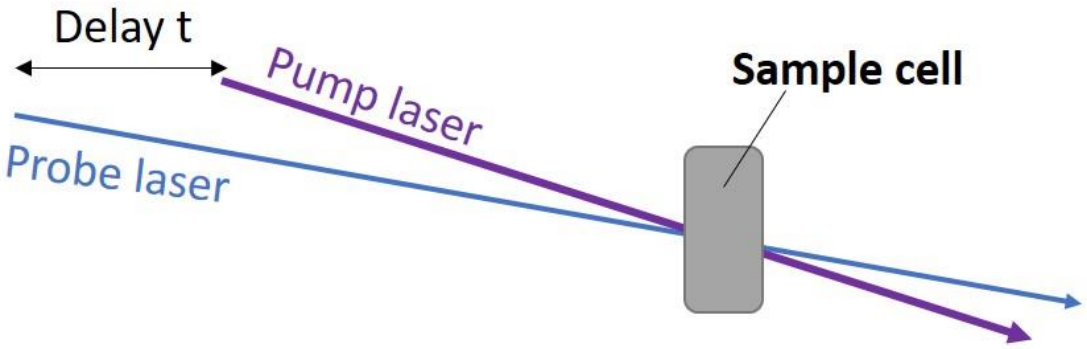

Figure 2.17 Schematic representation of the transient absorption principle.

Transient absorption spectroscopy is a time-resolved spectroscopy method which we used to provide quantitative information of the charge transfer of the HTM in perovskite solar cells. In this technique, a laser (pump laser) is used to promote a fraction of the molecules to an electronically excited state. A second laser (the probe laser) is passed through the sample with a delay t with respect to the pump laser. It is then possible to calculate the difference in absorbance (ΔA) between the species created following the laser pulse and the ground state species. By changing the time delay t between the pump and the probe, a ΔA profile as a function of time is obtained. The difference in absorbance is given by:

$$\Delta A(\lambda) = A_{pump} - A_{unpump} = \log \frac{I_{pump}(\lambda)}{I_{unpump}(\lambda)} \qquad \textbf{Equation 2.18}$$

Where A_{pump} correspond to the absorbance when the pump passes through the sample and A_{unpump} is the absorbance without any pump. I_{pump} and I_{unpump} are the light transmitted through an excited and non-excited sample.[191]

These measurements were performed at Imperial College London by Dr. Irene Sanchez Molina from the Haque group. A sample containing the titanium working electrode with the perovskite species and the HTM was initially measured by varying the probe wavelength to determine at which wavelength the signal had the highest

intensity. Measurements were then performed at that wavelength with or without HTM on mesoporous TiO_2 or Al_2O_3 electrodes. The decay rate of the signal provides information of the kinetics of electron transfer between the perovskite and HTM or TiO_2.

3 Small molecule [DATPA] HTMs

3.1 Introduction

In order to address the limitation of the expensive synthetic procedure of Spiro-OMeTAD[52], smaller triarylamines have attracted most attention due to their comparable optoelectronic properties, simplicity, ease of purification and batch-to-batch consistency[159]. The chemical structure of the HTM can significantly affect the hole transfer kinetics between the HTM and the perovskite and the HTM and the metal contact in perovskite solar cells[135,192]. The length of alkyl chain for instance, can influence the solubility, molecular ordering and charge transport of the HTMs thus affecting the performance of the solar cell[193,194]. Although the large majority of triarylamine HTMs include methoxy groups to tune the redox potential, little research has been done to study the effect of the alkyl chain on the properties of the HTM. In previous studies Hagfeldt[193] and co-workers demonstrated the importance of the substituents by tuning the position and length of the alkyl chain in four triphenylamine-based organic HTMs. In a different study, Nazeeruddin[195] and co-workers studied the influence of alkyl chain length on the power conversion efficiency of a series of hole transport material. Such reports are rare however, and there are still limited comprehensive studies of the effect of alkyl chain length on material and device properties. In the case of organic photovoltaics, studies have shown both increases and decreases in power conversion efficiency through increasing the length of alkyl chains[194,196–198], therefore more systematic understanding of this effect for HTMs in PSCs is important to acquire. In previous work reported by our group, a series of triphenylamine-based HTMs having two diacetylide-triphenylamine (DATPA) moieties was prepared by a simple synthetic route which allows easy tuning of electrochemical and other properties through varying the substituent R groups in the para position[199]. These materials were studied as HTMs in solid state dye-sensitised solar cells and showed promising properties in comparison with Spiro-OMeTAD.

In this project, a new series of diacetylide-triphenylamine (DATPA) derivatives with five different alkyl chains in the para position MeO, EtO, ^{n}PrO, ^{i}PrO and BuO (Figure 3.1) was synthesised, fully characterised and their function as hole-transport materials in perovskite solar cells (PSC) studied. Their thermal, optical and electrochemical properties were investigated along with their molecular packing and charge transport properties to analyse the influence of different alkyl chains in the solar cells parameters. The alkyl chain length of semiconducting molecules plays an important role for achieving high performance perovskite solar cells.

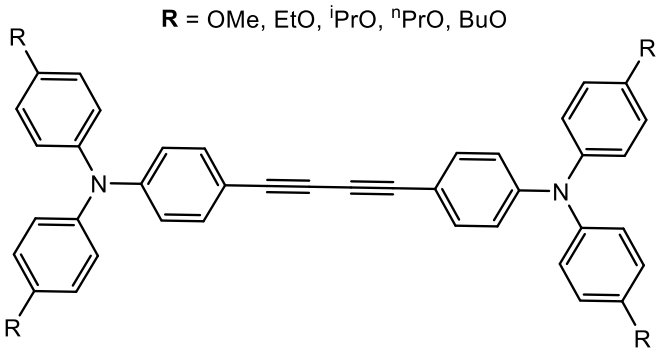

Figure 3.1 Chemical structure of HTMs used in this study. Each molecule is comprised of two triphenylamine moieties bridged with a diacetylene group.

3.2 Results and Discussion

3.2.1 Synthesis

The synthetic procedure reported for MeO-DATPA in previous work[199] in the Robertson group was revised and optimised to improve yields and reduce reactions times. The general synthetic route for the synthesis of the DATPA derivatives is shown in Scheme 3.1. Apart from EtO-DATPA, the method of synthesis involves five stages. The first step is a simple SN_2 reaction (Figure 3.2). 1-Ethoxy-4-iodobenzene is commercially available, and this step was not required for that example.

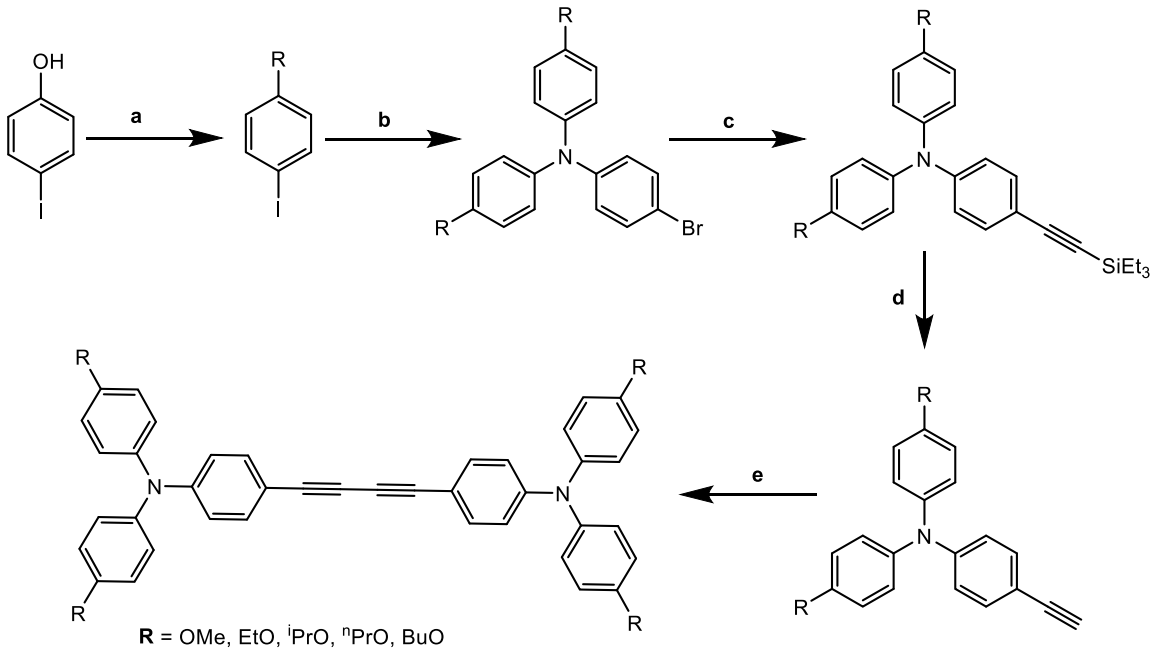

Scheme 3.1 Synthetic procedure for all HTMs. Reaction conditions: a) K_2CO_3, 18-crown-6, R-Br, DMF, 100 °C, 4hrs, N_2 b) CuI, 1,10-phenanthroline, KOH, MePh, 4-bromoaniline, N_2, 120°C; c) $C_8H_{16}Si$, CuI, piperidine, $(PPh_3)_2PdCl_2$, PPh_3,PhMe, N_2, 90 °C; d) 1 M TBAF, DCM, rt, N_2; e) CuCl, TMEDA, Molecular Sieves, DCM, air.

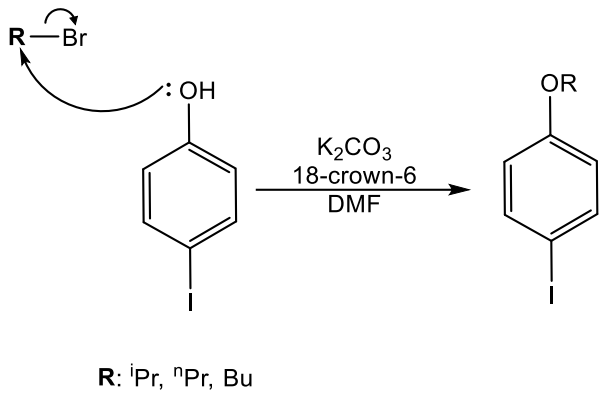

Figure 3.2 Mechanism for SN_2 reaction.

The triarylamine group with electron donating groups in the para position were formed using the copper catalysed Ullmann coupling. The "classic" Ullmann[200] reaction has many downsides including high copper loadings, high temperatures and long reaction times. Later, it was found that with addition of bidentate ligands lower copper loading and milder reaction temperatures were needed[201]. Although this method has been studied for a long time, the modified copper-mediated Ullmann still presents some downsides. The reaction is somehow unpredictable and generally affords modest yields of product as there are side products formed in the process. A non-polar solvent like toluene was used in which copper(I) was used as a catalyst, 1,10-phenantroline as ligand and KOH was used to quench the HI acid formed. Although such Cu-catalysed couplings have not reached the high levels that characterise the analogous palladium-catalysed chemistry, it is one of the most practical and economical methods for the synthesis of triarylamines.

The exact mechanism of the copper-catalysed amination remains under debate. There are several mechanism proposed, however the most recognised mechanism is a catalytic cycle that involves the oxidative addition of the aryl C–X (X=halogen) bond to Cu(I).[202–204]A rough picture of the possible catalytic cycle for the modified Ullmann coupling is displayed in Figure 3.3. This is an approximate representation of what may happen rather that a mechanism. The details of these general steps however remain uncertain, especially regarding the order of the oxidative addition and transmetallation steps.

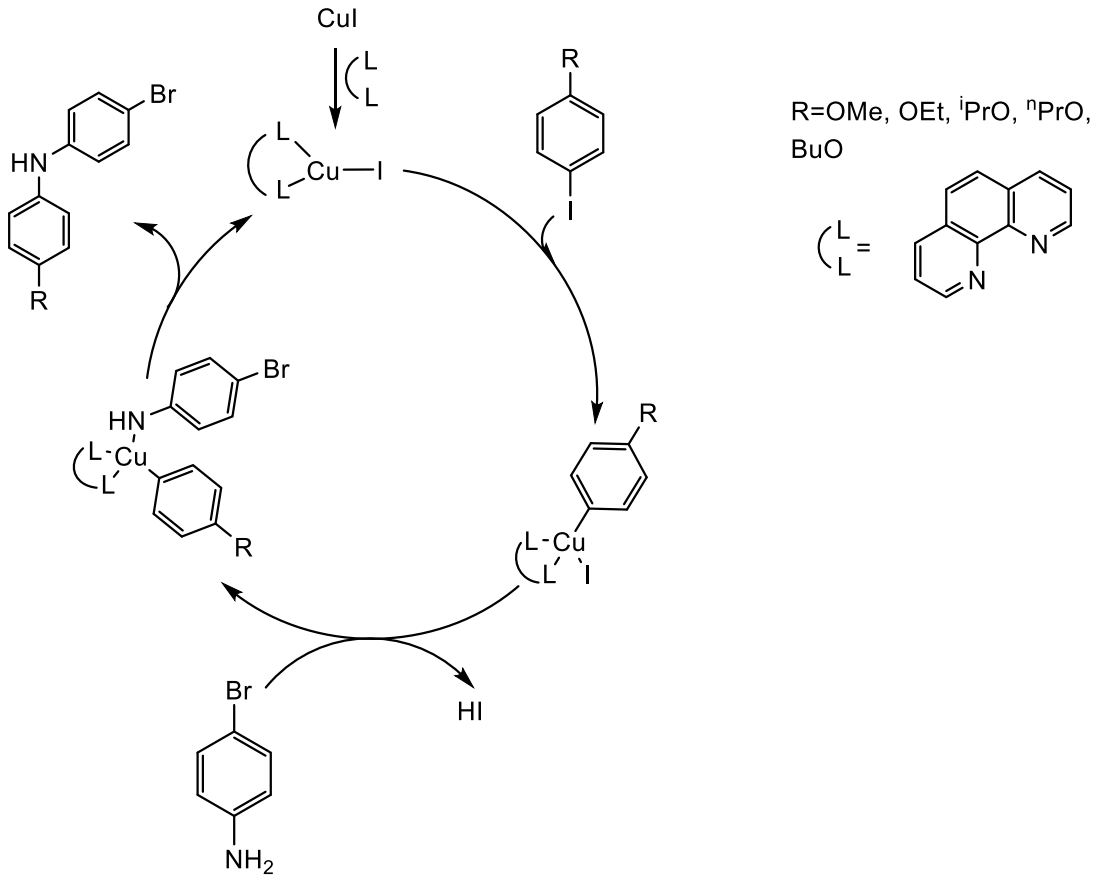

Figure 3.3 Proposed Catalytic Cycle for the Modified Ullmann coupling.[203,204]

In the third step, the acetylene was attached with a silyl protection group via Sonogashira cross coupling reaction[205]. This method is widely used for the coupling of a sp^2 hybridized carbon of a vinyl or aryl halide with a terminal sp carbon from an alkyne. The reaction is usually performed using a palladium complex as catalyst, copper iodide as co-catalyst and an amine as solvent or in large excess. The reaction also employed phosphine ligands to increase the efficiency of the reaction.[206]

Some uncertainty remains regarding the mechanisms of the Sonogashira coupling as it is difficult to isolate the organometallic intermediates from the reaction mixture to validate the process beyond any doubt. The proposed mechanism takes place through two independent catalytic cycles[207] (Figure 3.4).

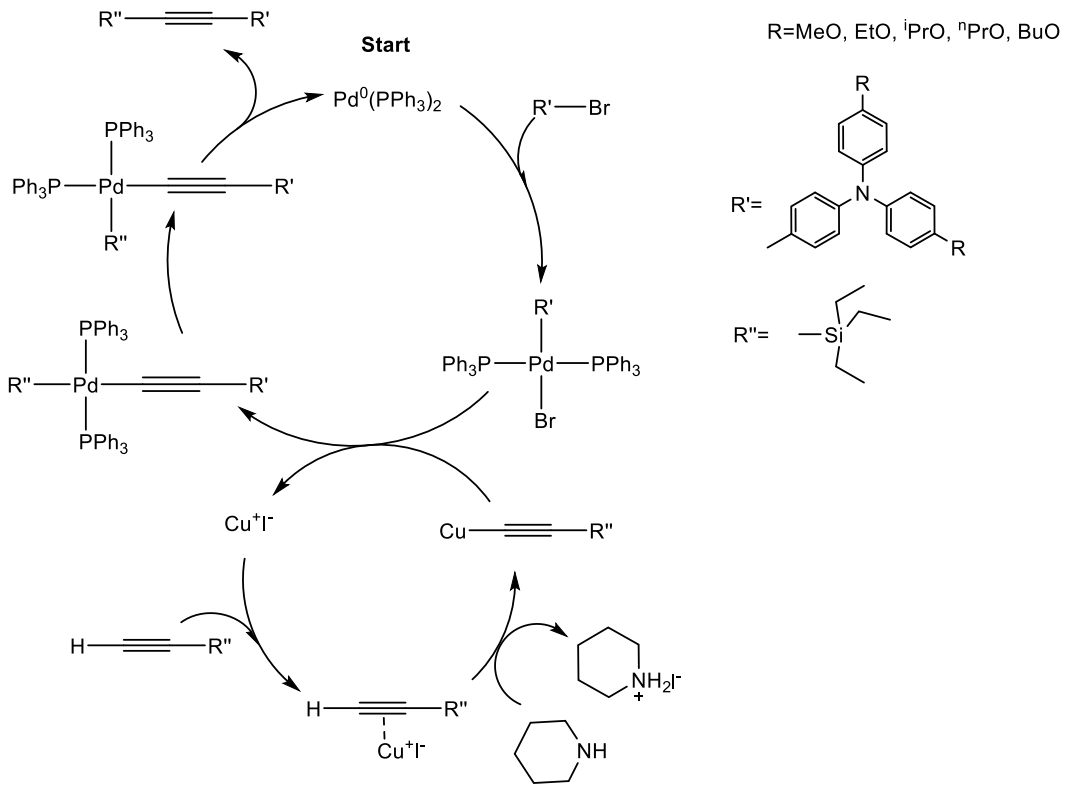

Figure 3.4 Proposed mechanism for the copper co-catalysed Sonogashira reaction

The first cycle starts with the species $Pd^0(PPh_3)_2$. This can be formed from Pd(0) complexes like $Pd(PPh_3)_4$ or from Pd(II) complexes such as $PdCl_2(PPh_3)_2$ through reductive elimination. The $Pd(PPh_3)_4$ reactant is air sensitive and requires to be stored in an inert atmosphere to avoid degradation over time. Thus, the more stable $PdCl_2(PPh_3)_2$ complex was used instead. The species $Pd^0(PPh_3)_2$ containing Pd in its zero oxidation state and coordinatively unsaturated with 14 electrons is very reactive. Therefore, the reaction was carried out under nitrogen atmosphere. After the reductive elimination, the oxidative addition of the organohalide to the Pd(0) formed the $[Pd^{(II)}R'(PPh_3)_2Br]$ adduct which was later transformed into $[Pd^{(II)}(PPh_3)_2R'(CCR'')]$ after transmetalation with the alkynyl-copper reagent formed in the second catalytic cycle. The final product is obtained through reductive elimination, after cis alignment of the adduct $[Pd^{(II)}(PPh_3)_2R'(CCR'')]$ takes place.

In the next step the silyl group was removed using TBAF (tetrabutylammonium fluoride) leaving the triarylamine unit with a terminal alkyne. The final product was

obtained through the oxidative homocoupling of the terminal alkyne under the presence of copper catalyst and an oxidising agent like air. The addition of nitrogen ligands such as TMEDA (N,N,N',N'- tetramethylethylenediamine) increased solubility of the Cu catalyst allowing the reaction to be carried out under mild conditions. This technique is commonly named Hay-Glaser coupling. The Hay-Glaser coupling is particularly appealing because only water is formed as the by-product of oxidation[208,209]. More recently it was found that the use of molecular sieves to remove the water generated during the reaction led to best results[210]. The details of the mechanism of copper-mediated oxidative homocoupling are still under discussion[211]. Of the several mechanisms proposed, the most broadly accepted was published in 1964 by Bohlmann[212] and the general picture is displayed in Figure 3.5. The process begins with the addition of the triple bond to the copper(I) species which enhances the acidity of the C-H bond and facilitates the deprotonation by an external base. The reaction is performed under air or oxygen to oxidise Cu(I) to Cu(II). After protonation, the acetylide formed a copper(II)-acetylide complex and the final product is formed after a reductive elimination.

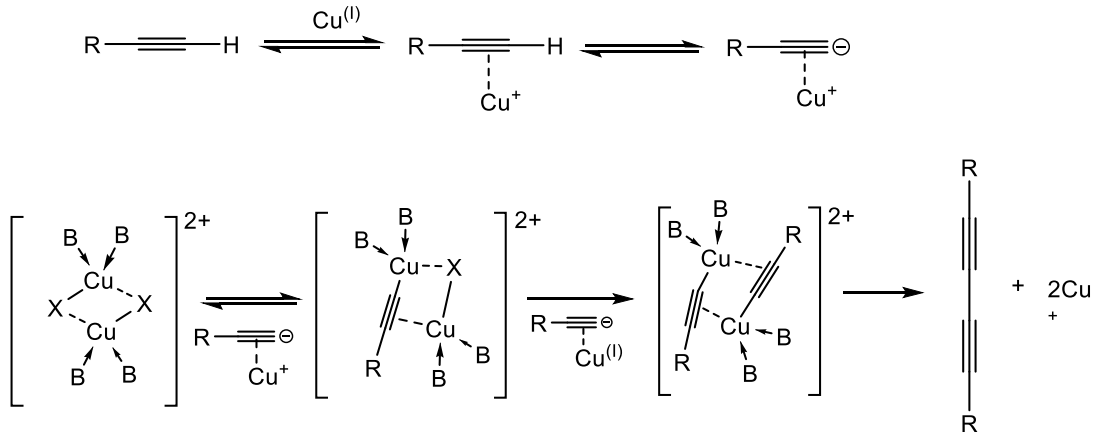

Figure 3.5 Bohlmann mechanism for Hay-Glaser coupling of acetylenes (B = Nitrogen ligand).[212]

3.2.2 Optical and electrochemical properties

The UV-Vis absorption spectra of the DATPA derivatives (EtO, ^{i}PrO, ^{n}PrO, BuO), measured in dichloromethane (DCM), are shown in Figure 3.6. All compounds exhibit an absorption peak at 389 nm independent of the substituent. Molar extinction coefficients were calculated for each compound using the Lambert-Beer law and results are displayed in Table 3.1. Additionally, photoluminescence (PL) spectra were recorded (dashed line, Figure 3.6). The results show similar PL spectra for all DATPA derivatives with a maximum emission at 493 nm.

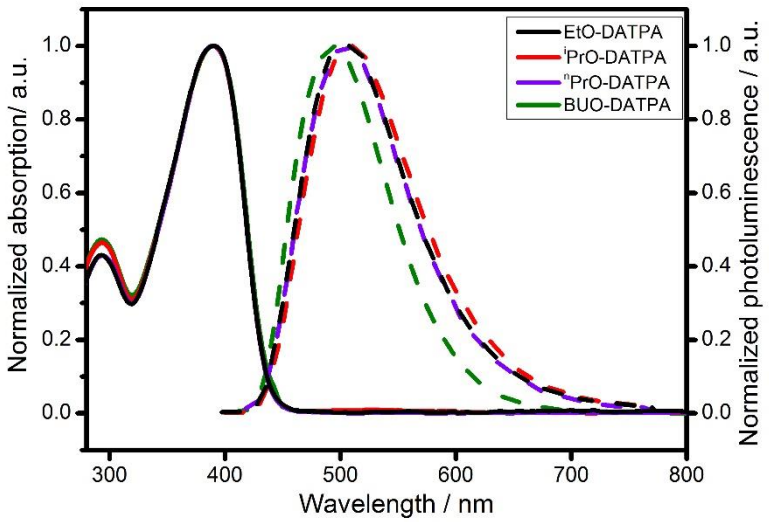

Figure 3.6 Normalized UV-Vis absorption (solid line) and emission (dashed line) of each DATPA derivative. EtO-DATPA (black line), ^{i}PrO-DATPA (red line), ^{n}PrO-DATPA (purple line) and BuO-DATPA (green line).

Optical gaps were determined from the intersection of the excitation and the emission spectra. Cyclic voltammograms (CV) of the DATPA series are displayed in Figure 3.7. The redox peaks of all HTMs are chemically and electrochemically reversible, indicating excellent stability and rapid electron transfer.

These materials present two oxidation peaks corresponding to one electron oxidation for each triarylamine unit. However, in cyclic voltammetry, the two oxidation processes are strongly overlapped because of their similar potentials.

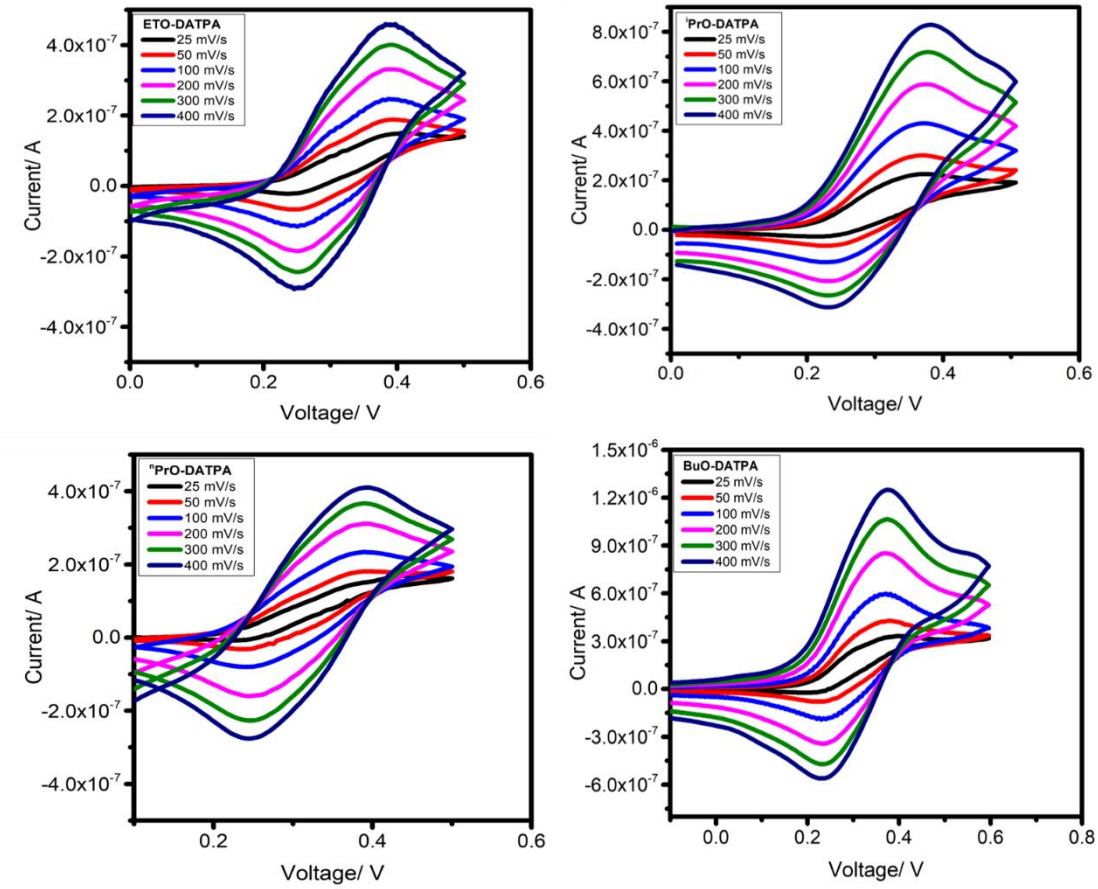

Figure 3.7 Cyclic voltammetry at different scan rates of EtO-DATPA, iPrO-DATPA, nPrO-DATPA and BuO-DATPA.

To distinguish both oxidation processes, square-wave voltammetry (SWV) was carried out (Figure 3.8). The similarity of the two redox potentials suggests a small interaction between the two triarylamine units. The HOMO energy level is of most importance for hole transfer from the perovskite and HTM and from molecule to molecule. The HOMO energy levels were calculated from the CV data using the following equation E_{HOMO}=-5.1-(E_{ox}), where E_{ox} is the oxidation potential of the HTM with reference to ferrocene. The extracted values are listed in Table 3.1. Overall these results indicate that the hole transfer from $CH_3NH_3PbI_3$ (-5.43 eV) to the HTM is energetically

favourable. Spiro-OMeTAD has a HOMO of -5.13 eV, which is at a higher energy than the materials reported here.

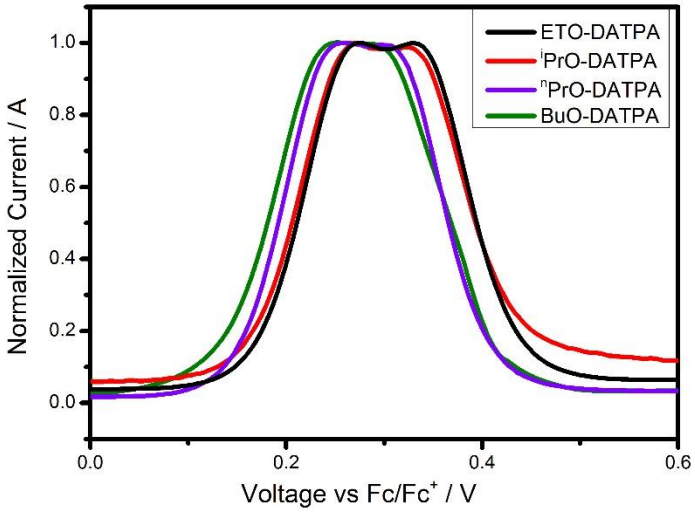

Figure 3.8 Square-wave voltammetry of EtO-DATPA (black line), iPrO-DATPA (red line), nPrO-DATPA (purple line) BuO-DATPA (green line).

Density Functional Theory (DFT) calculations were performed to predict the electronic properties of all HTMs using Gaussian 09 with B3LYP 6-31G(d) level of theory. Figure 3.9 shows the position of the HOMO–LUMO energy levels and their electron density on the molecules of all DATPA derivatives. The calculated trend of HOMO and LUMO matches the experimental data, and no significant difference was found among the DATPA series. The HOMO is delocalized over the π orbitals of the triphenylamine unit and the diacetylene bridge. The alkyl groups do not contribute to the HOMO energy level, therefore any change beyond the oxygen does not affect the optoelectronic properties, which coincides with the electrochemistry results. The LUMO electron density is localised on the diacetylene bridge and is also not significantly influenced by the substituents of the triphenylamine unit.

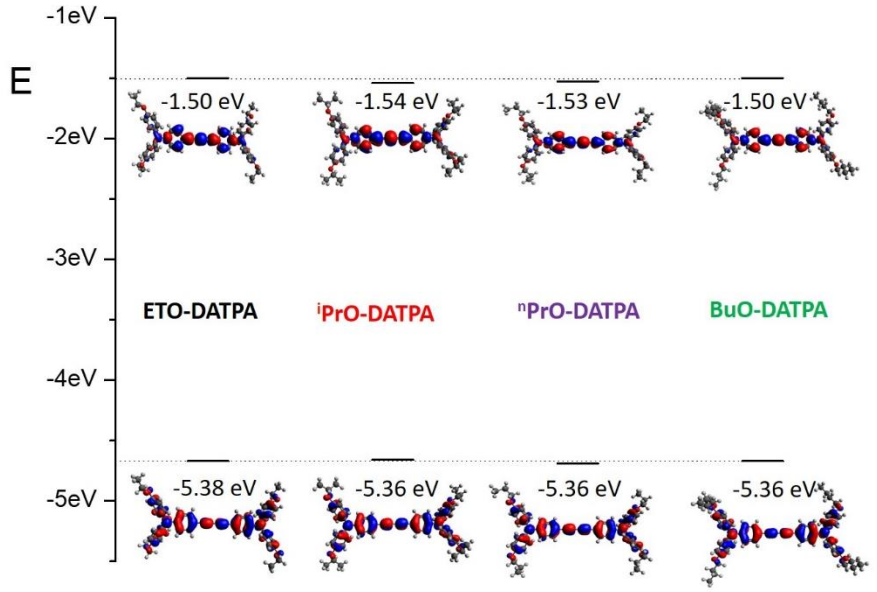

Figure 3.9 Molecular Orbital distribution of HOMO (bottom) and LUMO (top) for DATPA derivatives at B3LYP/6-31G(d) level of theory.

A summary of the optical and electrochemical properties of all DATPA derivative is presented in Table 3.1. As expected, different alkyl substituents do not significantly modify the optical and electrochemical properties of the hole transport materials. This confirms that this series is appropriate to compare the structural, morphological and interface effects of differing alkyl chains without any complicating changes to the optoelectronic properties.

Table 3.1 Summary of the optical and electrochemical properties of the DATPA derivatives

HTM	λ_{max} (nm)	ε (cm^{-1} M^{-1})	λ_{em} (nm)[a]	E_{gap} (V)[b]	$E_{ox\ (1st)}$ (V)[c]	$E_{ox\ (2nd)}$ (V)[c]	E_{HOMO} (eV)[d]
EtO-DATPA	389	60300	504	2.85	+0.28	+0.33	-5.38
nPrO-DATPA	389	69200	504	2.85	+0.26	+0.30	-5.36
iPrO-DATPA	389	64280	508	2.84	+0.28	+0.33	-5.38
BuO-DATPA	389	65990	495	2.85	+0.26	+0.30	-5.36
Spiro-OMETAD	385	-	424	3.05	+0.03		-5.13

[a]Excitation at λ_{max}. [b]E_{gap} is the optical gap determined from the intersection of absorption and emission spectra. [c]From SWV and CV measurements and referenced to ferrocene. [d]E_{HOMO}(eV)= -5.1- (E_{ox})[213]

3.2.3 XRD Analysis

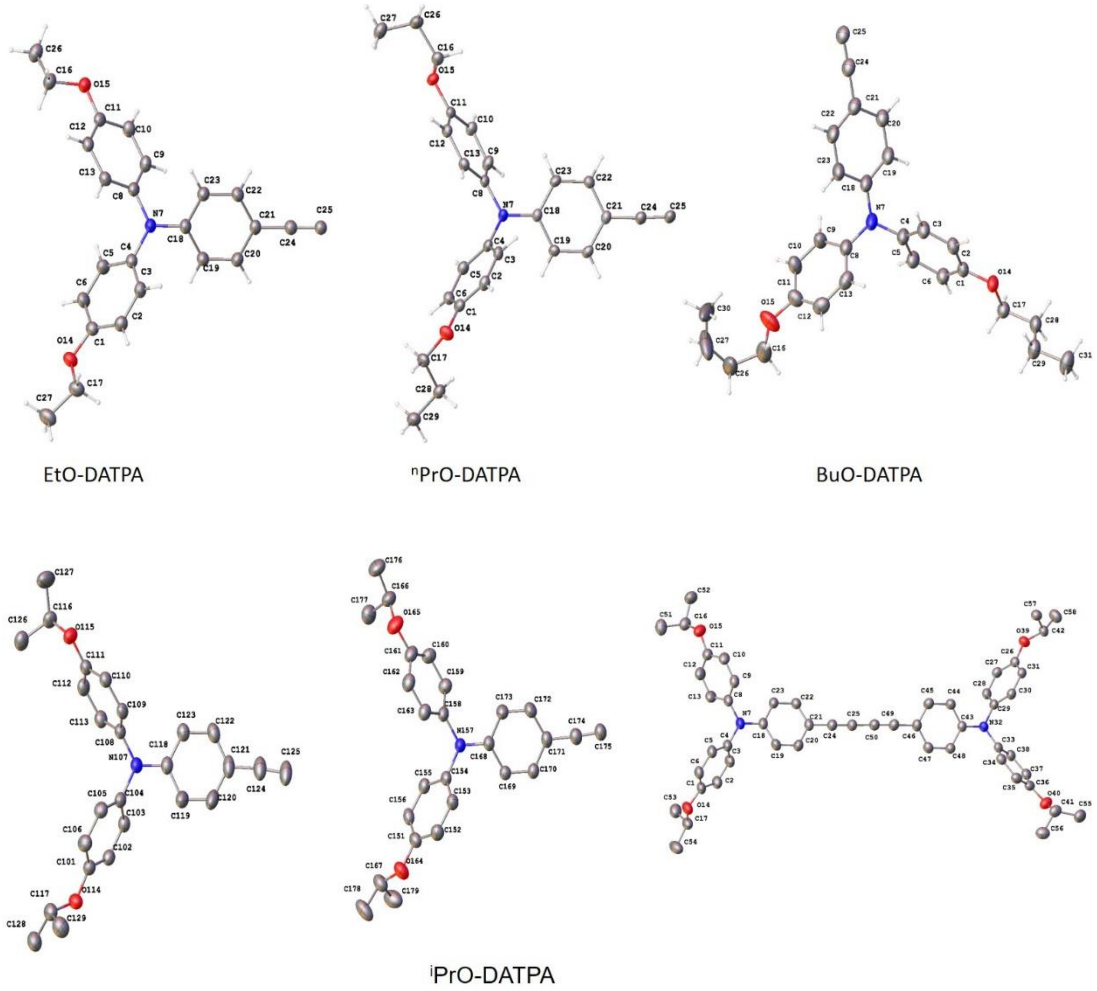

Figure 3.10 The asymmetric portion of the molecular structure of EtO-DATPA, nPrO-DATPA and BuO-DATPA.

Single crystals of the new molecules were grown by the slow solvent evaporation method to resolve the crystal packing by X-ray diffraction (XRD). The compounds were found to crystallize in the monoclinic space group $P2_1/n$ (EtO-DATPA, ^{n}PrO-DATPA), monoclinic space group $P2_1/c$ (BuO-DATPA) with half of the formula unit present in the asymmetric unit and the other half consisting of symmetry equivalent atoms (Figure 3.10); ^{i}PrO-DATPA crystallizes in the triclinic space group P-1 showing two independent molecules in the asymmetric unit (Figure 3.10). In every case the molecule crystallises without the presence of any solvent of lattice. The EtO-DATPA

molecules are packed in a layer-by-layer configuration with molecules arranged in a herringbone motif characterised by edge-to-face contacts (Figure 3.11). The intersection angle between two adjacent fragments is measured to be 72.18°. The distance between parallel fragments is too large to induce co-facial π··· π interactions. The molecules interact mainly via C-H··· π (3.154 Å) and C-H···HC formed by the CH groups of phenyls ($d_{CH\cdots HC}$=2.554 Å, 2.634 Å). The EtO-DATPA molecules also form intermolecular H-bonding interactions in the crystal lattice formed by the oxygen and the hydrogen atom of the aromatic rings ($d_{C\text{-}H\cdots O\text{-}R}$=2.715 Å, 2.804 Å, 2.916 Å).

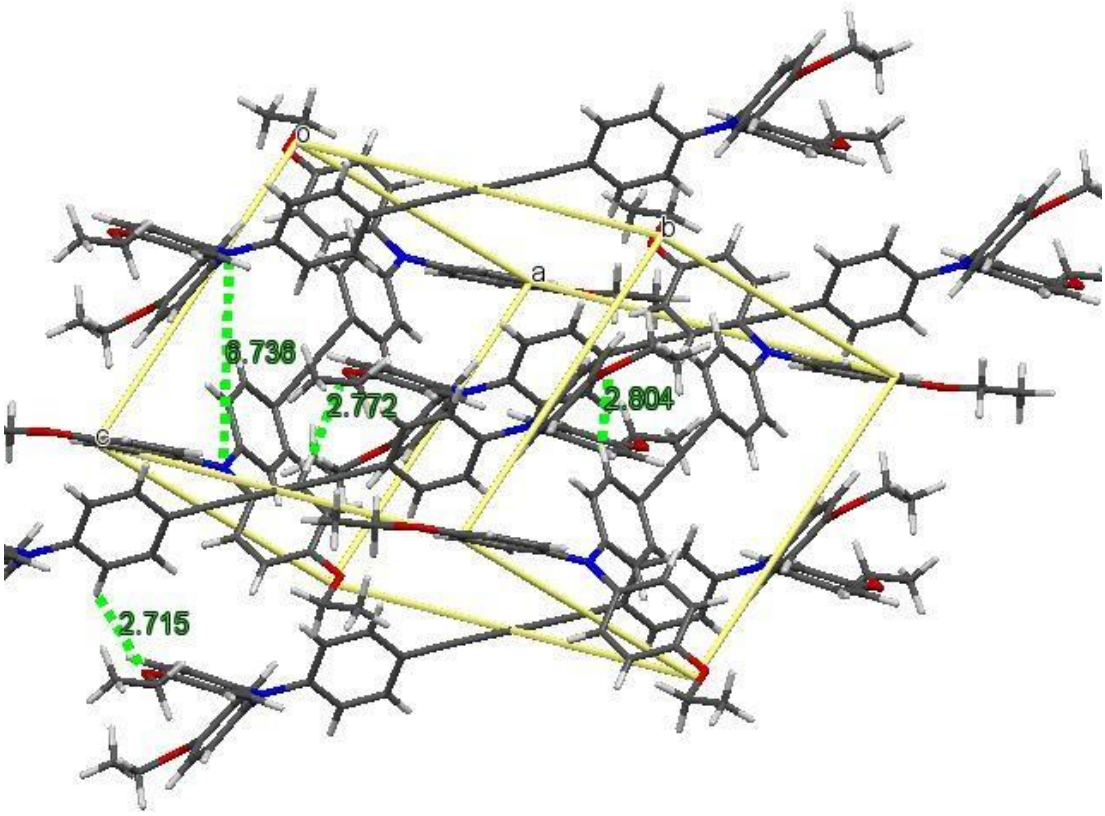

Figure 3.11 Crystal packing of EtO-DATPA.

The crystal structure of ^{n}PrO-DATPA also exhibits a layer-by-layer herringbone pattern (Figure 3.12). The T-shaped edge-to-face and the parallel-displaced stacking arrangement predominate. Although similar, the structure of ^{n}PrO-DATPA is stabilised via π···π interactions. The distance between two parallel fragments and the intersection angle of adjacent molecules were measured to be 3.44 Å and 46.63°

respectively. The ^{n}PrO-DATPA molecules also interact via C-H··· π (3.086 Å) and C-H···O-R (shortest distance found 2.725 Å).

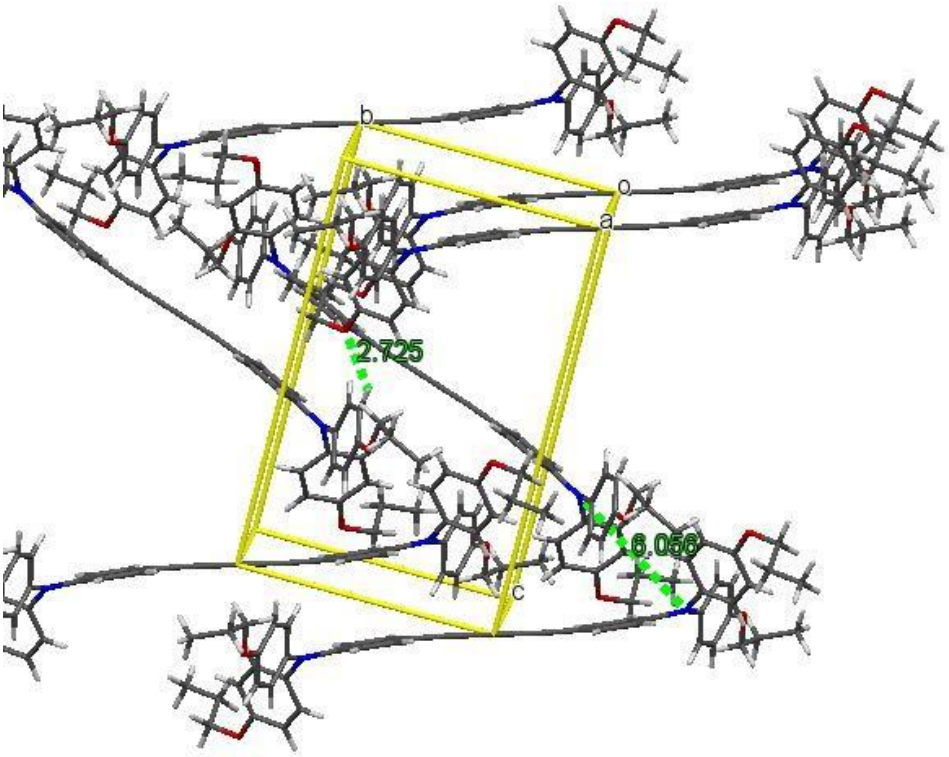

Figure 3.12 Crystal packing of ^{n}PrO-DATPA.

A more complex packing is observed for ^{i}PrO-DATPA (Figure 3.13). The X-ray crystal structure reveals three crystallographically unique molecules in the asymmetric unit (Figure 3.10). Two lie on crystallographic inversion centres while the third lies entirely in general positions. Each unit is surrounded by six molecules arranged in an alternating layered pattern with an intersection angle of 77.59°. The interactions arising in the structure of ^{i}PrO-DATPA are mainly C-H··· π (3.034 Å, 2.813 Å, and 2.875 Å) and C-H···O-R (shortest distance found 2.712 Å). Furthermore, C-H···O-R contact is also observed between the CH group of the alkyl chain and the oxygen atom (2.788 Å). The aromatic cores of the ^{i}PrO-DATPA are aligned with a very strong slipped π-stacking configuration such that no π··· π interactions are observed.

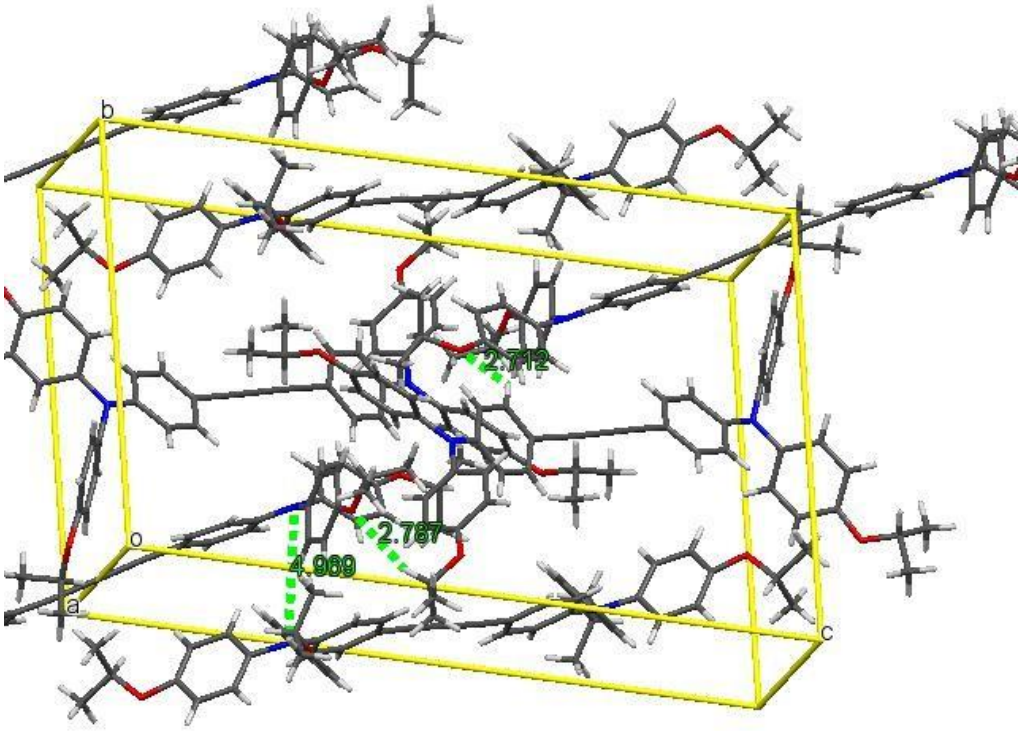

Figure 3.13 Crystal packing of ^{i}PrO-DATPA.

In the case of BuO-DATPA, the molecules are arranged in a zig-zag largely slipped stack packing (Figure 3.14). Similar to ^{i}PrO-DATPA, the aromatic cores have a very strong slipped π-stacking with an average distance of 4.820 Å which it is too large to induce π-orbital overlap in the crystalline structure. The bulkiness of the alkyl chain in the para position largely impacts the overlapping of the aromatic moieties resulting in the absence of face to face stacking. The crystal lattice shows C-H···O-R (2.665 Å), C-H···HC (2.270 Å, 2.304 Å) formed between one hydrogen atom of the alkyl chain and CH group of an aromatic ring. The molecules also interact via C-H··· π (2.720 Å) formed between an aromatic centroid and the alkyl chain.

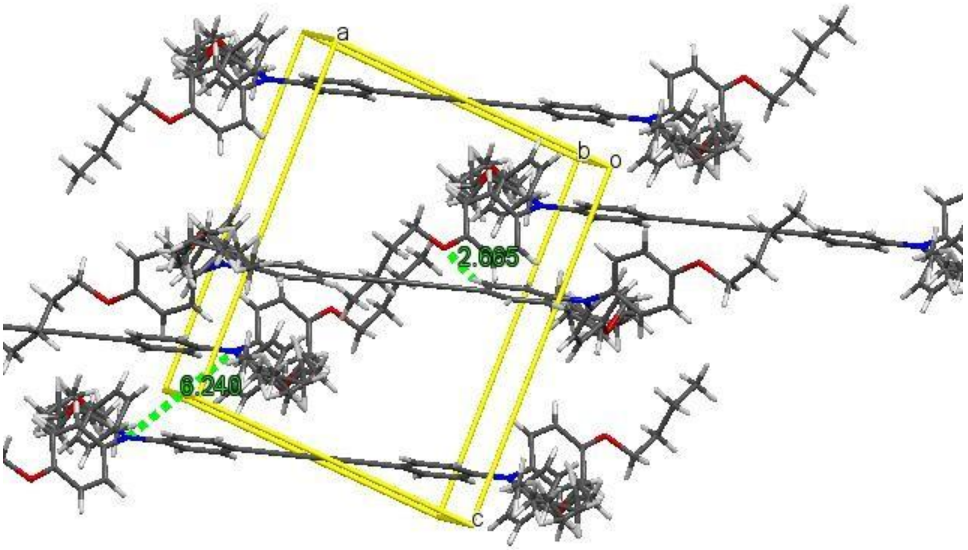

Figure 3.14 Crystal packing of BuO-DATPA.

The crystal packing of MeO-DATPA was reported and discussed in more detail in previous work within the Robertson group, showing a herringbone pattern, with one molecule in the asymmetric unit and a regular stacking distance between the molecules. Overall, it was observed that as the alkyl chain increases, the number of van der Waals interactions between alkyl chains also increases while the H-bonding contacts decrease. Among all of the examples, MeO-DATPA and EtO-DATPA showed the strongest and highest number of intermolecular interactions (H-bonding) while fewer H-bonds were found in the crystal lattice of BuO-DATPA but stronger van der Waals interactions within the alkyl chains. Longer alkyl chains result in the poorer stacking of the molecule and therefore weaker intermolecular interactions. Furthermore, it is known that closer molecular arrangements can facilitate charge transport in thin film devices[214]. A summary of the crystallographic data is depicted in Table A.1 in Appendix A2.

The X-ray powder diffraction patterns were experimentally obtained and compared with those calculated from their single-crystal data (Figure 3.15). The powder pattern of all DATPA derivatives showed some crystallinity, and were in agreement with the calculated pattern from single-crystal data.

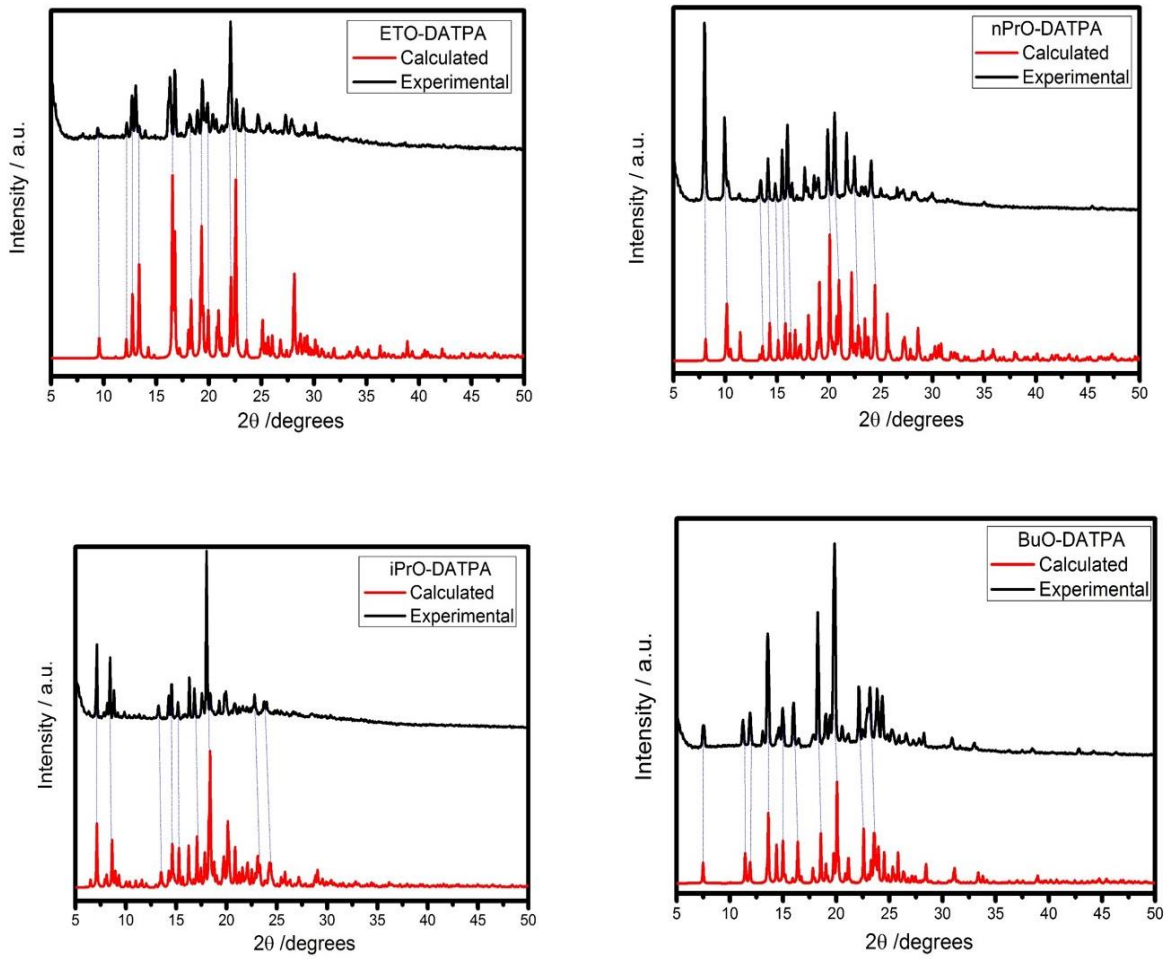

Figure 3.15 XRD powder patterns: simulated from single-crystal structures (red) and experimental (black).

3.2.4 Thermal properties

Thermal properties of the HTMs were evaluated by Differential Scanning Calorimetry (DSC), and the results are presented in Appendix A3. The DSC results showed a glass transition temperature (T_g) of 76.9 ºC, 69.5 ºC and 70.7 ºC for MeO-DATPA, EtO-DATPA and ^{i}PrO-DATPA. ^{n}PrO-DATPA and BuO-DATPA however do not present T_g. On the other hand, lower melting points were observed for longer alkyl chains. These observations can be explained by the difference in the crystal packing, and their intermolecular interaction observed in the XRD analysis.

Longer alkyl chains presented poorer stacking as the molecules are more disordered which results in weaker interactions. This explains why the BuO group led to the lowest melting point. The MeO and EtO groups led to the highest melting points and the strongest intermolecular interactions. We can also observe that branched ^{i}PrO has a higher melting point than the straight chain ^{n}PrO, although ^{n}PrO-DATPA (2.080 Å^3/molecule) has a more compact structure than ^{i}PrO-DATPA (2.212 Å^3/molecule). The ^{i}PrO chain typically has a smaller surface area which leads to weaker van der Waals interactions. However as we can observe in the crystal packing, ^{i}PrO leads to shorter C-H···O-R interactions, which likely explains the higher melting point in comparison to ^{n}PrO. A summary of the thermal properties is given in Table 3.2.

3.2.5 Hole Mobility

Charge mobility is an important parameter to evaluate the properties of hole-transport materials in photovoltaic devices. To investigate the hole mobilities, OFETs (Organic Field-Effect Transistors)[215,216] were fabricated for four of the compounds reported here (MeO-DATPA, EtO-DATPA, ^{n}PrO-DATPA and BuO-DATPA) and the mobilities were extracted from the saturation regime of the transfer characteristic curves (Figure 3.17). Details of the device fabrication and measurement are found in the Experimental section. It was not possible to fabricate a high-quality thin film for ^{i}PrO-DATPA. In general, the molecules with the shorter alkyl chains presented higher mobilities which can be attributed to stronger intermolecular interactions in the XRD analysis. A summary of the estimated hole mobilities is presented in Table 3.3.

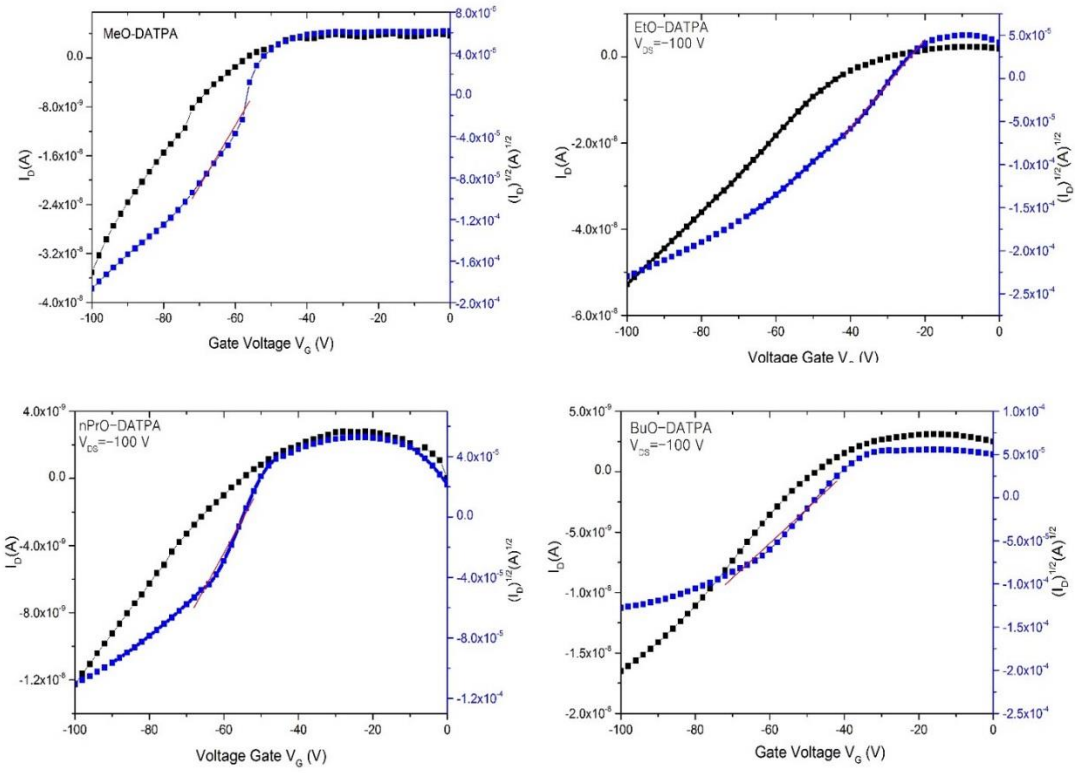

Figure 3.16 Transfer Characteristic Curves of MeO-DATPA, EtO-DATPA, ^{n}PrO-DATPA and BuO-DATPA (left to right) on a bottom gate/bottom contact organic field effect transistor.

Table 2.2 Charge transport and thermal properties

HTM	Hole Mobility μ_{FE} (cm^2/Vs)[a]	T_g (°C)[b]	T_m (°C)[b]
MeO-DATPA	$1.90x10^{-4}$	76.9	197.3
EtO-DATPA	$1.45x10^{-4}$	69.5	149.4
^{i}PrO-DATPA	x	70.7	160.8
^{n}PrO-DATPA	$1.11x10^{-4}$	x	148.0
BuO-DATPA	$8.81x10^{-5}$	x	118.9

[a]Estimated from OFET measurements. [b]Determined from differential scanning calorimetry (DSC).

3.2.6 Transient Absorption Spectroscopy

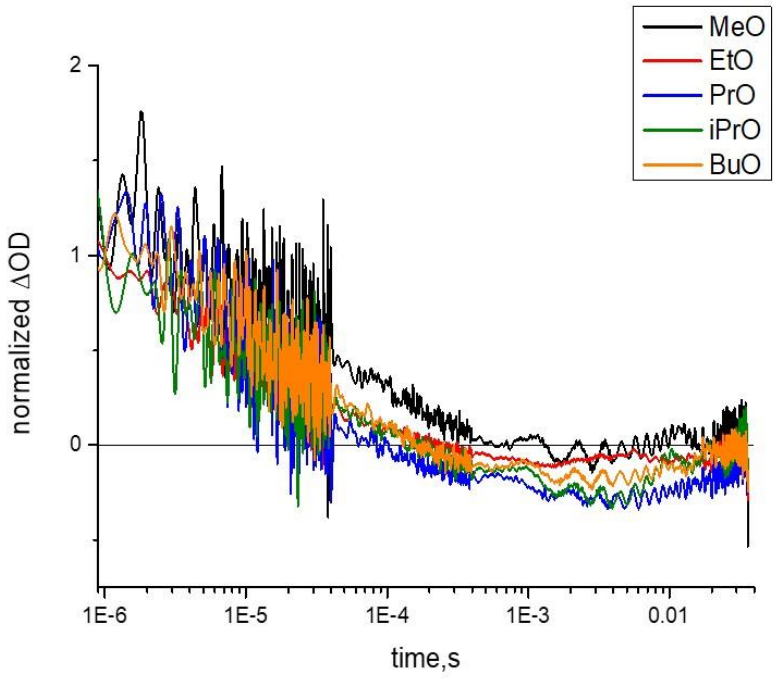

Figure 3.17 Normalized Transient Absorption spectra.

To further probe the performance in PSCs, the charge transfer dynamics occurring in an mp-TiO_2/$CH_3NH_3PbI_3$/HTM arrangement for all DATPA derivatives were obtained by ultrafast absorption spectroscopy (TAS). Samples were prepared by spin-coating of the perovskite onto a mesoporous TIO_2 layer and with the HTM on top. Details of the sample preparation and measurements are described in the experimental

section. The corresponding steady-state absorption spectra are shown in Figure 3.19, where all samples show the dominant spectral features of the perovskite layer $CH_3NH_3PbI_3$, with the onset at 800 nm and the bands corresponding to the oxidised HTMs (at 1600 nm). Figure 3.18 shows the TAS time profiles following 510 nm excitation probed at 1600 nm. All signals have a negative feature that arises from some charge separation already happening in the ground state, and the intensity of these bleaches correlates with the intensity of the band of the oxidised HTMs observed in the steady-state absorption spectra. The analysis of the normalised TAS time profiles also displays a hint of the lifetimes of the charge-separated states. From the results, MeO-DATPA presents the most long-lived signal indicating a greater charge-pair separation. Among the other DATPA derivatives, no significant differences of the lifetimes of the charge separation states were found.

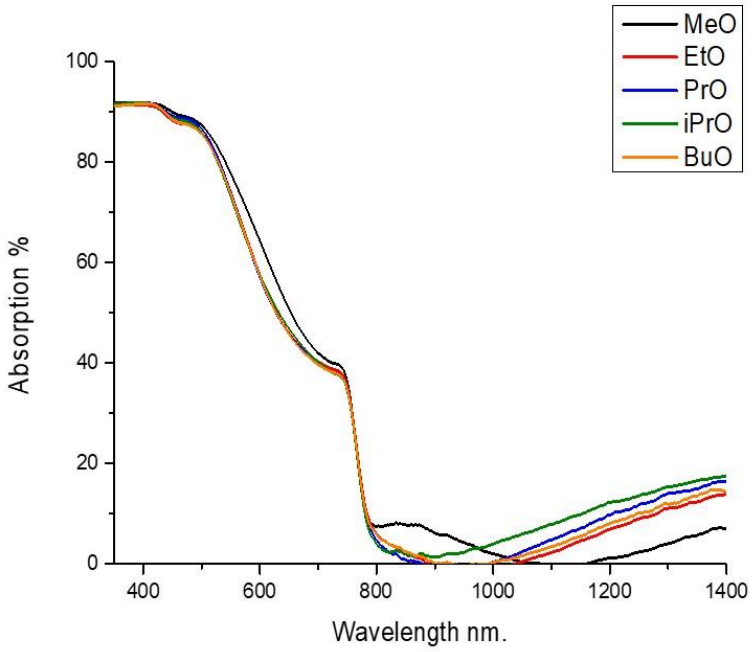

Figure 3.18 UV-Vis spectra of mp-TiO_2/$CH_3NH_3PbI_3$/HTM for all DATPA derivatives.

3.2.7 Solar Cells Studies

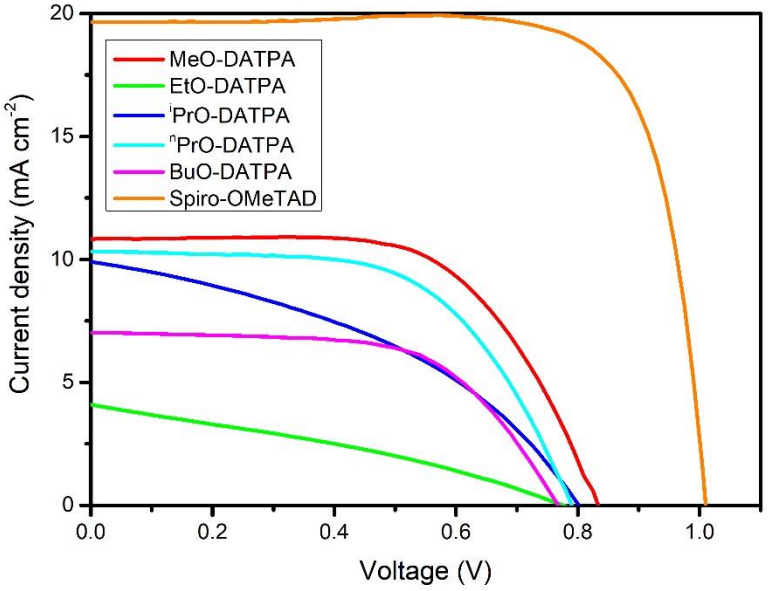

Figure 3.19 J–V curves of the champion PSCs with the DATPA series and Spiro-MeOTAD HTMs.

To investigate the effect of the alkyl chain of these HTMs in perovskite solar cells, a set of PSCs in the configuration FTO/bl-TiO_2/mp-TiO_2/$CH_3NH_3PbI_3$/HTM/Au was fabricated. All DATPA HTMs were doped using two times the concentration of additives typically used for Spiro-OMeTAD which include bis(trifluoromethylsulfonyl)imide lithium salt (Li-TFSI), 4-tert-butylpyridine and tris(2-(1H-pyrazol-1-yl)-4-tert-butylpyridine)-cobalt(III)tris(bis(trifluoromethylsulfonyl)imide) (FK209). Full details of the solar cell fabrication are given in the experimental section. Current-voltage scans were recorded using an AAA-rated solar simulator calibrated against a KG5 global (AM 1.5 G) solar irradiation. All devices were fabricated in a single continuous study over 7 repeat cells for each HTM to facilitate comparison. Figure 3.21 shows the box plots with the mean and standard deviation of the solar cell parameters and a summary can be found in Table 3.5. The J-V graphs of the champion cells are shown in Figure 3.20 and the results are summarised in Table 3.4 (champion cell).

Table 3 Summary of device performance for champion cells

HTM	PCE (%)	J_{sc} (mA cm^{-2})	V_{oc} (V)	FF (%)
MeO-DATPA	5.63	10.84	0.83	62.25
EtO-DATPA	1.02	4.10	0.77	32.19
^{n}PrO-DATPA	4.83	10.33	0.79	59.22
^{i}PrO-DATPA	3.24	9.89	0.80	41.11
BuO-DATPA	3.29	7.02	0.77	61.19
Spiro-OMeTAD	15.34	19.67	1.00	78.13

Despite the identical backbone structures and HOMO energy levels, the difference in the alkyl chain length had an effect on the photovoltaic device performances. Among the DATPA series, MeO-DATPA shows the highest performance with a PCE of 5.63%. Upon increasing the length of alkyl chain the performance of the devices decreases to 4.83% for nPrO-DATPA, 3.24% for iPrO-DATPA and 2.54% for BuO-DATPA. Also noticeable is the decrease in the short circuit current values (Jsc) for DATPA derivatives with longer alkyl chains from 10.84 mA cm^{-2} for MeO-DATPA to 7.02 mA cm^{-2} for BuO-DATPA. The methoxy substituent leads to the best semiconducting properties in comparison with the longer alkyl chains. The variance in PCE values can be attributed to the differences in the photocurrent density and fill factor which may have resulted from the higher hole mobility, greater charge-pair separation and optimal morphology. This is sustained by the results from the hole mobility data, transient absorption spectroscopy studies and XRD analyses discussed previously.

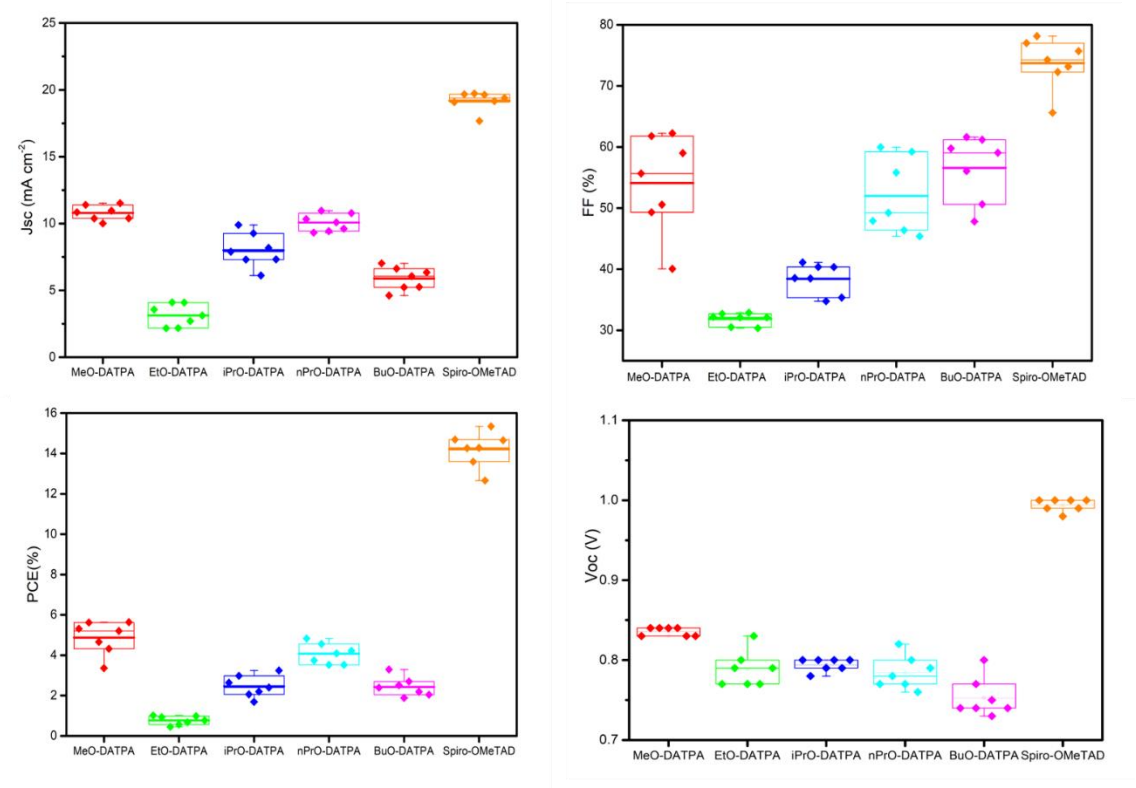

Figure 3.20 Solar cells parameters over 7 repeats for each HTM.

Table 4 Summary of the solar cell parameters

HTM	PCE (%)	J_{sc} (mA cm-2)	V_{oc} (V)	FF (%)
MeO-DATPA	4.87±0.82	10.79±0.56	0.84±0.0054	54.10±8.01
EtO-DATPA	0.77±0.22	3.13±0.82	0.79±0.022	31.83±1.01
^{n}PrO-DATPA	4.07±0.54	10.07±0.65	0.78±0.021	51.98±6.19
^{i}PrO-DATPA	2.46±0.51	7.99±1.27	0.79±0.0079	38.41±2.50
BuO-DATPA	2.43±0.47	5.88±0.87	0.75±0.024	56.59±8.01
Spiro-OMeTAD	14.51±0.87	19.19±0.71	0.99±0.0079	73.74±4.13

Our results are in agreement with the studies reported previously by Hagfeldt and Nazeeruddin. Previously, Hagfeldt and collaborators designed a series of triphenylamine-based HTMs by tuning the position and length of the alkyl chains

substituent on the molecular structure to study their effects on the photovoltaic parameters of perovskite solar cells. They found that the alkyl chain length influenced the solubility, molecular packing structure and charge transport. Simultaneously, Nazeeruddin and co-workers studied the effect of the alkyl chain length in small-molecule HTMs based on an anthra[1,2-b:4,3-b′:5,6-b″:8,7-b‴]- tetrathiophene (ATT) core on the performance of PSC devices. By replacing the methoxy groups with longer alkyl chaing lengths (butoxy, hexoxy and decoxy) an improvement of solubility was observed. Nevertheless, the device performances were significantly inferior than the MeO substituents. They concluded that the alkyl chain improves the stacking of the ATT core but decreases the hole-transport properties and therefore the device performance of the solar cell.

3.3 Conclusions

In summary, we have presented the synthesis and characterisation of a new series of diacetylide-triphenylamine (DATPA) derivatives to study their function in PSCs. These molecules have the same backbone structures but different alkyl chain length in the para position, i.e., ethoxy (EtO), propoxy (^{n}PrO), isopropoxy (^{i}PrO) and butoxy (BuO), compared also to the known MeO species. Although the length of the aliphatic side chain does not influence the optoelectronic properties of the molecules such as the HOMO levels, it strongly affects the charge transport properties and transfer dynamics of the molecules as well as the morphology and photovoltaic performance in PSCs. The molecules with shorter alkyl chains have a more ordered and compact structure which facilitates charge transport in the thin films. These results are in agreement with the previous work found by Hagfeldt and Nazeeruddin. The methoxy substituent shows the best semiconductive properties and PCE of 5.63% compared with the longer side chain. This is due to the molecular packing and faster charge transport. These findings provide insight information for the design of organic semiconductor for photovoltaic application in the future.

3.4 Experimental details

3.4.1 Chemical characterization

^{1}H and ^{13}C NMR spectra were recorded on a Bruker Advance 500 spectrometer (500 MHz). The deuterated solvents are indicated in the synthesis description. Chemical shifts, δ, are given in ppm, using the solvent residual as an internal standard. MS were recorded on Micro-Tof using electrospray ionisation (ESI) technique. Elemental analyses were carried out by Stephen Boyer at London Metropolitan University**.**

3.4.2 Synthesis

Materials and Synthesis

All reagents were purchased from either Sigma-Aldrich or Alfa-Aesar, and they were used as received without further purification unless otherwise stated. The synthetic procedure was based on the previous work[199] in the Robertson group with some modifications to improve yields and reduce reactions times. Appart from EtO-DATPA, the syntesis procedure required five steps. The reaction conditions are very similar for all the compounds, therefore an example of the experimental procedure is given for ^{i}PrO-DATPA.

1) 1-iodo-4-alkoxybenzene

4-iodophenol (22.73 mmol, 5 g), K_2CO_3 (68.19 mmol, 9.4 g), 18-crown-6 (0.227 mmol, 0.6 g) and DMF (40 ml) were all added into a round bottom flask and stirred under N_2 to which 2-bromopropane (45.19 mmol, 4.26 mL) was added. The mixture was stirred and refluxed for 4 hrs under N_2 at 90 ℃. A silica plug (PE/DCM 90/10) was run to afford the product.

a) 1-iodo-4-isopropoxybenzene

Product: transparent oil (6 g, 97% yield)

^{1}H NMR (500 MHz, Chloroform-d) δ 7.45 – 7.42 (m, 2H), 6.46 – 6.43 (m, 2H), 4.04 (hept, J = 6.0 Hz, 1H), 1.07 (d, J = 6.0 Hz, 6H).

b) 1-iodo-4-propoxybenzene

Product: transparent oil (11.07 g, 93% yield)

^{1}H NMR (500 MHz, Benzene-d_6) δ 7.38 – 7.35 (m, 2H), 6.42 – 6.33 (m, 2H), 3.38 (t, J = 6.5 Hz, 2H), 1.55 – 1.44 (m, 2H), 0.79 (t, J = 7.4 Hz, 3H).

c) 1-iodo-4-butoxybenzene

Product: transparent oil (5.57 g, 94% yield)

^{1}H NMR (500 MHz, Benzene-d_6) δ 7.41 – 7.33 (m, 2H), 6.39 – 6.36 (m, 2H), 3.42 (t, J = 6.4 Hz, 2H), 1.51 – 1.41 (m, 2H), 1.25 (dq, J = 14.7, 7.4 Hz, 2H), 0.79 (t, J = 7.4 Hz, 3H).

2) 4-bromo-N,N-bis(4-alkoxyphenyl)aniline

4-Bromoaniline (8.14 mmol, 1.4 g), CuI (0.4 mmol, 78 mg), 1,10-phenantroline (0.4 mmol, 72 mg), KOH (40.7 mmol, 2.3 g) were added into a Schlenk tube and dried under high vacuum for 30 min. A degassed solution of dried toluene (20 ml) and 4-iodoisopropoxybenzene (20.35 mmol, 5.33 g) were added into the previous mixture via cannula transfer. The reaction mixture was heated at 120 ℃ overnight under N_2. The cooled reaction mixture was washed with 5% HCl and 5% NaOH solution respectively, dried with $MgSO_4$ and solvent evaporated under vacuum. The residue was passed through a short silica in DCM and solvent removed under vacuum. The crude product was purified by column chromatography.

a) 4-Bromo-N,N-bis(4-ethoxyphenyl)aniline

Purification: Silica plug in DCM, column chromatography (SiO_2, Hexane/EtA 90/10)

Product: Pale yellow oil (1.2 g, 42% yield)

^{1}H NMR (500 MHz, Benzene-d_6) δ 7.00 – 6.94 (m, 4H), 6.79 – 6.75 (m, 2H), 6.73 – 6.70 (m, 4H), 3.57 (q, J = 7.0 Hz, 4H), 1.11 (t, J = 6.9 Hz, 6H).

b) 4-Bromo-N,N-bis(4-isopropoxyphenyl)aniline

Purification: Silica plug in DCM, column chromatography (SiO_2, Hexane/EtA 90/10)

Product: Pale yellow oil (1.3 g, 36% yield)

^{1}H NMR (400 MHz, Benzene-d_6) δ 7.16 (d, J = 4.0 Hz, 9H), 6.99 – 6.94 (m, 2H), 6.80–6.73 (m, 2H), 6.77 – 6.70 (m, 4H), 4.12 (h, J = 6.0 Hz, 2H), 1.11 (d, J = 6.0 Hz, 12H).

c) 4-Bromo-N,N-bis(4-propoxyphenyl)aniline

Purification: Silica plug in DCM, column chromatography (SiO_2, Hexane/EtA 90/10)
Product: Pale yellow oil (3.5 g, 50.7% yield)
^{1}H NMR (500 MHz, Benzene-d_6) δ 7.19 – 7.17 (m, 2H), 7.00 – 6.97 (m, 4H), 6.82 – 6.77 (m, 2H), 6.75 – 6.72 (m, 4H), 3.53 (t, J = 6.4 Hz, 4H), 1.60 – 1.53 (m, 4H), 0.85 (t, J = 7.4 Hz, 6H).

d) 4-Bromo-N,N-bis(4-propoxyphenyl)aniline

Purification: Silica plug in DCM, column chromatography (SiO_2, Hexane/EtA 90/10)
Product: Pale yellow oil (2.97 g, 55% yield)
^{1}H NMR (500 MHz, Benzene-d_6) δ 7.19 – 7.16 (m, 2H), 7.01 – 6.97 (m, 4H), 6.80 – 6.74 (m, 6H), 3.60 (t, *J* = 6.4 Hz, 4H), 1.61 – 1.51 (m, 4H), 1.34 (h, *J* = 7.4 Hz, 4H), 0.82 (t, *J* = 7.4 Hz, 6H).

3) 4-alkoxy-N-(4-alkoxyphenyl)-N-(4-((triethyllsilyl)ethynyl)phenyl)aniline $(PPh_3)_2PdCl_2$ (81 mg, 0.12 mmol), CuI (0.46 mmol, 88 mg), PPh_3 (0.18 mmol, 48 mg) were added into a Schlenk tube and dried under vacuum for 30 minutes. 4-bromo-N,N-bis(4-isopropoxyphenyl)aniline (2.3 mmol, 1 g), piperidine (1.8 mL), triethylsilylacetylene (4.6 mmol, 0.83 mL) and toluene (15 mL) were all degassed and added to the previous mixture via cannula transfer. The solution was stirred under N_2 at 90 ℃ overnight. The cooled reaction mixture was passed through a short silica plug in DCM and solvent was removed. The crude was purified by column chromatography.

a) 4-Ethoxy-N-(4-ethoxyphenyl)-N-(4-((triethyllsilyl)ethynyl)phenyl)aniline

Purification: Silica plug in DCM, column chromatography (SiO_2, Hexanes/EtA 95/5)
Product: yellow oil (1.3 g, 95% yield)

^{1}H NMR (500 MHz, Benzene-d_6) δ 7.45 – 7.38 (m, 2H), 7.00 – 6.96 (m, 4H), 6.90 – 6.86 (m, 2H), 6.72 – 6.68 (m, 4H), 3.56 (q, J = 6.9 Hz, 4H), 1.18 – 1.07 (m, 15H), 0.72 (q, J = 7.9 Hz, 6H).

b) 4-Isopropoxy-N-(4-isopropoxyphenyl)-N-(4-((triethyllsilyl)ethynyl)phenyl)aniline
Purification: Silica plug in DCM, column chromatography (SiO_2, Hexanes/EtA 95/5)
Product: yellow oil (1.06 g, 92% yield)
^{1}H NMR (500 MHz, Benzene-d_6) δ 7.43 – 7.37 (m, 2H), 7.02 – 6.94 (m, 4H), 6.92 – 6.85 (m, 2H), 6.80 – 6.68 (m, 4H), 4.11 (hept, J = 6.0 Hz, 2H), 1.13 (t, J = 7.9 Hz, 9H), 1.10 (d, J = 6.0 Hz, 12H), 0.71 (q, J = 7.9 Hz, 6H).

c) 4-Propoxy-N-(4-propoxyphenyl)-N-(4-((triethyllsilyl)ethynyl)phenyl)aniline
Purification: Silica plug in DCM, column chromatography (SiO_2, Hexanes/EtA 95/5)
Product: yellow oil (3.22 g, 95% yield)
^{1}H NMR (500 MHz, Benzene-d_6) δ 7.43 – 7.40 (m, 2H), 7.01 – 6.98 (m, 4H), 6.91 – 6.88 (m, 2H), 6.74 – 6.70 (m, 4H), 3.52 (t, J = 6.5 Hz, 4H), 1.56 (dtd, J = 13.7, 7.4, 6.4 Hz, 4H), 1.13 (t, J = 7.9 Hz, 9H), 0.85 (t, J = 7.4 Hz, 6H), 0.72 (q, J = 7.9 Hz, 6H).

d) 4-Butoxy-N-(4-butoxyphenyl)-N-(4-((triethyllsilyl)ethynyl)phenyl)aniline
Purification: Silica plug in DCM, column chromatography (SiO_2, Hexanes/EtA 90/10).
Product: yellow oil (2.63 g, 93% yield).
^{1}H NMR (400 MHz, Benzene-d_6) δ 7.48 – 7.38 (m, 2H), 7.02 – 6.98 (m, 4H), 6.92 – 6.88 (m, 2H), 6.75 – 6.72 (m, 4H), 3.59 (t, *J* = 6.4 Hz, 4H), 1.61 – 1.49 (m, 4H), 1.41 – 1.26 (m, 4H), 1.14 (t, *J* = 7.9 Hz, 9H), 0.82 (t, *J* = 7.4 Hz, 6H), 0.72 (q, *J* = 7.8 Hz, 6H).

4) 4-ethynyl-*N*,*N*-bis(4-alkoxyphenyl)aniline

4-Isopropoxy-N-(4-isopropoxyphenyl)-N-(4-((triethyllsilyl)ethynyl)phenyl) aniline (1.6 mmol, 0.8 g) and 10 ml of DCM were placed into a round bottom flask, and the mixture was stirred under N_2 for 10 minutes. TBAF (2.5 mL) was then added to the previous solution, and the reaction was stirred for 2 hours under N_2 at room

temperature. The reaction was washed three times with a solution of 10% ammonium chloride (20 mL), dried with $MgSO_4$ and the solvent removed under vacuum. The crude product was purified by column chromatography.

a) 4-Ethynyl-N,N-bis(4-ethoxyphenyl)aniline

Purification: Silica plug in DCM, column chromatography (SiO_2, PE/DCM 90/10)
Product: yellow oil (0.86 g, 95% yield)
^{1}H NMR (500 MHz, Chloroform-d) δ 7.49 – 7.38 (m, 2H), 7.07 – 7.03 (m, 4H), 6.96 – 6.92 (m, 2H), 6.80 – 6.77 (m, 4H), 3.64 (q, J = 7.0 Hz, 4H), 2.85 (s, 1H), 1.18 (t, J = 7.0 Hz, 6H).

b) 4-Ethynyl-N,N-bis(4-isopropoxyphenyl)aniline

Purification: Silica plug in DCM, column chromatography (SiO_2, PE/DCM 90/10)
Product: yellow oil (0.57 g, 94% yield)
^{1}H NMR (500 MHz, Benzene-d_6) δ 7.36 – 7.33 (m, 2H), 6.99 – 6.96 (m, 4H), 6.88 – 6.84 (m, 2H), 6.75 – 6.68 (m, 4H), 4.11 (h, J = 6.0 Hz, 2H), 2.77 (s, 1H), 1.10 (d, J = 6.1 Hz, 12H).

c) 4-Ethynyl-N,N-bis(4-propoxyphenyl)aniline

Purification: Silica plug in DCM, column chromatography (SiO_2, PE/DCM 90/10)
Product: yellow oil (2.22 g, 95% yield)
^{1}H NMR (500 MHz, Benzene-d_6) δ 7.38 – 7.35 (m, 2H), 7.03 – 6.96 (m, 4H), 6.91 – 6.85 (m, 2H), 6.74 – 6.70 (m, 4H), 3.52 (t, J = 6.4 Hz, 4H), 2.77 (s, 1H), 1.61 – 1.50 (m, 4H), 0.85 (t, J = 7.4 Hz, 6H).

d) 4-Ethynyl-N,N-bis(4-butoxyphenyl)aniline

Purification: Silica plug in DCM, column chromatography (SiO_2, PE/DCM 90/10)
Product: yellow oil (1.82 g, 92% yield)
^{1}H NMR (400 MHz, Benzene-d_6) δ 7.40 – 7.34 (m, 2H), 7.03 – 6.97 (m, 4H), 6.91 – 6.85 (m, 2H), 6.76 – 6.69 (m, 4H), 3.59 (t, J = 6.4 Hz, 4H), 2.77 (s, 1H), 1.59 – 1.51 (m, 4H), 1.39 – 1.28 (m, 4H), 0.82 (t, J = 7.4 Hz, 6H).

5) 4,4'-(buta-1,3-diyne-1,4-diyl)bis(*N*,*N*-bis(4-alkoxyphenyl)aniline)

CuCl (0.15 g, 1.5 mmol) was weighed out directly into a round bottomed flask, TMEDA (0.7 mL) was combined in one portion and later DCM (15 mL) was added slowly while stirring. 4 Å molecular sieves (3 g) were added to the mixture and after 5 min of stirring, a solution of 4-ethynyl-N,N-bis(4-isopropoxyphenyl)aniline (0.57 g, 1.5 mmol) in DCM (5 mL) were added to the previous solution and the mixture stirred for 1.5 hours at room temperature. The reaction was washed three times with a solution of 10% ammonium chloride (10 mL) , dried with $MgSO_4$ and the solvent remove under vacuum. The crude product was purified by column chromatography.

a) 4,4'-(Buta-1,3-diyne-1,4-diyl)bis(N,N-bis(4-ethoxyphenyl)aniline)
(EtO-DATPA)

Purification: Column chromatography (SiO_2, PE/EtA 98/2), recrystallization (Hexane/DCM)

Product: yellow powder (0.62 g. 73% yield).

^{1}H NMR (500 MHz, Benzene-d_6) δ 7.35 – 7.30 (m, 4H), 6.98 – 6.94 (m, 8H), 6.85 – 6.78 (m, 4H), 6.75 – 6.67 (m, 8H), 3.56 (q, J = 7.0 Hz, 8H), 1.10 (t, J = 6.9 Hz, 12H).

^{13}C NMR (126 MHz, Chloroform-*d*) δ 155.91 , 149.35 , 139.69 , 133.26, 127.33 , 118.52 , 115.39 , 112.07 , 82.16 , 73.10 , 63.68 , 14.89.

MS EI (m/z): $[M]^+$ 713.3348. Anal. Calcd for $C_{48}H_{44}N_2O_4$: C. 80.87; H: 6.22; N. 3.93 analysed C, 80.83; H, 6.15; N, 4.04.

b) 4,4'-(Buta-1,3-diyne-1,4-diyl)bis(N,N-bis(4-isopropoxyphenyl)aniline)
^{i}PrO-DATPA

Purification: Column chromatography (SiO_2, PE/EtA 98/2), recrystallization (Hexane/DCM)

Product: yellow powder (0.48 g, 84% yield)

^{1}H NMR (500 MHz, Benzene-d_6) δ 7.33 – 7.30 (m, 4H), 6.98 – 6.95 (m, 8H), 6.83 – 6.80 (m, 4H), 6.73 – 6.70 (m, 8H), 4.12 (p, J = 6.0 Hz, 4H), 1.10 (d, J = 6.0 Hz, 24H).

^{13}C NMR (126 MHz, Chloroform-*d*) δ 154.82, 149.36, 139.57, 133.25, 127.33, 118.55, 116.75, 112.03, 82.19, 77.22, 73.09 , 70.18 , 22.13.

MS EI (m/z): $[M]^+$ 768.3911. Anal. Calcd for $C_{52}H_{52}N_2O_4$: C. 81.22; H: 6.82; N. 3.64 analysed C, 81.09; H, 6.90; N, 3.48.

c) 4,4'-(Buta-1,3-diyne-1,4-diyl)bis(N,N-bis(4-isopropoxyphenyl)aniline)

^{n}PrO-DATPA

Purification: Column chromatography (SiO_2, PE/EtA 98/2), recrystallization (Hexane/DCM)

Product: yellow powder (2 g, 91% yield)

^{1}H NMR (500 MHz, Benzene-d_6) δ 7.37 – 7.30 (m, 4H), 7.00 – 6.95 (m, 8H), 6.84 – 6.80 (m, 4H), 6.74 – 6.70 (m, 8H), 3.52 (t, J = 6.4 Hz, 8H), 1.56 (h, J = 7.3 Hz, 8H), 0.85 (t, J = 7.4 Hz, 12H).

^{13}C NMR (126 MHz, Chloroform-d) δ 156.12 , 149.38 , 139.64 , 133.26 , 127.33 , 118.48 , 115.40 , 112.02 , 82.17 , 77.21 , 73.09 , 69.76 , 22.64 , 10.55 . MS EI (m/z): $[M]^+$ 768.3887. Anal. Calcd for $C_{52}H_{52}N_2O_4$: C. 81.22; H: 6.82; N. 3.64 analysed C, 81.05; H, 6.95; N, 3.72.

d) 4,4'-(Buta-1,3-diyne-1,4-diyl)bis(N,N-bis(4-butoxyphenyl)aniline)

BuO-DATPA

Purification: Column chromatography (SiO_2, PE/EtA 98/2), recrystallization (Hexane/DCM)

Product: yellow powder (1.5 g. 88 % yield).

^{1}H NMR (500 MHz, Benzene-d_6) δ 7.38 – 7.30 (m, 4H), 7.00 – 6.97 (m, 8H), 6.85 – 6.81 (m, 4H), 6.76 – 6.71 (m, 8H), 3.60 (t, J = 6.4 Hz, 8H), 1.61 – 1.51 (m, 8H), 1.40 – 1.28 (m, 8H), 0.82 (t, J = 7.4 Hz, 12H). ^{13}C NMR (126 MHz, Chloroform-d) δ 156.14, 149.38, 139.62, 133.26, 127.33, 118.47, 115.39, 112.01, 82.18, 77.22, 73.10, 67.93, 65.86, 31.39, 19.27, 15.29, 13.86.

MS EI (m/z): $[M]^+$ 824.4507. Anal. Calcd for $C_{56}H_{60}N_2O_4$: C. 81.52; H: 7.33; N. 3.40 analysed C, 81.39; H, 7.40; N, 3.42.

3.4.3 Optical characterization

Solution UV-Visible absorption spectra were recorded using a Jasco V-670 UV/Vis/NIR spectrometer controlled with SpectraManager software. Photoluminescence (PL) spectra were recorded with a Fluoromax-3 fluorimeter controlled by ISAMain software. All samples were measured in a 1 cm cell at room temperature in DCM as solvent. Concentrations of $2.5x10^{-5}$ M and $1x10^{-6}$ M were used for UV/Vis and PL respectively.

3.4.4 Electrochemical characterization

All cyclic voltammetry measurements were carried out in freshly distilled CH_2Cl_2 using 0.3M [TBA][BF_4] electrolyte in a three-electrode system with each solution being purged with N_2 prior to measurement. The working electrode was a Pt disk, the reference electrode was Ag/AgCl, and the counter electrode was a Pt rod. All measurements were made at room temperature using a μUTOLAB Type III potentiostat, driven by the electrochemical software GPES. Cyclic voltammetry (CV) measurements used scan rates of 100 mV/s: square wave voltammetry (SWV) was carried out at a step potential of 4 mV, square wave amplitude of 25 mV, and a square wave frequency of 10 Hz, giving a scan rate of 40 mV/s. Ferrocene was used as the internal standard in each measurement.

3.4.5 Thermal characterization

Differential scanning calorimetry (DSC) was performed on NETZSCH STA 449F1 at a scan rate of 5 K min^{-1} under a nitrogen atmosphere in DSC/TG aluminium pan. The measurement range was 25 ℃ to 250 ℃.

3.4.6 Computational details

All calculations were carried out using the Gaussian 09[217] program with Lee Yang–Parr correlation functional (B3LYP) level of theory. All atoms were described by the 6-31G(d) basis set. All structures were input and processed through the Avogadro[218] software package.

3.4.7 Organic Field-Effect Transistors

The Ossila low-density pre-fabricated substrates (channel length 0.1 mm width 0.03 mm) with a bottom gate/bottom contact were used to fabricate OFET devices. The substrates were treated with HMDS (Hexamethyldisilazane) to optimise the silicon surface property. A solution of the HTM (5 mg/mL) in dichlorobenzene was stirred at room temperature. The Ossila substrate was covered with the solution by drop-casting. The electric characteristics of the fabricated OFETs were measured using a Keithley 2612A System SourceMeter. Mobilities were calculated using the following equation

$$\mu_{FE} = \left(\frac{\sqrt{\partial I_{DS}}}{\partial V_G}\right)^2 \cdot \left(\frac{2L}{WC_i}\right)$$

Where Z is the channel width, L the channel length, C_i the capacitance, V_G the gate voltage and I_{DS} is the drain current and $\sqrt{\partial I_{DS}}/\partial V_G$, the slope of the Transfer Characteristic Curves in the saturation regime.[215,216]

3.4.8 Transient Absorption Spectroscopy

Transient Absorption Spectroscopy were measurement by Dr. Irene Sanchez Molina at Imperial College London.

Sample preparation

A solution of mesoporous TiO_2 in terpineol (Dyesol 30 nm TiO_2, weight ratio 1:2) was spin coated on a 10 mm by 10 mm glass square, with an acceleration of 2000 rpm for 30 s. The subtrates were cleaned with isopropanol (IPA) in a sonicator for 5 minutes before spin coating. After spin coating, the substrates were placed into a 450 ℃ oven for 1 hour and cooled down to room temperature before deposition of the perovskite layer. For the deposition of the perovskite layer 1M solution of PbI_2 and CH_3NH_3I in DMSO was prepared. This solution was spin coated onto the glass slides covered with the mesoporous oxide via a 3-step spin coating process: (i) 1000 rpm, 10s, 2000 acc; (ii) 5000 rpm, 20 s, 2000 acc; (iii) 6000 rpm, 20 s, 2000 acc. Toluene (300 μL) was dropped on the substrates by the end of the second step. The films were then annealed at 50 ℃ for 20 min and at 100 ℃ for 25-30 min and cooled down to room temperature.

A 20 mg/mL solution in chlorobenzene of the corresponding HTM was spin-coated onto the perovskite layer at 2000 rpm for 30 s, with an acceleration of 2000 rpm.

Measurements

UV-Vis was performed on a PerkinElmer UV/VIS Spectrometer Lambda 25. Photoluminescence spectra were recorded on a Horiba Yobin-Ybon Fluorolog-3 spectrofluorometer, using an excitation wavelength of 450 nm and slit widths of 10 nm. For pump-probe micro to millisecond transient absorption spectroscopy, films were excited by a dye laser (Photon Technology International GL-301, sub-nanosecond pulse width) pumped by a pulsed nitrogen laser (Photon Technology International GL-3300). A quartz halogen lamp (Bentham IL1) was passed through a monochromator and used to probe changes in the absorption characteristics of the film as a function of time after the laser excitation. The probe light was detected using home-built silicon (≤1000 nm) or InxGa1-xAs (>1000 nm) photodiodes and an oscilloscope. Unless otherwise stated, films were kept under flowing N_2 during the measurements. All micro to millisecond transient absorption spectroscopy measurements were conducted employing 450 nm laser pulses (25 μJ/cm^2).

3.4.9 Perovskite Solar Cells and Characterisation

Perovskite solar cells were fabricated by Dr. Joel Troughton at Swansea University. Etched FTO glass substrates (NSG Pilkington, TEC7) were cleaned sequentially in detergent, deionised water, acetone and ethanol, before undergoing 10 minutes of O_2 plasma treatment. A compact TiO_2 layer was deposited on the FTO glass substrates thtough spray pyrolysis of a 0.2M solution of titanium diisopropoxide bis(acetylacetonate) in isopropanol at 450 ℃. Upon cooling, a mesoporous layer of TiO_2 nanoparticles was spincoated from a 2:7 wt suspension of Dyesol 30NR-D paste in ethanol (4500 rpm, 30 s), followed by sintering at 550 ℃ for 30 minutes. A $CH_3NH_3PbI_3$ perovskite precursor solution was prepared by dissolving 576 mg PbI_2, and 199 mg CH_3NH_3I in a 4:1 (volume ratio) solution of DMF:DMSO. The perovskite precursor solution (100 μL) was deposited onto the TiO_2 films and spincoated at 4000 rpm for 30 seconds, with 200 μL of ethyl acetate dropped onto the spinning substrate 10 seconds prior to the end of the spincoating process. Perovskite films were annealed

at 100 ℃ for 10 minutes. In the case of the spiro-OMeTAD, a 85 mg/mL solution of spiro-OMeTAD in chlorobenzene was prepared with dopants including bis(trifluoromethylsulfonyl)imide lithium salt (Li-TFSI) (20 µL/mL of a 520 mg/mL solution in acetonitrile), 4-tert-butylpyridine (tBp, 30 µL/mL) and tris(2-(1H-pyrazol-1-yl)-4-tertbutylpyridine)-cobalt(III) tris(bis(trifluorome-thylsulfonyl)imide) (FK209, 10 µL/mL of a 300 mg/mL solution in acetonitrile). For the other HTMs, the same weight of material was dissolved in chlorobenzene with 2 times the volume of additives. The HTM solution was spincoated onto the perovskite films at 4000 rpm for 30 seconds before 80 nm thick gold (Au) contacts were thermally evaporated onto devices. Current-voltage measurments were performed using a AAA-rated solar simulator (Oriel Sol3A) calibrated against a KG5-filtered reference diode (Oriel 91150-KG5). Solar cells were masked to 0.1 cm^2 and scanned both from forward to reverse bias and viceversa at 100 mV/s.

4 Polymeric HTMs with triarylamine side chains

4.1 Introduction

Polymeric triphenylamines present some improved properties compared to their low molecular weight equivalents such as excellent film forming which allow an easy and low-cost manufacture of large scale technologies.[219–221] One of the most notable improvements is that polymers have higher glass transition temperatures (T_g) and do not crystallise easily bringing an important potential advantage for the stability and reproducibility of the devices. Furthermore, the hydrophobic properties of polymers act as a protecting layer for the perovskite film to ambient which enhance the solar cell stability.[219,220]

Polymeric materials have been widely employed as promising HTMs in OLED and OPV technologies for many years and by the time perovskite solar cells[222] were introduced, there was already many available polymers including: poly(3-hexylthiophene)(P3HT)[192], Poly[2,6-(4,4-bis-(2-ethylhexyl)-4H-cyclopenta[2,1-b;3,4-b']dithiophene)-alt-4,7(2,1,3-benzothiadiazole)] (PCPDTBT)[166], poly[N-9'-heptadecanyl-2,7-carbazole-alt-5,5-(4',7'-di-2-thienyl-2',1',3'-benzothiadiazole)] (PCDTBT),[223] poly-triarylamine (PTAA)[224] and others.[156] These materials were not designed for perovskite solar cells and they absorb light, therefore they can compete with the perovskite absorber in the inverted solar cell architecture.

Electronic functional polymers are typically divided into two groups: main-chain and side chain. Most polymers used in perovskite cells are main chain polymers. Side-chain polymers have been studied before in organic electroluminescence devices (EL)[225] and organic field effect transistors (OFET)[226,227] because they are comparable with their low molecular weight analogues in terms of the electronic properties presenting also high solubility and good thermal properties. Nevertheless, to the best

of our knowledge side-chain polymers haven't been studied before in perovskite solar cells. Furthermore, there is no report comparing the effect of the corresponding monomers and polymers in solar cell performance. Here we investigate two different monomers namely M:OO and M:ON with their corresponding side-chain polymer coded as P:OO and P:ON (Figure 4.1). Two different substituted Styrenic triarylamines were prepared followed by their radical polymerization using AIBN to study their properties and function as HTMs in perovskite solar cells.

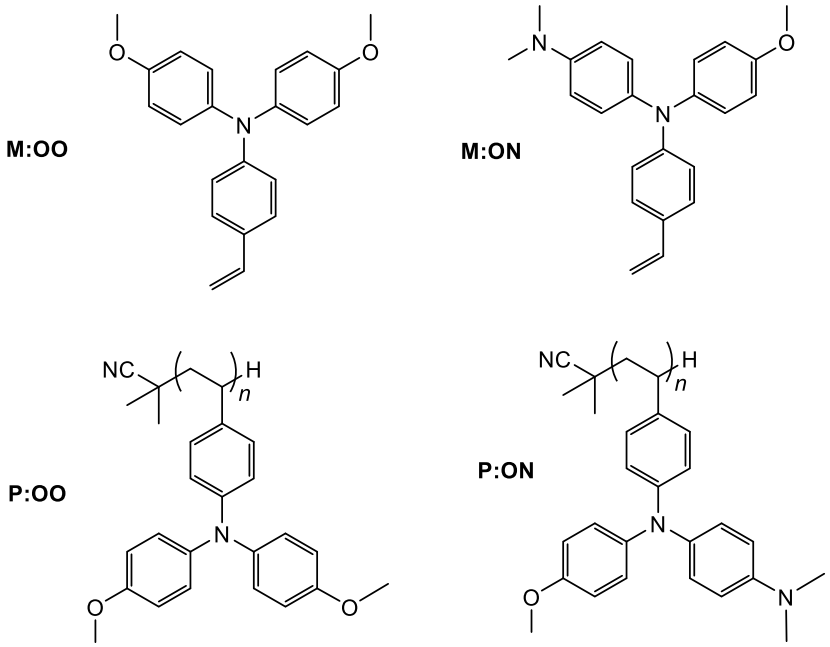

Figure 4.1 Chemical structure of the HTMs used in this study.

4.2 Results and Discussion

4.2.1 Synthesis

In a previous study, Jager[228] and co-workers synthesized similar triarylamines with different substituents which were later polymerized by nitroxide-mediated polymerisation (NMP) to prepared block copolymers for directional charge transfer. In this work the P:OO and P:ON were prepared by the free radical polymerization of 4-ethenyl-*N*,*N*-bis(4-methoxyphenyl)benzenamine (M:OO) and 4-ethenyl-*N*,*N*-bis(4-Methoxy,4-(dimethylamino)diphenyl-amine (M:ON) respectively. Triarylamines

containing a styrene unit were synthesized by the palladium catalysed Buchwald-Hartwig[229] coupling due to its adaptability for multigram scale. The synthetic route is shown in scheme 4.1 and detailed synthetic procedures can be found in the experimental section. All materials were characterised in detail by nuclear magnetic resonance (NMR) (^{1}H and ^{13}C), elemental analysis and mass spectrometry (MS).

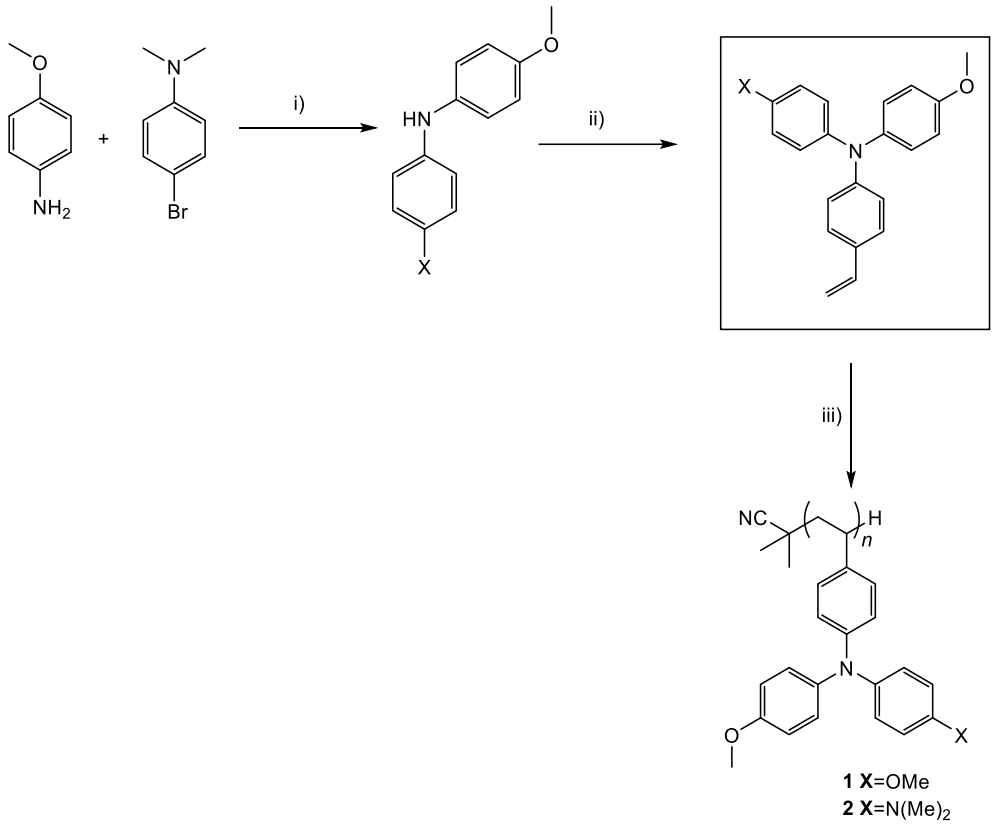

Scheme 4.1 Schematic representation of the synthesis of triarylamines by Hartwig-Buchwald coupling and preparation of the polymers by radical polymerization. Reaction conditions: i) $Pd_2(dba)_3$, phosphine ligand, NaOtBu, toluene, 18 hrs, 80 ℃, N_2 ii) $Pd_2(dba)_3$, phosphine ligand, bromostyrene, NaOtBu, toluene, 12 hrs, 110 ℃ iii) AIBN, toluene, 120 (See Experimental section for details).

4.2.2 Optical and electrochemical properties

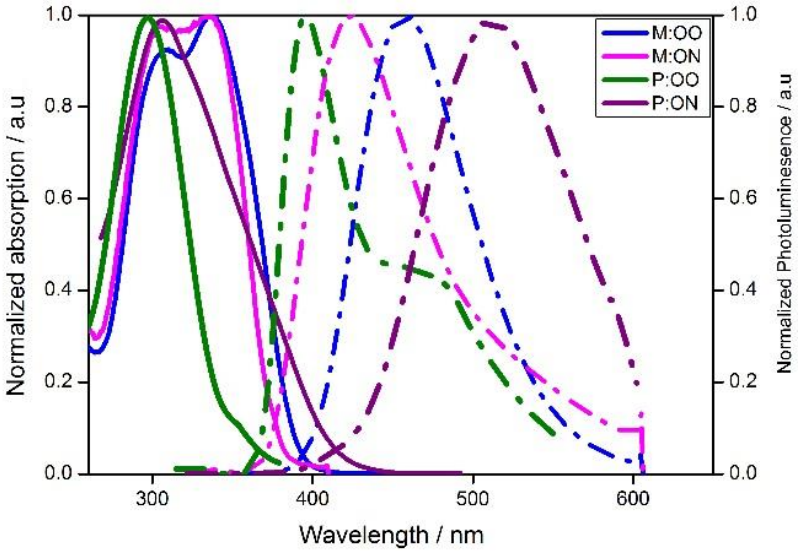

Figure 4.2 Normalized UV-Vis absorption (solid line) and emission (dashed line) of monomers and polymers.

The optical properties of monomers and polymers were investigated by UV/Vis and photoluminescence (PL) spectroscopy in solution with dichloromethane. The UV-Vis absorption spectra are presented in Figure 4.2 (solid line). All compounds exhibit a strong absorption around 300 nm almost independent of the substituents. The absorption peaks are located around 300 nm. Absorption peaks of the investigated polymers and monomers are located in the UV region with no significant absorption in the visible region. Transparent HTMs with no absorption in the visible region 390 to 700 nm provide additional advantages and flexibility as they can be used in other solar cells architectures such as inverted and tandem structures where it is important that there is not competition with the perovskite layer. The monomers exhibit two adjacent bands corresponding to π-π* and n-π* absorption, while for the polymers one single band from n-π* absorption is observed. Photoluminescence spectra are illustrated in Figure 4.2 (dashed line). In contrast to UV-Vis, the emission energies are significantly influenced by the substituents. The symmetric substitution (M:OO and P:OO) leads to emission at 457 and 395 nm respectively whereas the emission maxima are shifted to longer wavelength for the asymmetric substitutions (M:ON and P:ON)

and are found at 424 and 530 nm. This trend could be explained as an effective S1 energy stabilisation due to the presence of electron-donating groups of various strengths, likely linked with rotation around the N-aryl bond after excitation. Moreover, a hypsochromic shift is observed upon polymerization, which can be attributed to both the loss of the conjugated double bond and the steric shielding effect (solvent exclusion). The polymers have a more rigid and compact structure, which leads to steric shielding of the interior units. Hence, lower interaction with the solvent molecules leads to less stabilisation of the emissive state explaining the observed blue-shifted emission. The optical band gaps were determined from the intersection of the excitation and the emission spectra and are presented in Table 4.1 at the end of this section.

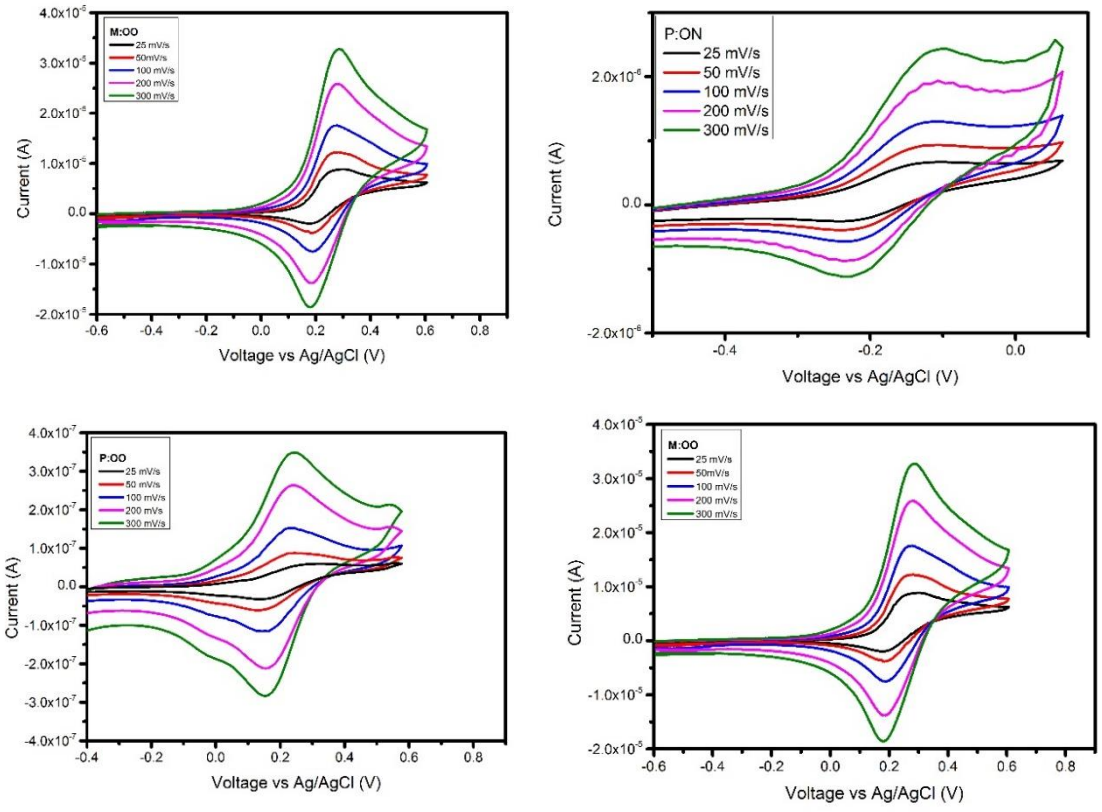

Figure 4.3 Cyclic voltammetry traces at different scan rates of M:OO, P:OO, M:ON and P:ON.

The oxidation potential and derived energy levels of the HTMs are fundamental parameters for constructing high-performance PSCs. The electrochemical properties were investigated by cyclic voltammetry (CV) and square-wave voltammetry. From the CV measurements (Figure 4.3), it can be noted that the redox peaks of all the HTMs are highly chemically and electrochemically reversible, indicating excellent chemical stability and rapid electron transfer.

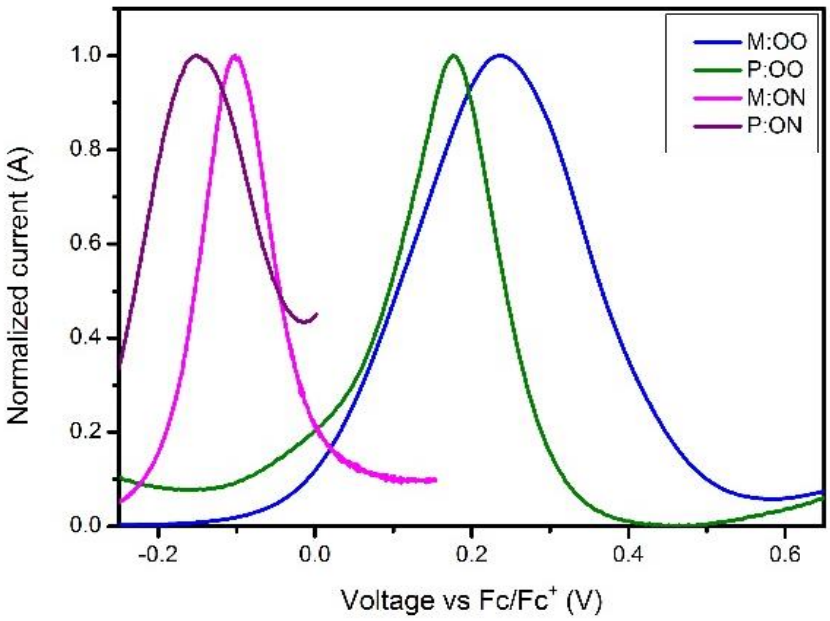

Figure 4.4 Square-wave voltammetry of the monomers and polymers. M:OO (blue line), M:ON (pink line), P:OO (green line) and P:ON (purple line).

The HOMO energy levels of the compounds were estimated from the half-wave potential using ferrocene/ferrocenium as an internal standard in square-wave voltammetry (Figure 4.4) experiments. The four compounds show an oxidation process assigned to the oxidation of the triarylamine moiety. The influence of the substituents is reflected by a shift in the potential of the redox couple. The oxidation of M:OO and P:OO occurs around +0.22 V and +0.19 V, whereas the electron donating Me_2N- substituent of M:ON and P:ON causes a shift to lower potentials (-0.1 V and -0.15 V) thus increasing their HOMO energy level to -5.0 eV and -4.95 eV respectively. This makes M:ON and P:ON significantly stronger donor molecules than M:OO, P:OO

and Spiro-OMeTAD. These observations were explained with Density Functional Theory calculations using Gaussian 09[217] with B3LYP 6-31(d) level of theory in DCM.

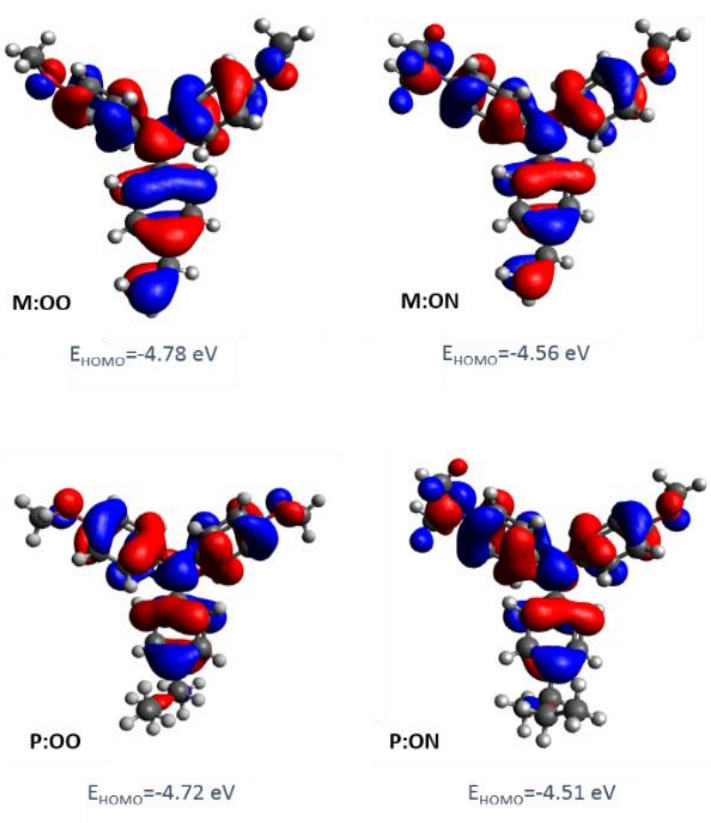

Figure 4.5 Molecular Orbital distribution of HOMO of monomers and polymer model derivatives at B3LYP/6-31G(d)level of theory.

For the polymers, a model of the monomer fragment with saturated alkyl chain was used to calculate their electronic properties. The calculated trend of HOMO energy levels matches the experimental data. The HOMO energy levels delocalized over the π orbitals of the triphenylamine unit and the peripheral substituents. The delocalisation of the HOMO onto the peripheral substituents (Figure 4.5) explains the large shift in the oxidation potential upon changing the substituent from MeO- to Me_2N-. A summary of the optical and electrochemical properties of these materials is presented in Table 4.1. These results indicate an energetically-favourable hole transfer from the perovskite ($MAPbI_3$) to the HTM in all cases (Figure 4.6).

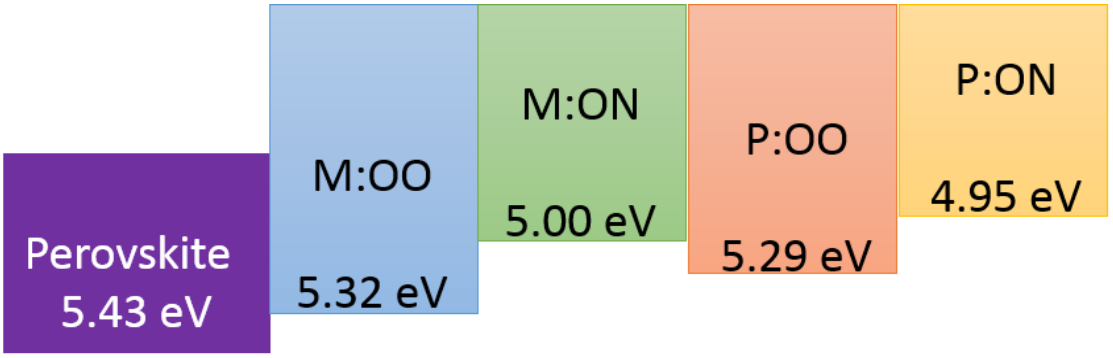

Figure 4.6 Energy diagram for perovskite ($CH_3NH_3PbI_3$), monomers and polymers.

Table 4.1 Summary of the optical, electrochemical and thermal properties

HTM	λ_{max} (nm)	ε (cm^{-1} M^{-1})	λ_{em} (nm)[a]	E_{gap} (V)[b]	E_{ox} (V)[c]	E_{HOMO} (eV)[d]
M:OO	308*,336	22500	457	3.15	+0.22	-5.32
M:ON	309*,334	23500	424	3.29	-0.10	-5.00
P:OO	300*	19000	395	3.39	+0.19	-5.29
P:ON	307*	23000	511	2.99	-0.15	-4.95
Spiro-OMeTAD	385	-	424	3.05	+0.03	-5.13

[a]Excitation at λ_{max}*. [b]Optical gap, determined from the intersection of the excitation and emission spectra.[c]From SWV measurments and referenced to ferrocene. [d]E_{HOMO}(eV)=-5.1-$E_{ox.}$ [213]

4.2.3 Thermal properties

Thermal properties of the monomers and polymers were determined by Differential Scanning Calorimetry (DSC), and the results are displayed in the supporting information (Figure 4.7). Both polymers (P:OO and P:ON) showed the same glass transition temperature of 253 ℃. On the other hand monomers M:OO and M:ON, do not present T_g. The M:OO exhibit a melting point of 75 ℃ and no melting point was found for M:ON. These results confirm that the polymers form a more stable amorphous glassy state and higher thermal stability.

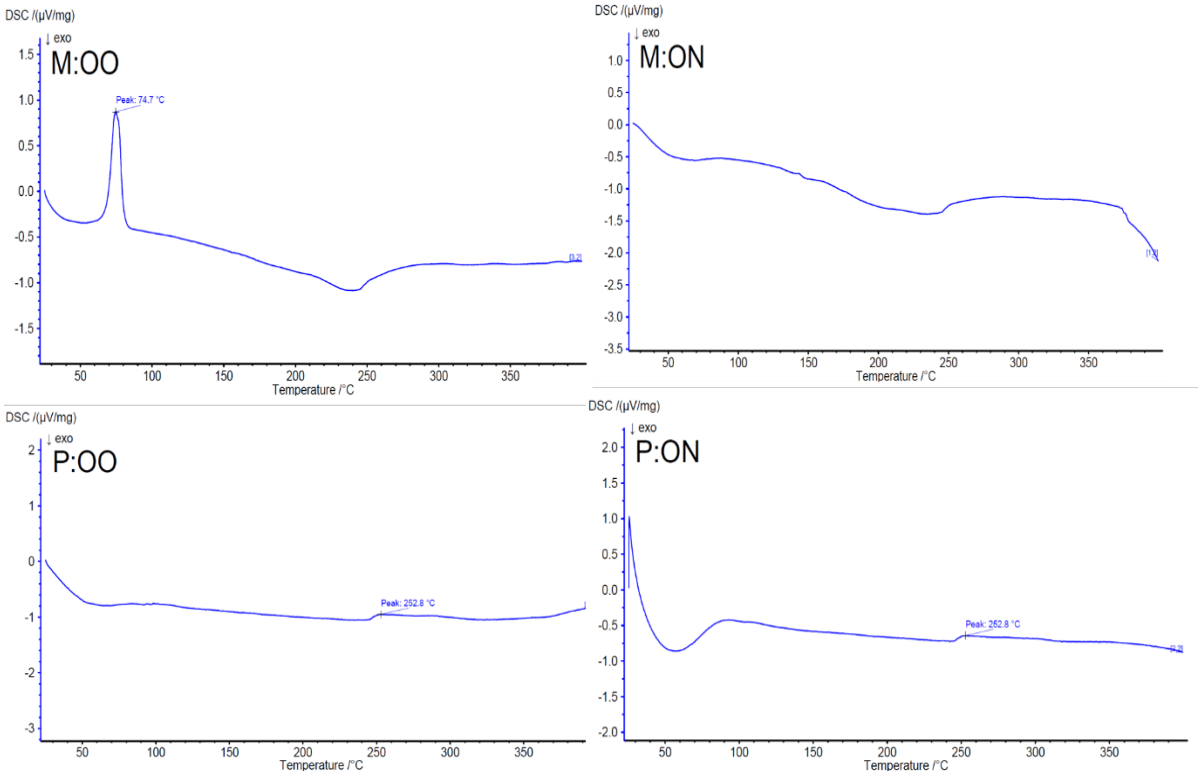

Figure 4.7 Differential scanning calorimetry curves.

4.2.4 Transient Absorption Spectroscopy

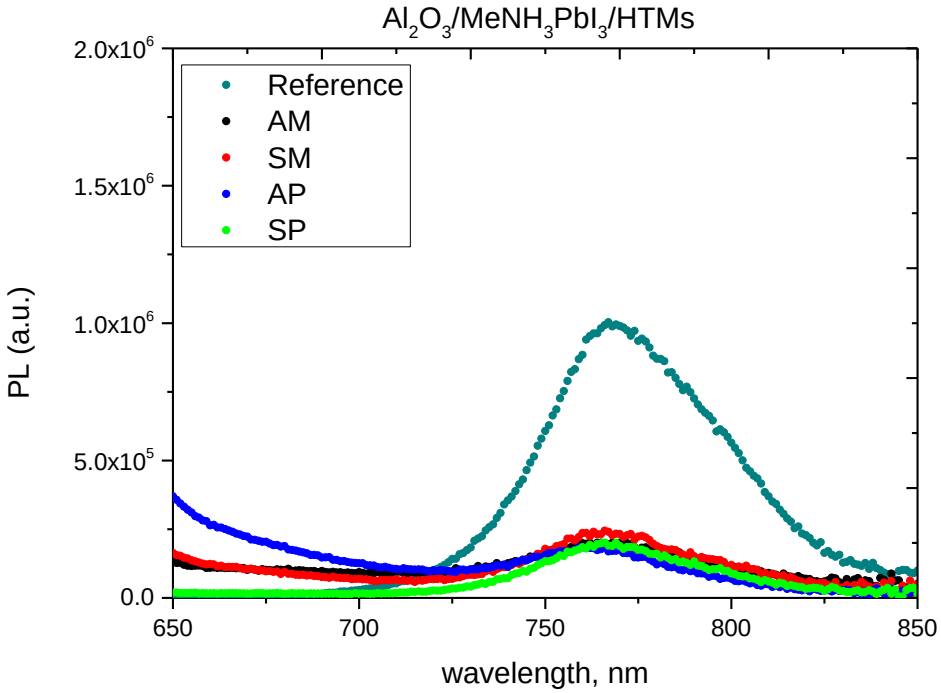

Figure 4.8 Steady-State Photoluminescence in a Al_2O_3/$MeNH_3PbI_3$/HTM architecture. AM is M:ON, SM is M:OO, AP is P:ON and SP is P:OO.

To investigate the ability of the monomers and polymers to extract holes, we measured steady-state and transient photoluminescence (PL) decay. Samples were prepared by spin-coating of the perovskite onto a mesoporous Al_2O_3 layer with the HTM on top. Details of the sample preparation and measurments are described in the experimental section. The perovskite exhibited a strong PL peak near 760 nm as shown in Figure 4.8 and PL is largely quenched when any of the HTMs (M:OO, P:OO, M:ON and P:ON) were coated onto the perovskite, indicating an effective charge extraction into the HTM. From the transient PL decays (Figure 4.9), it was found that monomers reduce the lifetime of the perovskite emission more effectively than polymers, indicating more effective charge extraction.

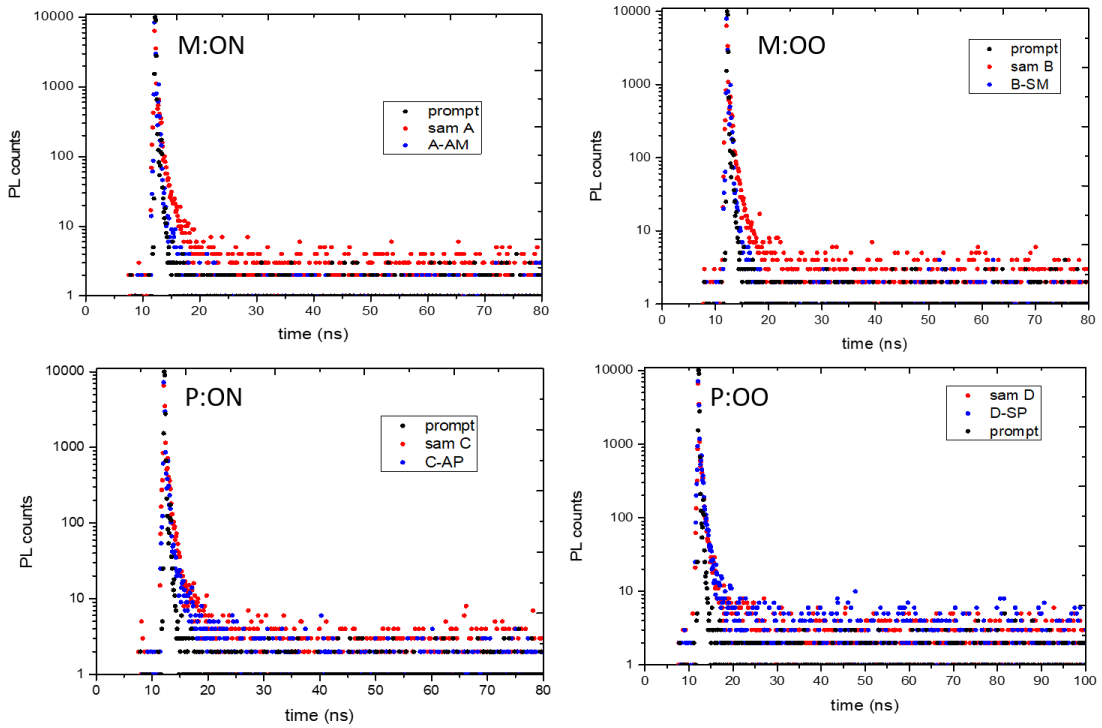

Figure 4.9 Transient PL decay of monomers and polymers.

4.2.5 Solar Cells Studies

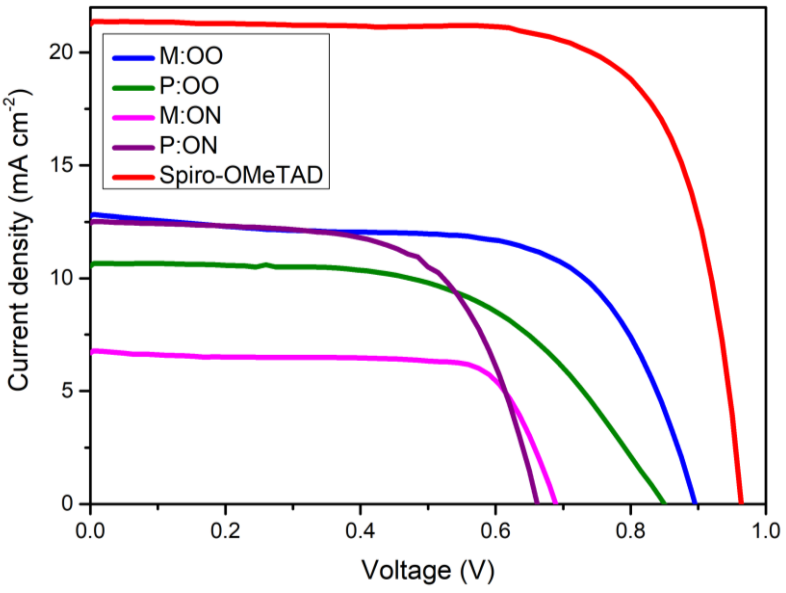

Figure 4.10 J-V curves of the champion PSCs of the new HTMs and spiro-OMeTAD.

We prepared a set of perovskite solar cells in the configuration FTO/bl-TiO_2/mp-TiO_2/$CH_3NH_3PbI_3$/HTM/Au. All HTMs were doped using similar concentrations of additives [LiTFSi] and tBP (tert-butylpyridine) as described in the supporting information. The current density-voltage (J-V) characteristics were measured under simulated air mass 1.5 global (AM 1.5G) solar irradiation. Figure 4.10 shows the J-V curves characteristic of the champion devices and results are summarised in Table 4.2. All devices were fabricated in a single continuous study over 15 repeat cells for each HTM to facilitate comparison between the reported HTMs and Spiro-OMeTAD. Spiro-OMeTAD presented the highest efficiency of 15.09 %. The corresponding values for M:OO, P:OO and P:ON of 7.48%, 5.28% and 5.14% are reasonably good considering that this work represents the first solar cells study with these HTMs and that Spiro-OMeTAD has gone through extensive optimisation of doping and processing procedures for many years.

Table 4.2 Summary of photovoltaic parameters of the champion cells

HTM	**PCE (%)**	**J_{sc} (mA cm^{-2})**	**V_{oc} (V)**	**FF (%)**
M:OO	7.48	12.81	0.89	65.54
P:OO	5.14	10.61	0.85	57.17
M:ON	3.52	6.79	0.68	76.19
P:ON	5.28	12.49	0.65	64.73
Spiro-OMeTAD	15.09	20.56	0.95	63.81

Figure 4.10 shows the box plots with the mean and standard deviation of the solar cell parameters and the results are summarised in Table 4.3.

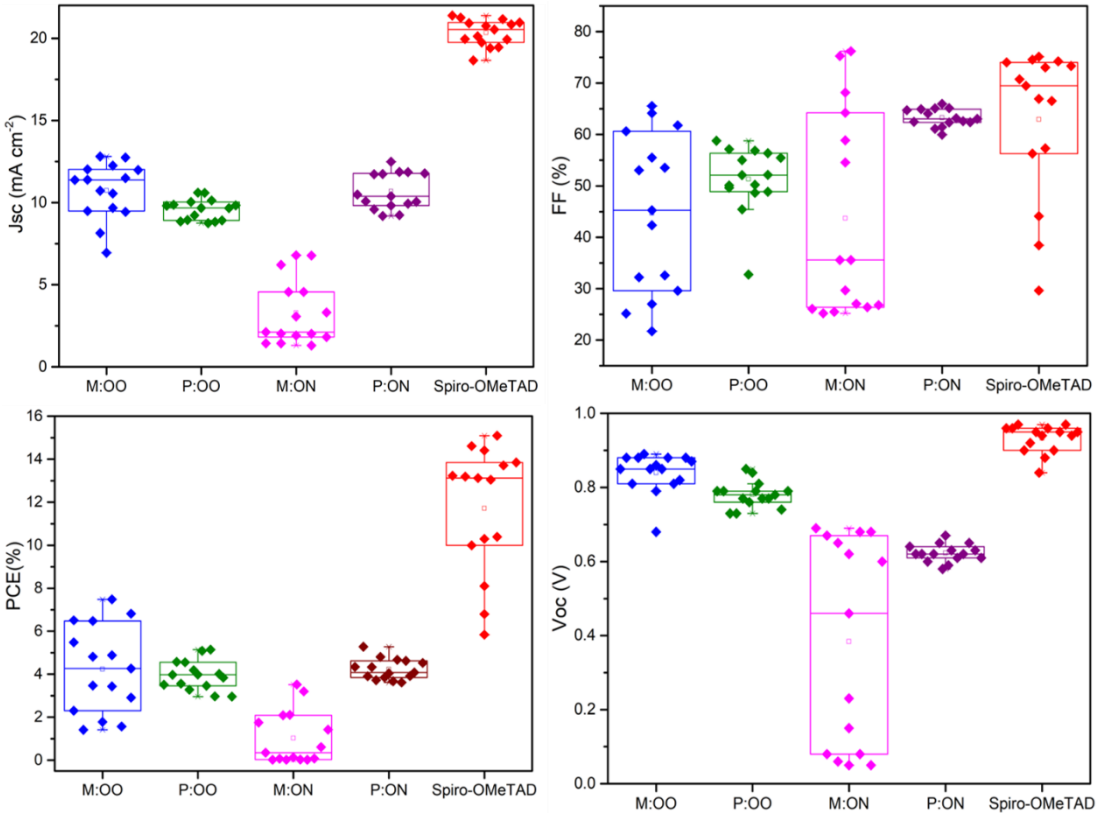

Figure 4.11 Box plot of photovoltaic parameters of PSCs over 15 repeats for each HTM.

There is a small increase in the average short circuit current (J_{sc}) values upon increasing the electron donating character of the polymers from 9.58±0.63 mA cm^2 for P:OO to 10.68±1.11mA cm-2 for P:ON. On the other hand, the HOMO levels of P:ON and M:ON are higher than P:OO and M:OO leading to smaller open circuit voltage (V_{oc}) values; 0.84±0.054 V and 0.78±0.035V for M:OO and P:OO and 0.38±0.28 V and 0.62±0.023 for M:ON and P:ON. Comparing M:OO and P:OO, the variance in PCE values is attributed to the differences in the photocurrent density which may have resulted from the more efficient charge extraction sustained by the result from the transient PL decay.

Table 4.3 Summary of the mean and standard deviation of photovoltaic parameters measured over 15 repeat cells.

HTM	PCE (%)	J_{sc} (mA cm^{-2})	V_{oc} (V)	FF (%)
M:OO	4.24±2.03	10.74±1.71	0.84±0.054	44.67±15.54
P:OO	3.94±0.68	9.58±0.63	0.78±0.035	51.31±6.41
M:ON	1.03±1.23	3.29±1.99	0.38±0.28	43.67±19.98
P:ON	4.22±0.48	10.68±1.11	0.62±0.023	63.24±1.71
Spiro-OMeTAD	11.71±2.96	20.37±0.80	0.93±0.038	62.92±14.67

As can be seen from the box plot (Figure 4.11), in comparison with both monomers and Spiro-OMeTAD, the polymers exhibit photovoltaic parameters with significantly smaller standard deviation, leading to average PCE 3.94%± 0.68 for P:OO and 4.22%±0.48 whereas for spiro-OMeTAD, M:OO and M:OO average values are 11.7%±2.96, 4.24%±2.03 and 1.03%±1.23. The difference in FF values are even greater with polymers showing 51.3%±6.4 for P:OO and 63.2%±1.7 and spiro-OMeTAD, M:OO and M:ON presenting 62.92%±14.67, 44.67%±15.54 and 43.67%±19.98. These result can be attributed to the difference in the morphology. The polymers form more stable amorphous state and have higher thermal stability which result in a more homogenous film deposition during the device fabrication.

4.3 Conclusions

In conclusion, we present the synthesis and characterisation of two styrenic triphenylamine-based monomers and their corresponding side-chain polymers for use as HTMs in perovskite solar cells. The structures contained different electron-donating groups in the para-position. The effect of the substituents on the redox potential result in a potential window from -0.15 to 0.22 V. The optical, electrochemical, thermal properties and device performance of the monomers and polymers were compared in terms of their structure. From this study, it was found that despite offering lower

efficiencies in comparison with spiro-OMeTAD and monomers, the polymers presented higher reproducibility in the solar cells parameters. The polymers have significantly smaller standard deviation in the power conversion efficiency and fill factor data which is mainly due to the better and more stable amorphous films resulting in a more homogeneous film. The results found in this work may encourage further efforts on polymeric HTMs with redox side groups for perovskite solar cells which may have advantages in manufacture and scale up due to enhanced reproducibility.

4.4 Experimental details

4.4.1 Chemical characterization

^{1}H and ^{13}C NMR spectra were recorded on a Brucker Advance 500 spectrometer (500 MHz for ^{1}H and 124 MHz for ^{13}C). The deuterated solvents are indicated in the synthesis description. Chemical shifts, δ, are given in ppm, using the solvent residual as an internal standard. MS were recorded on Bruker ESI Micro-Tof equipped with LC using electrospray ionization (ESI). Elemental analyses were carried out by Stephen Boyer at London Metropolitan University.

4.4.2 Synthesis

Materials and Synthesis

All reagents were purchased from either Sigma-Aldrich or Alfa-Aesar and they were used as received without further purification unless otherwise stated.

4-Ethenyl-N,N-bis(4-methoxyphenyl)benzenamine $Pd_2(dba)_3$ (1.31 mmol, 1.2g), tri-o-tolylphosphine (6.5 mmol, 2 g), 4,4' Dimethoxydiphenylamine (43.62 mmol, 10 g) and NaOtBu (50 mmol, 4.8 g) were added into a Schleck tube and dried under vacuum for 30 minutes. 4-Bromostyrene (5.8 mmol, 0.7 g) and toluene (30 mL) were all degassed and added to the reaction mixture and the contents heated at 110 ℃ overnight under N_2. The crude material was purified first by an extraction with water following by a silica plug (70:30 Hex/EtA) of the organic phase. Solvent was removed from the solution under vacuum and the product purified by flash column chromatography (SiO_2, Hexane/EtOAc 80:20) to afford a yellow powder (5.3 g, 52.5%

yield). ^{1}H NMR (500 MHz, DMSO-d_6) δ 7.31 – 7.24 (m, 2H), 7.05 – 6.98 (m, 4H), 6.96 – 6.88 (m, 4H), 6.76 – 6.69 (m, 2H), 6.61 (dd, J = 17.6, 11.0 Hz, 1H), 5.61 (dd, J = 17.6, 1.2 Hz, 1H), 5.08 (dd, J = 10.9, 1.3 Hz, 1H), 3.75 (s, 6H). ^{13}C NMR (126 MHz, DMSO-d6) δ 119.65, 115.43, 111.73, 55.72 , 39.77 , 39.59. Anal. Calcd for $C_{22}H_{21}NO_2$: C, 79.73; H, 6.39; N, 4.23; found: C, 79.81; H, 6.50; N, 4.34.): [M]+ calcd 331.42 found 331.16.

4-Methoxy-4'-(dimethylamino)diphenylamine 4-bromo-N,N-dimethylaniline (5 g, 25 mmol), p-anisidine (3.7 g, 30 mmol), $Pd_2(dba)_3$ (115 mg, 0.125 mmol), JohnPhos ligand (74 mg, 0.250 mmol) and NaOtBu (3.35 g, 35 mmol) were were added into a Schlenk tube and dry under high vacuum for 60 minute. Previously degassed dry toluene (66 mL) was added and the mixture was stirred at 80 ºC for 48 hrs under N_2. The crude material was purified first by an extraction with water/DCM and a silica plug (70:30 Hex/EtOAc). Solvent was removed from the solution under vacuum and the product was purified by flash column chromatography (SiO_2, hexane/EtOAc/ 9.9:0.10) to afford a yellow powder (5.3 g, 52.5% yield). ^{1}H NMR (500 MHz, Benzene-d6) δ 6.97 – 6.90 (m, 2H), 6.83 – 6.74 (m, 4H), 6.65 – 6.60 (m, 2H), 4.73 (s, 1H), 3.37 (s, 3H), 2.56 (s, 6H).

4-Ethenyl-N,N-bis(4-Methoxy-4'(dimethylamino)diphenylamine $Pd_2(dba)_3$ (0.25 mmol, 0.23 g), tri-o-tolylphosphine (1.24 mmol, 0.38 g), 4-Methoxy-4'-(dimethylamino)diphenylamine (8.26 mmol, 2 g) and NaOtBu (9.5 mmol, 0.9) were added into a Schlenk tube and dried under vacuum for 30 minutes. 4-Bromostyrene (5.8 mmol, 0.7 g) and toluene (15 mL) were all degassed and added to the reaction mixture and the contents heated at 110 °C overnight under N_2. The crude material was purified by an extraction with water following by a silica plug (70:30 Hex/EtA). Solvent was removed from the solution under vacuum and the product purified by flash column chromatography (SiO_2, Hexanes up to Hexanes/EtOAc 80: 20) to afford a thick yellow oil (1.6 g, 80% yield). ^{1}H NMR (500 MHz, DMSO-d6) δ 7.28 – 7.21 (m, 2H), 7.05 – 6.97 (m, 2H), 7.00 – 6.91 (m, 2H), 6.94 – 6.86 (m, 2H), 6.77 – 6.66 (m, 4H), 6.60 (dd, J = 17.6, 11.0 Hz, 1H), 5.58 (dd, J = 17.6, 1.2 Hz, 1H), 5.05 (dd, J =

10.9, 1.2 Hz, 1H), 3.74 (s, 3H), 2.88 (s, 6H). ^{13}C NMR (126 MHz, DMSO-d6) δ 148.93, 148.11, 140.62, 136.72, 136.47, 128.92, 127.48, 127.35, 126.79, 118.83, 115.30, 114.02, 111.27, 55.71, 40.82, 39.7. Anal. Calcd for $C_{23}H_{24}N_2O$: C, 80.20; H, 7.02; N, 8.13; found: C, 80.05; H, 7.16; N, 8.05.): [M]+ calcd 344.46 found 345.196.

The polymers were synthesised bv Dr. Ben Lake from Professor Michael Shaver group at the University of Edinburgh using the following procedure:

P:OO was synthesised *via* free radical polymerisation (FRP). An ampoule was charged with 4-methoxy-*N*-(4-methoxyphenyl)-*N*-(4-vinylphenyl)aniline (1.0 g, 3.0 mmol), AIBN (5.0 mg, 30 μmol) and anhydrous toluene (2 ml). The resulting solution was heated at 120°C for 20 hours. After this time, the reaction mixture was cooled to ambient temperature. The reaction mixture was added dropwise to methanol (75 ml), inducing the precipitation of the polymer, which was collected by filtration. It was necessary to re-dissolve (in a minimum of THF) and re-precipitate (in methanol) the collected polymer to ensure that all remaining monomer was removed. Finally, the purified polymer was dried *in vacuum*, yielding an off-white solid (0.55 g). ^{1}H NMR (500 MHz, DMSO-d_6) δ 1.4 – 1.6 (chain, 3H), 3.5 – 3.8 (OMe, 6H), 6.3 – 7.0 (aromatic, 12H).

P:ON was synthesised using the same procedure described above. The purified polymer was dried *in vacuum*, yielding a yellow solid (0.50 g). ^{1}H NMR (500 MHz, DMSO-d_6) δ 1.5 – 1.7 (chain, 3H), 2.7 – 3.2 (NMe_2, 6H), 3.5 – 3.8 (OMe, 3H), 6.5 – 7.3 (aromatic, 12H).

4.4.3 Thermal Characterisation

Differential scanning calorimetry (DSC) was performed on NETZSCH STA 449F1 at a scan rate of 5 K min^{-1} under nitrogen atmosphere in DSC/TG aluminium pan. The measurement range was 25 ℃ to 300 ℃.

4.4.4 Optical characterization

Solution UV-Visible absorption spectra were recorded using a Jasco V-670 UV/Vis/NIR spectrometer controlled with SpectraManager software. Photoluminescence (PL) spectra were recorded with a Fluoromax-3 fluorimeter controlled by ISAMA software. All samples were measured in a 1 cm cell at room temperature with dichloromethane as solvent. Concentrations of 5 x 10^{-5} M and 2 x 10^{-6} M were used for UV/Vis and PL respectively.

4.4.5 Electrochemical characterization

All cyclic voltammetry measurements were carried out in freshly distilled CH_2Cl_2 using 0.3 M [TBA][BF_4] electrolyte in a three electrode system, with each solution being purged with N_2 prior to measurement. The working electrode was a Pt disk. The reference electrode was Ag/AgCl and the counter electrode was a Pt rod. All measurements were made at room temperature using a μAUTOLAB Type III potentiostat driven by the electrochemical software GPES; square wave voltammetry (SWV) was carried out at a step potential of 2 mV, square wave amplitude of 25 mV, and a square wave frequency of 25 Hz. Ferrocene was used as the internal standard in each measurement.

4.4.6 Computational details

All calculations were carried out using the Gaussian 09 program with Lee Yang–Parr correlation functional (B3LYP) level of theory. All atoms were described by the 6-31G(d) basis set. All structures were input and processed through the Avogadro software package.

4.4.7 Time resolved photoluminescence

Time resolved photoluminescence measurmenrs were performed by Dr. Irene Sanchez Molina at Imperial College London. A 35 % dilution of an AI-7 Al_2O_3 paste in H_2O was made up and stirred overnight. Squares of VWR super premium microscope slides were rinsed in IPA in a sonicator for five minutes prior to spin coating. The solution of alumina was pipetted onto the microscope slides while on the vacuumed O-ring.

The paste was spun at 4500 rpm, for 30 seconds. The films were then placed in a 150 ℃ oven for 1 hour and left to cool for 20 minutes. For the deposition of the perovskite layer 1M solution of PbI_2 and $MeNH_3I$ in DMSO was prepared. This solution was spin-coated onto the glass slides covered with the mesoporous oxide via 3-step spin coating process: (i) 1000 rpm, 10 s, 2000 acc; (ii) 5000 rpm, 20 s, 2000 acc; (iii) 6000 rpm, 20 s, 2000acc. Toluene (300 μL) was dropped on the substrates by the end of the second step. The films were then annealed at 50 ℃ for 20 min and at 100 ℃ for 25-30 min and cooled down to room temperature. A 20 mg/mL solution in chlorobenzene of the corresponding HTM was spin-coated onto the perovskite layer at 200 rpm for 30 s, with an acceleration of 2000 rpm. UV-Vis was performed on a PerkinElmer UV/VIS Spectrometer Lambda 25. Photoluminescence spectra were recorded on a Horiba Yobin-Ybon Fluorolog-3 spectrofluorometer, using an excitation wavelength of 450 nm and slit widths of 10 nm. Time-correlated single-photon counting was recorded using a Deltaflex spectrometer (Horiba Yobin-Tbon), using an excitation of 404 nm and measuring the emission of the perovskite at 770 nm.

4.4.8 Perovskite Solar Cells and Characterisation

Perovskite solar cells were fabricated by Dr. Joel Troughton at Swansea University. FTO substrates (7 Ω/sq) were etched with zinc powder and HCl (2M aqueous solution) to give the desired electrode patterning. The substrates were cleaned in a solution of detergent and deionised water before sequential sonication in deionised water, acetone and isopropanol and a 10 minute oxygen plasma treatment to remove the last traces of organics. The FTO substrates were subsequently coated with a compact layer of TiO_2 (50 nm) by spray pyrolysis deposition using titanium diisopropoxide bis(acetylacetonate) in anhydrous ethanol as precursor solution (Volume ratio 1:9). After cooling from 450 ℃, a dilute suspension of TiO_2 nanoparticles (2:7 wt, Dyesol 30NR-D: ethanol) was deposited by spin coating (4500 rpm, 30 seconds). The samples were then heated at 150 ℃ for 10 minutes, followed by sintering at 550 ℃ for 30 minutes. Upon cooling, samples were immediately transferred to a N_2-filled glovebox (H_2O and O_2 levels < 0.5 ppm). The perovskite ($CH_3NH_3PbI_3$) layer was deposited by spin-coating a solution containing 576 mg of PbI_2 and 199 mg of MAI in a mixture of 0.8 mL DMF and 0.2 mL of DMSO (4000 rpm, 30 seconds), with 100 μL of ethyl

acetate deposited 10 seconds before the end of the spin cycle. The substrates were then annealed at 100 ℃ for 10 minutes in the glovebox. The HTMs were dissolved in chlorobenzene (75 mg/mL) with the standard additives 5-tert-butylpyridine (32 μL) and lithium bis(trifluoromethanesulfonyl) imide (20 μL, 520 mg/mL solution in acetonitrile). Hole transport solutions were spin-coated at 4000 rpm for 30 seconds, after which a 80 nm thick gold electrode was evaporated at 10^{-4} Torr. For measuring the performance of the solar cells, simulated sunlight was generated using an AAA-rated solar simulator (Newport) calibrated with KG-5 filtered Si reference cell (Newport).

5 HTMs based on star-shaped triarylamine molecules

5.1 Introduction

Small organic molecules and polymers semiconductors have both been widely used in optoelectronic devices. There are several advantages in using polymers over small organic molecules. One of the most important advantages is that usually polymers present high glass transition temperatures providing high morphology stability which result in more reproducible devices. Polymeric materials usually form smooth and uniform thin films which allow an easy control and low cost manufacture of large scale technologies. Because polymers can be designed to have high solubility, it is possible to used cheap deposition methods (such as spin-coating, doctor blading, screen printing) without sacrificing the quality of the film. Furthermore, the hydrophobic nature of polymeric materials serves as a protection for the perovskite film to humidity improving the stability of the solar cell.[221,230] Nevertheless, polymeric hole transport materials usually present lower efficiencies than their low molecular weight equivalents. Small molecules have a number of advantages over polymeric materials and generally present improvement in devices efficiencies. Small molecules have a uniform and well-defined composition and they are usually easy to purify by standard techniques (recrystallization, column chromatography, etc). In comparison to polymers, the synthesis of small molecules is highly reproducible and it is relatively easy to tune their properties by conventional molecular engineering. Although small molecules are usually soluble in common organic solvent, however these can significantly influence the packing in the thin-film. Therefore, one of the greatest challenges of small molecules is the stability and control of their morphology in the solid state[221].

One of the strategies to overcome the problems of both small molecules and polymers is the use of star-shaped molecules as HTM . The star-shaped molecules have a central

aromatic core with multiple "arm" functional units attached to the core. These molecules combine the best of both groups i.e. well-defined structures and physical properties, high thermal stability, good solubility and good film-forming properties.[230,231]

These materials have been widely used in organic field effect transistors[232] and organic light-emitting diodes[233] and more recently they have attracted attention as hole transporting materials in organic solar cells[234]. There are some star-shaped HTMs that have been used in perovskite solar cells (PSCs)[235–237]. Ko[236] and co-workers reported a hole transporting material with a planar central amine coded as OMeTPA-FA and compare this with the non-planar structure. The planar structure showed better charge-separation and higher hole mobilities which result in an overall power conversion efficiency in perovskite solar cells of 13.63%. More recently, Grätzel[237] and collaborators reported two new dopant-free star-shaped TPA-based hole transporting material for perovskite solar cells. However, these reports are limited especially for triphenylamine-based hole transport materials. Here we report new types of star-shaped TPA-based hole transporting materials for perovskite solar cells coded as STR1 and STR0. These molecules contain a central triarylamine unit and three TPA units in the peripheres linked with the core by an acetylene bridge. In STR0 we incorporate a partially bridged triphenylamine in the central unit of the star-shaped structure. These result in a quasi-planar structure, where the phenyl groups of the central TPA are constrained by two oxygen bridges. The chemical structures of STR1 and STR0 are illustrated in Figure 5.1. These structures have never been studied and to the best of our knowledge there are no reports of star-shaped TPA-based hole transporting materials containing oxygen bridged in the central core. Kaji[238] and colleagues studied the properties of partially oxygen-bridged triarylamine dimers as hole transport materials. These compounds formed an on-top π-stacking arrangement in their crystal structure which led to high carrier mobilities. Kuratsu[238–240] and co-workers reported the synthesis of 2,2′:6′,2″:6″,6-trioxytriphenylamine (label as TOT) and 2,2′:6′,2″-dioxytriphenylamine (label as DOT) and their magnetic properties. These reports inspired the design of STR0.

5.2 Results and Discussion

5.2.1 Synthesis

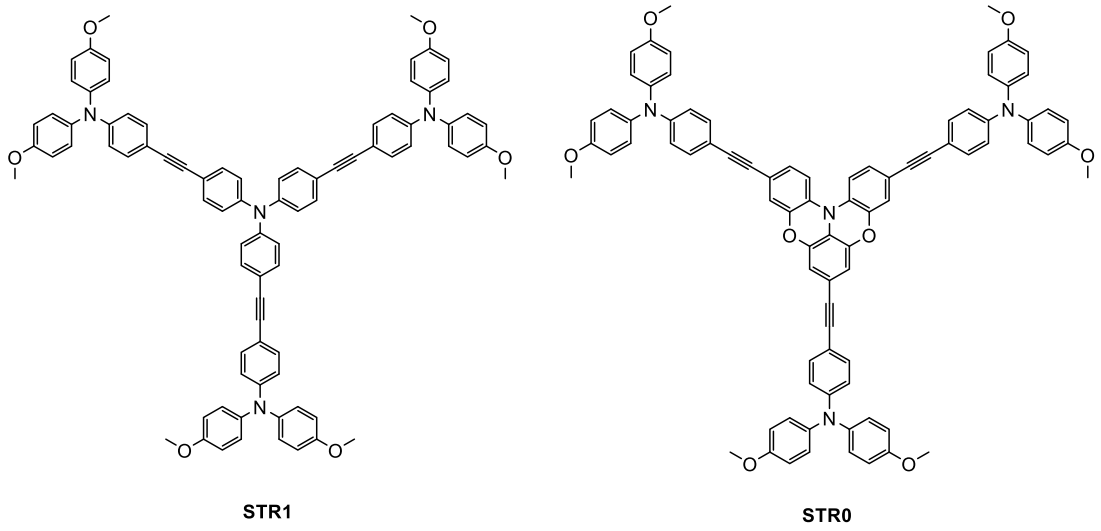

Figure 5.1 Chemical structure of HTMs used in this study.

The molecular structure of the two HTMs coded as STR1 and STR0 is illustrated in Figure 5.1. The synthesis of STR1 is outlined in Scheme 5.1. Triphenylamine (**1a**) was brominated with n-bromosuccinimide (NBS) in DMF to give **1**, followed by a Sonogashira coupling with **3** (4-ethynyl-N,N-bis(4-methoxyphenyl)aniline) to afford STR1. The synthesis of 4-ethynyl-N,N-bis(4-methoxyphenyl)aniline (**3**) illustrated in Scheme 5.1 is identical to the procedure described in Chapter 3. For the synthesis of STR0 (Scheme 5.2), 2,6-difluoronitrobenzene (**2b**) was first prepared by oxidation of 2,6-difluroaniline (**2a**) using sodium perborate tetrahydrate (PBS-4) in acetic acid. Compound **2c** was prepared by an aromatic nucleophilic substitution reaction of **2b** with 2-bromophenol. The reduction of the nitro group of **2c** using iron powder in acetic acid gave **2d** in good yield. The intramolecular cyclization of **2d** under Pd(0)-mediated cross-coupling was performed to yield **2e** in moderate yield which was later brominated using pyridinium tribromide to yield **2**. Finally a Sonogashira coupling reaction of **2** with **3** was performed to afford the final product **STR0.** The analytical and spectroscopic data of both HTMs are consisted with the formulated structures.

Scheme 5.1 Schematic diagram of the synthesis of the HTMs

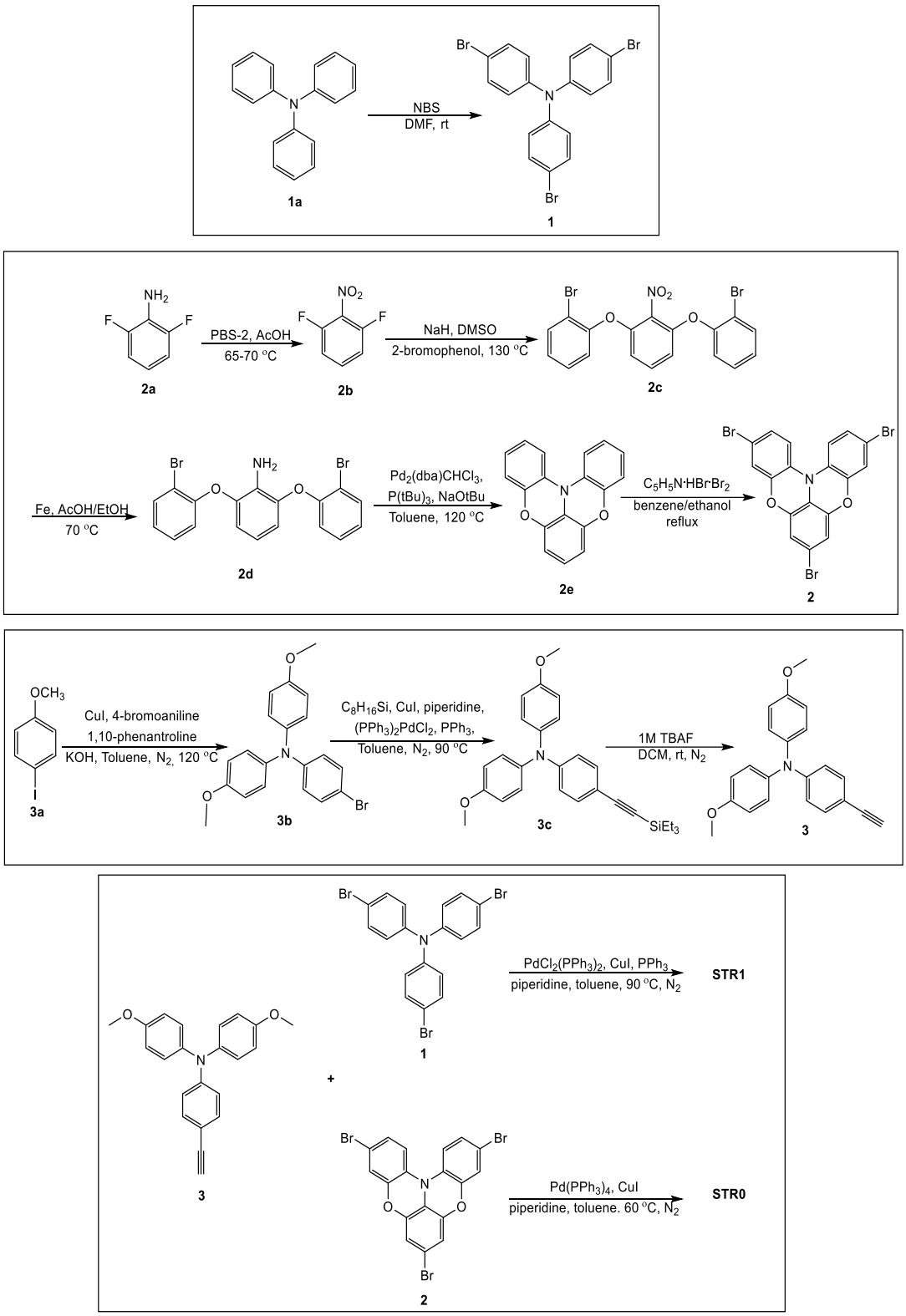

5.2.2 Optical and electrochemical properties

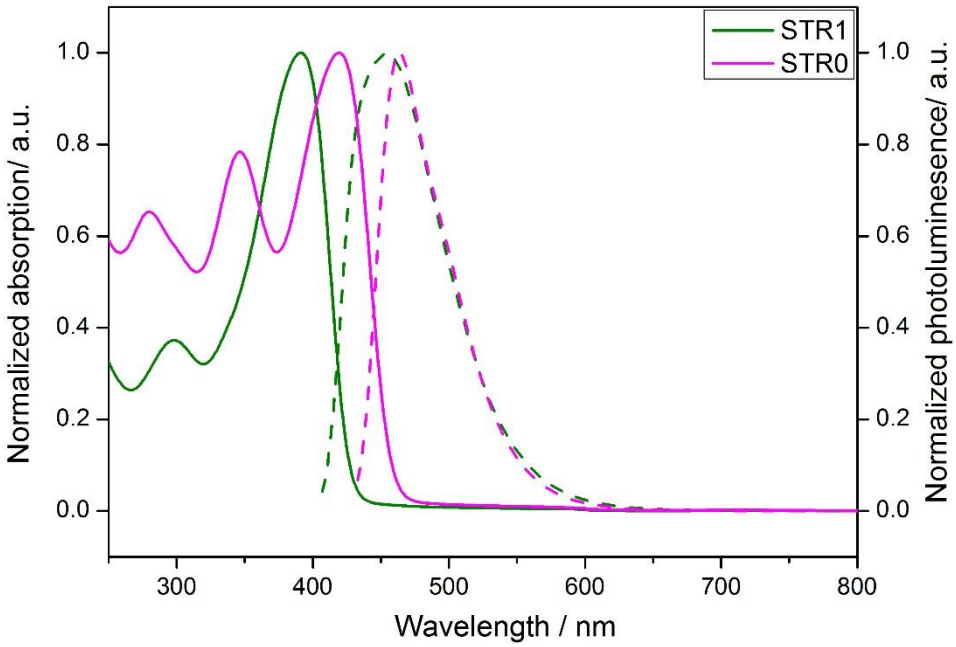

Figure 5.2 Normalized UV-Vis absorption (solid line) and emission (dashed line) of STR1 (green line) and STR0 (pink line).

The optical properties of the two HTM were investigated by UV/Vis and photoluminescence spectroscopy. The absorption and emission spectra of STR0 and STR1 were measured in dichloromethane. The spectra are shown in Figure 5.2. The absorption spectrum of STR1 exhibits an intense peak at 392 nm whereas STR0 shows a strong absorption band at 419 nm. The emission spectra of STR1 and STR0 show a similar red-shift from 454 nm for STR1 to 464 nm for STR0. Once the central unit is replaced for the bridge triphenylamine unit, there is a large red shift of 27 nm in the maximum wavelength for the absorption spectra and 10 nm in emission spectra. The red-shift of STR0 can be explained by the more planar configuration of the central triarylamine due to small torsion angle of the phenyl units and the more delocalized π-conjugation which reduce the energy gap between HOMO and LUMO. Additionally, molar extinction coefficients were calculated for each compound using the Lambert-Beer law and results are displayed in Table 5.1 at the end of the section.

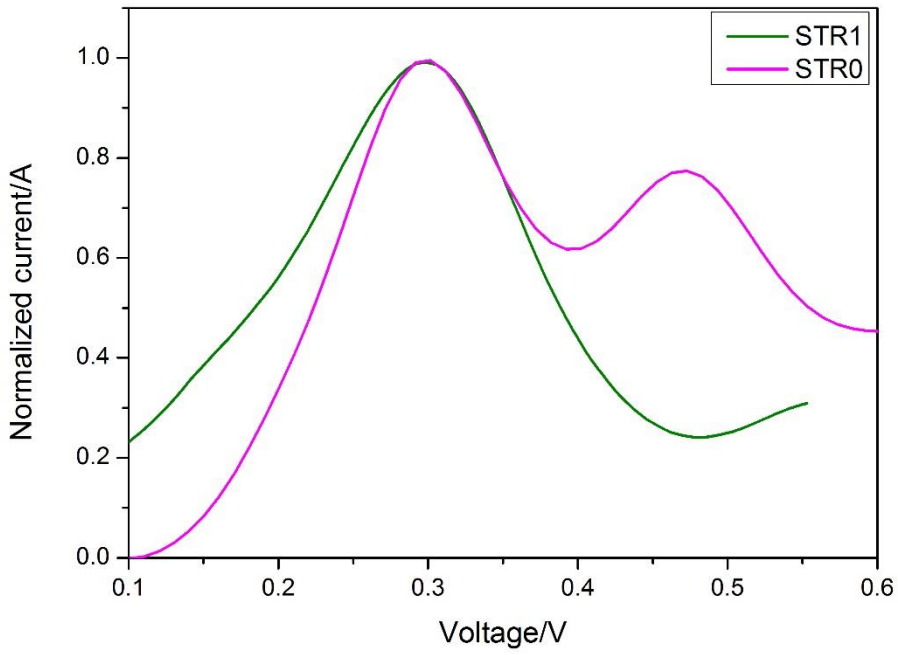

Figure 5.3 Square-wave voltammetry of STR1 (green line) and STR0 (pink line).

The HOMO energy levels were estimated experimentally from square-wave voltammetry (Figure 5.3) using ferrocene/ferrocenium as an internal standard. The results were calculated using the following equation E_{HOMO}= -5.1 –(E_{ox}), where E_{ox} is the oxidation potential of the HTM with reference to ferrocene. The results show that the HOMO energy levels of both HTM is at -5.40 eV which is slightly lower than spiro-OMeTAD (-5.13 eV). The oxidation potential of spiro-OMeTAD was obtained from a previous report in the Robertson group.[199] These outcomes indicate an energetically favourable hole transfer from the perovskite ($CH_3NH_3PbI_3$) to the HTM.

Density functional theory (DFT) method with the Gaussian 09[217] program at B3LYP/6-31G(d) level was used to predict the electronic properties of STR1 and STR0. The electron density of the optimized structures of the HOMO and LUMO energy levels are shown in Figure 5.4. The HOMO energy level determined by computational studies are similar for both hole-transport material. The HOMO is delocalized mainly over π orbitals of central triphenylamine core, the acetylene bridge

and the adjacent aromatic rings of the peripheral units. The LUMO is located over the part of two of the peripheral triphenylamine units and it is extended to part of the triphenylamine core. The calculated HOMO energy values of STR1 and STR0 are similar which coincides with the experimental results. (E_{HOMO}= -4.614 eV for STR0 and E_{HOMO}= -4.652 eV).

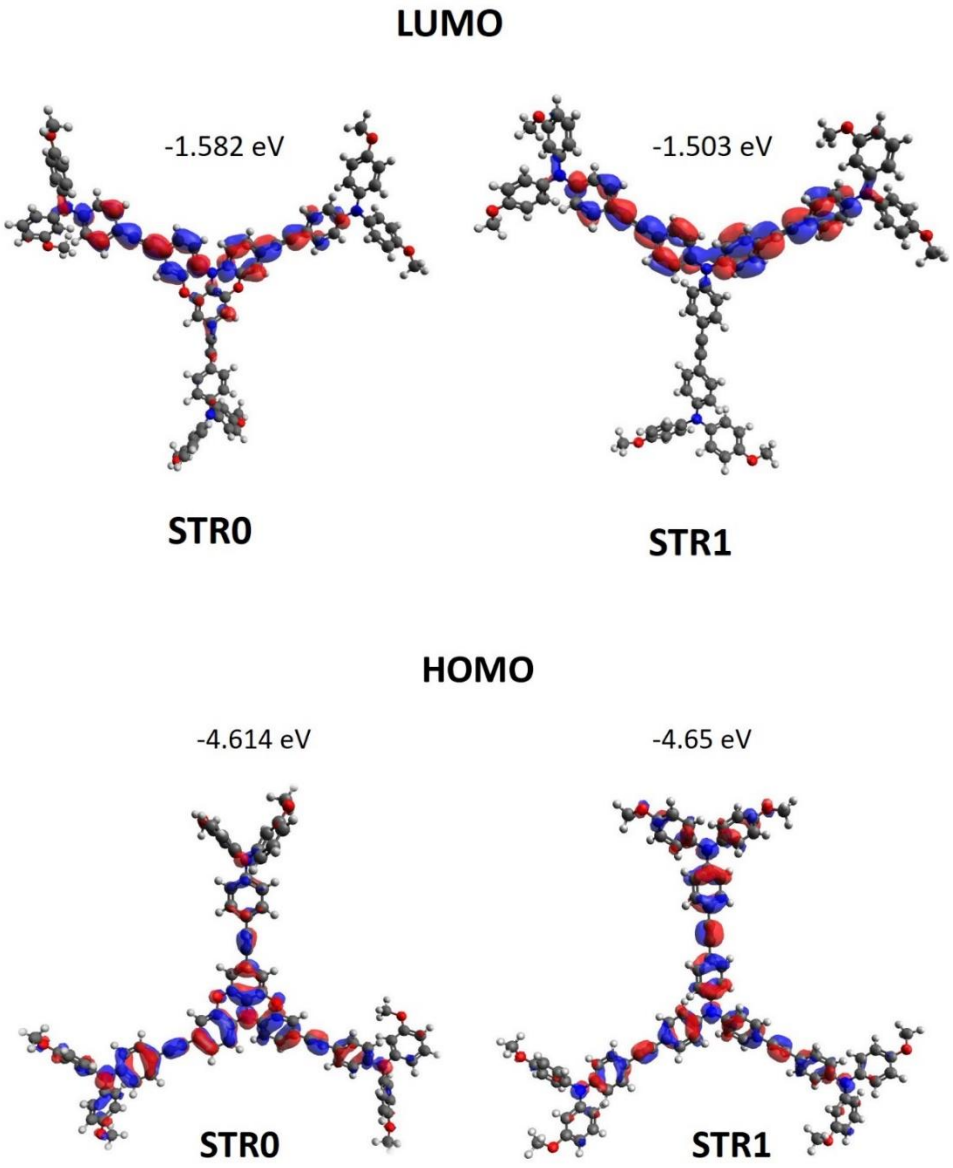

Figure 5.4 Molecular Orbital distribution of HOMO of STR1 and STR0 at B3LYP/6-31G(d)level of theory.

5.2.3 Hole Mobility

The hole mobilities were determined by fabricating organic field effect transistor (OFET) of STR1 and spiro-OMeTAD. It was not possible to obtain reliable results for STR0 due to the poor compatibility of STR0 in these type of devices. The hole mobilities were extracted from the saturation regime of the transfer characteristic curves (Figure 5.5). Details of the device fabrication and measurements are provided in the experimental section. The hole mobility of STR1 was found to be 7.13 x 10^{-5} cm^2/Vs at a constant drain-source voltage of -60 V. This value is significantly higher than that of pristine spiro-OMETAD (4.36 x 10^{-6} cm^2/Vs) under the same conditions.

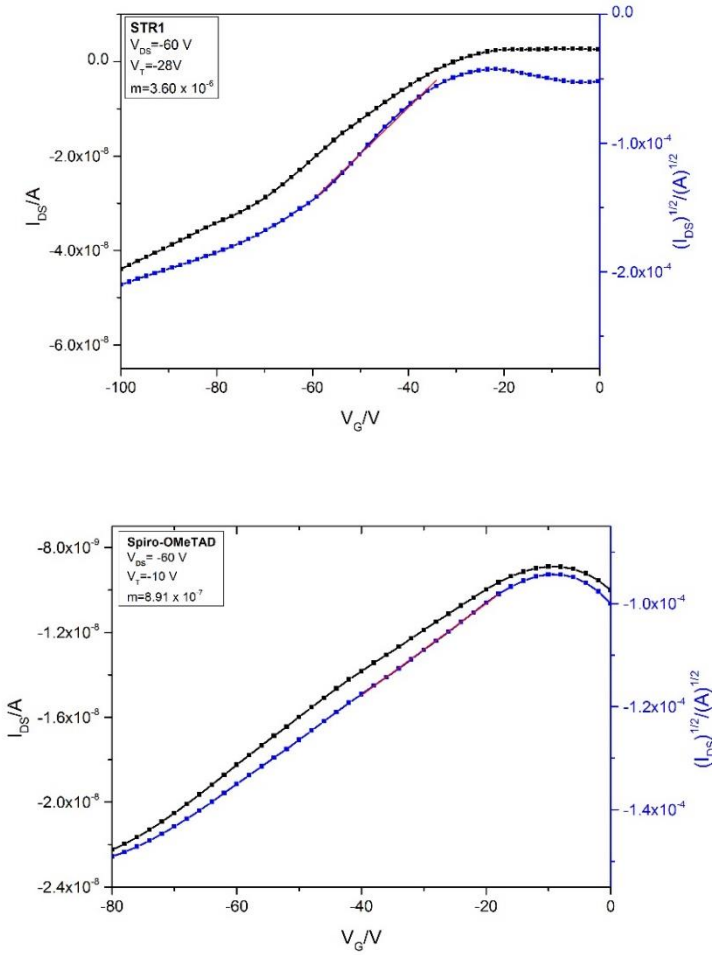

Figure 5.5 Transfer Characteristic Curves of STR1 and spiro-OMeTAD on a bottom gate/bottom contact organic field effect transistor.

5.2.4 Thermal properties

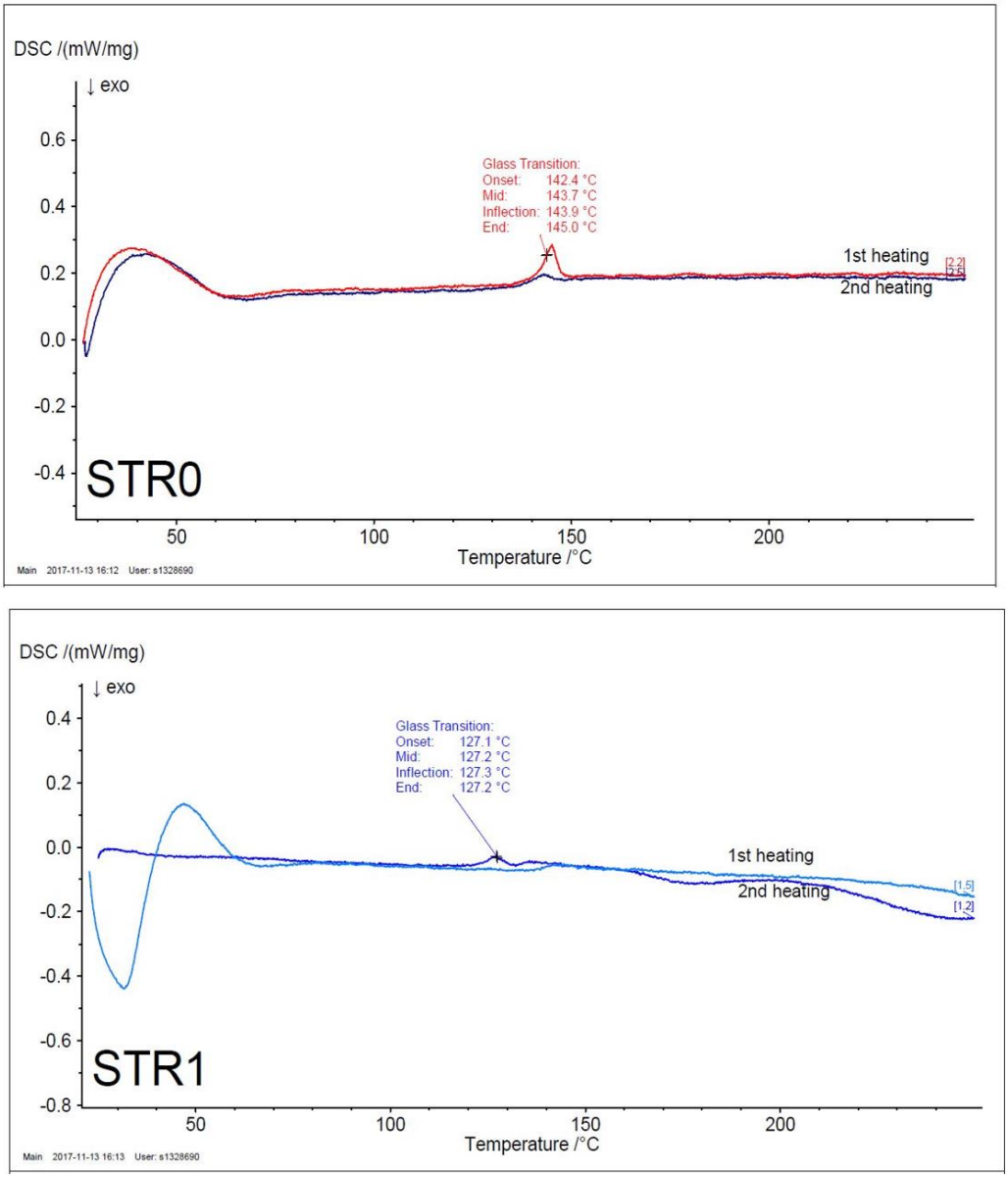

Figure 5.6 Differential scanning calorimetry curves.

Usually solar cells can work at temperatures of up to 80 ℃. The glass transition temperature (T_g) of STR1 estimated by differential scanning calorimetry (DSC) measurements is 127 ℃ suggesting good morphology stability. The result is depicted in Figure 5.6. A summary of the optical, electrochemical, charge transport and thermal properties of the HTMs are depicted in Table 5.1.

Table 5.1 Summary of the optical, electrochemical, charge transport and thermal propertoes of STR1 and STR0.

HTM	λ_{max} (nm)	ε (cm^{-1} M^{-1})	λ_{em*} (nm)[a]	E_{ox} (V)[b]	E_{HOMO} (eV)[c]	T_g (°C)[d]	Hole Mobility (cm^2/Vs)[e]
STR1	**391***	150000	454	0.30	-5.40	127	7.13×10^{-5}
STR0	347,**419***	97000	465	0.30	-5.40	x	x
Spiro-OMETAD	385					x	4.36×10^{-6}

[a]Excitation at λmax. [b]From SWV measurments and referenced to ferrocene. [c]E_{HOMO}(eV)=-5.1 $E_{ox.}$[213] [d]Determined from differential scanning calorimetry (DSC).[e]Estimated from OFET measurements.

5.2.5 Solar Cells Studies

To investigate the performance of STR0 and STR1 as hole transport materials, a set of perovskite solar cells were fabricated. The device architecture adopted in this study was FTO/bl-TiO_2/mp-TiO_2/$CH_3NH_3PbI_3$/HTM/Au. For comparative analysis, devices with spiro-OMeTAD as HTM were fabricated. The HTMs were doped using identical steps and similar concentrations of addives (Li-TFSI, 4-terbutylpyridine and FK209) For reliable comparative analysis, all devices were fabricated in a single continuous study over 8 repeat cells for STR1 and STR0 and 16 repeat devices for spiro-OMeTAD. Figure 5.7 show the photocurrent density-voltage (J-V) curves of the champion cells and Table 5.2 gives the corresponding photovoltaic parameters.

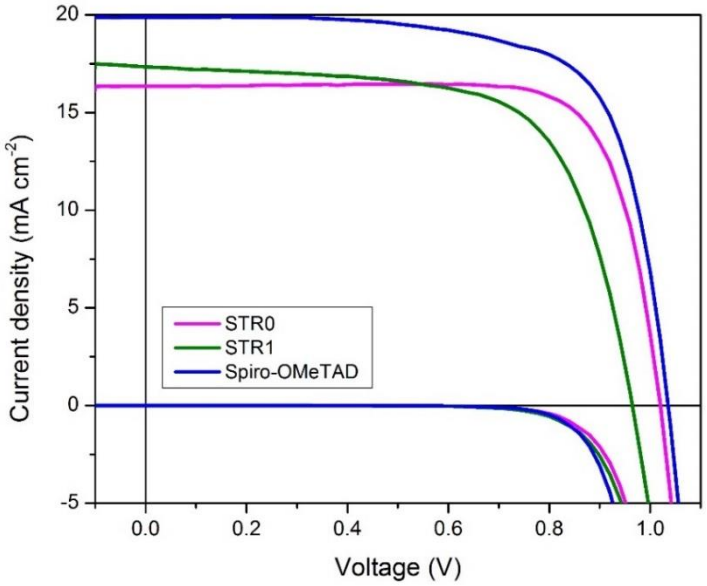

Figure 5.7 J–V curves of the champion PSCs with STR1, STR0 and Spiro-MeOTAD as HTMs.

The best cell of STR0 gave an open-circuit voltage (V_{oc}) of 1.02 V, a short-circuit current density (J_{sc}) of 16.35 mA cm^{-2} and a fill factor (FF) of 77.81%, affording a PCE of 13.32% under illumination. Under the same conditions the best STR1-based device gave V_{oc} of 0.95 V, J_{sc} of 17.35 mA cm^{-2} and FF of 66.90 %, yielding a PCE of 11.52 %. These results are comparable to the PCE pf 15.23% obtained with the best spiro-OMeTAD-based cell. Figure 5.8 shows the box plots with the mean and standard deviation of the solar cell parameters and the results are summarised in Table 5.3.

Table 5.2 Summary of the photovoltaic parameters of the champion cells.

HTM	PCE (%)	J_{sc} (mA cm^{-2})	V_{oc} (V)	FF (%)
STR0	13.32	16.35	1.02	77.81
STR0 no additives	3.98	16.00	0.93	26.03
STR1	11.52	17.35	0.95	66.90
STR1 no additives	0.64	5.31	0.82	14.27
Spiro-OMeTAD	15.23	19.88	1.03	71.96

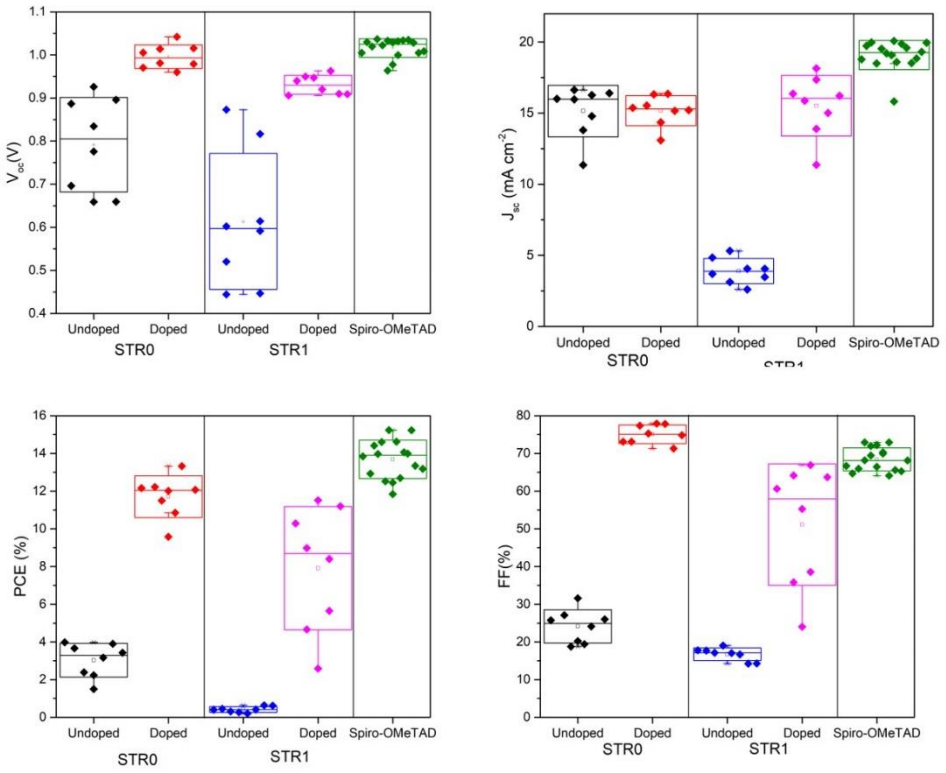

Figure 5.8 Box plot of photovoltaic parameters of PSCs with STR1, STR0 and spiro-OMeTAD measured just after fabrication.

Table 5.3 Summary of the solar cell parameters measured just after fabrication

HTM	PCE (%)	J_{sc} (mA cm^{-2})	V_{oc} (V)	FF (%)
STR0 No additives	3.02±0.90	15.12±1.79	0.82±0.10	22.77±3.33
STR0 additives	11.71±1.11	15.17±1.06	0.99±0.03	75.09±2.47
STR1 no additives	0.33±0.19	3.26±1.54	0.56±0.12	19.44±7.59
STR1 additives	7.91±3.27	15.53±2.13	0.93±0.02	51.13±16.08
Spiro-OMeTAD	13.68±1.02	19.09±1.03	1.02±0.02	68.42±3.04

Solar cells using STR1 and STR0 as HTM without dopants were fabricated for comparative analysis. The results are shown in the box plot (Figure 5.8) and in Table 5.3 the average values of the photovoltaic parameter along with their standard deviation are presented. Both HTMs present better device performance with the

additives. However, it was interesting to find that STR0-based cells afford a maximum PCE value of 4%, an impressive maximum J_{sc} of 16.63 mA cm^{-2} and a close distribution of the device parameters. The high values could be possible attributed to the reduced grain boundaries due to the good film forming properties of STR0. From the box plot it is possible to examine the reproducibility of the cells performance. The data indicate good device reproducibility in particular for STR0 and spiro-OMeTAD which show small standard deviation values in all the photovoltaic parameters. Despite offering similar V_{oc} and J_{sc}, the PCE values of STR1-based cells are lower than that of STR0 and Spiro-OMeTAD which can be attributed to the significant lower fill factor. On the other side it is important to note the high fill factor of the STR0-based cells which are considerably higher than that of spiro-OMeTAD. The fill factor is a parameter that measures the quality of the solar cells and high values usually indicate low series resistance, good interfacial morphology, high charge transport and uniform films[241,242]. These results suggest that STR0 form more homogenous films during the device fabrication. The close distribution of the J_{sc}, V_{oc} and PCE values gives also a hint of the good homogeneity of the films.

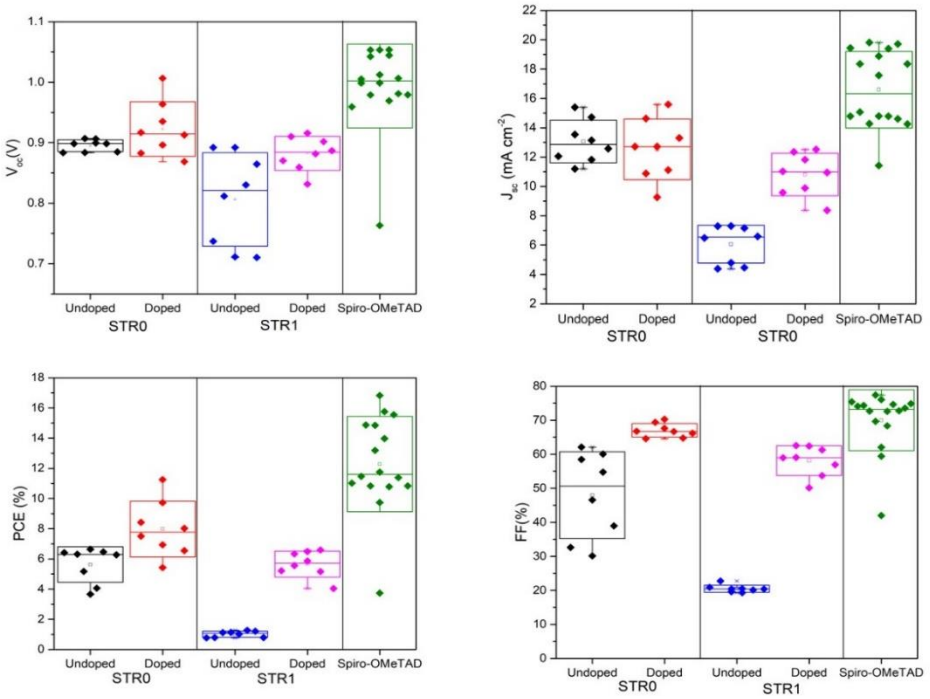

Figure 5.9 Box plot of photovoltaic parameters of PSCs with STR1,STR0 and spiro-OMeTAD after two weeks of storing.

To compare the stability of the STR0, STR1 and spiro-OMeTAD -based solar cells, the devices were tested after two weeks storing at room temperature without encapsulation. For better comparison the results are presented in the box plot (Figure 5.9) and the extracted average values with their standard deviations are presented in Table 5.4. The devices based on doped STR1 and STR0 showed a relatively small decrease of the photovoltaic parameters, however it is important to notice that the standard deviation did not significantly change. For spiro-OMeTAD a couple of the devices presented an improvement in the fill factor due to a slightly increase in the $J_{sc.}$ However, on average the device parameter for spiro-OMeTAD-based cells decrease. It is especially noticeable the lower reproducibility of the fill factor values and the increase of the standard deviation values.

For devices without additives, STR1 presented a slightly better efficiency due to an increase of both V_{oc} and J_{sc}. More important is to note that after two weeks storing, the devices based-on STR0 with no additives showed a significant improvement of the device performance, showing a maximum PCE value of 6.63% in comparison with their initial values (max PCE of 4%).

Table 5.4 Summary of the solar cell parameters measured after 2 weeks storing

HTM	PCE (%)	J_{sc} (mA cm^{-2})	V_{oc} (V)	FF (%)
STR0 No additives	5.62±1.17	13.06±1.45	0.90±0.01	47.97±12.76
STR0 additives	7.93±1.84	12.53±2.06	0.92±0.05	67.03±2.02
STR1 no additives	1.01±0.20	6.06±1.29	0.81±0.08	20.50±1.05
STR1 additives	5.66±0.86	10.81±1.45	0.88±0.03	58.14±4.37
Spiro-OMeTAD	12.28±3.10	16.59±2.6	0.99±0.07	70.01±8.93

These results are consistent with the studies reported previously. Hyeju Choi and collaborators[243] designed a star-shaped hole-transporting material with a planar amine named OMeTPA-FA and compare it with the non-planar structure. The planar triphenylamine demonstrated better charge-separation, higher hole mobility, superior photovoltaic performance in perovskite solar cells and better device stability which were similar to spiro-OMeTAD. The superior stability of the planar HTM over the non-planar analogue was attributed to the well packing structure on the $MAPbI_3$ due to its planar configuration.

5.3 Conclusions

In conclusion, we present the synthesis and characterisation of two novel star-shaped triphenylamine (TPA) based hole transporting materials STR1 and STR0 for application in perovskite solar cells. The structure contains a central TPA unit as core and three TPA units in the peripheral. The core unit in STR0 is an oxygen-bridged TPA. The optical, electrochemical, thermal properties and device performance of STR1, STR0 and Spiro-OMeTAD were compared. In presence of STR0 as HTM, a PCE of 13.32% was achieved which is comparable to that devices based on the well-known doped spiro-OMeTAD (15.23%). After two weeks of storing, it was interesting to find that although the average photovoltaic performance of STR1 and STR0 decrease, the distribution of the device parameters were consistent in comparison with spiro-OMeTAD where a significant increase in the standard deviation of the fill factor were found. Furthermore, it is also important to notice the high photocurrent density found for the STR0-based solar cells without additives and the improvement of the device parameters after two weeks of storing. From this study, it was found that STR0 showed superior device parameters than STR1 and better reproducibility and stability than spiro-OMeTAD. STR0 showed higher fill factor and smaller standard deviations in the power conversion efficiency and fill factor data after two weeks of storing which is mainly due to the better and more stable amorphous resulting in a more homogeneous film sustain by its higher glass transition temperature (145 ℃) presented previously.

5.4 Experimental details

5.4.1 Chemical characterization

^{1}H and ^{13}C NMR spectra were recorded on a Brucker Advance 500 spectrometer (500 MHz and 124 MHz). The deuterated solvents are indicated in the synthesis description. MS were recorded on Bruker ESI Micro-Tof equipped with LC using electrospray ionization (ESI). Elemental analyses were carried out by Stephen Boyer at London Metropolitan University.

5.4.2 Synthesis

Materials and Synthesis

All reagents were purchased from either Sigma-Aldrich or Alfa-Aesar, and they were used as received without further purification unless otherwise stated.

Tris (4-bromophenyl) amine To a solution of triphenylamine (2g, 8.16 mmol) in DMF (15 mL), NBS (4.64g, 26.11 mmol) in DMF (10 mL) was added drop-wise at 0℃ and the mixture was stirred for 12 hrs at room temperature. 10 mL of distilled water was added to the reaction mixture, which was extracted with dichloromethane. The organic layer was washed with 10 % solution of $Na_2S_2O_3$ and 5 % solution of KOH, dried over anhydrous $MgSO_4$ and the solvent evaporated under vacuum. The crude was purified by column chromatography (SiO_2, hexanes/DCM 90/10) to afford the product as white powder. ^{1}H NMR (500 MHz, chloroform-*d*) δ 7.40 – 7.36 (m, 6H), 6.97 – 6.93 (m, 6H).

4-Bromo-N,N-bis(4-methoxyphenyl)aniline A mixture of 4-bromoaniline (58.13 mmol, 10 g), 1-iodo-4-methoxybenzene (145 mmol, 34g), 1,10-phenantroline (11.63 mmol, 2.1g) in toluene (200 mL) was heated and stirred under nitrogen atmosphere. CuI (11.63 mmol, 2.21g) and KOH (465 mmol, 26g) were added quickly at 110 ℃. The mixture was stirred for 12 hrs at 135 ℃ under N_2 atmosphere. The cooled reaction was washed with 5% solution of HCl and 5% solution of KOH, dried over $MgSO_4$ and solvent evaporated under vacuum. The crude was passed through a quick silica plug

in DCM and the product purified by column chromatography (SiO_2, hexanes/DCM from 100 to 80: 20) to obtain a white powder (12g, 55%). ^{1}H NMR (500 MHz, benzene-d_6) δ 7.19 – 7.16 (m, 2H), 6.97 – 6.93 (m, 4H), 6.77 – 6.73 (m, 2H), 6.70 – 6.66 (m, 4H), 3.29 (s, 6H).

4-Methoxy-N-(4-methoxyphenyl)-N-(4-((triethyllsilyl)ethynyl)phenyl)aniline 4-bromo-N-N-bis(4-methoxyphenyl)aniline (31.25 mmol, 12g), $(PPh_3)_2PdCl_2$ (1.56 mmol, 1.1g), CuI (6.25 mmol, 1.2g), PPh_3 (2.5 mmol, 0.66g) were added into a rount bottom flask and dried under vacuum for 30 minutes. At the same time, a solution of piperidine (250 mmol, 25 mL) and triethylsilylacetylene (56 mmol, 10 mL) in toluene (200 mL) were stirred and degassed for 30 minutes, added to the first mixture and the mixture stirred at 100 ℃ for 12 hrs under nitrogen atmosphere. The reactions was stopped by the addition of 50 mL of NH_4Cl and washed with a 10% solution HCl and 10% solution KOH. The crude was passed through a quick silica plug in DCM and the product purified by column chromatography(SiO_2, hexane/DCM from 100 to 70:30) to obtain a orange oil (13 g, 93%).^{1}H NMR (500 MHz, benzene-d_6) δ 7.44 – 7.40 (m, 2H), 6.98 – 6.94 (m, 4H), 6.89 – 6.85 (m, 2H), 6.68 – 6.64 (m, 4H), 3.27 (s, 6H), 1.14 (t, J = 7.9 Hz, 9H), 0.72 (q, J = 7.9 Hz, 6H).

4-Ethynyl-N,N-bis(4-methoxyphenyl)aniline A mixture of 4-methoxy-N-(4-methoxyphenyl)-N-(4-((triethyllsilyl)ethynyl)phenyl)aniline (29.1 mmol, 12.91g) in DCM (150 mL) was stirred under nitrogen for 10 minutes. TBAF (44 mL) was added to the previous solution and the mixture was stirred for 3 hrs under nitrogen atmosphere. The reaction was stopped by the addition of a saturated solution of NH_4Cl and the organic phase was extracted with DCM and dried over $MgSO_4$. The crude was passed through a short silica plug and DCM and the solvent removed under nitrogen to obtained a white powder (8.91g, 93%).^{1}H NMR (500 MHz, Benzene-d_6) δ 7.38 – 7.34 (m, 2H), 6.99 – 6.91 (m, 4H), 6.86 – 6.83 (m, 2H), 6.69 – 6.65 (m, 4H), 3.28 (s, 6H), 2.77 (s, 1H).

STR1 A mixture of tris(4-bromophenyl)amine (2.07 mmol, 1 g), $(PPh_3)_2PdCl_2$ (0.456 mmol, 0.29 g), CuI (0.09 mmol, 16 mg), PPh_3 (0.414 mmol, 0.108 g) and piperidine (30 mL) in toluene (20 mL) were stirred and degassed for one hour. A degassed solution of 4-ethynyl-N,N-bis(4-methoxyphenyl)aniline was added drop-wise over 5 hours at 100 ℃ under nitrogen atmosphere and the mixture stirred for 12 under the same conditions. The reaction was stopped by the addition 20 mL of NH_4Cl and washed with a 10% solution HCl and 10% solution KOH. The crude was passed through a quick silica plug in DCM and the product purified by column chromatography (SiO_2, Hex/DCM from 100 to 20:80) to obtain a yellow powder (0.85 34 %). ^{1}H NMR (500 MHz, Benzene-d_6) δ 7.53 – 7.49 (m, 6H), 7.41 – 7.38 (m, 6H), 7.03 – 6.98 (m, 12H), 6.98 – 6.94 (m, 6H), 6.82 – 6.78 (m, 6H), 6.70 – 6.67 (m, 12H), 3.28 (s, 18H). ^{13}C NMR (126 MHz, Benzene-d_6) δ 156.55, 148.89, 146.37, 140.37, 132.60, 127.97, 127.07, 127.57, 124.01, 119.61, 118.75, 114.87, 90.37, 88.66, 54.66. MS EI (m/z): [M]+ 1227.46. Anal. Calcd for $C_{84}H_{66}N_4O_6$: C: 82.20; H: 5.42; N: 4.56 analysed C: 82.12; H: 5.37; N: 4.63.

1,3-Difluoro-2-nitrobenzene was synthesised on large scale by Yaroslav Zems from the Robertson group. Sodium perborate tetrahydrate (3.90 mol, 600 g) and glacial acetic acid (4500 mL) were added to a 10000 mL flask equipped with a magnetic stir bar. The suspension was stirred vigorously and slowly (over 3 hours) brought to 65 ℃. The mixture became clearer until the contents of the flask were completely transparent. A solution of 2,6-difrluoroaniline (0.774 mol, 100 g) in glacial acetic acid (500 mL) was added dropwise to the solution over 4 hours. The contents were brought to 70℃ and stirred for an additional 2 hours. The flask was brought back to room temperature and was allowed to stand overnight. The cooled reaction was filtered over Celite 545 (1 inch) to remove borate and unreacted perborate. The solvent was removed under reduced pressure (approx. 4L) and the rest was poured onto 3L of deionized water and extracted with diethyl ether (4 X 500 mL). The solvent was once again removed under reduced pressure and the residual oil re-dissolved in DCM (400 mL), dried over sodium sulphate (50 g). The whole mixture was filtered over Celite 545 (2 inch) and the solvent removed under reduced pressure to yield a brown/dark yellow oil which

was fractionally distilled (76 ℃, 756 microns) to afford a bright yellow oil which solidifies in the receiving flask into a bright yellow/white solid (86 g, 70%). ^{1}H NMR (500 MHz, Methylene Chloride-d_2) δ 7.56(tt, J=8.7, 5.9 Hz, 1H), 7.18-7.09(m, 2H). ^{13}C NMR (126 MHz, Methylene Chloride-d_2) δ 156.32, 156.30, 154.25, 154.23, 134.01, 133.93, 133.85, 113.71, 113.68, 113.56, 113.52, 54.43, 54.22, 54.00, 53.78, 54.57).

2,6-Bis(2-bromophenoxy)nitrobenzene NaH (223 mmol, 9 g, 60% in oil) was weighted directly in a round bottom flask and dried under vacuum for 30 min. Dry DMSO (160 mL) was added to the previous flask and the solution were heated at 66℃ for 1 hour under nitrogen. 2-bromophenol (22 mL, 203 mmol) was added to the NaH solution with a syringe and the mixture heated for 1 hour at the same temperature. After cooling to room temperature, 2,6-difluoronitrobenzene (14 g, 88 mmol) was added and the reaction was heated at 130 C for 3 hours under nitrogen. The cooled mixture was poured in a saturated solution of ammonium chloride and mixture extracted with dichloromethane. The organic phase was dried over sodium sulphate, filtered and the solvent remove under reduced pressure. The crude solid was recrystallized in ethanol to obtain the product as white crystals (22 g, 55%).^{1}H NMR (500 MHz, Benzene-d_6) δ 7.22 (dd, J = 8.0, 1.5 Hz, 2H), 6.70 – 6.62 (m, 4H), 6.49 (ddd, J = 8.0, 7.2, 1.7 Hz, 2H), 6.41 (t, J = 8.5 Hz, 1H), 5.98 (d, J = 8.5 Hz, 2H). ^{13}C NMR (126 MHz, Chloroform-d) δ 151.67, 149.97, 134.19, 133.88, 130.92, 129.03, 126.91, 122.22, 115.73, 110.94.

2,6-Bis(2-bromophenoxy)aniline A solution of 2,6-bis(2-bromophenoxy)nitro-benzene (26.8 mmol, 12.5 g) in glacial acetic acid (250 mL) and ethanol (250 mL) was added Fe powder (140 mmol, 7.7 g) at 0℃. The reaction was allowed to stir at 70℃ for 2 hrs. The reaction was concentrated under reduced pressured and the resulting material was diluted in distillate water and washed with a saturated solution of $NaHCO_3$ until the pH was basic. The mixture was extracted with ethyl acetate (3x300 mL), dried over $MgSO_4$ and the solvent removed under reduce pressure to give an oily product (10.57 g, 90%).^{1}H NMR (500 MHz, Chloroform-d) δ 7.65 (dd, J = 7.9,

1.6 Hz, 2H), 7.29 – 7.26 (m, 2H), 7.02 (td, J = 7.7, 1.5 Hz, 2H), 6.97 (dd, J = 8.2, 1.5 Hz, 2H), 6.66 (d, J = 3.8 Hz, 3H), 4.06 (s, 2H). ^{13}C NMR (126 MHz, Chloroform-d) δ 153.62 , 144.11 , 133.77 , 130.77 , 128.68 , 124.59 , 118.59 , 116.98 , 114.96 , 113.61.

2,2':6'2''-Dioxytriphenylamine A mixture of tris(dibenzylideneacetone)dipalladium (0.262 mmol, 0.272 g), sodium t-butoxide (34.5 mmol, 3.31 g), tri-t-butylphosphine (1.15 mmol, 1.2 mL 0.1 M solution in toluene) and toluene (30 mL) was stirred under nitrogen atmosphere for 60 minutes. A solution of 2,6-bis(2-bromophenoxy)aniline (11.5 mmol, 10 g) in toluene (30 mL) was degassed and added to the previous solution. The reaction was stirred for 12 hrs at 120 ℃ under nitrogen atmosphere. The cooled reaction was passed through Celite 545 (1 inch) and a short silica plug using dichloromethane. The crude was recrystallized in hexane/DCM to afford a pale yellow powder.

Tris-4-bromo(2,2':6'2''-dioxytriphenylamine) Dioxytriphenylamine (0.94 g, 3.44 mmol) was dissolved in a mixed solvent of benzene (150 mL) and ETOH (100 mL) at refluxing temperature. Pyridinium bromide perbromide (33 g, 103 mmol) was added to the solution and the mixture was stirred for 3 hrs at refluxing temperature. During the first reaction a mixture of the tri-substitution and di-substitution product was obtained, therefore the reaction was done again under the same conditions. The crude product was recrystalized in ethanol to obtained a white powder (1.3 g, 74%).^{1}H NMR (500 MHz, Benzene-d_6) δ 6.79 (d, J = 2.2 Hz, 2H), 6.67 (dd, J = 8.6, 2.2 Hz, 2H), 6.40 (s, 1H), 6.36 (d, J = 8.6 Hz, 2H).

STR0 A mixture of tris-4-bromo(2,2':6'2''-dioxytriphenylamine (0.98 mmol, 0.5 g), $(PPh_3)_2PdCl_2$ (0.10 mmol, 72 mg), CuI(4 mg), 4-ethynyl-N,N-bis(4-methoxyphenyl)aniline (3.43 mmol, 1.98 g) and piperidine (30 mL) in toluene (20 mL) were degassed by freeze-pump thaw and mixture stirred for 72 hrs nitrogen atmosphere. The reaction was stopped by the addition 20 mL of NH_4Cl and the product extracted with DCM. The crude was passed through a quick silica plug in DCM and the product purified by column chromatography (SiO_2, Hex/DCM from 50:50 to

10:90) to obtain a pale yellow powder (0.35g 28 %). ^{1}H NMR (500 MHz, Acetone-d6) δ 7.44 (d, J = 8.4 Hz, 2H), 7.34 – 7.30 (m, 6H), 7.19 (dd, J = 8.4, 1.9 Hz, 2H), 7.14 – 7.09 (m, 12H), 7.06 (d, J = 1.9 Hz, 2H), 6.98 – 6.93 (m, 12H), 6.81 – 6.77 (m, 6H), 6.71 (s, 2H), 3.81 (d, J = 0.8 Hz, 18H). MS EI (m/z): [M]+ 1255.46. Anal. Calcd for $C_{84}H_{62}N_4O_8$: C. 80.36; H: 4.98; N. 4.46 analysed C, 80.27; H, 4.95; N, 4.56.

5.4.3 Optical characterization

Solution UV-Visible absorption spectra were recorded using a Jasco V-670 UV/Vis/NIR spectrometer controlled with SpectraManager software. Photoluminescence (PL) spectra were recorded with a Fluoromax-3 fluorimeter controlled by ISAMain software. All samples were measured in a 1 cm cell at room temperature in dichloromethane as solvent.

5.4.4 Electrochemical characterization

All square-wave voltammetry measurements were carried out in freshly distilled CH_2Cl_2 using 0.3 M [TBA][BF_4] electrolyte in a three-electrode system with each solution being purged with N_2 prior to measurement. The working electrode was a Pt disk, the reference electrode was Ag/AgCl, and the counter electrode was a Pt rod. All measurements were made at room temperature using a μUTOLAB Type III potentiostat, driven by the electrochemical software GPES. Ferrocene was used as the internal standard in each measurement.

5.4.5 Thermal characterization

Differential scanning calorimetry (DSC) was performed on NETZSCH STA 449F1 at a scan rate of 5 K min $^{-1}$ under a nitrogen atmosphere in DSC/TG aluminium pan. The measurement range was 25 ℃ to 250 ℃.

5.4.6 Computational details

All calculations were carried out using the Gaussian 09[217] program with Lee Yang–Parr correlation functional (B3LYP) level of theory. All atoms were described by the

6-31G(d) basis set. All structures were input and processed through the Avogadro[218] software package.

5.4.7 Organic Field-Effect Transistors

The Ossila low-density Pre-fabricated substrates (channel length 0.1 mm width 0.03 mm) with a bottom gate/bottom contact were used to fabricate OFET devices. The substrates were treated with HMDS (Hexamethyldisilazane) to optimise the silicon surface property. A solution of the STR1 (10 mg/mL) in chloroform was stirred at room temperature. The Ossila substrate was covered with the solution by drop-casting. The electric characteristics of the fabricated OFETs were measured using a Keithley 2612A System SourceMeter. Mobilities were calculated using the following equation:

$$\mu_{FE} = \left(\frac{\sqrt{\partial I_{DS}}}{\partial V_G}\right)^2 \cdot \left(\frac{2L}{WC_i}\right)$$

Where Z is the channel width, L the channel length, C_i the capacitance, V_G the gate voltage and I_{DS} is the drain current and $\sqrt{\partial I_{DS}}/\partial V_G$, the slope of the Transfer Characteristic Curves in the saturation regime.[215,216]

5.4.8 Perovskite Solar Cells and Characterisation

Perovskite solar cells were fabricated by Dr. Joel Troughton at Swansea University. Etched FTO glass substrates (NSG Pilkington, TEC7) were cleaned sequentially in detergent, deionised water, acetone and ethanol before undergoing 10 minutes of O_2 plasma treatment. A compact TiO_2 layer was deposited on the glass substrates through spray pyrolysis of a solution of titanium diisopropoxide bis(acetylacetonate) (0.2M in isopropanol) at 450 ℃. Upon cooling, a mesoporous layer of TiO_2 nanoparticles was spin-coated from a 2:7wt suspension of Dyesol 30NR-D paste in ethanol (4500 rpm for 30 seconds), followed by sintering at 550 ℃ for 30 minutes. A $CH_3NH_3PbI_3$ perovskite precursor solution was prepared by dissolving 576 mg PbI_2, and 199 mg CH_3NH_3I in a 4:1 vol solution of DMF:DMSO. The perovskite precursor solution (100 μL) was deposited onto the TiO_2 films and spin-coated at 4000 rpm for 30 seconds, with 200 μL of ethyl acetate dripped onto the spinning substrate

10 seconds prior to the end of the spin-coating process. Perovskite films were annealed at 100 ℃ for 10 minutes. A solution in dichlorobenzene for each HTM was prepared with dopants including bis(trifluoromethylsulfonyl)imide lithium salt (Li-TFSI) (20 μL/mL of a 520 mg/mL solution in acetonitrile), 4-tert-butylpyridine (tBP, 30 μL/mL) and tris(2-(1H-pyrazol-1-yl)-4-tertbutylpyridine)-cobalt(III) tris(bis(trifluoromethylsulfonyl)imide) (FK209, μL/mL of a 300 mg/mL solution in acetonitrile). The HTM solution was spin-coated onto perovskite films at 4000 rpm for 30 seconds before 80 nm thick Au contacts were thermally evaporated onto devices. Current-voltage measurements were performed using a AAA-rated solar simulator (Oriel Sol3A) calibrated against a KG5-filtered reference diode (Oriel 91150-KG5). Solar cells were masked to 0.1 cm^2 and scanned both from forward to reverse bias and vice versa at 100 mV/s.

6 Conclusions

Since their emergence in 2013, organic-inorganic perovskite solar cells have reached impressive efficiencies exceeding 22% making them the rising star in the photovoltaic field and creating an enormous interest to the academic community. Such rapid development of this technology over a short period has been possible due to the knowledge and experience from previous research in dye-sensitised solar cells (DSSC), organic photovoltaic (OPCs), light emitting diodes (OLEDs) and other related fields but also due to the unique properties of the perovskite materials, including high panchromatic absorption, large carrier diffusion length and low non-radiative recombination. Nevertheless, despite offering high efficiencies, perovskite solar cells suffer from stability, reproducibility and durability problems. One promising approach to solve these issues is by modifying the hole transporting material.

Triphenylamine derivatives have been widely used as hole transporting materials due to their physical and electrochemical properties. To investigate the influence of HTMs on PSCs three different types of triphenylamine-based HTMs have been studied, namely small molecules, polymer and star-shaped molecules. These novel hole transporting materials were fully characterised through thermal, electrochemical, spectroscopic and computational techniques, showing suitable properties for application in perovskite solar cells.

A new series of diacetylenetriphenylamine (DATPA) derivatives with five different alkyl chains in the para position (MeO, EtO, ^{n}PrO, ^{i}PrO and BuO) were used as HTMs in perovskite solar cells (Chapter 3). The length of the alkyl chain did not modify the HOMO levels but it strongly impacted on the hole transport properties as well as the morphology and device performance in perovskite solar cells. Shorter alkyl chains showed more ordered and compact structure which resulted in higher charge transport and better device performance. It was found that the molecule with the methoxy substituent gave the best semiconductive properties in comparison with the longer aliphatic chain, affording a PCE of 5.63%.

Two monomers (M:OO and M:ON) and their corresponding side-chain polymers (P:OO and P:ON) containing styrene units were studied as hole transporting materials in perovskite solar cells and compared in terms of their structure (Chapter 4). The polymers formed more stable amorphous glassy states and showed higher thermal stability than the monomers. Power conversion efficiencies of 7.48% for M:OO, 5.14% for P:OO, 5.28% for P:ON and 3.52 for M:ON were obtained. Despite the lower efficiencies, the polymers showed superior reproducibility in comparison with Spiro-OMeTAD and the monomers.

Two star-shaped triphenylamine-based molecules (STR1 and STR0) were used as hole transport materials in PSCs. These materials presented higher power conversion efficiencies in comparison with the small molecules and polymers in the previous sections. When STR0 was used as the HTM a PCE of 13.32% was obtained which is comparable to the devices based on spiro-OMeTAD. Furthermore, these materials also showed good reproducibility and stability in the devices.

In total this work provides three series of triarylamine-based hole transport materials for perovskite solar cell application and enables a comparison of the pros and cons of different design structures: small-molecule, polymeric and star-shaped. Although, the small molecules presented the highest device performance in comparison with polymers, the reproducibility and stability of the devices were very poor. Polymers on the other hand showed high reproducibility but low device efficiencies. Device performance, reproducibility and stability are important for commercialisation purposes. Therefore, we approached these issues by designing star-shaped molecules which combine the advantages of both groups of small molecules and polymers. The star-shaped molecules presented the best properties for an ideal hole transport material affording a PCE of 13.63% and high reproducible and stable devices. These outcomes are significant for the future design of organic semiconductors for photovoltaic applications.

Appendix

A.1 Computational Studies

Computational calculations can be employed to support the experimental data and improve our understanding of the system under investigation. They can also be used to predict the properties of new material and in the design of novel systems. In the case of hole-transport-materials for perovskite solar cells, computational calculations were performed to approximate the energy values and distribution of the highest occupied molecular orbital (HOMO) and the lowest unoccupied molecular orbital (LUMO).

The methodology used in this work is *ab initio* molecular theory which is a quantum mechanics approach. The energy and other related properties of a molecule that do not change with time can be calculated by solving the time independent Schrödinger (Equation 2.10)

$$\hat{\mathrm{H}}\Psi = E\Psi \qquad \textbf{Equation A.1}$$

Where Ψ is the wavefunction. The wavefunction is a function of the positions of all fundamental particles in the system. E (scalar) is the total energy of the system. The Hamiltonian $\hat{\mathrm{H}}$ is an operator that comprises all the terms that contribute to the energy of a given system[244,245].

$$\hat{\mathrm{H}} = \hat{T}_e + \hat{T}_n + \hat{V}_{nn} + \hat{V}_{ne} + \hat{V}_{ee} \qquad \textbf{Equation A.2}$$

Where $\hat{T}_i$ and $\hat{V}_{ij}$ are the corresponding kinetic and potential energy operators, *n* denoted nuclei and *e* denotes electrons. Nevertheless, the exact solution of the Schrödinger equation can only be solved for the hydrogen atom and it is impossible to extend for systems with more than one electron. For this reason, a series of mathematical approximations have been adopted to compute solutions of the Schrödinger equation that are commonly described as *ab initio* methods.

The Hamiltonian (Equation 2.11) contains the nuclear and electronic correlation terms implying that particles are not moving independently of all the others. The Born-Oppenheimer[246] approximation is the assumption that the nuclear and electronic motions can be separated (Equation 2.12).

$$\Psi_{Total} = \Psi_{electronic} \cdot \Psi_{nuclear} \qquad \textbf{Equation A.3}$$

This approximation is reasonable because the mass of a typical nucleus is about 2000 times that of an electron and therefore moves much slowly with respect to the electrons. The electrons respond instantaneously with respect to any motion of the nuclei. In other words the nuclei is fixed in reference to the electrons and the electronic motion is assumed to depend only on the position of the fixed nuclei. Therefore, for a given nuclear arrangement it is possible to neglect the nuclear kinetic energy term ($\hat{T}_n = 0$) and the internuclear attraction potential energy term is a constant ($\hat{V}_{nn} = constant$). The Hamiltonian can be reduced to an electronic Hamiltonian:

$$\hat{\mathrm{H}} = \hat{T}_e + \hat{V}_{ne} + \hat{V}_{ee} \qquad \textbf{Equation A.4}$$

By making this assumption the nuclear-electron potential energy can be calculated with relative ease as the electrons just see a fixed set of positive charges. Even with the Born-Oppenheimer approximation it is not possible to solve the Schrödinger equation for systems larger than H_2^+. This is because the electron-electron interactions are difficult to calculate. The electronic field of one electron will influence the position of a second and so on and both charge and spin need to be considered.[247]

One method used to deal with the electron-electron interactions is the Hartree-Fock (HF) theory. The HF theory reduces the multi-electron problem by ignoring instantaneous interaction of the electrons and assuming that each electron feels an average field of all the other electrons in the system. The electrons are then seen as separate entities which are described by individual one-electron wavefunctions and the overall energy term is assumed to be a sum of each individual wavefunction. The individual one-electron wavefunctions are called molecular orbitals. All electrons are characterised by a spin number (up or down) and so far this factor has been neglected. To take into account the spin of the electron and Pauli's exclusion principle (stating

that two electrons with identical spin cannot occupy the same orbital), a Fock operator is used instead of the Hamiltonian. The Fock operator comprises the one-electron Hamiltonian, an operator to take account of coulombic repulsions and a modification to the coulumbic repulsions to account for the Pauli exclusion principle. By considering this, a fairly good approximation of the total energy of the system can be calculated. Nevertheless, Hartree-Fock theory neglects electron correlation by considering that each electron feels an average electron density and completely ignores instantaneous interaction of electron pairs with opposite spin. These considerations cause the results to be less accurate for some systems.[247,248]

A.1.1 Density Functional Theory

Density Functional Theory (DFT) is one of the most popular methods in computational chemistry. In comparison with Hartree-Fock methods, in DFT there are less parameters to calculate because the electron density is a function of only three positional variables (x,y,z) and is independent of the number of electrons in the system whereas for the electronic wavefunction in the Hartree-Fock method the position of each electron has parameters associated with it. In principle DFT is similar to the *ab initio* methods. It requires to have individual equations for each electron using the so-called Kohn-Sham (KS) equations. The density then can be calculated in terms of a set of N non-interacting one-electron orbitals (Equation 2.14).[248,249]

$$\rho(r) = \sum_{i=1}^{n} |\Psi(r)|^2 \qquad \textbf{Equation A.5}$$

The energy of the system is given by the functional E(ρ):

$$E(\rho) = E_T + E_V + E_J + E_{XC} \qquad \textbf{Equation A.6}$$

Where E_T is the electronic kinetic energy term, E_V is the potential of the nuclear-electron attraction, E_J is the electron-electron repulsion term (Coulomb interaction) and E_{XC} is the exchange and correlation energy. The exact form of E_{XC} is unknown, therefore approximations must be used. The three approximations used are: Local Density Approximation (LDA), Generalised Gradient Approximation (GGA) and Hybrid Density Functional Theory. The LDA approximation assumes that the electron

density is constant at any given point and can be treated as a uniform electron gas. This approach is especially useful for metallic systems. An improvement to the LDA approximation is possible by taking into account the gradient of the electron density using the GGA calculations. Most GGA functionals contain a modified term which is added to the LDA functional. Hybrid DFT methods combine DFT and HF theory to compute the exact value of the electron-electron functional and approximate the electron correlation functional. By doing this, higher accuracy calculations can be obtained. In this work, calculations were carried out using an hybrid functional noted as B3LYP (Becke, three-parameter, Lee-Yang-Parr)[250] which is one of the most accurate functions for the study of organic compounds.[249,251,252]

For both DFT and HF methods, the equations are solved by an iterative procedure called the self-consistent field calculation (SCF). The idea is to start by proposing a set of trial wavefunctions (electron density) and from this to obtain a new set of wavefunctions (electron density). These new wavefunctions are then used in the next calculation and the process is repeated until the results converge and the energy is minimised.

As the nuclei are fixed, generally the wavefunction (Ψ) describe the spatial portion of the electrons. The wavefunction (Ψ) is defined by a basis set used to describe each atom. A basis set uses a linear combination of a series of functions (basis functions) to generate wavefunctions for molecular orbitals. Usually, a sum of Gaussian functions with varying exponents is used to define this basis set and approximate the atomic radial function[252].

$$\Psi = \sum_i C_i \, \varphi_i \qquad \textbf{Equation A.7}$$

In this case, solving complicated wavefunctions is not required and the calculations are simplified to find the best coefficients to describe the orbitals. Thus the values of the weighting coefficients are varied until the wavefunction generated minimises the energy of the given system. It is important to remember that basis sets are optimised for atoms not molecules. When an atom become part of a molecule, the size, charge, shape might change significantly. Therefore, it is important to add polarisation and

diffusion functions on the basis set noted as '*' and '+' respectively. Some popular basis sets include 3-21G*, 6-31G*, 6-311G*. The larger the basis sets (with higher numbers) are, the more accurate the calculations will be. Nevertheless, larger basis sets also require higher computational time and cost. The basis set used in this work was 6-31G*[253] which is a split-valence basis set where G stands for gaussian-type orbitals and a polarisation function is added, noted as '*'. The core and the valence electrons are modelled separately. One basis function consisting of six gaussian-type orbitals (GTOs) is used for the core and two basis functions (one comprising three GTO and the other one GTO) are employed for the valence electrons.[252,254]

A.1.2 Geometry optimisation and solvent effect

In a geometry optimisation calculation the structure of a molecular system is iteratively adjusted until a stationary point on the potential energy surface is found. A potential energy surface (PES) is a mathematical function that describes the energy of a molecular system in terms of its structure. Generally, the calculation of the entire potential energy surface is complicated as this would require immense computational time and cost. Therefore, the first derivative of the energy known as the gradient is calculated and when this value is zero it is identified as a stationary point (Equation 2.17). In other words, a point on the PES where the forces acting on the atoms are zero is called a stationary point.

$$\frac{dE}{dx} = kx \qquad \textbf{Equation A.8}$$

All successful geometry optimisations always reach a stationary point. Nevertheless, this might not always be the one we are looking for. This can be a minimum, a maximum or a saddle point. To determine if the structure is the minimum energy a frequency calculation is carried out after the structure is optimised. This is computed with the second derivative of the energy (Equation 2.18).

$$\frac{d^2E}{dx^2} = k \qquad \textbf{Equation A.9}$$

The minimum stationary points are of interest for the purpose of this work. A minimum on the PES can be characterised by curvatures that are all positives which means there are no negative frequencies (k positive).

All the experiments presented here were performed in a solvent (UV, electrochemistry, emission, etc). Therefore, in order to compare the computational calculation more accurately with the experimental results, the geometry was optimised in the presence of a solvent. This is achieved by using a polarizable continuum model (PCM) in the calculation. This method modelled the solvent as a medium with a constant dielectric constant rather than discrete molecules. The magnitude of the dielectric constant depends on the nature of the solvent[252,254].

All molecular structures were drawn using the software Avogadro to obtain the initial coordinates, and optimised under vacuum. Then the structures were optimised using a dichloromethane polarisable continuum model. All calculations were carried out using the Gaussian 09[217] program with Lee Yang–Parr correlation functional (B3LYP) level of theory. All atoms were described by the 6-31G(d) basis set. The molecular orbital isosurfaces were generated with the software Avogadro[218] which illustrates where the HOMO and LUMO are located on the molecule.

A.2 X-ray crystallographic data

Table A.1 Summary of X-ray crystallographic data for DATPA derivatives

	EtO-DATPA	**^{n}PrO-DATPA**	**^{i}PrO-DATPA**	**BuO-DATPA**
Formula	$C_{48}H_{44}N_2O_4$	$C_{52}H_{52}N_2O_4$	$C_{52}H_{52}N_2O_4$	$C_{56}H_{60}N_2O_4$
$D_{calc.}$/ g cm^{-3}	1.233	1.228	1.154	1.181
μ/mm^{-1}	0.078	0.077	0.072	0.572
Formula Weight	712.85	768.95	768.95	825.06
Colour, shape	Yellow,block	yellow	orange	orange
Shape	block	plate	block	block
Max Size/mm	0.24	0.55×0.29×0.09	0.51	0.25
Mid Size/mm	0.16		0.23	0.24
Min Size/mm	0.14		0.10	0.14
T/K	120.0	120.0	120.0	120.0
Crystal System	monoclinic	monoclinic	triclinic	monoclinic
Space Group	$P2_1/n$	$P2_1/n$	P-1	$P2_1/c$
a/Å	9.8398(3)	12.0510(4)	12.4603(2)	11.82431(7)
b/Å	18.2197(5)	10.2594(3)	14.8711(4)	13.11889(7)
c/Å	10.8932(3)	17.3214(5	24.3863(6)	14.97854(9)
α/°	90	90	100.569(2)	90
β/°	100.468(3)	103.750(3)	90.6323(17)	93.5009(5)
γ/°	90	90	94.7035(18)	90
V/Å^3	1920.41(10)	2080.17(12)	4425.56(18)	2319.16(2)
Z	2	2	4	2
Z'	0.5	0.5	2	0.5
Θ_{min}/°	3.071	0.71073	2.992	3.745
Θ_{max}/°	29.756	MoK$_\alpha$	28.282	76.172
Measured Refl.	34735	43687	88294	56181
Independent Refl.	5021	4742	21939	4833
Reflections Used	4479	3662	16792	4563
R_{int}	0.0308	0.0557	0.0382	0.0378
Parameters	332	367	1061	320
Restraints	0	0	0	45
Largest Peak	0.249	0.208	0.565	0.472
Deepest Hole	-0.216	-0.173	-0.259	-0.389
GooF	1.080	1.051	1.059	1.028
wR_2 (all data)	0.1211	0.0994	0.2062	0.1559
wR_2	0.1174	0.0943	0.1920	0.1536
R_1 (all data)	0.0540	0.0578	0.0996	0.0598
R_1	0.0475	0.0405	0.0783	0.0578

A.3 Differential Calorimetry Curves of the DATPA derivatives

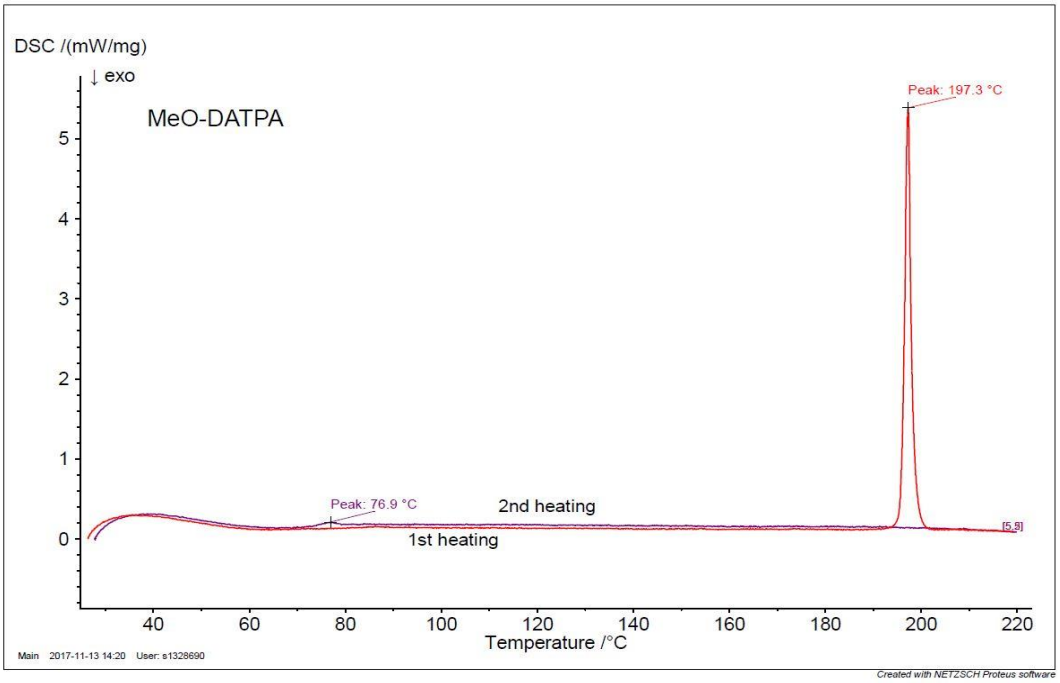

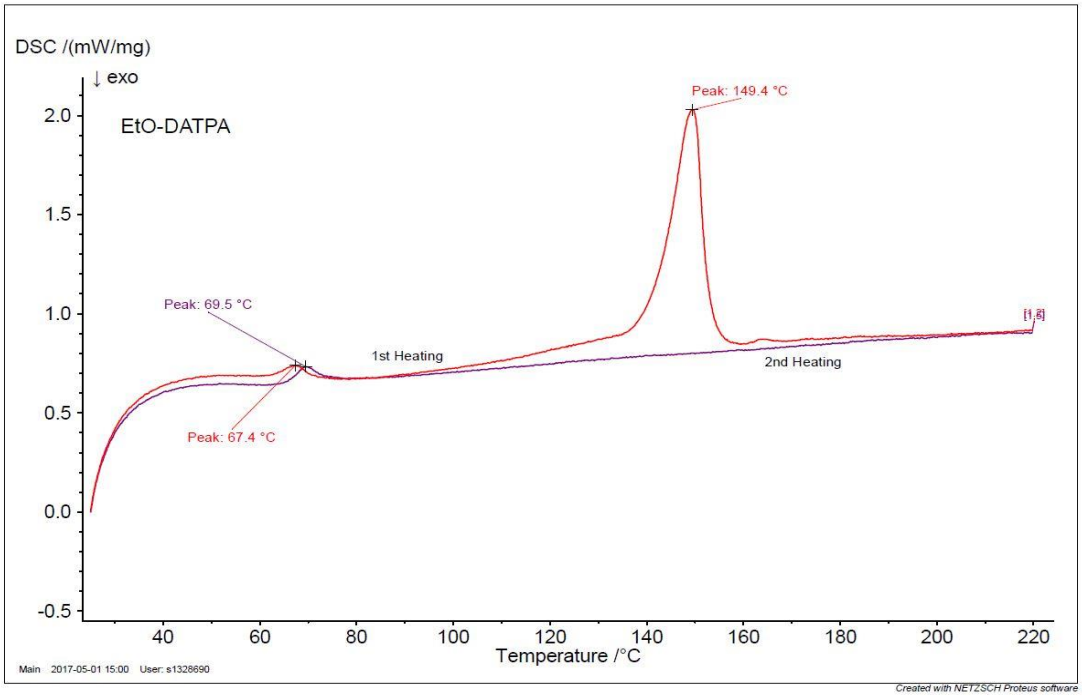

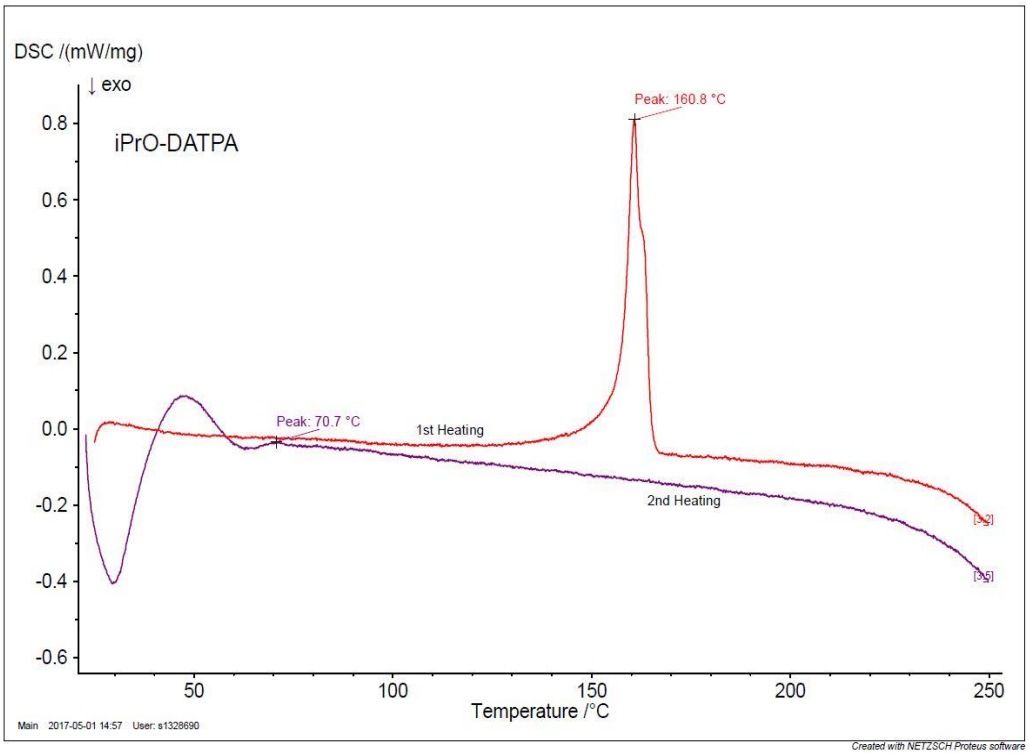
DSC /(mW/mg)
↓ exo
iPrO-DATPA
Peak: 160.8 °C
Peak: 70.7 °C
1st Heating
2nd Heating
Temperature /°C
Main 2017-05-01 14:57 User: s1328690
Created with NETZSCH Proteus software

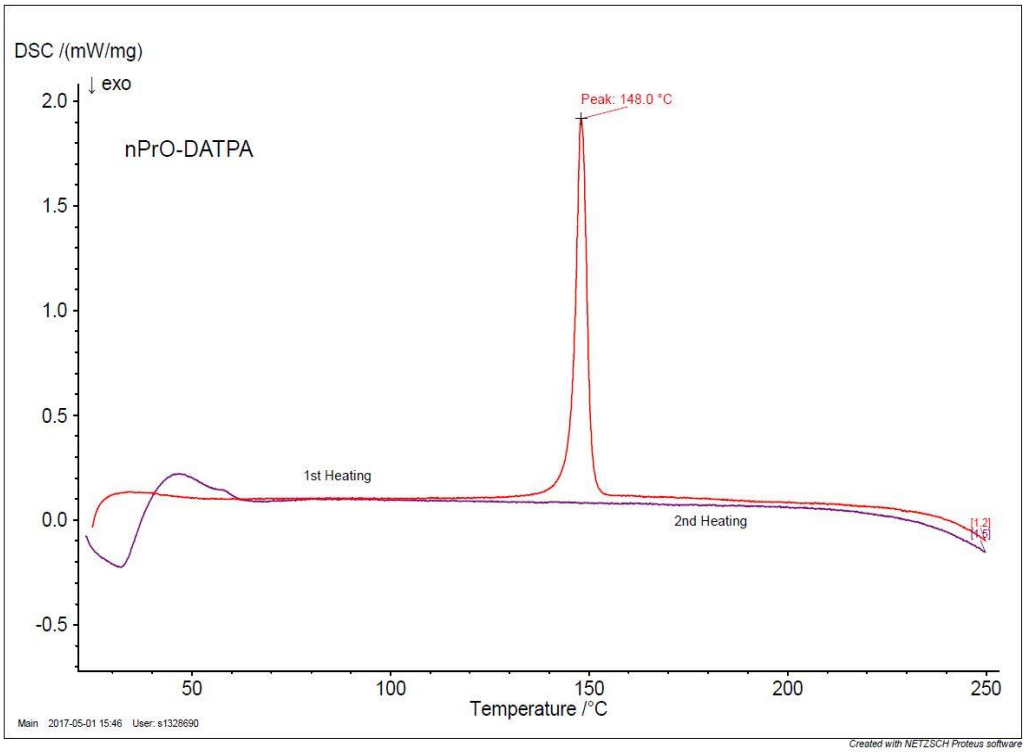
DSC /(mW/mg)
↓ exo
nPrO-DATPA
Peak: 148.0 °C
1st Heating
2nd Heating
Temperature /°C
Main 2017-05-01 15:46 User: s1328690
Created with NETZSCH Proteus software

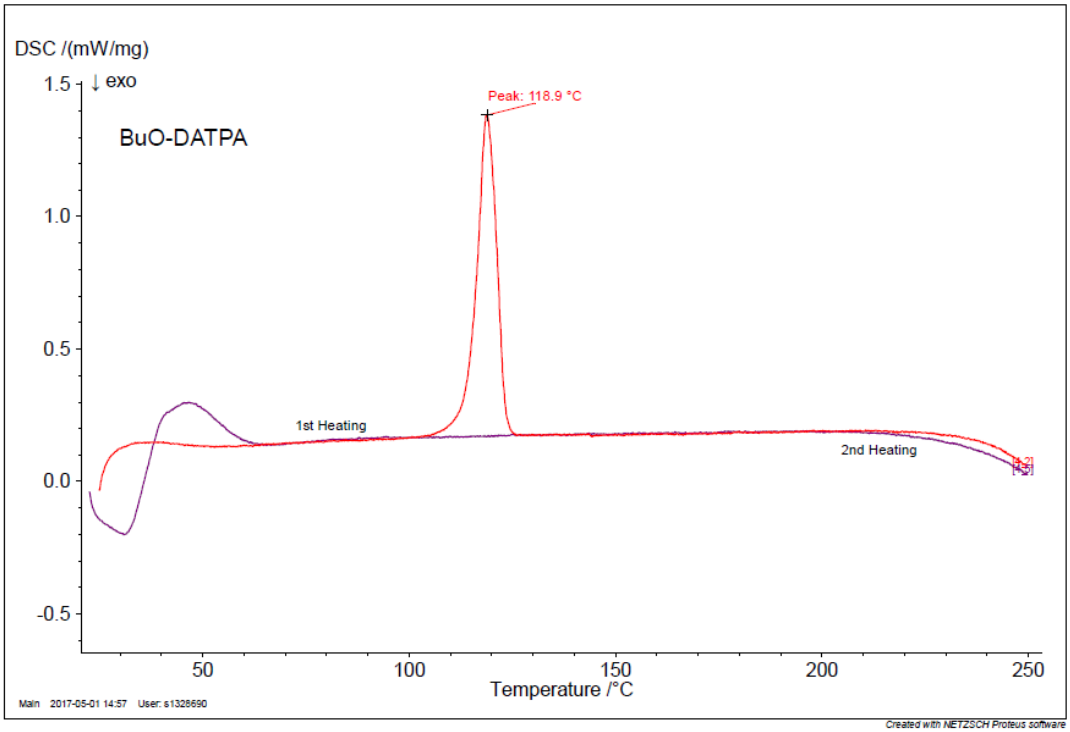
DSC /(mW/mg)
↓ exo
1.5
1.0
0.5
0.0
-0.5
BuO-DATPA
Peak: 118.9 °C
1st Heating
2nd Heating
50
100
150
200
250
Temperature /°C
Main 2017-05-01 14:57 User: s1328690
Created with NETZSCH Proteus software

References

1. U.S. Energy Information Administration. International Energy Outlook 2016. *International Energy Outlook 2016* **484,** 1–2 (2016).
2. IEA. Key World Energy Statistics 2016. *Key World Energy Statistics* (2016). doi:10.1787/9789264039537-en
3. Sato M. Thermochemistry of the formation of fossil fuels. *Spec. Publ. - Geochemical Soc.* **2,** 271–283 (1991).
4. Armaroli N. and Balzani V. Towards an electricity-powered world. *Energy Environ. Sci.* **4,** 3193 (2011).
5. Dresselhaus M. S. and Thomas I. L. Alternative energy technologies. *Nature* **414,** 332–7 (2001).
6. Armaroli, N. & Balzani, V. *Energy for a Sustainable World - From the Oil age to a Sun Powered Future*. *Energy for a Sustainable World* (Wiley-VCH Verlag GmbH & Co. KGaA, 2011).
7. Mitchell J. F. B. The 'greenhouse' effect and climate change. *Am. Geophys. Union* 115–139 (1989).
8. IEA (2016), *CO_2 Emissions from Fuel Combustion 2016*, IEA, Paris.
9. NASA: Climate Change and Global Warming. Available at: *http://climate.nasa.gov/*. (Accessed: 20th July 2017)
10. UNFCCC. The Paris Agreement(2014). Available at: http://unfccc.int/paris_agreement/items/9485.php. (Accessed: 20th July 2017)
11. Mark Z J. Review of solutions to global warming, air pollution, and energy security. *Energy Environ. Sci* **2,** 148–173 (2009).
12. Check R., Percent, K. & Shingles, E. *The Future of Solar Energy*. MIT 3–6 (2015).
13. Holm, D. & McIntosh, J. Renewable energy – the future for the developing world. *Renew. Energy Focus* **9,** 56–61 (2008).
14. Eisenberg R. and Nocera D. Overview of the forum on solar and renewable energy. *Inorg. Chem.* **44,** 6799–6801 (2005).
15. Bolton J. R. Solar Fuels. *Science (80).* **202,** 705–711 (1978).
16. Lewis N. S. and Nocera D. G. Powering the planet: Chemical challenges in solar energy utilization. *Proc. Natl. Acad. Sci.* **103,** 15729–15735 (2006).
17. Smets A., Jäger K., Isabella O., Swaaij R. and Zeman M. *Solar Energy: The physics and engineering of photovoltaic conversion technologies and systems*. Delf Univ. Technol. 1–420 (2014)

18. Lewis N. S., Crabtree G., Nozik A. J., Wasielewski M. R. and Alivisatos P. Basic Research Needs for Solar Energy Utilization. *Basic Energy Sci. Work. Sol. Energy Util.* 276 (2005).

19. A.E. Becquerel. Recherches sur les effets de la radiation chimique de la lumière solaire au moyen des courants électriques. *Comptes Rendus l'Académie des Sci.* **9,** 145–149 (1839).

20. A.E. Becquerel. Mémoire sur les effets électriques produits sous l'infl uence des rayons solaires. *Comptes Rendus l'Académie des Sci.* **9,** 561–567 (1839).

21. Hertz H. Ueber einen Einfluss des ultravioletten Lichtes auf die electrische Entladung. *Ann. Phys.* **267,** 983–1000 (1887).

22. Planck M. Ueber das Gesetz der Energieverteilung im Normalspectrum. *Ann. Phys.* **309,** 553–563 (1901).

23. Einstein A. Über einen die Erzeugung und Verwandlung des Lichtes betreffenden heuristischen Gesichtspunkt. *Ann. Phys.* **322,** 132–148 (1905).

24. First T. and Cell P. A Short History of Photovoltaic (PV) Cells. *Genes. Energy* 1–12 (2015).

25. Colinge J. P. C. and C. A. *Physics of Semiconductor Devices*.**10,** (Kluwer Academic Publishers, 1995).

26. Hu C. C. *Modern Semiconductor Devices for Integrated Circuits*. (Prentice Hall, 2010).

27. Battaglia C., Cueva A. and De Wolf A. High-efficiency Crystalline Silicon Solar Cells: Status and Perspectives. *Energy Environ. Sci.* **9,** (2016).

28. Williams R. Bequerel. Photovoltaic effect in binary compounds. *J. Chem. Phys.* **32,** 1505–1514 (1960).

29. Green M. A. *et al.* Solar cell efficiency tables (version 49). *Prog. Photovoltaics Res. Appl.* **25,** 3–13 (2017).

30. NREL. *Best Research - Cell Efficiencies* 1 (2015). Available at: https://www.nrel.gov/pv/assets/images/efficiency-chart.png. (Accessed: 21st July 2017)

31. Shockley W. and Queisser H. J. Detailed balance limit of efficiency of p-n junction solar cells. *J. Appl. Phys.* **32,** 510–519 (1961).

32. Saga T. Advances in crystalline silicon solar cell technology for industrial mass production. *NPG Asia Mater.* **2,** 96–102 (2010).

33. Renfrow S. PV FAQs: *What Is the Energy Payback for PV? Solar Energy Technologies Program* (Fact Sheet).

34. Poortmans J. and Arkhipov V. *Thin film solar cells : fabrication, characterization and applications*. (Wiley, 2007).

35. Green M. A. Thin-film solar cells: Review of materials, technologies and commercial status. in *Journal of Materials Science: Materials in Electronics* **18,** 15–19 (Springer US, 2007).

36. Lee T. D. and Ebong A. Thin film solar technologies- a review. *IEEE Conference Publication*. 33–42 (2015).

37. ZSW: ZSW Sets New World Record for Thin-film Solar Cells. *Press Release* June 15 (2016).

38. Todorov T. K., Reuter K. B. and Mitzi D. B. High-efficiency solar cell with earth-abundant liquid-processed absorber. *Adv. Mater.* **22,** E156–E159 (2010).

39. Wang W. *et al.* Device characteristics of CZTSSe thin-film solar cells with 12.6% efficiency. *Adv. Energy Mater.* **4,** 1301465 (2014).

40. Yastrebova N. V. High-efficiency multi-junction solar cells (2007). Centre for Research in Photonics, University of Ottawa, April 2007

41. Zeitouny J., Katz E. A., Dollet A. and Vossier A. Band Gap Engineering of Multi- Junction Solar Cells : Effects of Series Resistances and Solar Concentration. *Sci. Rep.* 1–9 (2017).

42. New efficiency record set with dual-junction solar cell. Available at: https://cleantechnica.com/2014/12/03/new-solar-cell-efficiency-record-set-46/. (Accessed: 29th July 2017)

43. Vlachopoulos N., Liska P., Augustynski J. and Graetzel M. Very efficient visible light energy harvesting and conversion by spectral sensitization of high surface area polycrystalline titanium dioxide films. *J. Am. Chem. Soc.* **110,** 1216–1220 (1988).

44. O'Regan B. and Grätzel M. A low-cost, high-efficiency solar cell based on dye-sensitized colloidal TiO_2 films. *Nature* **353,** 737–740 (1991).

45. Nazeeruddin M. K. *et al.* Engineering of efficient panchromatic sensitizers for nanocrystalline TiO2-based solar cells. *J. Am. Chem. Soc.* **123,** 1613–1624 (2001).

46. Robertson N. Optimizing dyes for dye-sensitized solar cells. *Angewandte Chemie - International Edition* **45,** 2338–2345 (2006).

47. Listorti A., O'Regan B. and Durrant J. R. Electron transfer dynamics in dye-sensitized solar cells. *Chemistry of Materials* **23,** 3381–3399 (2011).

48. Snaith H. J. and Schmidt-Mende L. Advances in liquid-electrolyte and solid-state dye-sensitized solar cells. *Adv. Mater.* **19,** 3187–3200 (2007).

49. Hara K., Arakawa H. *Dye-sensitized Solar Cells*. (CRC Press, 2003).

50. Kakiage K. *et al.* Highly-efficient dye-sensitized solar cells with collaborative sensitization by silyl-anchor and carboxy-anchor dyes. *Chem. Commun.* **51,** 15894–15897 (2015).

51. Tennakone K., Kumara G. R. and Wijayantha, K. G. U. The suppression of the recombination of photogenerated carriers in a dye-sensitized nano-porous solid-state photovoltaic cell. *Semicond. Sci. Technol.* **11,** 1737–1739 (1996).

52. Bach U. *et al.* Solid-state dye-sensitized mesoporous TiO_2 solar cells with high photon-to-electron conversion efficiencies. *Nature* **395,** 583–585 (1998).

53. Docampo P. *et al.* Lessons learned: From dye-sensitized solar cells to all-solid-state hybrid devices. *Adv. Mater.* **26,** 4013–4030 (2014).

54. Mineralogy Database. **2015,** http://webmineral.com/ (2015).

55. Gao P. *et al.* Organohalide lead perovskites for photovoltaic applications. *Energy Environ. Sci.* **7,** 2448–2463 (2014).

56. Green M. A., Ho-Baillie A. and Snaith, H. J. The emergence of perovskite solar cells. *Nat. Photonics* **8,** 506–514 (2014).

57. Weber D. $CH_3NH_3PbX_3$, ein Pb(II)-System mit kubischer Perowskitstruktur $CH_3NH_3PbX_3$, a Pb(II)-System with Cubic Perovskite Structure. **33,** 1443–1445 (1978).

58. Era M., Morimoto S., Tsutsui T. and Saito S. Organic-inorganic heterostructure electroluminescent device using a layered perovskite semiconductor $(C_6H_5C_2H_4NH_3)_2PbI_4$. *Appl. Phys. Lett.* **65,** 676–678 (1994).

59. Kagan C.R., Mitzi D.B and Dimitrakopoulos C.D. Organic-inorganic hybrid materials as semiconducting channels in thin-film field-effect transistors. *Science* **286,** 945–7 (1999).

60. Kojima A., Teshima K., Shirai Y. and Miyasaka T. Organometal Halide Perovskites as Visible-Light Sensitizers for Photovoltaic Cells. *J. Am. Chem. Soc.* **131,** 6050–6051 (2009).

61. Im J.-H., Lee C.-R., Lee J.-W., Park S.-W. and Park N.-G. 6.5% efficient perovskite quantum-dot-sensitized solar cell. *Nanoscale* **3,** 4088 (2011).

62. Chung I., Lee B., He J., Chang R. P. H. and Kanatzidis M. G. All-solid-state dye-sensitized solar cells with high efficiency. *Nature* **485,** 486–489 (2012).

63. Burschka J. *et al.* Tris(2-(1 *H* -pyrazol-1-yl)pyridine)cobalt(III) as p-type dopant for organic semiconductors and its application in ighhly efficient solid-state dye-sensitized solar cells. *J. Am. Chem. Soc.* **133,** 18042–18045 (2011).

64. Salbeck J., Yu N., Bauer J., Weissörtel F. and Bestgen H. Low molecular organic glasses for blue electroluminescence. *Synth. Met.* **91,** 209–215 (1997).

65. Kim H.-S. *et al.* Lead iodide perovskite sensitized all-solid-state submicron thin film mesoscopic solar cell with efficiency exceeding 9%. *Sci. Rep.* **591,** (2012).

66. Lee M. M., Teuscher J., Miyasaka T., Murakami T. N. and Snaith H. J. Efficient Hybrid Solar Cells Based on Meso-Superstructured Organometal Halide Perovskites. *Science.* **338,** 643–647 (2012).

67. Liu M., Johnston M. B. and Snaith H. J. Efficient planar heterojunction perovskite solar cells by vapour deposition. *Nature* **501,** 395–398 (2013).

68. Etgar L. *et al.* Mesoscopic $CH_3NH_3PbI_3/TiO_2$ Heterojunction Solar Cells. *J. Am. Chem. Soc.* **134,** 17396–17399 (2012).

69. Docampo P., Ball J. M., Darwich M., Eperon G. E. and Snaith, H. J. Efficient organometal trihalide perovskite planar-heterojunction solar cells on flexible polymer substrates. *Nat. Commun.* **4,** 2761 (2013).

70. Burschka J. *et al.* Sequential deposition as a route to high-performance perovskite-sensitized solar cells. *Nature* **499,** 316–319 (2013).

71. Jung H. S. & Park N.-G. Perovskite Solar Cells: From Materials to Devices. *Small* **11,** 10–25 (2015).

72. Marinova N., Valero S. and Delgado, J. L. Organic and perovskite solar cells: Working principles, materials and interfaces. *J. Colloid Interface Sci.* **488,** 373–389 (2017).

73. Wang X., Fang Y., He L., Wang Q. and Wu T. Influence of compact TiO_2 layer on the photovoltaic characteristics of the organometal halide perovskite-based solar cells. *Mater. Sci. Semicond. Process.* **27,** 569–576 (2014).

74. Vivo P. *et al.* Influence of TiO_2 compact layer precursor on the performance of perovskite solar cells. *Org. Electron.* **41,** 287–293 (2017).

75. Ostapchenko V., Huang Q., Zhang Q. and Zhao C. Effect of $TiCl_4$ Treatment on Different TiO_2 Blocking Layer Deposition Methods. *Int. J. Electrochem. Sci* **12,** 2262–2271 (2017).

76. Cojocaru L. *et al.* Surface Treatment of the Compact TiO_2 Layer for Efficient Planar Heterojunction Perovskite Solar Cells. *Chem. Lett.* 2015, **44**, 674–67

77. Che M. *et al.* F-doped TiO_2 Compact Film for High-Efficient Perovskite Solar Cells. *Int. J. Electrochem. Sci* **120221,** 1064–1074 (2017).

78. Wang J. *et al.* Performance enhancement of perovskite solar cells with Mg-doped TiO_2 compact film as the hole-blocking layer. *Appl. Phys. Lett.* **106,** 121104 (2015).

79. Wojciechowski K., Saliba M., Leijtens T., Abate A. and Snaith H. J. Sub-150 °C processed meso-superstructured perovskite solar cells with enhanced efficiency. *Energy Environ. Sci.* **7,** 1142–1147 (2014).

80. Lin S.-Y., Su T.-S., Hsieh T.-Y., Lo P.-C. and Wei, T.-C. Efficient Plastic Perovskite Solar Cell with a Low-Temperature Processable Electrodeposited TiO_2 Compact Layer and a Brookite TiO_2 Scaffold. *Adv. Energy Mater.* 1700169 (2017).

81. Das S. *et al.* High-Performance Flexible Perovskite Solar Cells by Using a Combination of Ultrasonic Spray-Coating and Low Thermal Budget Photonic Curing. *ACS Photonics* **2,** 680–686 (2015).

82. Conings, B. *et al.* An easy-to-fabricate low-temperature TiO_2 electron collection layer for high efficiency planar heterojunction perovskite solar cells. *APL Mater.* **2,** 81505 (2014).

83. Hong, S. *et al.* A facile and low-cost fabrication of TiO_2 compact layer for efficient perovskite solar cells. *Curr. Appl. Phys.* **15,** 574–579 (2015).

84. Hadouchi W., Rousset J.-, Tondelier D.-, Geffroy, B. and Bonnassieux Y. Zinc Oxide as hole blocking layer for Perovskite solar cells deposited in atmospheric conditions. *RSC Adv.* 67715–67723 (2016).

85. Liu D. and Kelly T. L. Perovskite solar cells with a planar heterojunction structure prepared using room-temperature solution processing techniques. *Nat. Photonics* **8,** 133–138 (2013).

86. Duan J. *et al.* Low-temperature processed SnO_2 compact layer for efficient mesostructure perovskite solar cells. *Appl. Surf. Sci.* **391,** 677–683 (2017).

87. Hu Q. *et al.* Engineering of Electron-Selective Contact for Perovskite Solar Cells with Efficiency Exceeding 15%. *ACS Nano* **8,** 10161–10167 (2014).

88. Wang, J. T.-W. *et al.* Low-Temperature Processed Electron Collection Layers of Graphene/TiO_2 Nanocomposites in Thin Film Perovskite Solar Cells. (2013).

89. Wojciechowski K. *et al.* C_{60} as an Efficient n-Type Compact Layer in Perovskite Solar Cells. *J. Phys. Chem. Lett.* **6,** 2399–2405 (2015).

90. Ye M., Liu X., Iocozzia J., Liu X. and Lin Z. Nanostructured Materials for High Efficiency Perovskite Solar Cells. in 1–39 (Springer, Cham, 2016).

91. Kim H.-S. *et al.* High Efficiency Solid-State Sensitized Solar Cell-Based on Submicrometer Rutile TiO_2 Nanorod and $CH_3NH_3PbI_3$ Perovskite Sensitizer. *Nano Lett.* **13,** 2412–2417 (2013).

92. Kazim S., Nazeeruddin M. K., Grätzel M. and Ahmad S. Perovskite as light harvester: A game changer in photovoltaics. *Angew. Chemie - Int. Ed.* **53,** 2812–2824 (2014).

93. Yang Y. *et al.* The size effect of TiO_2 nanoparticles on a printable mesoscopic perovskite solar cell. *J. Mater. Chem. A* **3,** 9103–9107 (2015).

94. Sung S. Do *et al.* 50 nm sized spherical TiO_2 nanocrystals for highly efficient mesoscopic perovskite solar cells. *Nanoscale* **7,** 8898–8906 (2015).

95. Mo S.D., and Ching W.Y. Electronic and optical properties of three phases of titanium dioxide: Rutile, anatase, and brookite. *Phys. Rev. B. Condens. Matter* **51,** 13023–13032 (1995).

96. Bai Y., Mora-Seró I., De Angelis F., Bisquert J. and Wang, P. Titanium Dioxide Nanomaterials for Photovoltaic Applications. *Chem. Rev.* **114,** 10095–10130 (2014).

97. Jiang Q., Sheng X., Li Y., Feng X. and Xu T. Rutile TiO_2 nanowire-based perovskite solar cells. *Chem. Commun.* **50,** 14720–3 (2014).

98. Cai B. *et al.* An acid-free medium growth of rutile TiO_2 nanorods arrays and their application in perovskite solar cells. *J. Mater. Chem. C* **3,** 729–733 (2015).

99. Dharani S. *et al.* High efficiency electrospun TiO_2 nanofiber based hybrid organic-inorganic perovskite solar cell. *Nanoscale* **6,** 1675–9 (2014).

100. Salazar R. *et al.* Use of Anodic TiO_2 Nanotube Layers as Mesoporous Scaffolds for Fabricating $CH_3NH_3PbI_3$ Perovskite-based solid-state solar cells. *ChemElectroChem* **2,** 824–828 (2015).

101. Wu W.-Q. *et al.* Hierarchical Oriented Anatase TiO_2 Nanostructure arrays on Flexible Substrate for Efficient Dye-sensitized Solar Cells. *Sci. Rep.* **3,** 1–7 (2013).

102. Yang W. *et al.* A facile synthesis of anatase TiO_2 nanosheets-based hierarchical spheres with over 90% {001} facets for dye-sensitized solar cells. *Chem. Commun.* **47,** 1809–1811 (2011).

103. Mahmood K., Swain B. S. and Amassian A. Highly Efficient Hybrid Photovoltaics Based on Hyperbranched Three-Dimensional TiO_2 Electron Transporting Materials. *Adv. Mater.* **27,** 2859–2865 (2015).

104. Wu W.-Q., Huang F., Chen D., Cheng Y.-B. and Caruso R. A. Thin Films of Dendritic Anatase Titania Nanowires Enable Effective Hole-Blocking and Efficient Light-Harvesting for High-Performance Mesoscopic Perovskite Solar Cells. *Adv. Funct. Mater.* **25,** 3264–3272 (2015).

105. Wu W.-Q. *et al.* Recent progress in hybrid perovskite solar cells based on n-type materials. *J. Mater. Chem. A,* **5,** 10092–10109 (2017).

106. Han G. S. *et al.* Retarding charge recombination in perovskite solar cells using ultrathin MgO-coated TiO_2 nanoparticulate films. *J. Mater. Chem. A*, **3,** 9160–9164 (2015).

107. Yang M. *et al.* Improved charge transport of Nb-doped TiO_2 nanorods in methylammonium lead iodide bromide perovskite solar cells. *J. Mater. Chem. A,* **2,** 19616–19622 (2014).

108. Yin G. et al. Enhancing Efficiency and Stability of Perovskite Solar Cells through Nb-Doping of TiO_2 at Low Temperature. ACS Appl. Mater. Interfaces. **9**,12, 10752-10758 (2017)

109. Kim H. Bin *et al.* Enhancement of photovoltaic properties of $CH_3NH_3PbBr_3$ heterojunction solar cells by modifying mesoporous TiO_2 surfaces with carboxyl groups. *J. Mater. Chem. A* **3,** 9264–9270 (2015).

110. Li Y. *et al.* Mesoporous SnO_2 nanoparticle films as electron-transporting material in perovskite solar cells. *RSC Adv.* **5,** 28424–28429 (2015).

111. Ke W. *et al.* Low temperature solution-processed tin oxide as an alternative electron transporting layer for efficient perovskite solar cells. *J. Am. Chem. Soc.* **137,** 6730–6733 (2015).

112. Bi D. *et al.* Using a two-step deposition technique to prepare perovskite ($CH_3NH_3PbI_3$) for thin film solar cells based on ZrO_2 and TiO_2 mesostructures. *RSC Adv.* **3,** 18762 (2013).

113. Hwang S. H. *et al.* Size-controlled SiO_2 nanoparticles as scaffold layers in thin-film perovskite solar cells. *J. Mater. Chem. A* **2,** 16429–16433 (2014).

114. Carnie M. J. *et al.* Performance enhancement of solution processed perovskite solar cells incorporating functionalized silica nanoparticles. *J. Mater. Chem. A* **2,** 17077–17084 (2014).

115. Tavakoli M. M. *et al.* Highly Efficient Flexible Perovskite Solar Cells with Antireflection and Self-Cleaning Nanostructures. **9,** 10287–10295 (2015).

116. Butler K. T., Frost J. M. and Walsh A. Band alignment of the hybrid halide perovskites $CH_3NH_3PbCl_3$, $CH_3NH_3PbBr_3$ and $CH_3NH_3PbI_3$. *Mater. Horiz.* **2,** 228–231 (2015).

117. Kulkarni, S. A. *et al.* Band-gap tuning of lead halide perovskites using a sequential deposition process. *J. Mater. Chem. A* **2,** 9221 (2014).

118. Yang W. S. *et al.* High-performance photovoltaic perovskite layers fabricated through intramolecular exchange. *Science.* **348** (2015).

119. Lee J.-W., Seol D.-J., Cho A.-N. and Park N.-G. High-Efficiency Perovskite Solar Cells Based on the Black Polymorph of $HC(NH_2)_2PbI_3$. *Adv. Mater.* **26,** 4991–4998 (2014).

120. Pellet N. *et al.* Mixed-Organic-Cation Perovskite Photovoltaics for Enhanced Solar-Light Harvesting. *Angew. Chemie Int. Ed.* **53,** 3151–3157 (2014).

121. Ogomi Y. *et al.* $CH_3NH_3Sn_xPb_{(1-x)}I_3$ Perovskite Solar Cells Covering up to 1060 nm. *J. Phys. Chem. Lett.* **5,** 1004–1011 (2014).

122. Bi D. *et al.* Efficient luminescent solar cells based on tailored mixed-cation perovskites. *Sci. Adv.* **2,** (2016).

123. Giustino F. and Snaith H. J. Toward Lead-Free Perovskite Solar Cells. *ACS Energy Lett.* **1,** 1233–1240 (2016).

124. Sun Y.-Y. *et al.* Discovering lead-free perovskite solar materials with a split-anion approach. *Nanoscale* **8,** 6284–6289 (2016).

125. Noel N. K. *et al.* Lead-Free Organic-Inorganic Tin Halide Perovskites for Photovoltaic Applications. *Energy Environ. Sci.* **7,** 3061–3068 (2014).

126. Konstantakou M. *et al.* A critical review on tin halide perovskite solar cells. *J. Mater. Chem. A* **2,** 17018 (2017).

127. Babayigit A., Ethirajan, A., Muller, M. & Conings, B. Toxicity of organometal halide perovskite solar cells. *Nat. Mater.* **15,** 247–251 (2016).

128. Kong M. *et al.* Nontoxic $(CH_3NH_3)_3Bi_2I_9$ perovskite solar cells free of hole conductors with an alternative architectural design and a solution-processable approach. *RSC Adv.* **7,** 35549–35557 (2017).

129. Park B.-W. *et al.* Bismuth Based Hybrid Perovskites $A_3Bi_2I_9$(A: Methylammonium or Cesium) for Solar Cell Application. *Adv. Mater.* **27,** 6806–6813 (2015).

130. Dong Q. *et al.* Encapsulation of Perovskite Solar Cells for High Humidity Conditions. *ChemSusChem* **9,** 2597–2603 (2016).

131. Binek A. *et al.* Recycling Perovskite Solar Cells To Avoid Lead Waste. *ACS Appl. Mater. Interfaces* **8,** 12881–12886 (2016).

132. Wang L., Li, G.-R., Zhao, Q. and Gao, X.-P. Non-precious transition metals as counter electrode of perovskite solar cells. *Energy Storage Mater.* **7,** 40–47 (2017).

133. Zhang L. *et al.* The effect of carbon counter electrodes on fully printable mesoscopic perovskite solar cells. *J. Mater. Chem. A* **3,** 9165–9170 (2015).

134. Li Z. *et al.* Laminated Carbon Nanotube Networks for Metal Electrode-Free Efficient Perovskite Solar Cells. *ACS Nano* **8,** 6797–6804 (2014).

135. Ameen S. *et al.* Perovskite Solar Cells: Influence of Hole Transporting Materials on Power Conversion Efficiency. *ChemSusChem* **9,** 10–27 (2016).

136. Zhu L. *et al.* Efficient $CH_3NH_3PbI_3$ perovskite solar cells with 2TPA-n-DP hole-transporting layers. *Nano Res.* **8,** 1116–1127 (2015).

137. Tress W. *et al.* The role of the hole-transport layer in perovskite solar cells - Reducing recombination and increasing absorption. in *2014 IEEE 40th Photovoltaic Specialist Conference, PVSC 2014* 1563–1566 (IEEE, 2014).

138. Chen S. *et al.* Exploring the Limiting Open-Circuit Voltage and the Voltage Loss Mechanism in Planar $CH_3NH_3PbBr_3$ Perovskite Solar Cells. *Adv. Energy Mater.* **6,** 1600132 (2016).

139. Shao Y., Yuan Y. and Huang J. Correlation of energy disorder and open-circuit voltage in hybrid perovskite solar cells. *Nat. Energy* **1,** 15001 (2016).

140. Back H. *et al.* Achieving long-term stable perovskite solar cells via ion neutralization. *Energy Environ. Sci. Energy Environ. Sci* **9,** 1258–1263 (1258).

141. Juarez-Perez E. J. *et al.* Role of the Selective Contacts in the Performance of Lead Halide Perovskite Solar Cells. *J. Phys. Chem. Lett.* **5,** 680–685 (2014).

142. Christians J. A., Fung R. C. M. and Kamat P. V. An Inorganic Hole Conductor for Organo-Lead Halide Perovskite Solar Cells. Improved Hole Conductivity with Copper Iodide. *J. Am. Chem. Soc.* **136,** 758–764 (2014).

143. Sun W. *et al.* Room-temperature and solution-processed copper iodide as the hole transport layer for inverted planar perovskite solar cells. *Nanoscale* **8,** 15954–15960 (2016).

144. Ito S. *et al.* Carbon-Double-Bond-Free Printed Solar Cells from TiO_2/$CH_3NH_3PbI_3$/CuSCN/Au: Structural Control and Photoaging Effects. *ChemPhysChem* **15,** 1194–1200 (2014).

145. Qin P. *et al.* Inorganic hole conductor-based lead halide perovskite solar cells with 12.4% conversion efficiency. *Nat. Commun.* **5,** 1–6 (2014).

146. Zuo C. and Ding L. Solution-Processed Cu_2O and CuO as Hole Transport Materials for Efficient Perovskite Solar Cells. *Small* **11,** 5528–5532 (2015).

147. You, J. *et al.* Improved air stability of perovskite solar cells via solution-processed metal oxide transport layers. *Nat. Nanotechnol.* **11,** 75–81 (2015).

148. Chen W. *et al.* Efficient and stable large-area perovskite solar cells with inorganic charge extraction layers. *Science.* **350,** 944–948 (2015).

149. Lv, M. *et al.* Colloidal $CuInS_2$ Quantum Dots as Inorganic Hole-Transporting Material in Perovskite Solar Cells. *ACS Appl. Mater. Interfaces* **7,** 17482–17488 (2015).

150. Ito S. Inorganic Hole-Transporting Materials for Perovskite Solar Cell. in *Organic-Inorganic Halide Perovskite Photovoltaics* 343–366 (Springer International Publishing, 2016).

151. Daskeviciene M. *et al.* Carbazole-based enamine: Low-cost and efficient hole transporting material for perovskite solar cells. *Nano Energy* **32,** 551–557 (2017).

152. Wang H. *et al.* Facile Synthesis and High Performance of a New Carbazole-Based Hole-Transporting Material for Hybrid Perovskite Solar Cells. *ACS Photonics* **2,** 849–855 (2015).

153. Ramos F. J. *et al.* Rational design of triazatruxene-based hole conductors for perovskite solar cells. *RSC Adv.* **5,** 53426–53432 (2015).

154. Nishimura H. *et al.* Hole-Transporting Materials with a Two-Dimensionally Expanded π-System around an Azulene Core for Efficient Perovskite Solar Cells. *J. Am. Chem. Soc.* **137,** 15656–15659 (2015).

155. Lv S. *et al.* Simple Triphenylamine-Based Hole-Transporting Materials for Perovskite Solar Cells. *Electrochim. Acta* **182,** 733–741 (2015).

156. Calió L., Kazim S., Grätzel M. and Ahmad S. Hole-Transport Materials for Perovskite Solar Cells. *Angew. Chemie Int. Ed.* **55,** 14522–14545 (2016).

157. Dhingra P., Singh P., Rana P. J. S., Garg A. and Kar P. Hole-Transporting Materials for Perovskite-Sensitized Solar Cells. *Energy Technol.* **4,** 891–938 (2016).

158. Thelakkat M. Star-Shaped, Dendrimeric and Polymeric Triarylamines as Photoconductors and Hole Transport Materials for Electro-Optical Applications. *Macromol. Mater. Eng.* **287,** 442 (2002).

159. Agarwala P. *et al.* A review on triphenylamine (TPA) based organic hole transport materials (HTMs) for dye sensitized solar cells (DSSCs) and perovskite solar cells (PSCs): evolution and molecular engineering. *J. Mater. Chem. A* **5,** 1348–1373 (2017).

160. Krüger J. *et al.* High efficiency solid-state photovoltaic device due to inhibition of interface charge recombination. *Appl. Phys. Lett.* **79,** 2085–2087 (2001).

161. Jeon N. J. *et al. o*-Methoxy Substituents in Spiro-OMeTAD for Efficient Inorganic–Organic Hybrid Perovskite Solar Cells. *J. Am. Chem. Soc.* **136,** 7837–7840 (2014).

162. Maciejczyk M. *et al.* SFX as a low-cost 'Spiro' hole-transport material for efficient perovskite solar cells. *J. Mater. Chem. A* **4,** 4855–4863 (2016).

163. Lv S. *et al.* Mesoscopic $TiO_2/CH_3NH_3PbI_3$ perovskite solar cells with new hole-transporting materials containing butadiene derivatives. *Chem. Commun.* **50,** 6931 (2014).

164. Li H. *et al.* A Simple 3,4-Ethylenedioxythiophene Based Hole-Transporting Material for Perovskite Solar Cells. *Angew. Chemie Int. Ed.* **53,** 4085–4088 (2014).

165. Yaghoobi Nia N., Matteocci F., Cina L. and Di Carlo A. High Efficiency Perovskite Solar Cell Based on Poly (3-hexylthiophene) (P3HT): The Influence of P3HT Molecular Weight and Mesoscopic Scaffold Layer. *ChemSusChem* 1–10 (2017).

166. Yu Z. *et al.* High-efficiency perovskite solar cells employing a conjugated donor–acceptor co-polymer as a hole-transporting material. *RSC Adv.* **7,** 27189–27197 (2017).

167. Stringer M. *et al.* Efficient perovskite photovoltaic devices using chemically doped PCDTBT as a hole-transport material. *J. Mater. Chem. A* **30,** 1410 (2017).

168. Heo J. H. *et al.* Efficient inorganic–organic hybrid heterojunction solar cells containing perovskite compound and polymeric hole conductors. *Nat. Photonics* **7,** 486–491 (2013).

169. Owen A. Fundamentals of UV-visible spectroscopy. *Vasa* **1,** 1–136 (1996).

170. Uv V. S. Introduction to Ultraviolet - Visible Spectroscopy (UV) 1. *Society* 1–5 (2009).

171. Atkins P. W. Shriver and Atkins' inorganic chemistry. *Shriver Atkin's Inorg. Chem.* 851 (2010). doi:978-0-19-926463-6

172. Lakowicz J. R. Instrumentation for Fluorescence Spectroscopy 2.1. in *Principles of Fluorescence Spectroscopy* 36 (Wiley-VCH Verlag GmbH & Co. KGaA, 2006).

173. Deshpande S. S. *Principles and applications of luminescence spectroscopy. Critical reviews in food science and nutrition* **41,** (2001).

174. Molecular Expressions Microscopy Primer: Fluorescence - Jablonski Diagram - Interactive Tutorial. Available at: http://micro.magnet.fsu.edu/primer/java/jablonski/lightandcolor/index.html. (Accessed: 19th August 2017)

175. Bard A. J. and Faulkner L. R. *Electrochemical methods : fundamentals and applications*. (Wiley, 2001).

176. Kissinger T. and Heineman W. Cyclic Voltammetry. *J. Chem. Educ.* 702–706 (2010).

177. Smyth M. Cyclic voltammetry. *TrAC Trends Anal. Chem.* **13,** 341 (1994).

178. Mirceski V. *et al.* Square-Wave Voltammetry: A Review on the Recent Progress. *Electroanalysis* **25,** 2411–2422 (2013).

179. Square wave voltammetry Application Note S-7. *Princet. Appl. Res.* 1–5 (1957). doi:10.1021/ac00279a004

180. Bragg W. H. and Bragg, W. L. The Reflection of X-rays by Crystals. *Proc. R. Soc. London* **88,** 428–438 (1913).

181. Turton R. J. *The Physics of Solids*. (Oxford University Press, 2000).

182. Pecharsky V. and Zavalij P. *Fundamentals of Crystalline State and Crystal Lattice*. *Fundamentals of Powder Diffraction and Structural Characterization of Materials* (Springer US, 2009).

183. Van B. Zeghbroeck. Carrier Transport. (2011). Available at: http://ecee.colorado.edu/~bart/book/book/chapter2/ch2_7.htm. (Accessed: 19th August 2017)

184. Shuai Z., Wang L. and Song C. Hopping Mechanism. in 7–41 (2012). *Theory of Charge Transport in Carbon Electronic Materials* doi:10.1007/978-3-642-25076-7_2

185. Coropceanu V. *et al.* Charge transport in organic semiconductors. *Chem. Rev.* **107,** 926–52 (2007).

186. Zaumseil J. and Sirringhaus H. Electron and ambipolar transport in organic field-effect transistors. *Chem. Rev.* **107,** 1296–1323 (2007).

187. PerkinElmer. Differential Scanning Calorimetry (DSC) A Beginner's Guide. 1–9 (2014).

188. Höhne G. W. H., Hemminger W. F. and Flammershein H.-J. *Differential Scanning Calorimetry*. (2003).

189. Epoxy Technology Inc. Glass Transition Temperature for Epoxies. *Available URL http//www.epotek.com* 1–2 (2012).

190. Dittrich T. *Materials Concepts for Solar Cells*. (Imperial College press, 2014). doi:10.1142/p937

191. Berera R., van Grondelle R. and Kennis J. T. M. Ultrafast transient absorption spectroscopy: Principles and application to photosynthetic systems. *Photosynthesis Research* **101,** 105–118 (2009).

192. Bi D., Yang L., Boschloo G., Hagfeldt A. and Johansson E. M. J. Effect of Different Hole Transport Materials on Recombination in $CH_3NH_3PbI_3$ Perovskite-Sensitized Mesoscopic Solar Cells. *J. Phys. Chem. Lett.* **4,** 1532–1536 (2013).

193. Zhang J. *et al.* Constructive Effects of Alkyl Chains: A Strategy to Design Simple and Non-Spiro Hole Transporting Materials for High-Efficiency Mixed-Ion Perovskite Solar Cells. *Adv. Energy Mater.* **6,** 1502536 (2016).

194. Song C. E. *et al.* Impact of the Crystalline Packing Structures on Charge Transport and Recombination via Alkyl Chain Tunability of DPP-Based Small Molecules in Bulk Heterojunction Solar Cells. *ACS Appl. Mater. Interfaces* **8,** 12940–12950 (2016).

195. Zimmermann I. *et al.* High-Efficiency Perovskite Solar Cells Using Molecularly Engineered, Thiophene-Rich, Hole-Transporting Materials: Influence of Alkyl Chain Length on Power Conversion Efficiency. *Adv. Energy Mater.* **7,** 1601674 (2017).

196. Back J. Y. *et al.* Alkyl Chain Length Dependence of the Field-Effect Mobility in Novel Anthracene Derivatives. *ACS Appl. Mater. Interfaces* **7,** 351–358 (2015).

197. Deng D. *et al.* Effects of Shortened Alkyl Chains on Solution-Processable Small Molecules with Oxo-Alkylated Nitrile End-Capped Acceptors for High-Performance Organic Solar Cells. *Adv. Energy Mater.* **4,** 1400538 (2014).

198. Cherniawski B. P. *et al.* The effect of hexyl side chains on molecular conformations, crystal packing, and charge transport of oligothiophenes. *J. Mater. Chem. C* **5,** 582–588 (2017).

199. Planells M. *et al.* Diacetylene bridged triphenylamines as hole transport materials for solid state dye sensitized solar cells. *J. Mater. Chem. A* **1,** 6949 (2013).

200. Ullmann F. Ueber eine neue Bildungsweise von Diphenylaminderivaten. *Berichte der Dtsch. Chem. Gesellschaft* **36,** 2382–2384 (1903).

201. Beletskaya I. P. and Cheprakov A. V. Copper in cross-coupling reactions: The post-Ullmann chemistry. *Coord. Chem. Rev.* **248,** 2337–2364 (2004).

202. Sambiagio C., Marsden S. P., Blacker, A. J. and McGowan P. C. Copper catalysed Ullmann type chemistry: from mechanistic aspects to modern development. *Chem. Soc. Rev.* **43,** 3525–50 (2014).

203. Sperotto E., van Klink G. P. M., van Koten G. and de Vries J. G. The mechanism of the modified Ullmann reaction. *Dalt. Trans.* **39,** 10338 (2010).

204. Okano K., Tokuyama H. and Fukuyama T. Copper-mediated aromatic amination reaction and its application to the total synthesis of natural products. *Chem. Commun. (Camb).* **50,** 13650–13663 (2014).

205. Sonogashira K., Tohda Y. and Hagihara N. A convenient synthesis of acetylenes: catalytic substitutions of acetylenic hydrogen with bromoalkenes, iodoarenes and bromopyridines. *Tetrahedron Lett.* **16,** 4467–4470 (1975).

206. Chinchilla R. and Nájera, C. The Sonogashira reaction: A booming methodology in synthetic organic chemistry. *Chem. Rev.* **107,** 874–922 (2007).

207. Chinchilla R. and Nájera C. Recent advances in Sonogashira reactions. *Chem. Soc. Rev.* **40,** 5084–121 (2011).

208. Siemsen P., Livingston R. C. and Diederich F. Acetylenic coupling: A powerful tool in molecular construction. *Angewandte Chemie - International Edition* **39,** 2632–2657 (2000).

209. Sindhu K. S. and Anilkumar G. Recent advances and applications of Glaser coupling employing greener protocols. *RSC Adv.* **4,** 27867–27887 (2014).

210. Vilhelmsen M. H., Jensen J., Tortzen C. G. and Nielsen M. B. The Glaser-Hay Reaction: Optimization and Scope Based on 13 C NMR Kinetics Experiments. *European J. Org. Chem.* **2013,** 701–711 (2013).

211. Jover J., Spuhler P., Zhao L., McArdle C. and Maseras F. Toward a mechanistic understanding of oxidative homocoupling: the Glaser–Hay reaction. *Catal. Sci. Technol.* **4,** 4200–4209 (2014).

212. Bohlmann F., Schönowsky H., Inhoffen E. and Grau G. Polyacetylenverbindungen, LII. Über den Mechanismus der oxydativen Dimerisierung von Acetylenverbindungen. *Chem. Ber.* **97,** 794–800 (1964).

213. Cardona C. M., Li W., Kaifer A. E., Stockdale D. and Bazan G. C. Electrochemical Considerations for Determining Absolute Frontier Orbital Energy Levels of Conjugated Polymers for Solar Cell Applications. *Adv. Mater.* **23,** 2367–2371 (2011).

214. Anthony J. E. Functionalized acenes and heteroacenes for organic electronics. *Chemical Reviews* **106,** 5028–5048 (2006).

215. Christopher R. Newman, *et al.* Introduction to Organic Thin Film Transistors and Design of n-Channel Organic Semiconductors. (2004). doi:10.1021/CM049391X

216. Horowitz G. Organic Field-Effect Transistors. *Adv. Mater.* **10,** 365–377 (1998).

217. Frisch M.J., Trucks G.W., Schlegel H.B., Scuseria G.E., Robb M.A., Cheeseman J.R., Scalmani G., Barone V., Mennucci B., Petersson G.A., Nakatsuji H., Caricato M., Li X., Hratchian H. P., Izmaylov A.F., Bloino J., Zheng G., Sonnenberg J.L, Hada M., M. Eh D. J. F. Gaussian 09. (2010).

218. Avogadro 1.1.0. Available from: http://sourceforge.net/projects/avogadro/.

219. Yasuda T. Triphenylamine-based amorphous polymers for bulk-heterojunction photovoltaic cells. *IOP Conf. Ser. Mater. Sci. Eng.* **54,** 12015 (2014).

220. Iwan A. and Sek D. Polymers with triphenylamine units: Photonic and electroactive materials. *Progress in Polymer Science (Oxford)* **36,** 1277–1325 (2011).

221. Usta H. and Facchetti A. Polymeric and Small-Molecule Semiconductors for Organic Field-Effect Transistors. in *Large Area and Flexible Electronics* 1–100 (Wiley-VCH Verlag, 2015). doi:10.1002/9783527679973.ch1

222. Isakova A. and Topham P. D. Polymer strategies in perovskite solar cells. *Journal of Polymer Science, Part B: Polymer Physics* **55,** 549–568 (2017).

223. Wong-Stringer M. *et al.* Efficient perovskite photovoltaic devices using chemically doped PCDTBT as a hole-transport material. *J. Mater. Chem. A* **30,** 1410 (2017).

224. Yang B., Mahjouri-Samani M., Rouleau C. M., Geohegan D. B. and Xiao K. Low temperature synthesis of hierarchical TiO_2 nanostructures for high performance perovskite solar cells by pulsed laser deposition. *Phys. Chem. Chem. Phys.* **18,** 27067–27072 (2016).

225. Jhun Mo Son, Sakaki Y., Ogino K. and Sato, H. Synthesis of polymers for hole and electron transport materials in organic electroluminescent devices. *IEEE Trans. Electron Devices* **44,** 1307–1314 (1997).

226. Hüttner S., Sommer M., Steiner U. and Thelakkat M. Organic field effect transistors from triarylamine side-chain polymers. *Cit. Appl. Phys. Lett* **96,** (2010).

227. Barea E. M. *et al.* Determination of charge carrier mobility of hole transporting polytriarylamine-based diodes. *Thin Solid Films* **518,** 3351–3354 (2010).

228. Schroot R., Schubert U. S. and Jäger M. Block Copolymers for Directional Charge Transfer: Synthesis, Characterization, and Electrochemical Properties of Redox-Active Triarylamines. *Macromolecules* **48,** 1963–1971 (2015).

229. Rauws T. R. M. and Maes B. U. W. Transition metal-catalyzed N-arylations of amidines and guanidines. *Chem. Soc. Rev. Chem. Soc. Rev* **41,** 2463–2497 (2012).

230. Kanibolotsky A. L., Perepichka I. F. and Skabara, P. J. Star-shaped pi-conjugated oligomers and their applications in organic electronics and photonics. *Chem. Soc. Rev.* **39,** 2695–2728 (2010).

231. Thelakkat M. Star-shaped, dendrimeric and polymeric triarylamines as photoconductors and hole transport materials for electro-optical applications. *Macromolecular Materials and Engineering* **287,** 442–461 (2002).

232. Paek S., Cho N., Cho S., Lee J. K. and Ko J. Planar star-shaped organic semiconductor with fused triphenylamine core for solution-processed small-molecule organic solar cells and field-effect transistors. *Org. Lett.* **14,** 6326–6329 (2012).

233. Thomas K. R. J., Lin J. T., Tao Y. T. and Ko, C. W. New star-shaped luminescent triarylamines: Synthesis, thermal, photophysical, and electroluminescent characteristics. *Chem. Mater.* **14,** 1354–1361 (2002).

234. Paek S. *et al.* Efficient Organic Solar Cells with Star-Shaped Small Molecules Comprising of Planar Donating Core and Accepting Edges. *J. Phys. Chem. C 118* (**47**), 27193–27200 (2014).

235. Do K. *et al.* Star-shaped hole transporting materials with a triazine unit for efficient perovskite solar cells. *Chem. Commun.* **50,** 10971 (2014).

236. Choi H. *et al.* Efficient perovskite solar cells with 13.63 % efficiency based on planar triphenylamine hole conductors. *Chem. A Eur. J.* **20,** 10894–10899 (2014).

237. Zhang F. *et al.* Dopant-free star-shaped hole-transport materials for efficient and stable perovskite solar cells. *Dye. Pigment.* **136,** 273–277 (2017).

238. Wakamiya A. *et al.* On-Top π-Stacking of Quasiplanar Molecules in Hole-Transporting Materials: Inducing Anisotropic Carrier Mobility in Amorphous Films. *Angew. Chemie Int. Ed.* **53,** 5800–5804 (2014).

239. Kuratsu M., Kozaki M. and Okada, K. 2,2′:6′,2″:6″,6-Trioxytriphenylamine: Synthesis and Properties of the Radical Cation and Neutral Species. *Angew. Chemie Int. Ed.* **44,** 4056–4058 (2005).

240. Kuratsu M. Organic-Inorganic Hybrid Magnets based on di- and tri-oxytriphenylamines.Thesis

241. Qi B. and Wang J. Fill factor in organic solar cells. *Phys. Chem. Chem. Phys.* **15,** 8972 (2013).

242. Jao M.-H., Liao H.-C. and Su W.-F. Achieving a high fill factor for organic solar cells. *J. Mater. Chem. A* **4,** 5784–5801 (2016).

243. Choi H. *et al.* Efficient perovskite solar cells with 13.63 % efficiency based on planar triphenylamine hole conductors. *Chemistry* **20,** 10894–9 (2014).

244. Hayward, D. O. *Quantum Mechanics for Chemists*. *Royal Society of Chemistry* (Royal Society of Chemistry, 2002). doi:10.1017/CBO9781107415324.004

245. Schrödinger E. An undulatory theory of the mechanics of atoms and molecules. *Phys. Rev.* **28,** 1049–1070 (1926).

246. Born M. and Oppenheimer R. Zur Quantentheorie der Molekeln. *Ann. Phys.* **389,** 457–484 (1927).

247. Dorsett H. and White A. Overview of molecular modelling and ab initio molecular orbital methods suitable for use with energetic materials. *Def. Sci. Technol. Organ.* 45 (2000).

248. Sherrill C. D. An Introduction to Hartree-Fock Molecular Orbital Theory. *Sch. Chem. Biochem. Georg. Inst. Technol.* 1–8 (2000).

249. Koch W. and Holthausen M. C. *Wolfram Koch , Max C . Holthausen A Chemist ' s Guide to Density Functional Theory*. *Neural Networks* **3,** (2001).

250. Lee C., Yang W. and Parr R. G. Development of the Colle-Salvetti correlation-energy formula into a functional of the electron density. *Phys. Rev. B* **37,** 785–789 (1988).

251. Burke K. and Wagner L. O. DFT in a nutshell. *International Journal of Quantum Chemistry* **113,** 96–101 (2013).

252. Cramer C. J. Essentials of Computational Chemistry Theories and Models Second Edition.

253. Ditchfield R., Hehre W. J. and Pople J. A. Self- Consistent Molecular- Orbital Methods. IX. An Extended Gaussian- Type Basis for Molecular- Orbital Studies of Organic Molecules. *J. Chem. Phys.* **54,** 724–728 (1971).

254. Foresman J. B. and Frisch A.. Exploring chemistry with electronic structure methods: A guide to using Gaussian. 269 (1996).

Publications

Effect of alkyl chain length on the properties of triphenylamine-based hole transport materials and their performance in perovskite solar cells.

Fuentes Pineda, Rosinda; Troughton, Joel; Planells, Miquel; Sanchez Molina, Irene; Muhith, Farmin; Nichol, Gary Stephen; Haque, Saif Ahmed; Watson, Trystan M.; Robertson, Neil.

In: Physical Chemistry Chemical Physics, 12.12.2017